Experimental Investigation of Magnetohydrodynamic Flow For An Intense Proton Target

A Dissertation Presented

by

Hee Jin Park

to

The Graduate School

in Partial Fulfillment of the

Requirements

for the Degree of

Doctor of Philosophy

in

Mechanical Engineering

Stony Brook University

May 2009

Stony Brook University

The Graduate School

Hee Jin Park

We, the dissertation committee for the above candidate for the

Doctor of Philosophy degree,

hereby recommend acceptance of this dissertation.

Foluso Ladeinde, Dissertation Co-Advisor,
Professor, Department of Mechanical Engineering

Harold G. Kirk, Dissertation Co-Advisor,
Physicist, Department of Physics, Brookhaven National Laboratory

---

Lili Zheng, Chairperson of Defense,
Professor, Department of Mechanical Engineering

Kirk T. McDonald , Outside Member,
Professor, Physics Department, Princeton University

James Glimm, Outside Member,
Professor, Department of Applied Math. & Stat., Stonybrook University

This dissertation is accepted by the Graduate School.

Lawrence Martin
Dean of the Graduate School

Abstract of the Dissertation

Experimental Investigation of Magnetohydrodynamic Flow For An Intense Proton Target

by

Hee Jin Park

Doctor of Philosophy

in

Mechanical Engineering

Stony Brook University

2009

Efficient production of pions can be achieved by colliding an intense proton beam with a high-Z target. The experiments of Hg jet on the interaction of an intense proton beam in magnetic field has been carried out for the thesis work. The primary diagnostics in this work employed the technique of back-illuminated laser shadow photography to freeze the transient events. The images are recorded by several high speed cameras. The performance of the optical diagnostic system is presented.

Flowing mercury in a magnetic field causes induced currents, which produce distortions of the mercury jet. The effect of Lorentz force is investigated theoretically in a stability analysis of the conducting flow in the presence of a magnetic field. The effects of Lorentz force on the vortices are also investigated

qualitatively. The role of joule damping as a loss on a time scale of magnetic damping term in global kinetic energy is discussed.

Quantitative and qualitative data analysis using image processing based on probability approach is described. The experimental measurement of the various dynamic behaviors of Hg jet in magnetic field through image processing is presented. In experiment, it is observed that the imposition of magnetic field tends to suppress the fluctuating motion in Hg jet and correspondingly the jet surface is more stabilized, where the Re is large enough and the Re_m is 0.26. Finally, the disruption of Hg jet with the proton beam and the magnetic field effect to its suppression are presented. The collected images of beam-jet interaction shows the response of Hg jet due to the proton beam induced energy deposition. The filament velocity induced by the energy deposition and the time response of the velocity in magnetic field is presented, where joule damping effect is explained. The experimental results investigated the the performance and feasibility of utilizing liquid jet as a target for future accelerator. The experimental key components were designed and constructed at Princeton University, ORNL, MIT Plasma Science and Fusion Center, CERN, and BNL respectively.

Table of Contents

List of Figures **xv**

List of Tables **xvi**

Acknowledgements **xvii**

Nomenclature **xxi**

1 Introduction **4**

1.1 Neutrino Factory For High Power Neutrino Beam 4

1.1.1 The concept of neutrino factory 4

1.1.2 Neutrino physics 6

1.2 A High Power Target For Neutrino Factory 7

1.2.1 Material consideration for a high power target 7

1.2.2 Moving metallic target for pion production 8

1.2.3 Free mercury jet flow in magnetic field for a high power target 9

1.2.4 Impact of the MHD mercury jet experiment for an intense proton target 11

1.3 Mercury Target Issues 12

1.3.1 Mercury jet disruption by energy deposition from an intense proton beam 12

1.3.2 Magnetohydrodynamic issues in mercury jet target . . 13

1.3.3 Overview of experimental investigation of MHD flow and discussion 14

2 Magnetohydrodynamics of Conducting Flow in Magnetic Field 21

2.1 Governing Equations for MHD Flow 23

2.1.1 Electromagnetic equations 23

2.1.1.1 *electromagnetic relation in a linear material* . 24

2.1.1.2 *Maxwell's equations* 25

2.1.2 The Navier Stokes and magnetic induction equations in a conducting liquid flow 2

2.1.2.1 *magnetic Reynolds number* 29

2.1.2.2 *frozen-in theorem in magnetic induction equation* 31

2.1.2.3 *the diffusion limit in induction equation* . . . 32

2.2 The Energy Equation in MHD 32

2.2.1 Energetics and effects of Lorentz force 33

2.2.2 Proton beam induced energy deposition and equation of state 35

2.2.3 Magnetic damping with joule dissipation 37

2.3 Vorticity Equations in MHD flow 39

2.3.1 Governing equations for vorticity 40

2.3.2 Vorticity suppression 41

2.3.2.1 *spanwise magnetic field effect to vorticity suppression* 42

2.3.2.2 *longitudinal and transverse magnetic field effect to vorticity suppression*

2.4 One Dimensional Pipe Flow in Transverse Magnetic Field . . . 45

2.4.1 Non-dimensional form of the governing equations using cylindrical coordinates 46

2.4.1.1 *boundary conditions in pipe flow* 46

2.4.2 Exact solutions of pipe flow in magnetic field 47

2.5 Stability of Conducting Flow in a Magnetic Field 48

2.5.1 Propagation of waves at an interface separating two flows in magnetic field 49

111 2.5.2 Magnetic pressure and tension 51

112 **3 Experimental Method for Investigation of Magnetohydrodynamic Mercury Jet Flo**
113 3.1 Optical Diagnostics as a Principal Diagnostics of High Power Target Experiment 57
114 3.1.1 Working principle of shadowgraph for optical diagnostics 57
115 3.1.2 Development of optical diagnostic system 59
116 3.1.2.1 *the optical imaging system and Viewports design* 60
117 3.1.2.2 *the consideration for focusing and tilting alignment of optics* 64
118 3.1.2.3 *high speed cameras and light sources* 65
119 3.1.2.4 *radiation-hardness* 68
120 3.1.2.5 *scintillating fiber channel* 69
121 3.1.3 Schematic of electronic trigger and high speed camera control 70
122 3.2 Windows Consideration as Viewports for Observation 72
123 3.2.1 Fiducial mark on windows 72
124 3.2.2 Impact resistance test 73
125 3.2.3 Pressure leaking test of sapphire windows 73
126 3.3 Integrated Experimental Setup for High Power Target 74
127 3.3.1 Mercury loop system in solenoid magnet 74
128 3.3.1.1 *the considerations in nozzle design* 75
129 3.3.2 Water jet observation for nozzle performance test . . . 76

130 **4 Experimental Investigation of Mercury Jet Flow in Magnetic Fields 89**
131 4.1 Image Analysis for Data Reduction 90
132 4.1.1 Image acquisition 90
133 4.1.2 Image processing 91
134 4.1.3 Study on the scaling length and the location of center of window 94

4.2 Motion of Mercury Jet and Stability in Magnetic Field 95
4.2.1 Jet deflection and surface flattening 95
4.2.2 Trajectory of mercury jet projectile in magnetic field . 102
4.3 Dynamics of Liquid Jet Flow From Nozzle 104
4.3.1 Jet equations for analysis 104
4.3.2 Pressure loss and magnetic effect to the Hg delivery pipe 106
4.3.2.1 *pressure loss in pipe flow* 108
4.3.2.2 *the measurement of wall tap pressure* 113

5 Interaction of an Intense Proton Beam with Hg Jet in Magnetic Field134
5.1 High Energy Proton Beam Structure 134
5.1.1 Proton synchrotron machine 134
5.1.2 Proton beam pulse length 136
5.1.3 Proton beam envelope by optics and camera screen . . 137
5.2 MARS Simulation for Energy Deposition to Mercury Jet by Proton Beam138
5.2.1 Physics model 138
5.2.2 Mercury jet modeling in MARS code 139
5.2.3 Energy deposition to mercury jet 140
5.2.3.1 *energy deposition in magnetic field* 140
5.2.3.2 *geometric distribution of energy deposition in elliptic Hg jet cross section*
5.2.3.3 *proton beam spot size to the energy deposition* 142
5.3 Observation of Interaction and Hg Jet Response to The Energy Deposition by Proton Bea
5.3.1 Hg jet pressurization by energy deposition of proton beam144
5.3.2 Observation of proton beam interaction and jet breakup 145
5.3.2.1 *energy deposition calculation with low intensity of proton beam and its ob*
5.3.2.2 *energy deposition calculation with high intensity of proton beam and its o*

5.3.3 Hg jet disruption and magnetic suppression of the disruption 147
5.3.3.1 *characteristics of beam structure in disruption length, harmonic 8 and 16*
5.3.3.2 *disruption length with 14 GeV proton beam* . 149
5.3.3.3 *disruption length with 24 GeV proton beam* . 150
5.3.3.4 *validation of measurements of Viewport 3 through comparison with Viewp*

6 Mercury Jet Surface Development in Magnetic Field 177
6.1 Filament Model on Jet Surface 177
6.1.1 Geometry of viewing mercury filaments 177
6.1.2 Distribution of filaments on jet surface 179
6.1.3 Approximation of filaments velocity 180
6.1.3.1 *first order approximation* 180
6.2 Observation of Filaments Development on Mercury Jet Surface 181
6.2.1 Image calibration 181
6.2.1.1 *image calibration with proton beam arrival signal* 181
6.2.1.2 *time delay structure of proton beam to light source triggering* 182
6.2.2 Parameter optimization with uncertainty 183
6.2.2.1 *linear curve fit for estimation of model* 183
6.2.2.2 *Levenberg-Marquardt minimization* 186
6.2.3 Filaments distribution and uncertainty of measurement 188
6.2.3.1 *onset of filamentation on jet surface* 188
6.2.3.2 *measurement of traveled distance of filament* . 188
6.2.4 Linear regression with the first order polynomial 190
6.2.4.1 *curve fit function* 190
6.2.4.2 *parameter estimation using multiple data points* 191
6.2.4.3 *filaments velocity distribution on jet surface* . 191

6.3 Velocity of Filaments on Mercury Jet Surface 193
6.3.1 Magnetic dissipation of energy 193
6.3.2 Time response of filaments in magnetic field 193
6.3.2.1 *averaged time response of filament in magnetic field* 193
6.3.2.2 *instantaneous time response of filament in magnetic field* 194
6.3.3 Beam induced filaments velocity in magnetic field . . . 195
6.3.3.1 *filaments velocity with 14 GeV beam in magnetic field* 195
6.3.3.2 *filaments velocity with 24 GeV beam in magnetic field* 195

7 Conclusions **208**

Bibliography **215**

A Tabular Data for Chapter 3 and Chapter 5 **222**
A.1 Specifications of Optics 222
A.2 Characteristic Response of 25 W Laser 224
A.3 Mercury Properties 225
A.4 Beam Program List and Disruption Length Measurements . . 226

B Image Data for Chapter 6 **237**
B.1 Images for filament velocity measurement at Viewport 2 . . . 237

C Mathematical Derivation for Chapter 2 **254**
C.1 The governing equations for MHD in cylindrical coordinates . 254
C.2 Derivation of Rayleigh's instability at an interface separating two flows in magnetic field2
C.2.1 *kinematic boundary condition at interface* 256
C.2.2 *hydrodynamic stability in magnetic field* 257
C.2.3 *dynamic boundary condition at interface* 258

List of Figures

1.1 Pion yield versus atomic mass number of the target at three proton beam energies, Osaki

1.2 Pion yield from Hg targets versus tilt angle between the target/beam axis and the solenoi

1.3 Geometry of key elements of target system and Viewports, showing the overlap between t

1.4 Schematics of the relative overelap between proton beam axis, Hg jet axis , and solenoid r

2.1 Wave-shaped interface separating two different fluids traveling at different average speeds

2.2 Axes and electrodes of circular duct. 54

2.3 Energy decay in magnetic field. a.)Normalized energy decay. b.)Dissipation of normalized

3.1 Displacement of light beam for shadowgraph. 78

3.2 Design of optical layout and installation of 4 Viewports of primary containment vessel. a.

3.3 Photograph of optical head assembly and its illumination of laser. a.) Front view of optic

3.4 Polished fiber end, 50X and 800X magnifications, respectively 81

3.5 Schematic of synchronized signal of high speed camera and laser pulse. 82

3.6 The triggering time for high speed camera upon beam arrival. 83

3.7 Schematic of electrical triggering and high speed camera control in tunnel for experiment.

3.8 Top fiducial on the front window and bottom fiducial on the rear window. a.) Photo of fi

3.9 Photographs of the entire MERIT experiment. a.) Sectional side view of mercury loop sy

4.1 Image data conversion for image analysis. a.) Collected image data. b.) 2 bit scaled imag

4.2 Sensitivity of threshold in a 2 bit scaled image conversion. . . 118
4.3 Jet height determination from image analysis. a.) Histogram of number of events in the j
4.4 Mercury jet flows as observed from the 3 Viewports. The jet flows from left to right on ea
4.5 Same as Fig. 4.4 but with a jet velocity of 20 m/s. a.) B=0T. b.) B=0T. c.) B=0T. d.) I
4.6 Calculated solenoid magnetic induction field map. a.) Radial field map. b.) Axial field m
4.7 Hg jet height measurement in magnetic fields. a.) Histogram fitting of number of events.
4.8 Comparison of Hg jet deflection ratio at 15 T to that at 10 T. a.) Numerical calculation c
4.9 Intermittency of Hg jet at Viewport 2. The jet velocity is 15 m/s. a.) B=0T. b.) B=5T.
4.9 Intermittency of Hg jet at Viewport 2. The jet velocity is 20 m/s. e.) B=0T. f.) B=5T. g
4.10 Surface fluctuations in a magnetic field. 127
4.11 Trajectory of beam axis and Hg jet axis projectile with respect to magnetic axis in magne
4.12 Hg jet angle at the center of magnetic axis (Viewport 2) as a function of magnetic field.12
4.13 Boundary layer induced by a jet emerging from a nozzle. . . . 130
4.14 Stream velocity and boundary layer thickness for various values of density ratio.131
4.15 Pipe inlet pressure for the driving jet. a.) Static pressure. b.) Dynamic pressure. 132
4.16 Longitudinal Hg jet flow velocity in magnetic field. a.) Velocity at each Viewport depend

5.1 Infrastructures for experiment at CERN. a.) Proton synchrotron and TT2 tunnel for expe
5.2 Installation of integrated experimental components in tunnel TT2/TT2A for high power t
5.3 Schematics of beam to jet interaction in magnetic field and the location of each Viewport
5.4 1 σ proton beam size at the center of magnet by optics (Efthymiopoulos, 2008).157
5.5 1 σ proton beam size by camera screen (Skoro, 2008). a.) 14 GeV beam. b.) 24 GeV bea
5.6 Beam size measured by phosphor screen monitor as a function of time interval between be
5.7 Modeling in MARS code for energy deposition calculation (Striganov, 2009). a.) Sectiona
5.8 Influence of magnetic field to the energy deposition distribution to Hg jet considering exp
5.9 Radial energy deposition distribution along jet axis. a.) Along jet axis. b.) Along radial a

5.10 Energy deposition distribution per proton according to the variation of beam spot size alo
5.11 Peak energy deposition and total energy deposition per proton according to the beam spo
5.12 Peak energy deposition of total number of protons. 165
5.13 Photographs of the Hg jet interaction with 16 TP, 14 GeV proton beam at 5 T. Captured
5.13 Photographs of the Hg jet interaction with 16 TP, 14 GeV proton beam at 5 T. Captured
5.13 Photographs of the Hg jet interaction with 16 TP, 14 GeV proton beam at 5 T. Captured
5.14 Qualitative comparison of the jet response incident by interaction of low intensity (3 Tp)
5.15 Qualitative comparison of the jet response incident by interaction of high intensity (10 Tp
5.16 Standard deviation of disruption length as a function of disruption length and the functio
5.17 Proton beam pulse structure of harmonic 8 and harmonic 16 in 14 GeV and 6 TP. 172
5.18 Disruption length of Hg jet depending on the beam pulse structure as a function of 14 Ge
5.19 Disruption length of Hg jet as a function of 14 GeV beam intensity and magnetic field. H
5.20 Disruption length of Hg jet and its estimation as a function of 24 GeV beam intensity and
5.21 Validation of disruption measurement for the evaluation of evolution of disruption length

6.1 Schematic geometry of viewing mercury filaments. 197
6.2 Time structures between light source enabling and proton beam arrival. 198
6.3 Photographs of filament evolution on the Hg jet surface as a function of time at 25 μs fra
6.4 Location on the Hg jet surface for velocity measurement of 14 points of filament. The sho
6.5 Illustration of curve fit for parameters estimation. a.) Multiple data points. b.) 3 data po
6.6 Approximation of velocity and onset time of filaments shown in Fig. 6.3. The beam is 10
6.7 Time response of instantaneous filament velocity at jet surface in Fig. 6.3 as a function of
6.8 Time response of averaged filament velocity as a function of magnetic field. a.) 14 GeV, 2
6.9 Time response of instantaneous filament velocity as a function of magnetic field. a.) 14 G
6.10 Filament velocity as a function of 14 GeV beam intensity and magnetic field.206
6.11 Filament velocity as a function of 24 GeV beam intensity and magnetic field.207

276 A.1 Measurement of characteristic response of 25 laser used for high speed camera at Viewpor

277 B.1 Photo of continuous 15 frames of captured image. The timing for the 1^{st} image is given ir
278 B.2 Location on the Hg jet surface for velocity measurement of filaments. The numbers above
279 B.3 Photo of continuous 15 frames of captured image. The timing for the 1^{st} image is given ir
280 B.4 Location on the Hg jet surface for velocity measurement of filaments. The numbers above
281 B.5 Photo of continuous 15 frames of captured image. The timing for the 1^{st} image is given ir
282 B.6 Location on the Hg jet surface for velocity measurement of filaments. The numbers above
283 B.7 Photo of continuous 15 frames of captured image. The timing for the 1^{st} image is given ir
284 B.8 Location on the Hg jet surface for velocity measurement of filaments. The numbers above
285 B.9 Photo of continuous 15 frames of captured image. The timing for the 1^{st} image is given ir
286 B.10 Location on the Hg jet surface for velocity measurement of filaments. The numbers above
287 B.11 Photo of continuous 15 frames of captured image. The timing for the 1^{st} image is given ir
288 B.12 Location on the Hg jet surface for velocity measurement of filaments. The numbers above
289 B.13 Photo of continuous 15 frames of captured image. The timing for the 1^{st} image is given ir
290 B.14 Location on the Hg jet surface for velocity measurement of filaments. The numbers above
291 B.15 Photo of continuous 15 frames of captured image. The timing for the 1^{st} image is given ir
292 B.16 Location on the Hg jet surface for velocity measurement of filaments. The numbers above

List of Tables

3.1 Specifications of high speed cameras. 87

3.2 Effects of irradiation up to an equivalent radiation dose of 1 Mrad on the reflectance and

4.1 Error estimation of fiducial length at each viewport. 115

4.2 Pressure head losses by geometry in pipe for mercury loop. . . 116

5.1 Measurement of vertical distances of center of jet from magnetic axis and jet size for mod

A.1 Specifications of optical components in optical diagnostics. . . 222

A.2 Properties of mercury. 225

A.3 Measured disruption length and beam shot program. 226

B.1 Properties of shots used for filaments velocity analysis. 237

ACKNOWLEDGEMENTS

The author greatly appreciates the indispensable guide and constant encouragements from Dr. Harold Kirk at Brookhaven National Laboratory and Prof. Foluso Ladeinde, who served as the author's dissertation advisor.

The author would like to express a special appreciation to Prof. Kirk McDonald at Princeton University and Dr. Thomas Tsang at Brookhaven National Laboratory for their contribution to the procedures used in this work.

The author would also like to thank Prof. Lili Zheng for agreeing to be the Chair of his dissertation committee, Prof. James Glimm, for agreeing to serve on the dissertation committee, Prof. Roman Samulyak, for valuable suggestions on the analysis of the experimental results.

This work was supported in part by the Unites States Department of Energy Contract No. DE-AC02-98CH10886. The experiment was carried out at CERN (European Organization for Nuclear Research) in Gevenva, Swizerland and the analysis performed at Brookhaven National Laboratory. The text of this dissertation in part is a reprint of the materials as it appears in Review of Scientific Instruments **79**, 045111(2008). The co-authors listed in the publication directed and supervised the research that forms the basis for this dissertation.

Nomenclature

$\mathbf{B}$	Magnetic induction field, T (Wb/m^2)
$\mathbf{H}$	Magnetic field, A/m
$\mathbf{E}$	Electric field, N/C (V/m); Global kinetic energy, J
$\mathbf{J}$	Current density, A/m^2
$\mathbf{V}$	Electric potential, V
$\mathbf{D}$	Electric displacement field, C/m^2; Energy dissipation, J/s
$\mathbf{P}$	Polarization density, C/m^2; Probability; Particle momentum, $J \cdot s/m$
$\mathbf{M}$	Magnetization density, $J/(T\ m^3)$
$\mathbf{J}$	Jacobian matrix
T	Temperature, °C (K); Time, s
$\mathbf{B}_o$	Applied magnetic field, T (Wb/m^2)
v	Directional fluid velocity, m/s; Mean velocity, m/s
U	Mean velocity in the x coordinate direction, m/s
e	Specific internal energy, J/kg
x, y, z	Cartesian coordinates, m
μ	Magnetic permeability, H/m (N/A^2)
ε	Electrical permittivity, F/m $(C^2/(N\ m^2))$
χ_e	Electrical susceptibility
χ_m	Magnetic susceptibility
ε_o	Electrical permittivity of free space, F/m $(C^2/(N\ m^2))$
μ_o	Magnetic permeability of free space, H/m (N/A^2)
t	Time, s
ϵ	Amplitude of a sinusoidal wave, m

α_v	Volume coefficient of thermal expansion, K^{-1}
c_p, c_v	Specific heat capacity, $J/(g\ K)$
λ	Wavelength of a sinusoidal wave, m
c	Wave velocity, m/s
p	Pressure, N/m^2
ρ	Density, kg/m^3
g	Gravity, m/s^2
M	Mass, kg; Molar mass, g/mol
ζ	Intermittency factor
Γ	Surface tension, N/m
γ	Ratio of specific heats, c_p/c_v
η	Absolute viscosity, $kg/(m\ s)$
ν	Kinematic viscosity, η/ρ, m^2/s
σ	Electrical conductivity, S/m; Standard deviation
κ	Compressibility, m^2/N
L	Characteristic length; Pipe length, m
τ	Joule damping term
I_T	Initial intensity of light, cd
I_o	Intensity of light, cd
ω	Vorticity, s^{-1}
ψ	Stream function, m^2/s
ϕ	Velocity potential, m^2/s
ϕ_E	Electric potential, V
E_{dep}	Energy deposition, J/g
f	Focal length, m; Force, N; Friction factor

τ	Wall shear stress, N/m^2
ξ	free surface perturbation, m
h	Head loss, m
K	Loss coefficient; Bulk modulus, N/m^2
A	Cross sectional area, m^2
e	Surface roughness, m; Error, %
a	Radius of circular pipe, Radius of jet, m
c	Local speed of sound, m/s
d	Diameter of circular pipe, Diameter of nozzle, m
D	Diameter of jet, m
R	Gas constant, $J/(K\ mol)$; Radius of curvature of the centerline of the elbow, m
G	Pressure ratio
C	Contraction coefficient; Discharge coefficient; Constant
Q	Flow rate, m^3/s
r	Residual; Radial coordinates
β	Ratio of diameter
Re_m	Magnetic Reynolds number
Re	Reynolds number
Fr	Froude number
Al	Alfv en Number
Ha	Hartmann number
We	Weber number
N	Stuart number; Number of events; Augmented Jacobian matrix
$\nabla\cdot$	Divergence operator
$\nabla\times$	Curl operator

$\times$	Cross product operator
$\cdot$	Inner product operator; Multiplication

Superscripts

$'$	Differentiation with respect to variable; Perturbation; Fluctuation
$\cdot$	Differentiation with respect to time

Subscripts

x, y, z	Component values over the cartesian coordinates
o	Component mean value, Initial value at the nozzle
R	Reference location
a	Air
l	Liquid
T	Transpose of matrix

Nomenclature

B	Magnetic induction field
H	Magnetic field
E	Electric field; Global kinetic energy
J	Current density
V	Electric potential
D	Electric displacement field; Energy dissipation
P	Polarization density
M	Magnetization density; Molar mass
T	Temperature
R	Gas constant
B_o	Applied magnetic field
v	Directional fluid velocity; Mean velocity
U	Mean velocity in the x coordinate direction
e	Specific internal energy
$x,\ y,\ z$	Cartesian coordinates
μ	Magnetic permeability
ε	Electrical permittivity
χ_e	Electrical susceptibility
χ_m	Magnetic susceptibility
ε_o	Permeability of free space
μ_o	Permittivity of free space
t	Time
ϵ	Amplitude of a sinusoidal wave; Emittance
β	Amplitude function
α_v	Volume coefficient of thermal expansion
κ	Electrical conductivity
c_p, c_v	Specific heat capacity
β	Amplitude function
λ	Wavelength of a sinusoidal wave
c	Wave velocity
p	Pressure
ρ	Density
g	Gravity
ζ	Intermittency factor
Γ	Surface tension
γ	Ratio of specific heats

η	Absolute viscosity
ν	Kinematic viscosity
σ	Electrical conductivity; Standard deviation; Gaussian beam profile
L	Characteristic length; Luminosity; Pipe length
τ	Joule damping term
I_T	Initial intensity of light
I_o	Intensity of light
ω	Vorticity
ψ	Jet growth rate with respect to time
f	Focal length; Force; Friction factor
τ	Wall shear stress
ξ	free surface perturbation
h	Head loss
K	Loss coefficient
A	Cross sectional area
e	Surface roughness; Error
a	Radius of circular pipe
d	Diameter of circular pipe
R	Radius of curvature of the centerline of the elbow
G	Pressure ratio
C	Contraction coefficient; Discharge coefficient
Q	Flow rate
β	Ratio of diameter
Re_m	Magnetic Reynolds number
Re	Reynolds number
Fr	Froude number
Al	Alfven Number
Ha	Hartmann number
We	Weber number
N	Stuart number; Number of events
$\nabla\cdot$	Divergence operator
$\nabla\times$	Curl operator
$\times$	Cross product operator
$\cdot$	Inner product operator

Superscripts

$'$	Differentiation with respect to variable; Perturbation; Fluctuation

$\cdot$	Differentiation with respect to time

Subscripts

x, y, z	Component values over the cartesian coordinates
o	Component mean value
R	Reference location

Chapter 1

Introduction

Accelerator-based sources of exceptionally intense, tightly focused beams of x rays and ultraviolet radiation make possible both basic and applied research in fields from physics to biology to technology that are not possible with more conventional equipment. The development of a high-intensity source of muons can be useful for the production of high-energy neutrino, thereby opening the door for a broad range of important new physics experiments such as neutrino oscillation. The concept is to use a high-intensity proton beam incident on a mercury jet to produce pions which decay to give the muons. These muons is magnetically captured, accelerated, and then inserted into a storage ring.

1.1 Neutrino Factory For High Power Neutrino Beam

1.1.1 The concept of neutrino factory

Accelerators are used to accelerate primary particle beams such as protons and electrons. The required statistics in the collision processes demand a very

high flux of primary particles. On interaction of the primary particles with a target, it is possible to produce secondary beams of elementary particles like pions, neutrons, and gammas. Primary protons pass through a linear accelerator and further through a synchrotron, bunch compressors, and accumulators to achieve a beam with a certain energy, intensity and beam structure. This beam is directed toward a target. On interaction with the target, secondary particles of different kinds are produced. A neutrino factory is the ultimate tool for producing a high-intensity neutrino beam to study neutrino oscillations. The neutrino factory is based on a new concept of an accelerator that produces a high-intensity, high-energy beam of muon and electron neutrinos. It will allow an investigation of a new domain in neutrino physics such as

- High intensity. Its flux is 10^3 times greater than conventional neutrino beams.
- High energy. It features a very high beam energy of 20 to 50 GeV.
- In a neutrino factory, the muon sign can be selected. Thus, it is possible to deliver particles and anti-particles.

The basic concept of the Neutrino Factory is the production of muon neutrinos and anti-electron neutrinos from the decay of muons that are circulating in a storage ring. An intense proton beam is delivered to a target, where pions are produced. These pions are collected in a solenoidal magnetic field, which can capture both charged states of pions. The pions decay into muons in a decay channel. The muon beam has both a large energy spread and transverse

emittance. The energy spread is reduced using a phase rotation, while emittance is improved by ionization cooling. The cooled beam is accelerated (in a linac followed by two recirculating linacs) to energies of 20 to 50 GeV and injected into a storage ring.

1.1.2 Neutrino physics

Muons are a promising source of neutrinos. They have a short lifetime of $2.2\mu s$. Muons cannot be produced directly, so pions have to be produced first. The first stage of a neutrino factory is thus a high-power proton driver that deliver protons onto a target, where pions are produced. These pions have to be collected and transported. After about 20m, most of the pions decay into muons. A neutrino beam can be produced from the decay of high-energy muons:

- Pions from $Proton + Material \longrightarrow \pi^{\pm} + X$
- Muons from $\pi^{\pm} \longrightarrow \mu^{\pm}\nu_{\mu}(\overline{\nu_{\mu}})$
- Neutrinos from $\mu^{\pm} \longrightarrow e^{\pm}\overline{\nu_{\mu}}\nu_{e}(\nu_{\mu}\overline{\nu_{e}})$

At this stage, the muon beam has a low phase space density and resembles more a cloud than a beam. The next step is to create a usable muon beam. Phase rotation as well as ionization cooling is applied to reduce the energy spread and the emittance of the muon beam. Once the beam is cooled, it can be accelerated to a final energy of 20 to 50 GeV. In the final stage of a

neutrino factory, the accelerated muons are injected into a storage ring with long straight sections.

1.2 A High Power Target For Neutrino Factory

1.2.1 Material consideration for a high power target

The intensity of the muon beam is directly proportional to the power of the proton beam which initiates the process. Considering that a high intensity proton beam is required in order to generate the required muons, the choice of the target material becomes a particularly important issue. Modeling studies (Osaki, Palmer, Zisman, Gallardo, 2001) point to high-Z materials being more efficient at producing pions of both signs, whereas low-Z materials are better at preventing the absorption of the produced pions. The pion yield per proton increases with the atomic number of the target, as shown in Fig. 1.1 from a MARS calculation. A high-Z material is desirable because the pion production cross-section increases with increasing Z. However, the intense proton beam would melt a target made of a solid high-Z material. A target system using a flowing stream of mercury could recycle the spent target. Several types of target material have been proposed including copper, graphite, and mercury.

Since these targets are envisaged as being stationary, one must consider the problem of removing the energy deposited by the beam without interfering with the production of the particles.

1.2.2 Moving metallic target for pion production

While schemes for moving solid targets can be envisaged (Thieberger, Kirk, Weggel, McDonald, 2003), a flowing liquid target is simpler, and mercury as a high Z material presents itself as the liquid metal. The liquid target should be in the form of a free jet, rather than being confined in containment, since the beam-induced cavitation of the liquid metal can be destructive to solid walls in the immediate vicinity of the interaction region. Another issue associated with the proton beam is the effect of the energy that it deposits in the target. The temperature of the target rises almost instantaneously after the beam pulse, resulting in large internal stresses that might crack a solid target or disperse a liquid target (Kirk *et al*, 2001). In the case of a liquid jet target, the dispersal of the jet by the beam should not be destructive to the surrounding target system components and should not adversely affect pion production during subsequent beam pulses, either on the microsecond scale, if several micro-pulses are extracted from a proton synchrotron, or on the scale of the macro-pulse period. The operation of a liquid metal jet inside a strong magnetic field raises several magnetohydrodynamic issues such as possible deformation of the jet's shape and trajectory, as well as the effect of the magnetic field on the beam-induced dispersal of the jet.

1.2.3 Free mercury jet flow in magnetic field for a high power target

The free mercury jet in magnetic field is proposed for a high power target to overcome the issues described in the above chapter. The concept is to use a high intensity proton beam incident on a Hg jet to produce pions which decay to give the muons (Gabriel *et al*, 2001). The key elements of the target system are an intense proton source, mercury jet, and capture of the generated pions in a high field solenoidal magnet (McDonald, 2001). The schematics of the key elements of the target system is described in Fig. 1.3.

Previous studies (Osaki, Palmer, Zisman, Gallaro, 2001) indicated that pion yield is maximized with a mercury target in the form of a 1 cm diameter at the interacting center, tilted by about 150 milliradian with respect to the magnetic axis. The target is tilted with respect to the axis of the capture solenoid, thus permitting the pions, whose trajectories are spirals, to leave the side of the target with a minimal probability for re-entering the target volume. The pion yield per proton increases with the atomic number of the target, as shown in Fig. 1.1 from a MARS calculation. For 24 GeV protons, a high-Z target is superior in yield. As the pions emerge from the target at large angles to the beam, and follow helical paths that may intersect the target at more than one point, it is advantageous for the target to be in the form of a narrow rod, tilted at a small angle to the magnetic axis. As shown in Fig. 1.2, suitable parameters for a mercury target are a tilt angle of 150 mrad and a target radius of 5 mm.

Based on the previous studies described in the above, the experimental setup parameters are determined. The layout of experimental setup is briefly described in the below and will be more discussed in chapter 3. Fig. 1.4 shows the detailed schematic of the overlap between key components of the experiment. The trajectory of the mercury jet overlaps with the proton beam over 30 cm. The velocity of the jet is 15 m/s. The facility is a closed piping loop, constructed primarily of 316 stainless steel, and designed to circulate liquid mercury. The parameters of the proton beam and solenoid system are determined by the required conditions of particle production rates (Alessi *et al*, 1998). Basic system parameters consist of a proton energy 24 GeV, number of protons in one bunch $\approx 3 \times 10^{13}$. Only 10 % of the beam power is absorbed inside the target. The solenoid length is 100 cm, inside radius is 7.5 cm, and a maximum magnetic field is 15 T. The solenoid magnet is titled at 67 milliradian angle with respect to the beam. The beam arrives at an angle 34 milliradian with respect to the jet which has a radius ≈ 0.5 cm, as schematically shown in Fig. 1.4. The 24 GeV proton beam is directed on to the solenoid at 67 milliradian off the solenoid axis, so that most high momentum particles do not travel straight down the beam line (Gallardo *et al*, 2001). If there are no magnetic and gravitational effects on the mercury jet trajectory, the beam should enter at the bottom surface of Hg jet at Viewport 1, which is located at approximately 30 cm from the nozzle and the beam should exit on the top surface of Hg jet at Viewport 3, which is located at approximately 60 cm from the nozzle. The required jet velocity is determined by two conditions: 1),

the need to replenish the target before the arrival of subsequent proton beam pulse, and 2), it should be high enough to overcome the deceleration force induced by Lorentz force (Hassanein, Kinkashbaev, 2001).

Initial tests involving the interaction of proton beams on mercury targets were performed at the Brookhaven Alternating Gradient Synchrotron (AGS) (Kirk *et al*, 2001), and continued at the CERN ISOLDE facility (Lettry *et al*, 2003). The BNL test featured a 24 GeV proton beam interacting with a free mercury jet with a nozzle diameter of 1 cm and a velocity of 2.5 m/s. The delivered proton bunch was focused to <1 mm radius, resulting in a peak energy deposition of 80 J/g, delivering 24 GeV proton beam at 15 Hz (Tsoupas *et al*, 2003). These initial tests did not have a magnetic field on the target. A parallel effort was undertaken to study the effects of high velocity mercury jets in the presence of high-magnetic fields, but with no proton beam.

1.2.4 Impact of the MHD mercury jet experiment for an intense proton target

The previous experiments did not perform the mercury jet in a high magnetic field interacting with an intense proton beam. In this work, we integrated the mercury jet, solenoid magnet, and intense proton beam all together. The performance and feasibility of utilizing liquid metal jet as a target for an intense proton beam is explored experimentally, which is the explicit objective of the experiment. The liquid jet target concept is recyclability otherwise the target would be destroyed. Therefore, the power of the target has to be eval-

uated in terms of the replacing capability and validated experimentally. In order to validate the performance of the target, the MHD jet behavior in a strong magnetic field has to be investigated. The response of the mercury jet due to the energy deposition by interacting with an intense proton beam has to be studied and the magnetic field effect to the disruption of mercury jet has to be studied, as well. The experimental results reveals that the effect of the Lorentz force to the jet stabilization as well as the deflection of jet. The experimental results will provide feasibility of utilizing liquid metal jet as a target for an intense proton beam. Also, the results will validate the phenomenology of conduction flow in magnetic field based on the MHD theory.

1.3 Mercury Target Issues

1.3.1 Mercury jet disruption by energy deposition from an intense proton beam

The production of large fluxes of particles using high energy, high intensity proton pulses impinging on solid or liquid targets presents unique problems which have not yet been entirely solved. The large amount of power deposition required in the material coupled with the short pulse duration produce large, almost instantaneous local heating. The resulting sudden thermal expansion can result in damage causing stresses in solids and in the violent disruption of liquid jets. The volume expansion initiates vibrations in the material. The amplitude of these vibrations is such that stresses that exceed the strength of the material can be generated, causing mechanical failure (Thieberger *et al*,

2003).

The interaction of the proton beam with the mercury target leads to very high heating rates in the target. When proton beam energy reaches approximately 100 kJ/pulse range, the heat from the beam could melt or crack a high-Z target.

1.3.2 Magnetohydrodynamic issues in mercury jet target

Liquid metal jets are proposed as potential target candidates because the heat energy can be removed along with the moving liquid. There are three important problems that are associated with the use of liquid metal targets in these environments. First, as the liquid jet penetrates the magnetic field, perturbations in jet motion and deceleration may occur because of the large field gradients at the entrance and exit of the solenoid. Second, during the intense pulse of energy deposition in a short time, the resultant stress could break up the target. Third, the liquid jet can develop instabilities in the strong inhomogeneous magnetic field and after beam interaction, because of the jet break up induced by the energy deposition of beam. Theses instabilities can change the jet shape into one that is significantly less efficient for pion production (Hassanein, Kinkashbaev, 2001).

Mercury flow in a magnetic field experiences induced currents, which cause the jet to produce transverse forces normal to jet axis direction resulting deflection normal to jet axis (Gallardo *et al*, 2001). In addition, axial currents

are induced if the jet axis does not coincide with the magnetic field axis. These axial currents produce elliptical distortions of the mercury jet. Faraday's law can be used to obtain the azimuthal current density from changing the axial field in the local coordinate system of the Hg jet. The transverse component of the magnetic field normal to the jet axis also varies along the trajectory of the mercury jet. The axial current density can be related to the changing transverse component of the magnetic field normal to the jet axis. These axial currents produce a magnetic force. This force will be balanced by a restoring force from the surface tension of the mercury, and with the condition that the mercury is an incompressible liquid, will produce an elliptic deformation of the mercury jet.

1.3.3 Overview of experimental investigation of MHD flow and discussion

A proof-of-principle experiment at the CERN Proton Synchrotron that combined a free mercury jet target with a 15T solenoid magnet and a 24 GeV primary proton beam was performed. The experiment validates the target concept for producing an intense secondary source of muons by showing the jet repetition rate to replace the disrupted target by the energy deposition from an intense proton beam. The PS runs in a harmonic-16 mode and can fill up to 2×10^{12} protons/bunch. The spot RMS size in experiment is approximately 1.5 mm. This allows up to 30 $\times 10^{12}$ protons per pulse on the mercury target, generating a peak energy deposition of 180 J/g. For this experiment, a high

magnetic field pulsed solenoid with a bore of 15 cm is designed. This magnet is capable of delivering a pulsed peak field of 15 T. which is cooled to 80 K by liquid nitrogen to reduce the resistance of its copper coils. The Hg jet delivery system generates a mercury jet from 1 cm diameter nozzle with velocities up to 15 m/s. The primary diagnostic of the beam-jet interaction is optical. A set of four view-ports along the interaction region is connected by imaging fiber-optic bundles to four high speed cameras.

Each pulse of the proton beam delivered to this system constitutes a separate experiment. About 360 beam pulses are utilized in a beam-on-demand mode at CERN. These pulses span a range of intensities and time intervals between the multiple extracted bunches per pulse. The magnet operates over a range of field strengths of 0 15 T.

In chapter 2, the full MHD governing equation using Maxwell's equations are presented. Various modeling of conducting flow in a magnetic field are formed, where the contribution of Lorentz force to the hydrodynamic equations is presented and discussed. The formulated and reviewed theory is introduced to explain and support the MHD experimental results.

In chapter 3, the detailed layout of experimental setup and its installation are presented. The design of each key components for the experiment such as nozzle, solenoid magnet and mercury loop system is presented. As a primary diagnostics, the scientific development of optical diagnostics employing the high speed cameras and infrared lasers to freeze the transient motion of mercury jet is presented and the performance of the scientific instrument as

well as the methodology to capture images are discussed in detail.

In chapter 4, 5, and 6, MHD behaviors of the mercury jet in a magnetic field are discussed based on the observation from the experiments. Also, the characteristics of the mercury jet in a magnetic field interacting with an intense proton beam are presented. The key results to validate the feasibility of the High-Z liquid target is addressed based on the experimental measurements and the beam pulse structures.

To conclude the study, the concluding remark are presented and the discussion based on the MHD theory and the experimental results is summarized in chapter 7. The discrepancy and/or consistency between expecting results from MHD theory and the experimental results are discussed and explained to leave a room for a future study.

This program explores the full variety of beam/target conditions anticipated in the design of Neutrino Factories driven by proton synchrotron of 4 MW beam power.

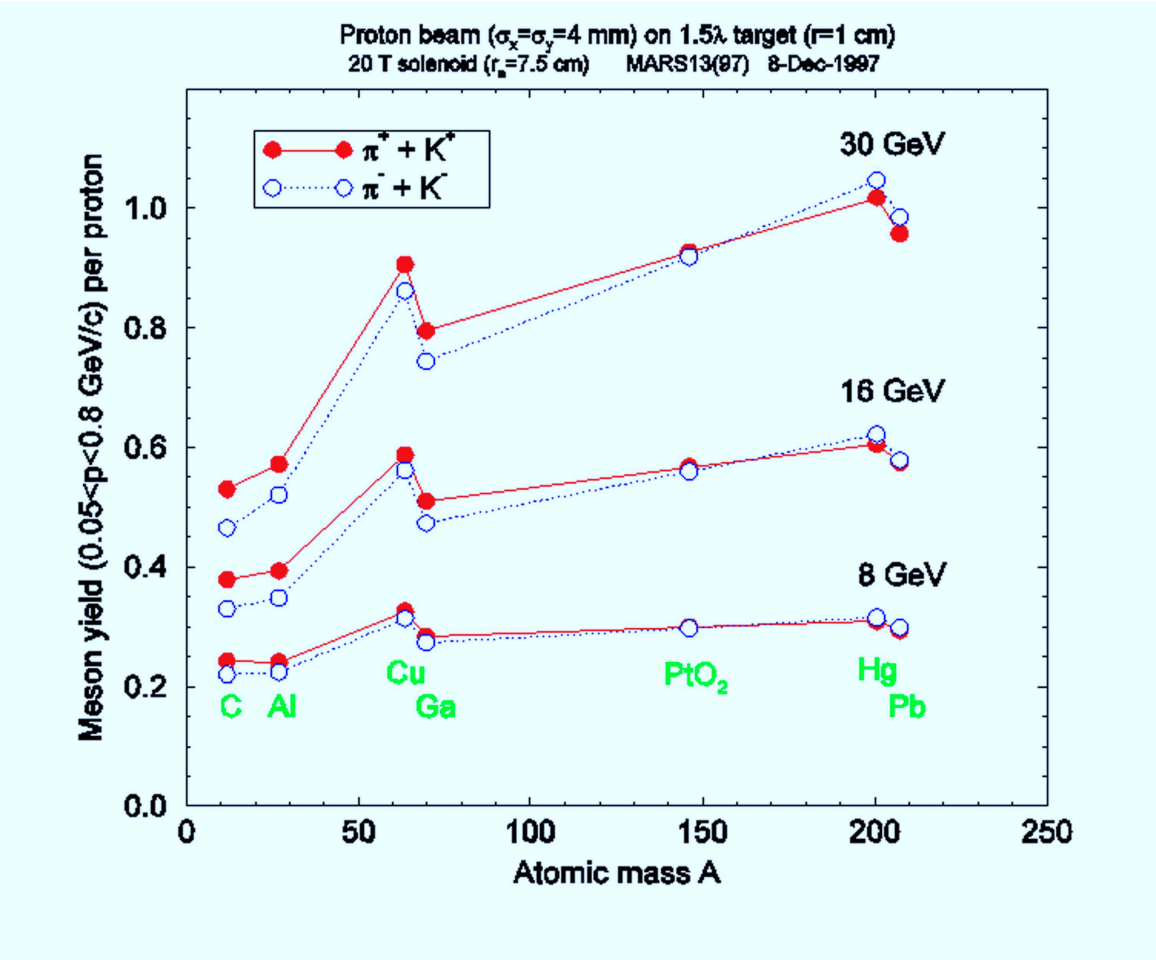

Figure 1.1: Pion yield versus atomic mass number of the target at three proton beam energies, Osaki (2001) and Mokhov (2000).

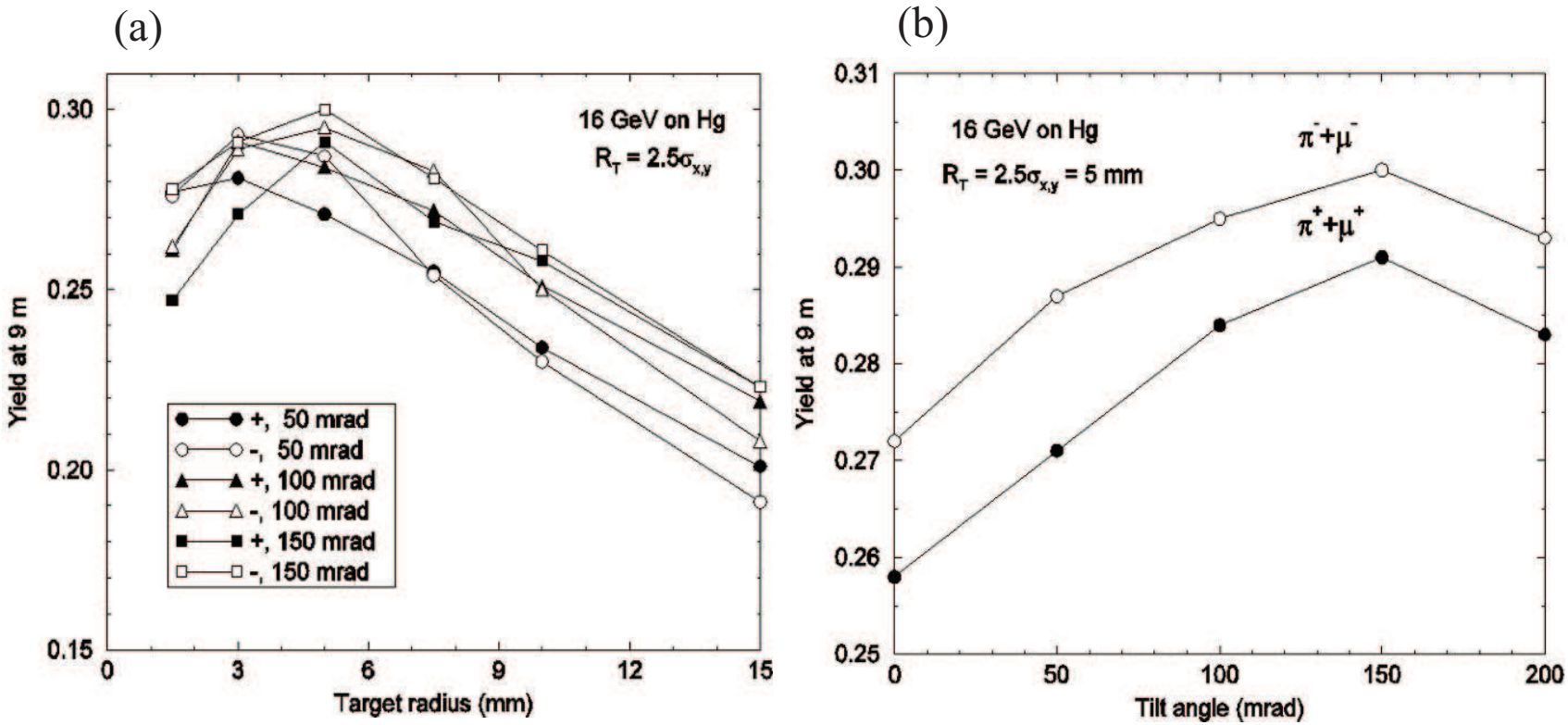

Figure 1.2: Pion yield from Hg targets versus tilt angle between the target/beam axis and the solenoid axis and versus the radius of the target, Osaki (2001) and Mokhov (2000). a.) Pion yield versus tilt angle. b.) Pion yield versus target radius.

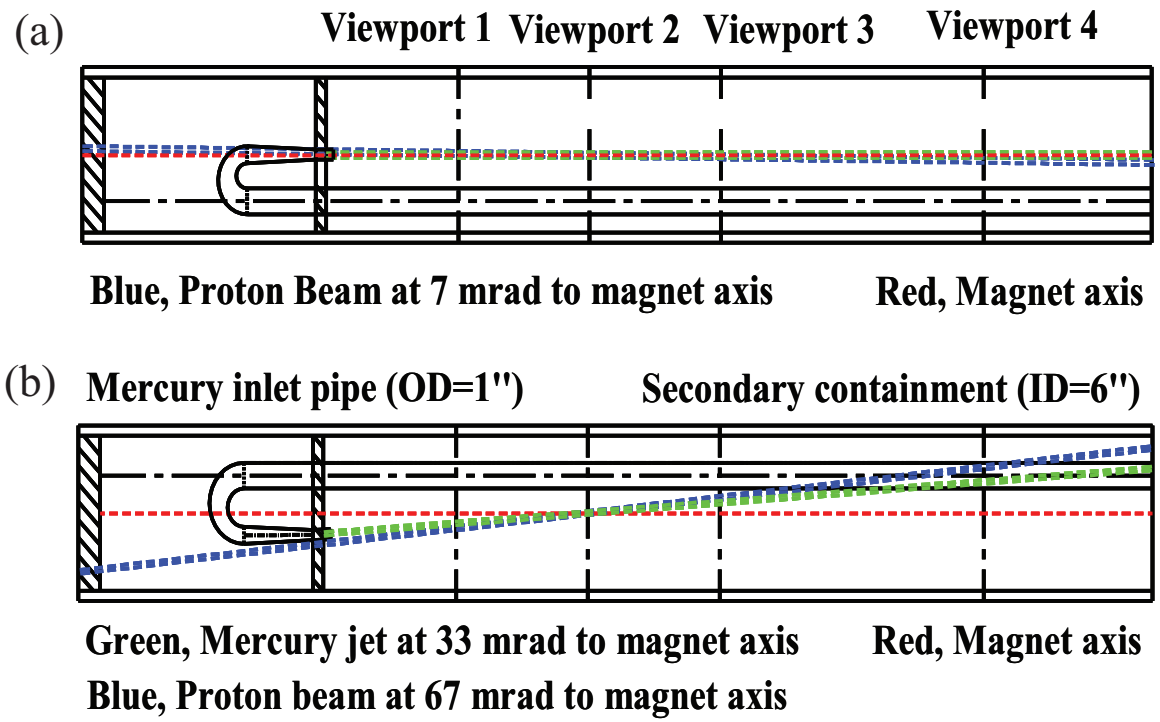

Figure 1.3: Geometry of key elements of target system and Viewports, showing the overlap between the mercury jet, magnetic axis, and the proton beam. a.) Top view. b.) Side view.

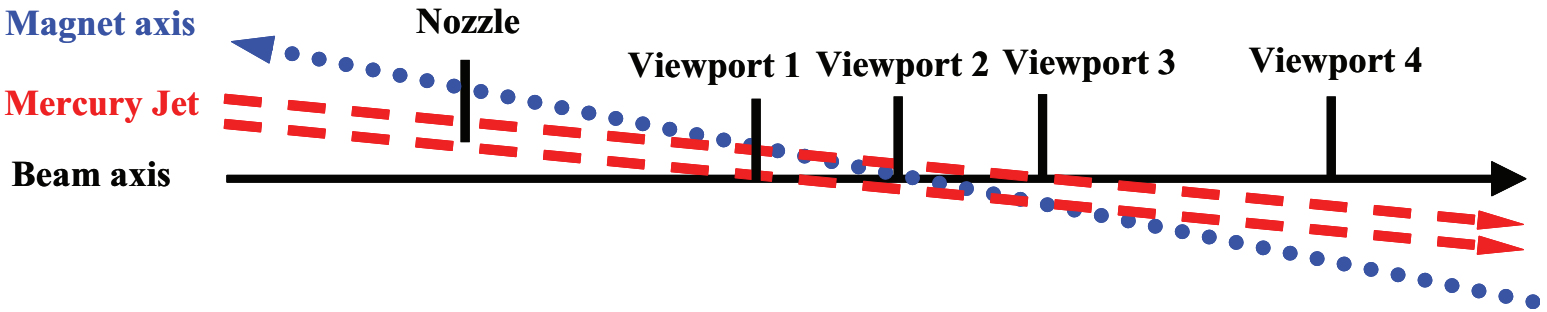

Figure 1.4: Schematics of the relative overelap between proton beam axis, Hg jet axis , and solenoid magnet axis.

Chapter 2

Magnetohydrodynamics of Conducting Flow in Magnetic Field

In this chapter, the issues of electrically conducting fluid in a pipe and jet flow in a magnetic field are presented. The governing equations for magnetohydrodynamics, based on electrodynamic relations of Maxwell's equation and hydrodynamic Navier-Stokes equation, are given and the effects of Lorenz force induced by magnetic field are discussed. The review of previous work provides a basis for these studies. Hartmann (1937) considered the flow between two parallel, infinite, non-conducting walls, with magnetic field applied normal to the walls. An exact solution was obtained for this case by Hartmann (1937). Shercliff (1953) solved the more general problem of three dimensional flow in a rectangular duct. Exact solutions demonstrated the fact that for large Hartmann number, the velocity distribution consists of a uniform core with a boundary layer near the walls. This result enabled the solution of the corresponding problem for a circular pipe in an approximate manner for large

Hartmann numbers, assuming walls of zero conductivities (Shercliff, 1956). Chang and Lundgren (1961) considered the effects of wall conductivity for the same problem. Gold (1962) considered a steady one-dimensional flow of an incompressible, viscous, electrically conducting fluid through a circular pipe in the presence of a uniform transverse field. A no-slip condition on the velocity is assumed at the electrically non-conducting wall because if the walls are conducting, there is a electromagnetic force on the wall and a corresponding force on thee fluid. The flow is along the z-axis, which coincides with the axis of the cylinder, and the uniform applied magnetic field is along the x-axis, which is normal to the flow direction. The solution is exact and valid for all values of the Hartmann number. The conducting liquid jet inside a strong magnetic field raises several magnetohydrodynamic(MHD) issues, such as the possible deformation of the jet's shape and trajectory, as well as the effect of the magnetic field on the beam-induced dispersal of the jet. The electrically conducting flow moving in a magnetic field experiences induced currents (Gallardo, 2002). These induced currents cause the jet to experience anisotropic pressure distribution with respect to the major and minor axis of jet cross section normal to the jet flowing axis while the jet penetrates the nonuniform magnetic field (Gallardo, 2002). In addition, axial currents are induced if the jet axis does not coincide with the magnetic field axis. These currents in turn produce transverse elliptical distortions of the mercury jet. Finally, the liquid jet can develop surface instabilities such as surface wavelength growing and jet breakup during both liquid motion in a inhomogeneous magnetic field and af-

ter the interaction of intense proton beam, because of the Rayleigh instabilities in a magnetic field and the sudden energy deposition leading to jet breakup. These instabilities can change the jet shape into a significantly less efficient target for pion production. The analytical approach to describe the behaviors of MHD conducting flow in a magnetic field is provided in this chapter.

2.1 Governing Equations for MHD Flow

2.1.1 Electromagnetic equations

In this section, we describe the electromagnetic relations that have been used in the derivation of the MHD governing equations. The following properties are defined as follows:

- polarization density $\mathbf{P}$: the vector field that expresses the density of permanent or induced electric dipole moments in a dielectric material. It is defined as the dipole moment per unit volume.
- magnetization density $\mathbf{M}$: the magnetic dipole moment per unit volume.
- electrical susceptibility χ_e: a measure of how easily a dielectric material polarizes in response to an electric field. This determines the electric permittivity of the material. It is defined as the constant of proportionality when relating an electric field $\mathbf{E}$ to the induced dielectric polarization density $\mathbf{P}$.
- magnetic susceptibility χ_m: the degree of magnetization of a material in response to an applied magnetic field.

- electric displacement field **D**: It accounts for the effects of bound charges within materials. It is the macroscopic field average of electric fields from charged particles that make up otherwise electrically neutral material. It can be considered the field after taking into account the response of a medium to an external field such as reorientation of electric dipoles.

- magnetic field strength **H**: A vector field that permeates space and which can exert a magnetic force on moving electric charge and on magnetic dipoles such as permanent magnets.

- electric field **E**: the electric force per unit charge. The direction of the field is taken to be the direction of the force it would exert on a positive test charge.

2.1.1.1 *electromagnetic relation in a linear material*

In a linear material, the polarization density **P** and magnetization density **M** are given by

$$\mathbf{P} = \chi_e \varepsilon_o \mathbf{E} \ , \tag{2.1}$$

$$\mathbf{M} = \chi_m \mathbf{H} \ , \tag{2.2}$$

where χ_e is the electrical susceptibility and χ_m is the magnetic susceptibility of the material. Electric displacement field, **D**, and magnetic induction

field, $\mathbf{B}$, are related to electric field, $\mathbf{E}$, and magnetic field $\mathbf{H}$ by

$$\mathbf{D} = \varepsilon_o \mathbf{E} + \mathbf{P} = \varepsilon \mathbf{E} \ , \tag{2.3}$$

$$\mathbf{B} = \mu_o (\mathbf{H} + \mathbf{M}) = \mu \mathbf{H} \ , \tag{2.4}$$

where ε is the electrical permittivity and μ is the magnetic permeability of the material.

2.1.1.2 *Maxwell's equations*

The solenoidal condition for the magnetic induction, indicating that there are no magnetic monopoles, is given by

$$\nabla \cdot \mathbf{B} = 0 \ , \tag{2.5}$$

That is there are no sources and sinks for magnetic field lines.

Faraday's law of magnetic induction is given by

$$\nabla \times \mathbf{E} = -\partial \mathbf{B} / \partial t \tag{2.6}$$

showing that a spatially varying electric field can induce a magnetic field.

Charge conservation gives

$$\nabla \cdot \mathbf{E} = \rho^* / \varepsilon_o \ , \tag{2.7}$$

where $\rho^* = \varepsilon_o (n^+ - n^-)$ is the charge density, n^+ is the number of ions, and n^- is the number of electrons.

Ampère's law is given by

$$\nabla \times \mathbf{B} = \mu \mathbf{j} + \mu\varepsilon \partial \mathbf{E}/\partial t \ , \tag{2.8}$$

where the last term on the right hand side is the displacement current. Introducing the fundamental units of mass M, length L, velocity v, and time t, we consider the dimensions of the displacement current in Eqn. (2.8). The dimensions of the magnetic field B, electric field E, and the speed of light c itself respectively are considered for simplicity.

$\nabla \times \mathbf{E} \sim \frac{E}{L}, \frac{\partial \mathbf{B}}{\partial t} \sim \frac{B}{t}$ gives $E = vB$. From the speed of light, $c = \frac{1}{\sqrt{\mu\varepsilon}}$, $\mu\varepsilon \partial \mathbf{E}/\partial t = \frac{1}{c^2} \partial \mathbf{E}/\partial t \sim \frac{1}{c^2}\frac{E}{t} = \frac{v}{c^2}\frac{B}{t} = \frac{B}{L}\frac{v^2}{c^2}$.

Therefore, The displacement current in Ampère's law can be neglected if the flow velocity is much less than the speed of light.

By assuming the flow obeys charge neutrality, $n^+ - n^- \ll n$, where n is the total number density, the charge density in Eqn. (2.7) can be neglected.

Finally, Ohm's law without Hall effect is given by

$$\mathbf{j} = \sigma(\mathbf{E} + \mathbf{v} \times \mathbf{B}) \ . \tag{2.9}$$

This is the generalization of the relation between voltage and current in a moving conductor. It provides the link between the electromagnetic equations and the fluid equations.

The electric charge is conserved, which is given by Kirchhoff's law:

$$\nabla \cdot \mathbf{j} = 0. \tag{2.10}$$

2.1.2 The Navier Stokes and magnetic induction equations in a conducting liquid flow

The motion of an electrically conducting fluid in the presence of magnetic field obeys the equations of magnetohydrodynamics. The fluid is treated as a continuum and the classical results of fluid dynamics and electro-dynamics are combined in the derivation of the equations. The first equation is from mass conservation:

$$\frac{\partial \rho}{\partial t} + \nabla \cdot (\rho \mathbf{v}) = 0 \ . \tag{2.11}$$

Next, Newton's second law of motion gives

$$\rho \frac{D\mathbf{v}}{Dt} = -\nabla p + \mathbf{F} \ , \tag{2.12}$$

where the external force $\mathbf{F}$ consists of several terms, such as the Lorentz force, given by $\mathbf{j} \times \mathbf{B}$, the gravitational force $\rho \mathbf{g}$, and the viscous force. The viscous term is given by a kinematic viscosity of the form $\rho \nu \nabla^2 \mathbf{v}$ for an incompressible flow. Thus, Eqns. (2.12) become

$$\rho \frac{\partial \mathbf{v}}{\partial t} + \rho(\mathbf{v} \cdot \nabla)\mathbf{v} = -\nabla p + \rho \mathbf{g} + \eta \nabla^2 \mathbf{v} + \mathbf{j} \times \mathbf{B} \ . \tag{2.13}$$

Note that the Lorentz force couples the fluid equations to the electromagnetic equations. Eqn. (2.13) can be reduced to a dimensionless form.

$$\frac{\partial \mathbf{v}}{\partial t} + \mathbf{v} \cdot \nabla \mathbf{v} = -\nabla p + \frac{\mathbf{g}}{\mathrm{Fr}^2} + \frac{1}{\mathrm{Re}} \nabla^2 \mathbf{v} + \mathrm{Al}(\mathbf{j} \times \mathbf{B}) \ , \tag{2.14}$$

where $\mathrm{Fr} = v/\sqrt{gL}$, $\mathrm{Re} = \rho vL/\eta$, $\mathrm{Re}_m = \mu\sigma vL$, and $\mathrm{Al} = B_o^2/\mu\rho v^2$ denote the Froude, Reynolds, magnetic Reynolds, and Alfvén numbers, respectively. The Hartmann number gives the ratio of magnetic forces to viscous forces. Thus, this number is the important parameter in cases where the inertial effects are small. On the other hand, the Stuart number gives the ratio of magnetic forces to inertial forces, Thus, this number is the important parameter where dealing with inviscid or turbulence. The Hartmann number Ha and Stuart number N are related through $\mathrm{Ha}^2 = \mathrm{ReRe}_m\mathrm{Al}$ and $\mathrm{N} = \mathrm{Re}_m\mathrm{Al}$. Note that the ratio of Hartmann number and Reynolds number represents a mixture parameters and involving viscous, magnetic, and inertial forces and can be thought of the square root of the product of the viscous and magnetic forces divided by the inertial forces.

We consider components of the magnetic induction field B_x, B_y, B_z. Note that the longitudinal magnetic field along the jet axis x and the transverse magnetic field normal to the jet axis are given by $B_x = B_X cos\theta - B_Y sin\theta, B_y = -B_X sin\theta + B_Y cos\theta$ respectively, where B_X is axial magnetic field and B_Y is radial magnetic field. Also note that the (x, y, z) coordinate system is related with the dynamics of jet dynamics and the (X, Y, Z) coordinate system is related with the magnetic field direction in solenoid. The nondimensionalized momentum equations in the (x, y, z) coordinate system in Fig. 2.1 is

represented as Eqn. (2.15) using Ohm's equation.

$$
\begin{aligned}
\frac{\partial v_x}{\partial t} + v_x \cdot \nabla v_x &= -\nabla p + \frac{1}{\mathrm{Re}}\nabla^2 v_x - \frac{\mathrm{Ha}_y^2}{\mathrm{Re}} v_x + \frac{\mathrm{Ha}_x \mathrm{Ha}_y}{\mathrm{Re}} v_y \ , \\
\frac{\partial v_y}{\partial t} + v_y \cdot \nabla v_y &= -\nabla p + \frac{1}{\mathrm{Re}}\nabla^2 v_y - \frac{\mathrm{Ha}_x^2}{\mathrm{Re}} v_y + \frac{\mathrm{Ha}_x \mathrm{Ha}_y}{\mathrm{Re}} v_x \ , \\
\frac{\partial v_z}{\partial t} + v_z \cdot \nabla v_z &= -\nabla p + \frac{1}{\mathrm{Re}}\nabla^2 v_z - \frac{\mathrm{Ha}_x^2}{\mathrm{Re}} v_z - \frac{\mathrm{Ha}_y^2}{\mathrm{Re}} v_z \ . \qquad (2.15)
\end{aligned}
$$

In MHD, to eliminate the electric field $\mathbf{E}$ and the electric current density $\mathbf{j}$, we use the Ampere's law and Ohm's law. Then, the Faraday's law gives the magnetic induction equation:

$$
\frac{\partial \mathbf{B}}{\partial t} = \nabla \times (\mathbf{v} \times \mathbf{B}) - \frac{1}{\mu\sigma} \nabla \times \nabla \times \mathbf{B} = \nabla \times (\mathbf{v} \times \mathbf{B}) + \frac{1}{\mu\sigma} \nabla^2 \mathbf{B} \qquad (2.16)
$$

2.1.2.1 *magnetic Reynolds number*

In Eqn. (2.16), the dimension of the term on the left hand side is $\frac{B}{t}$ and the second term on the right hand side is $\frac{B}{\sigma\mu L^2}$. Therefore, $\sigma\mu \sim \frac{t}{L^2}$. The magnetic induction equation can be reduced to a dimensionless form.

$$
\frac{\partial \mathbf{B}}{\partial t} = \nabla \times (\mathbf{v} \times \mathbf{B}) + \sigma\mu L v \nabla^2 \mathbf{B} \ , \qquad (2.17)
$$

where the quantity $\sigma\mu L v$ is a dimensionless number, Re_m, called the magnetic Reynolds number. Re_m is a measure of the size of the advection term , $\nabla \times (\mathbf{v} \times \mathbf{B})$, relative to the diffusion term, $\sigma\mu L v \nabla^2 \mathbf{B}$. Reynolds number Re measures the extent to which a convective process prevails over a diffusive

782 one. In viscous flow, the viscosity causes vorticity to diffuse in the face of
783 convection and the Reynolds number measures the power of convection over
784 diffusion of vorticity. In MHD, the conductivity causes convection to overcome
785 diffusion of the magnetic field to a degree measured by the magnetic Reynolds
786 number Re_m. If Re_m is large, convection dominates over diffusion and mag-
787 netic boundary layer near the fields are to be expected. The magnetic Prandtl
788 number measures the ratio of viscous diffusivity and magnetic diffusivity and
789 is defined as $\mathrm{Re}_m/\mathrm{Re}$. When it is small, magnetic fields diffuse much more
790 rapidly than vorticity and magnetic boundary layers are much thicker than
791 viscous layers. This makes for simplifications such as the neglect of viscosity
792 in the magnetic boundary layer.

793 In any region of length scale δ where convection and diffusion are equally
794 important, δ must be of order $1/\mu\sigma v$. Only within limited regions where B
795 changes significantly in a distance δ can the gradients be high enough for
796 diffusion and dissipation to matter. The characteristic time in the flow is the
797 transit time L/v, during which a field disturbance diffuses a distance of order
798 $(L/\mu\sigma v)^{1/2}$. This is much less than L if $\mathrm{Re}_m \gg 1$, in which case diffusion
799 is negligible. It will diffuse a distance of order $(t/\mu\sigma)^{1/2}$, which is negligible
800 in comparison with the length scale L if $L^2\mu\sigma/t \gg 1$. This is the required
801 criterion for the perfect conductivity approximation to be valid. At the other
802 extreme case where diffusion is dominant is that the medium diffuses to the
803 form it would be in stationary fluid, where no induced magnetic field would
804 occur. The ratio of the induced magnetic field and the imposed magnetic field

is of order $\mu\sigma vL$, which is Re_m. The low Re_m approximation is to ignore the induced field, to replace $\mathbf{B}$ by the known field $\mathbf{B}_o$ in all MHD equations.

2.1.2.2 *frozen-in theorem in magnetic induction equation*

If $\mathrm{Re}_m \gg 1$, the induction equation Eqn. (2.16) is approximated by

$$\frac{\partial \mathbf{B}}{\partial t} = \nabla \times (\mathbf{v} \times \mathbf{B}) \tag{2.18}$$

The timescale with changes due to the fluid motion from Eqn. (2.18) is given by $t_{motion} \sim \frac{L}{v}$. In the case $t_{motion} \ll t_{diffusion}$, which corresponds to $\mathrm{R}_m \gg 1$, the diffusion term is negligible. According to the frozen-flux theorem of Alfvén, in a perfectly conducting fluid, where $\mathrm{Re}_m \to \infty$, the magnetic field lines move with the fluid: the field lines are 'frozen' into the fluid. This theorem states that motions along the field lines do not change the field but motions transverse to the field carry the field with them. If the area of the flux tube is small, the field strength will be approximately constant across the area of the tube. Thus, the |B| $\times$ cross sectional area is constant so that the field strength becomes stronger if the cross sectional area is reduced by the fluid motion. The vorticity flux through any loop moving with the fluid is constant and the particles which initially lied on a vorticity line continue to do so. All the fluid particles which initially lie on a magnetic field line continue to do so in a perfect conductor.

2.1.2.3 *the diffusion limit in induction equation*

If $\mathrm{Re}_m \ll 1$, the induction equation Eqn. (2.16) is approximated by

$$\frac{\partial \mathbf{B}}{\partial t} = \frac{1}{\mu\sigma}\nabla^2\mathbf{B} \tag{2.19}$$

The timescale with changes due to field diffusion from Eqn. (2.19) is given by $t_{diffusion} \approx \sigma\mu L^2$. The diffusion equation indicates that any irregularities in an initial magnetic field will diffuse away and be smoothed out. The field will tend to be a simpler uniform field. This process of smoothing out will occur on the given diffusion timescale.

2.2 The Energy Equation in MHD

In general, the energy equation can be written in the form

$$\frac{\rho^\gamma}{\gamma - 1}\frac{D}{Dt}\left(\frac{p}{\rho^\gamma}\right) = -\mathbf{D} \ , \tag{2.20}$$

where $\mathbf{D}$ is the total energy loss function, γ is the ratio of specific heats, c_p/c_v. The energy loss function consists of thermal conduction, radiation, and heating. The heating consists of several terms, such as small scale magnetic wave heating, ohmic heating, and viscous heating. However, such losses (gains) can be neglected if the medium is either isentropic or adiabatic. There are cases where no energy is added to the flow and no energy losses occur. The adiabatic

term can be represented as follows, using Eqn. (2.11):

$$\rho^\gamma \frac{D}{Dt}(\frac{p}{\rho^\gamma}) = \frac{\partial p}{\partial t} + \mathbf{v}\cdot\nabla p + \gamma p \nabla\cdot\mathbf{v} = -(\gamma-1)\mathbf{D}. \tag{2.21}$$

To close the system of equations, an equation of state is needed, which is taken as ideal gas law:

$$p = \frac{\rho}{M}RT\ , \tag{2.22}$$

where M is molar mass and R is the gas constant ($8.3\ J\cdot mol^{-1}K^{-1}$).

2.2.1 Energetics and effects of Lorentz force

The energy equation that contains all the various types of energy, including kinetic energy, gravitational energy, the internal energy, and the magnetic energy is obtained using the MHD governing equations. The gravitational potential Φ is defined by $-\nabla\Phi = \mathbf{g}$. The kinetic energy is obtained by multiplying Eqn. (2.11) by $v^2/2$ and dotting Eqn. (2.12) with $\mathbf{v}$. The energy equation can then be written as

$$\frac{\partial}{\partial t}(\frac{1}{2}\rho v^2) + \nabla\cdot(\frac{1}{2}\rho v^2\mathbf{v}) = -\mathbf{v}\cdot\nabla p + \mathbf{v}\cdot(\mathbf{j}\times\mathbf{B}) - \mathbf{v}\cdot\rho\nabla\Phi + \mathbf{v}\cdot\eta\nabla^2\mathbf{v}\ . \tag{2.23}$$

The gravitational term can be expressed as follows using Eqn. (2.11) and the fact that $\partial\Phi/\partial t = 0$.

$$\mathbf{v}\cdot\rho\nabla\Phi = \nabla\cdot(\rho\Phi\mathbf{v}) + \frac{\partial}{\partial t}(\rho\Phi)\ . \tag{2.24}$$

Eqn. (2.24) gives the flux of the gravitational potential energy and the rate of change of gravitational potential energy in time. The Lorentz force term can be expressed as follows using Eqn. (2.9):

$$\mathbf{v} \cdot (\mathbf{j} \times \mathbf{B}) = -\mathbf{j} \cdot (\mathbf{v} \times \mathbf{B}) = -\frac{j^2}{\sigma} + \mathbf{j} \cdot \mathbf{E} \ . \tag{2.25}$$

Eqn. (2.25) is rearranged using Eqn. (2.6):

$$\mathbf{v} \cdot (\mathbf{j} \times \mathbf{B}) = -\frac{j^2}{\sigma} - \nabla \cdot (\frac{\mathbf{E} \times \mathbf{B}}{\mu}) - \frac{\partial}{\partial t}(\frac{B^2}{2\mu}) \ . \tag{2.26}$$

The pressure gradient term gives

$$-\mathbf{v} \cdot \nabla p = -\nabla \cdot (p\mathbf{v}) + p \nabla \cdot \mathbf{v} \ . \tag{2.27}$$

Eqn. (2.27) can also be expressed as follows using Eqn. (2.21):

$$p \nabla \cdot \mathbf{v} = -\frac{\partial}{\partial t}(\frac{p}{\gamma - 1}) - \nabla \cdot (\frac{p}{\gamma - 1}\mathbf{v}) - \mathbf{D} \ . \tag{2.28}$$

Substituting the foregoing relations, the full energy equation can be expressed as

$$\frac{\partial}{\partial t}[\frac{1}{2}\rho v^2 + \rho\Phi + \frac{p}{\gamma - 1} + \frac{B^2}{2\mu}] + \nabla \cdot \{[\frac{1}{2}\rho v^2 + \rho\Phi + \gamma\frac{p}{\gamma - 1}]\mathbf{v} + \frac{\mathbf{E} \times \mathbf{B}}{\mu}\} = -\frac{j^2}{\sigma} - \mathbf{D} \ . \tag{2.29}$$

2.2.2 Proton beam induced energy deposition and equation of state

Due to the sudden energy deposition by proton beam, it is worthy to consider the components of added energy and the state of energy from compressible density variation as well as ionization to the right hand side of full energy equation Eqn. (2.29. The instantaneous beam energy deposition is

$$E_{beam}(r) = E_{beam}(r) \cdot \delta(t - t_{beam}), \tag{2.30}$$

where

$$E_{beam}(r) = E_o exp[-\frac{r}{a}] \tag{2.31}$$

and

$$E_o = \frac{E_{beam}}{\pi r_{beam}^2}. \tag{2.32}$$

E_{beam} (r) is radial energy density distribution of the beam and the proton beam energy is assumed to be deposited as a δ function at time $t = t_{beam}$. E_{beam} is the peak energy deposition corresponding to the beam spot radius r_b. The equation of state (EOS) is considered as the sum of compression, ion thermal, and electron thermal terms. The EOS can be expressed for simplification. The compressible pressure P_c and energy E_c are

$$P_c = P_{co}[(\frac{\rho}{\rho_o})^\gamma - 1], \tag{2.33}$$

$$E_c = E_{co}[(\frac{\rho}{\rho_o})^{\gamma-1} - 1]\frac{\rho}{\rho_o} + P_{co}(1 - \frac{\rho}{\rho_o}), \tag{2.34}$$

where

$$P_{co} = \frac{\rho c^2}{\gamma} \quad , \quad E_{co} = \frac{P_{co}}{\gamma - 1}. \tag{2.35}$$

Ion and electron thermal pressure and energy are

$$E_I = 3nk(T - T_o) \quad , \quad P_I = G_I E_I \quad , \tag{2.36}$$

$$E_e = \frac{1}{2}\beta(T - T_o)^2 \quad , \quad \beta = \beta_o(\frac{\rho_o}{\rho})^{2/3} \quad , \quad P_e = G_e E_e, \tag{2.37}$$

where $n = \frac{\rho}{M}$ and k is Boltzmann's constant. Thus, the total energy and pressure are

$$E = E_c + E_I + E_e \quad , \quad P = P_c + P_I + P_e \quad , \tag{2.38}$$

where subscripts c, I, and e correspond to compression, ion thermal, and electron thermal components, respectively. G_I and G_e are the Gruneisen coefficients for the ion and electron. c is the speed of sound in the material. Initial mercury pressure P is 0 at $T = T_o = T_{melting}$ and normal density $\rho = \rho_o$. At higher temperatures, the mercury can be ionized and the resulting energy and pressure by free-electron component is added to the EOS. Accordingly, the solid state partition of the electron thermal energy and pressure decreases $(1 - f_z)$ times, where f_z is the ionization fraction.

2.2.3 Magnetic damping with joule dissipation

It is known that a static magnetic field can suppress motion of an electrically conducting liquid. If a conducting liquid moves through an imposed static magnetic field, electric currents are generated. These, in turn, lead to ohmic heating such as Joule dissipation. As the thermal energy of the fluid rises, there is a corresponding drop in its kinetic energy, and so the fluid decelerates. This is to suppress the motion of liquid jets. In many applications, it is believed that the imposition of a static magnetic field is used as one means of suppressing unwanted motion. Considering the uniform perpendicularly imposed magnetic field to the flow direction for simplicity, the damping effect of Lorentz force can be quantified. If the magnetic field is uniform, the Faraday' law requires that $\nabla \times \mathbf{E} = 0$. Using Ohm's law and the fact that the current density is solenoidal, the current relationship is given by

$$\nabla \cdot \mathbf{J} = 0 \quad , \quad \nabla \times \mathbf{J} = \sigma \mathbf{B} \cdot \nabla \mathbf{v} \ . \tag{2.39}$$

Thus, $\mathbf{J}$ is zero if $\mathbf{v}$ is independent of the magnetic field direction. By doing cross product of $\mathbf{J}$ and $\mathbf{B}$ and using the vector identity, Lorentz force per unit mass is given by

$$\mathbf{F} = -\frac{\mathbf{v}}{\tau} + \frac{\sigma(\mathbf{B} \times \nabla \phi_E)}{\rho} \ , \tag{2.40}$$

where $\tau = \rho/\sigma B^2$ is Joule damping term and ϕ_E is electrical potential, which is given by the divergence of Ohm's law: $\phi_E = \nabla^{-2}(B \cdot \omega)$. The Lorentz

force then simplifies to $-\mathbf{v}/\tau$ when the magnetic field and the vorticity field are mutually perpendicular. Thus, the perpendicular $\mathbf{v}$ to magnetic field declines on a time scale of τ, which clearly explains the mechanism of magnetic damping. The ratio of the damping time τ to the characteristic time L/v gives the interaction parameter $\mathrm{N} = \sigma B^2 L/\rho v$, which is also used for the indication of the ratio of the magnetic and inertial forces.

To investigate the role of Joule dissipation, consider the fully derived energy equation in inviscid flow.

$$\frac{dE}{dt} = -\frac{1}{\sigma\rho}\int \mathbf{J}^2 dV = -\mathbf{D} \ , \tag{2.41}$$

where $\mathbf{D}$ is joule dissipation and E is global kinetic energy.

$\mathbf{J}^2$ from Eqn. (2.39) was estimated (Davidson, 1999) and is given.

$$\frac{dE}{dt} \sim -(\frac{L_{min}}{L_{\parallel}})^2 \frac{E}{\tau} \ , \tag{2.42}$$

from which

$$E \sim E_o \ \ exp\ (-\tau^{-1}\int_0^t (L_{min}/L_{\parallel})^2 dt) \ , \tag{2.43}$$

where $L_{\parallel}$ is the characteristic length for the flow, parallel to the magnetic field. Fig. 2.3 (a) shows the decay of energy depending on the Joule damping term with various magnetic field. The energy is dissipated as a result of energy decay by Joule dissipation. So, the time constant required for energy dissipation is getting smaller as the magnetic field strength increases. As a result, the magnetic field affect to the integration of energy, which is shown in

Fig. 2.3 (b). It indicates that the flow decays on a time scale of τ provided that L_{min} and $L_{\|}$ are of the same order. However, the Lorentz force can not create or destroy linear (angular) momentum despite the Joule dissipation. This indicates that the flow can not be decayed on a time scale of τ and the Eqn. (2.42) and (2.43) infer that $L_{min}/L_{\|}$ must increase with time. Therefore, it is expected that these flow will experience anisotropy, with $L\|$ increasing as the flow evolves.

2.3 Vorticity Equations in MHD flow

The possibility of using an electromagnetic field for vortices control in conducting fluids needs to be investigated. Electromagnetic force can influence the stability of a flow, thus prevents its transition to turbulence by suppressing disturbances or changing mean velocity profiles. A significant drag reduction is possible when the surface boundary condition is modified to suppress the vortices. Transverse magnetic field does not reduce drag because the magnetic field increases the skin friction drag by directly altering the mean flow, so called Hartmann flow, even though turbulent fluctuations are significantly reduced. The longitudinal magnetic field does not directly interact with the mean flow although it can reduce turbulent fluctuations. Thus it is possible that the longitudinal magnetic field can result in drag reduction.

2.3.1 Governing equations for vorticity

It is useful to transform the governing equations in terms of vorticity transport. The equation for the vorticity ω of an incompressible conducting fluid in MHD is

$$\begin{aligned} &\frac{\partial \omega}{\partial t} + (\mathbf{v}\cdot\nabla)\omega - (\omega\ \cdot\nabla)\mathbf{v} \\ &= \nu\nabla^2\omega + \frac{1}{\rho}\nabla\times(\mathbf{j}\times\mathbf{B}) \\ &= \nu\nabla^2\omega + \frac{1}{\rho}\{(\mathbf{B}\cdot\nabla)\mathbf{j} - (\mathbf{j}\cdot\nabla)\mathbf{B}\}\ . \end{aligned} \tag{2.44}$$

The term $(\omega\cdot\nabla)\mathbf{v}$ in Eqn. (2.44) expresses the effect of stretching and turning vorticity lines. From the Faraday's law and $\partial\mathbf{B}/\partial t = 0$, the electric field in terms of an electric potential, ϕ_E, is

$$\mathbf{E} = -\nabla\phi_E\ . \tag{2.45}$$

From the Ohm's law, Kirchhoff's law, and Eqn. (2.45), the electromagnetic equation can be simplified as Eqn. (2.47) using nondimensionalized Ohm's law Eqn. (2.46).

$$\mathbf{j} = \mathrm{Re}_m(-\nabla\phi_E + \mathbf{v}\times\mathbf{B})\ . \tag{2.46}$$

$$\nabla^2\phi_E = \nabla\cdot(\mathbf{v}\times\mathbf{B})\ . \tag{2.47}$$

The important parameter in vortices dynamics is the Stuart number N ($= \mathrm{Re}_m \mathrm{Al} = \sigma \mathbf{B}^2 L/\rho v$), which is the ratio of the electromagnetic force to the inertial force. Therefore, one can fix the Reynolds number and change the Stuart number to see the effect of magnetic field over the vortices strength. The Hartmann numbers, $\mathrm{Ha} = \sqrt{\mathrm{ReN}}$, can be determined correspondingly. The Stuart number gives the ratio of Ha to Re. Thus, the Stuart number will indicate the stabilizing effect of magnetic field to the unique characteristic of transition to turbulence.

2.3.2 Vorticity suppression

The vorticity is suppressed by the magnetic field, transverse to the vorticity. The result is altered if the conductivity σ is nonuniform and varies with coordinates, in which case vorticity will be created. When a conducting liquid flows along a pipe with an axial magnetic field, there will be no magnetic effect if the motion is laminar, though the vorticity is perpendicular to the magnetic field, but if the flow is turbulent, adding the field damps the turbulence and reduces the Reynolds stresses and the frictional drag. Adding the field also raises the critical Reynolds number for instability of flow (Shercliff, 1965).

2.3.2.1 *spanwise magnetic field effect to vorticity suppression*

For a spanwise magnetic field, B $= (0, 0, B_z)$, the corresponding Lorentz force, f $= (f_x, f_y, f_z)$ can be represented as follows.

$$f_x = \mathrm{N}(-\frac{\partial \phi_E}{\partial y} B_z - B_z^2 v_x) \ ,$$
$$f_y = \mathrm{N}(\frac{\partial \phi_E}{\partial x} B_z - B_z^2 v_y) \ ,$$
$$f_z = 0 \ . \tag{2.48}$$

Introducing the stream function ψ,

$$\frac{\partial^2 \psi}{\partial x^2} + \frac{\partial^2 \psi}{\partial y^2} = -\omega_z \ , \tag{2.49}$$

where the spanwise vortex $\omega_z = \partial v_y / \partial x - \partial v_x / \partial y$. The Ohm's law Eqn. (2.47) yields

$$\frac{\partial^2 \phi_E}{\partial x^2} + \frac{\partial^2 \phi_E}{\partial y^2} = \omega_z \ , \tag{2.50}$$

where unity quantity of B_z is assumed.

From Eqn. (2.47) and (2.50), $\phi_E = \psi + const.$ Correspondingly this relation yields $\mathbf{f} = 0$. Therefore, the spanwise vortex flow is not affected by the spanwise magnetic field (Lim, 1998). However, it can reduce turbulent fluctuations without directly interacting with the mean flow.

2.3.2.2 *longitudinal and transverse magnetic field effect to vorticity suppression*

For longitudinal and transverse magnetic field $\mathbf{B} = (B_x, B_y, 0)$ in a two dimensional flow, Eqn. (2.47) yields $\nabla^2 \phi_E^2 = 0$ assuming that there is no velocity (v_z) onto the normal to the flow direction. The corresponding forces can be represented as follows:

$$
\begin{aligned}
f_x &= \mathrm{N}(B_y \frac{\partial \phi_E}{\partial z} - B_y^2 v_x + B_x B_y v_y) \ , \\
f_y &= \mathrm{N}(-B_x \frac{\partial \phi_E}{\partial z} - B_x^2 v_y + B_x B_y u_x) \ , \\
f_z &= \mathrm{N}(-B_y \frac{\partial \phi_E}{\partial x} + B_x \frac{\partial \phi_E}{\partial y} - B_x^2 v_z - B_y^2 v_z) \ .
\end{aligned} \tag{2.51}
$$

The effect of the longitudinal and transverse magnetic field on the strength of spanwise vortices can be shown from the vorticity equation where additional vortices term $\omega_{Lorentz} = \nabla \times \mathbf{f}$ caused by the Lorentz force has been added.

$$
\begin{aligned}
&\frac{\partial \omega_z}{\partial t} + (\mathbf{v} \cdot \nabla)\omega_z = (\omega_z \cdot \nabla)\mathbf{v} + \frac{1}{\mathrm{Re}} \nabla^2 \omega_z + \mathrm{N} \ (\ -B_x \frac{\partial^2 \phi_E}{\partial x \partial z} \\
&- B_y \frac{\partial^2 \phi_E}{\partial y \partial z} + B_x B_y (\frac{\partial v_x}{\partial x} - \frac{\partial v_y}{\partial y}) - B_x^2 \frac{\partial v_y}{\partial x} + B_y^2 \frac{\partial v_x}{\partial y} \ ) \ .
\end{aligned} \tag{2.52}
$$

If we consider the longitudinal magnetic field $\mathbf{B} = (B_x, 0, 0)$ and the transverse magnetic field $\mathbf{B} = (0, B_y, 0)$ independently, the corresponding force can

be shown in Eqn. (2.53), Eqn. (2.54) respectively.

$$
\begin{aligned}
f_x &= 0 \ , \\
f_y &= \mathrm{N}(-B_x \frac{\partial \phi_E}{\partial z} - B_x^2 v_y) \ , \\
f_z &= \mathrm{N}(B_x \frac{\partial \phi_E}{\partial y} - B_x^2 v_z) \qquad .
\end{aligned} \tag{2.53}
$$

$$
\begin{aligned}
f_x &= \mathrm{N}(B_y \frac{\partial \phi_E}{\partial z} - B_y^2 v_y) \ , \\
f_y &= 0 \ , \\
f_z &= \mathrm{N}(-B_y \frac{\partial \phi_E}{\partial x} - B_y^2 v_z) \ .
\end{aligned} \tag{2.54}
$$

Eqns. (2.53) and (2.54) clearly show that the Lorentz force retards the local velocity. The vorticity equation is shown as Eqn. (2.55), Eqn. (2.56).

$$
\frac{\partial \omega_z}{\partial t} + (\mathbf{v} \cdot \nabla)\omega_z = (\omega_z \cdot \nabla)\mathbf{v} + \frac{1}{\mathrm{Re}} \nabla^2 \omega_z + \mathrm{N}(-B_x \frac{\partial^2 \phi_E}{\partial x \partial z} - B_x^2 \frac{\partial v_y}{\partial x}) \ . \tag{2.55}
$$

$$
\frac{\partial \omega_z}{\partial t} + (\mathbf{v} \cdot \nabla)\omega_z = (\omega_z \cdot \nabla)\mathbf{v} + \frac{1}{\mathrm{Re}} \nabla^2 \omega_z + \mathrm{N}(-B_y \frac{\partial^2 \phi_E}{\partial y \partial z} + B_y^2 \frac{\partial v_x}{\partial y}) \ . \tag{2.56}
$$

The Lorentz force is negatively correlated with the spanwise vorticity. Therefore, the Lorentz force induced by the longitudinal and transverse magnetic field reduces the strength of the spanwise vorticity effectively.

2.4 One Dimensional Pipe Flow in Transverse Magnetic Field

In one-dimensional problem, the governing equations and the boundary conditions are assumed that there is only one component of the velocity, v_z, and only one component of the induced magnetic field, $\mathbf{B}_z$, along with the applied field $\mathbf{B}_o$, so that the total velocity and magnetic fields are given by

$$v_r = v_\theta = 0, \quad v_z = v_z(r,\theta), \quad B_r = B_o \cos\theta \ ,$$
$$B_\theta = -B_o \sin\theta, \quad B_z = B_z(r,\theta) \ . \tag{2.57}$$

Substituting these expressions into Eqn. (2.13) using cylindrical coordinates, we obtain

$$p(r,\theta,z) = -(1/2\mu)B_z^2 + O_1 z + O_2 \ , \partial p/\partial z = O_1 = constant \ , \tag{2.58}$$

$$O_1 = \eta[\frac{\partial^2 v_z}{\partial r^2} + (\frac{1}{r})\frac{\partial v_z}{\partial r} + (\frac{1}{r^2})\frac{\partial^2 v_z}{\partial \theta^2}] + (\frac{1}{r})B_\theta \frac{\partial B_z}{\partial \theta} + B_r \frac{\partial B_z}{\partial r} \ , \tag{2.59}$$

where O_2 is a constant.

Eqn. (2.5), Eqn. (2.11), Equation (2.57) are identically satisfied and Eqns. (2.16) become

$$\frac{1}{\mu\sigma}[\frac{\partial}{\partial r}(r\frac{\partial B_z}{\partial r}) + (\frac{1}{r})\frac{\partial^2 B_z}{\partial \theta^2}] + [B_r \frac{\partial}{\partial r}(r v_z) + \frac{\partial}{\partial \theta}(v_z B_\theta)] = 0 \ . \tag{2.60}$$

2.4.1 Non-dimensional form of the governing equations using cylindrical coordinates

The modified non-dimensional form of Navier-Stokes equations and the magnetic induction equations using cylindrical coordinates is expressed as follows:

$$\nabla^2 v_z - (\frac{\mathrm{Ha}^2}{\mathrm{Re}_m})[(\frac{\sin\theta}{r})\frac{\partial B_z}{\partial\theta} - \cos\theta\frac{\partial B_z}{\partial r}] = O \ , \tag{2.61}$$

$$\nabla^2 B_z - \mathrm{Re}_m[(\frac{\sin\theta}{r})\frac{\partial v_z}{\partial\theta} - \cos\theta\frac{\partial v_z}{\partial r}] = 0 \ , \tag{2.62}$$

where $\nabla^2 \equiv \frac{\partial^2}{\partial \mathrm{r}^2} + (\frac{1}{\mathrm{r}})\frac{\partial}{\partial \mathrm{r}} + (\frac{1}{\mathrm{r}^2})\frac{\partial^2}{\partial\theta^2}$, $\mathrm{Ha} = B_o a(\sigma/\eta)^{1/2}$, $\mathrm{Re}_m = \sigma\mu v a$, and $O = O_1 a^2/v\eta$.

Eqn. (2.61) and (2.61) apply to any general incompressible, steady magnetohydrodynamic duct flow. The restriction as to geometry and the conditions at the wall enters through the boundary conditions.

2.4.1.1 *boundary conditions in pipe flow*

No fluid slip at the wall is given by

$$v_z(a,\theta) = 0 \ , \tag{2.63}$$

where a is the radius of the cylinder, while the assumption of non-conducting walls implies that (Shercliff, 1953)

$$B_z(a,\theta) = 0 \ . \tag{2.64}$$

We can also obtain the current density **j** and the electric field **E** from Ampere's and Ohm's laws:

$$j_r = (\frac{1}{r})\frac{\partial B_z}{\partial \theta}, \quad j_\theta = -\frac{\partial B_z}{\partial r}, \quad j_z = 0 \ , \tag{2.65}$$

$$E_r = (1/\sigma)j_r + v_z B_\theta, \quad E_\theta = (1/\sigma)j_\theta - v_z B_r, \quad j_z = 0 \ . \tag{2.66}$$

2.4.2 Exact solutions of pipe flow in magnetic field

Shercliff (1953) uncoupled the Eqn. (2.61) and (2.62) by a linear transformation. The boundary conditions could also be reduced by the transformation. The velocity and magnetic field distribution are obtained from the uncoupled equations (Gold, 1962):

$$\begin{aligned} v_z = \frac{-Kv}{4\alpha}[e^{-\alpha\frac{r}{a}\cos\theta}\sum_{n=0}^{\infty}\epsilon_n\frac{I_n'(\alpha)}{I_n(\alpha)}I_n(\alpha\frac{r}{a})\cos n\theta \\ + e^{\alpha\frac{r}{a}\cos\theta}\sum_{n=0}^{\infty}(-1)^n\epsilon_n\frac{I_n'(\alpha)}{I_n(\alpha)}I_n(\alpha\frac{r}{a})\cos n\theta] \ , \end{aligned} \tag{2.67}$$

$$\begin{aligned} B_z = \frac{-\mathrm{Re}_m K B_o}{8\alpha^2}[e^{-\alpha\frac{r}{a}\cos\theta}\sum_{n=0}^{\infty}\epsilon_n\frac{I_n'(\alpha)}{I_n(\alpha)}I_n(\alpha\frac{r}{a})\cos n\theta \\ - e^{\alpha\frac{r}{a}\cos\theta}\sum_{n=0}^{\infty}(-1)^n\epsilon_n\frac{I_n'(\alpha)}{I_n(\alpha)}I_n(\alpha\frac{r}{a})\cos n\theta - 2\frac{r}{a}\cos\theta] \ , \end{aligned} \tag{2.68}$$

where $\alpha = \frac{1}{2}\mathrm{Ha}$, I_n is the modified Bessel function of order n, $\epsilon_n = 1$ for n=0, and $\epsilon_n = 2$ for n>0. Equation (2.65) and (2.66) are used to obtain the electric field **E**:

$$E_r = (\frac{a\mu v}{\mathrm{Re}_m r})\frac{\partial B_z}{\partial \theta} - v_z B_o \sin\theta \ . \tag{2.69}$$

I_n identities are given by

$$I_n(\alpha) = I_{-n}(\alpha) \ , I_n(-\alpha) = (-1)^n(\alpha) \ , I_n(\alpha)' = \frac{1}{2}(I_{n+1}(\alpha) + I_{n-1}(\alpha)) \ , \tag{2.70}$$

and

$$I_n(x) = \frac{1}{\pi}\int_0^\pi e^{x\cos\theta}\cos n\theta d\theta - \frac{1}{\pi}\int_0^\infty e^{-x\cosh u - nu} du \ . \tag{2.71}$$

2.5 Stability of Conducting Flow in a Magnetic Field

The problem of the flow of liquid metal jets in magnetic field arises in certain applications of magnetohydrodynamics. The stability of the flow of a conducting film in the presence of two components of the magnetic field (in the direction of the flow and normal to the surface) was investigated by B.A. Kolovadin (1965) using the approximation of small Reynolds numbers: The ratio of transverse magnetic field to longitudinal magnetic field changes due to the finite inclination of jet axis to the magnetic field axis. The magnitude of the inclination angle affects the stability of the liquid jets.

Theses instabilities can change the jet shape into one that makes the jet a significantly less efficient target for particle production. As described in Chapter 1, the particle production depends on several parameters such as jet size and jet angle. Thus, the unstable behaviors of jet in a magnetic field yields less or unexpected production of particle. In addition, the larger inclination of jet axis makes the jet size become bigger than the nominal jet size due to the increased magnetic field. Thus, the mercury jet interacting with beam will have different energy deposition leading to different particle production. Therefore, the stable motion of mercury jet is required for stable particle production and it then needs to be investigated.

2.5.1 Propagation of waves at an interface separating two flows in magnetic field

To investigate the surface wave motion of free jet in magnetic field, we followed the procedure of a direct extension of Currie (1993) to the case with a magnetic field. The detailed procedures and derivations are described in Appendix C.2.

We consider the (x, y, z) coordinate system in Fig. 2.1. The magnetic field along and normal to the Hg jet axis can be derived from the solenoid magnetic field map. From trigonometry, the longitudinal magnetic field along the jet axis and the transverse magnetic field normal to the jet axis are given by $B_x = B_X cos\theta - B_Y sin\theta, B_y = -B_X sin\theta + B_Y cos\theta$, respectively, where B_X is the axial component of the magnetic field and B_Y is the radial component.

To investigate the effect of sinusoidal wave perturbation at the interface, the equation of the interface is chosen to be $\xi(x,t) = \epsilon e^{i(2\pi/\lambda)(x-ct)} + a$, where ϵ is the wave amplitude, λ is the wavelength, and c is the wave propagation speed. Small perturbations from the basic flow in the form $v_{xi} = U_i + v'_{xi}$, $v_{yi} = v'_{yi}$, $p_i = P_i + p'_i$, $v'_{xi} = \frac{\partial \phi_i}{\partial x}$, $v'_{yi} = \frac{\partial \phi_i}{\partial y}$ are assumed, where ϕ_i is the velocity potential for the perturbation to the uniform wavy flows at the interface. Substituting the perturbed expressions into the equations of motion, neglecting second order terms in the perturbed quantities, and making use of the fact that U, P satisfy the flow equations and the current density in Lorentz force term can be represented using Ohm's law, we have the linearized equations governing the motion of disturbance, which yields the Rayleigh's stability equation of conducting flow in a magnetic field by replacing the perturbed quantities with the equation of motion. The Rayleigh's equation must be solved subject to the boundary conditions. The dynamic boundary condition at interface yields the effect of a magnetic field and the conditions of interfacing flows such as flow velocity and density to the wave velocity and wave number. Without a magnetic field, the quantity c has an imaginary part that results in the interfacial wave growing exponentially with time. Thus, the interface at the shear layer is unstable. However, the magnetic effects to the wave propagation velocity to reduce the wave amplitude and correspondingly the wavelength increases due to the magnetic field.

Several investigations have suggested that magnetic field suppresses turbulent fluctuations in conducting liquid by stabilizing the flow (Shercliff 1956,

Gold 1962, Kozyrev 1981, Bernshtam 1982) and the stabilizing action of the longitudinal component of a magnetic field is considerably weaker than that of the transverse component, where stabilization is judged by an increase in the characteristic wavelength of the flow and Re_{cr}.

2.5.2 Magnetic pressure and tension

Once the jet surface is stabilized and flattened by a magnetic field, the magnetic pressure caused by the Lorentz force is contributing to the hydrodynamic pressure. It gives rise to deflect the jet in directions perpendicular to the magnetic field. Considering that the continuity condition has to be satisfied, the Lorentz force makes the jet shape change elliptically. Therefore, the contributions of each magnetic pressure components to the isotropic hydrodynamic pressure needs to be investigated.

Lorentz force is $\mathbf{F} = \mathbf{J} \times \mathbf{B} = \frac{1}{\mu}(\nabla \times \mathbf{B}) \times \mathbf{B} = \frac{1}{\mu}(\mathbf{B} \cdot \nabla)\mathbf{B} - \frac{1}{2\mu}\nabla \mathbf{B}^2$. Suppose the Maxwell stress tensor $T_{ij} = \frac{1}{\mu}(B_{ij} - \frac{1}{2}\delta_{ij}B^2)$, which represents the deviatoric stress tensor of magnetic field. The divergence of the Maxwell stress tensor is represented as follows, which gives the same expression with Lorenz force.

$$\nabla \cdot T = \frac{1}{\mu}\begin{bmatrix}\frac{\partial}{\partial x} & \frac{\partial}{\partial y} & \frac{\partial}{\partial z}\end{bmatrix}\begin{bmatrix}\frac{B_x^2-B_y^2-B_z^2}{2} & B_xB_y & B_xB_z \\ B_yB_x & \frac{B_y^2-B_x^2-B_z^2}{2} & B_yB_z \\ B_zB_x & B_zB_y & \frac{B_z^2-B_x^2-B_y^2}{2}\end{bmatrix}$$

$$= \frac{1}{\mu}((\mathbf{B} \cdot \nabla)\mathbf{B} + (\nabla \cdot \mathbf{B})\mathbf{B} - \nabla(\frac{\mathbf{B}^2}{2})) \tag{2.72}$$

T has units of pressure. The shear is given by the off-diagonal elements of T and the diagonal elements of T correspond to the pressure acting on a differential area element. Total force on a volume is represented as follow.

$$F = \int\int\int_V \nabla \cdot T dV = \oint_S T \cdot dS \tag{2.73}$$

The conservation of momentum in inviscid flow is represented as follow.

$$\begin{aligned} &\frac{d}{dt}\int\int\int_V \rho \mathbf{v} dV + \oint_S \rho \mathbf{v}(\mathbf{v}\cdot\hat{n}) dS \\ &= -\oint_S p\hat{n} dS + \int\int\int_V \rho \mathbf{g} dV + \int\int\int_V \nabla \cdot T dV \end{aligned} \tag{2.74}$$

$$\frac{d\mathbf{v}}{dt} + (\mathbf{v}\cdot\nabla)\mathbf{v} = -\frac{1}{\rho}\nabla p + \mathbf{g} + \frac{1}{\rho}\nabla\cdot T = -\frac{1}{\rho}\nabla\mathbb{P} + \mathbf{g} \tag{2.75}$$

,where

$$\mathbb{P} = \begin{bmatrix} p - \frac{B_x^2 - B_y^2 - B_z^2}{2\mu} & -B_x B_y & -B_x B_z \\ -B_y B_x & p - \frac{B_y^2 - B_x^2 - B_z^2}{2\mu} & -B_y B_z \\ -B_z B_x & -B_z B_y & p - \frac{B_z^2 - B_x^2 - B_y^2}{2\mu} \end{bmatrix} \tag{2.76}$$

Note that the magnetic field increases the pressure by an amount $\mathbf{B}^2/2\mu$, in directions perpendicular to the magnetic field and decreases the pressure by the same amount in the parallel direction. Thus, the magnetic field gives rise to a magnetic pressure $\mathbf{B}^2/2\mu$, acting perpendicular to field lines, and a magnetic tension $\mathbf{B}^2/2\mu$, acting along field lines.

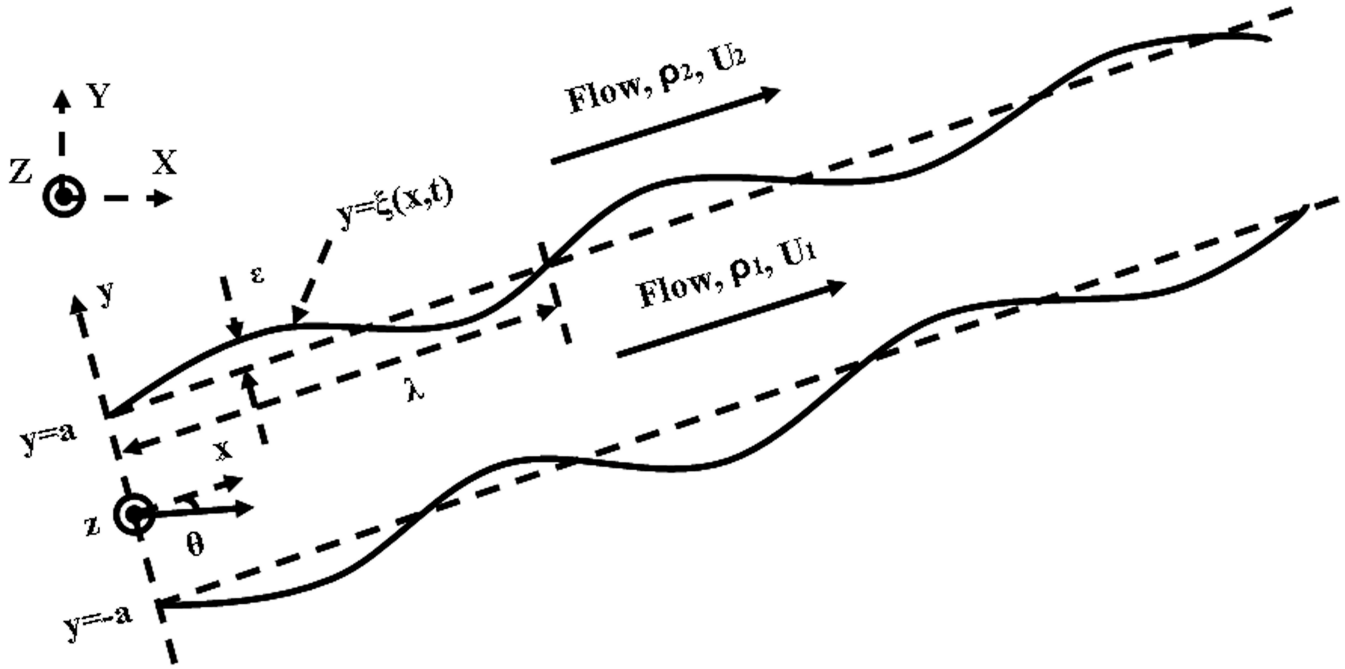

Figure 2.1: Wave-shaped interface separating two different fluids traveling at different average speeds.

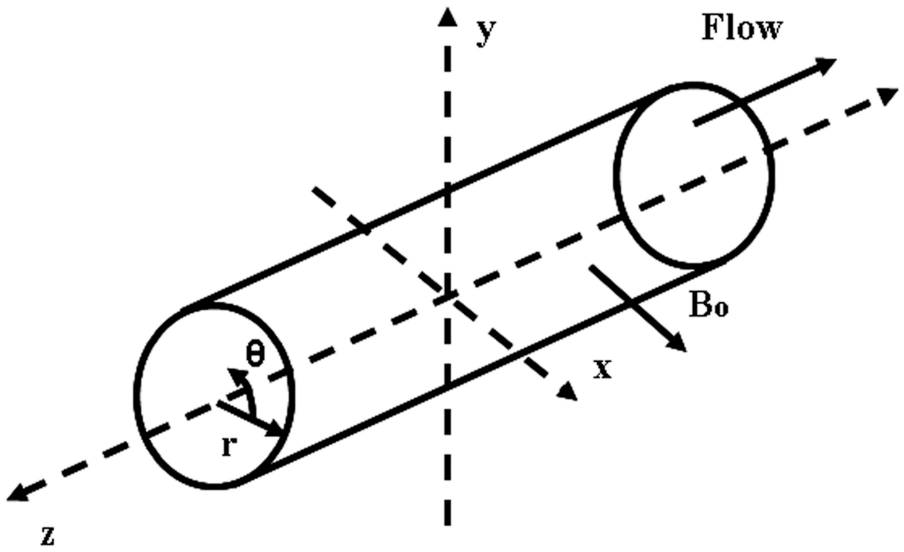

Figure 2.2: Axes and electrodes of circular duct.

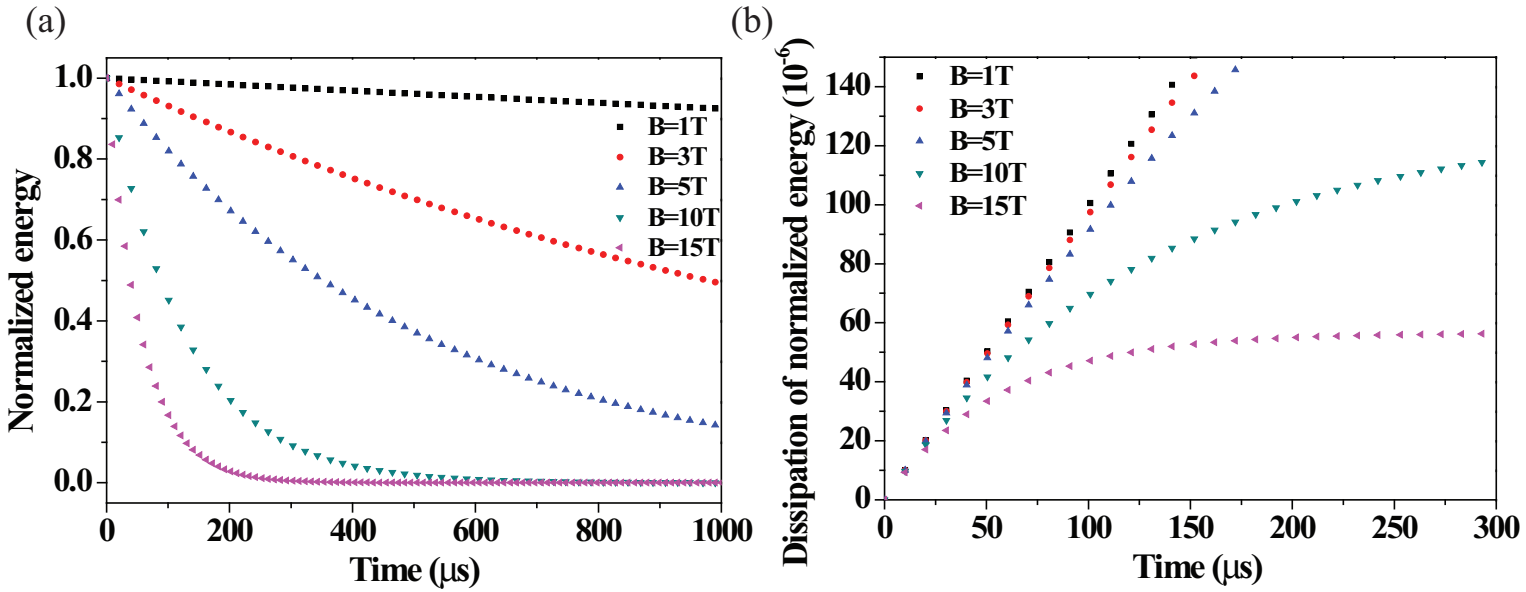

Figure 2.3: Energy decay in magnetic field. a.)Normalized energy decay. b.)Dissipation of normalized energy.

Chapter 3

Experimental Method for Investigation of Magnetohydrodynamic Mercury Jet Flow

The optical method is considered to investigate MHD processes. Optical methods have considerable advantages over other measurement techniques: they do not introduce any perturbations into the medium being investigated, they possess high sensitivity and accuracy, their response is practically instantaneous, which enables them to be used to investigate turbulent flows and transition states, since they provide the possibility of visually following the phenomenon being investigated, and they enable one to obtain the physical characteristics for the whole space being investigated at the same instant of time. Unlike other probeless methods, optical methods possess high spatial resolution. All these features enable optical methods to be widely employed in MHD experiments and underlie the need to search for new ways of using modern optical methods which have not yet been employed.

Direct visualization techniques for hydrodynamic examination have often been employed to investigate the dynamics of MHD flows. In this method, one measures the time taken for the particles to traverse a given path. Because no quantitative results can be deduced from direct visualization methods and difficulties often arise when investigating thin boundary layers in liquids, attention has turned to the use of optical techniques for the investigations of fluid dynamics and MHD (Fedin, 1973).

It should be noted that visualization is usually employed for qualitative investigations, but this method can also be used to measure the average flow velocity and a change in the velocity profile. To do this one measures merely the time taken for the particles to traverse a given path or the path traversed in a given time.

3.1 Optical Diagnostics as a Principal Diagnostics of High Power Target Experiment

3.1.1 Working principle of shadowgraph for optical diagnostics

Optical measurements have many advantages over other techniques. The major one is the absence of an instrument probe that could influence the flow field. The light beam can also be considered as essentially inertialess, so that very rapid transient effects can be studied.

Shadowgraph is often employed in studying shock and flame phenomena,

in which very large density gradients are present. It integrates the quantity measured over the length of the light beam. For this reason they are well suited to measurements in two dimensional fields, where there is no index of refraction or density variation in the field along the light beam.

In a shadowgraph system the linear displacement of the perturbed light is measured. Consider the illumination at the exit of the test section. Figure 3.1 shows the displacement of a light beam for shadowgraph. If the illumination is uniform entering the test section, it should still be closely uniform there. The beam is deflected by an angle α, which is a function of y. The illumination within the region defined by Δy at this position is within the region defined by Δy_{sc} at the screen. If the initial intensity of light is I_T, then at screen,

$$I_o = \frac{\Delta y}{\Delta y_{sc}} I_T \ . \tag{3.1}$$

If Z_{sc} is the distance to the screen, then the contrast is

$$\frac{\Delta I}{I_T} = \frac{I_o - I_T}{I_T} = \frac{\Delta y}{\Delta y_{sc}} - 1 \simeq -z_{sc} \frac{\partial \alpha}{\partial y} \ , \tag{3.2}$$

$$\frac{\Delta I}{I_T} = -\frac{z_{sc}}{n_a} \int \frac{\partial^2 n}{\partial y^2} dz = -\frac{z_{sc}}{n_a} \int \frac{\partial^2 \rho}{\partial y^2} \cdot \frac{\partial n}{\partial \rho} dz \ , \tag{3.3}$$

where n is the index of refraction of a homogeneous transparent medium and $n_a \simeq 1$ for the ambient air.

For gas, Eqn. (3.4) could be substituted into Eqn. (3.3). Eqn. (3.3) is

integrated twice to determine the density distribution. (Goldstein, 1991)

$$\frac{\partial^2 n}{\partial y^2} = C[-\frac{\rho}{T}\frac{\partial^2 T}{\partial y^2} + \frac{2\rho}{T^2}(\frac{\partial T}{\partial y})^2] \,, \tag{3.4}$$

where the constant C, called the Gladstone-Dale constant, is a function of the particular gas and T is temperature of medium on Kelvin scale.

Shadowgraph is used principally for qualitative descriptions of a density field. Because it yields information on the first and second derivatives of density, its application can be found in systems with steep gradients of density and temperature, such as flame fronts and shock waves.

Optical techniques are non-invasive and do not cause any perturbation of the subject being investigated. Furthermore, their sensitivity increases with photon intensity and the resolution of the subject can reach the diffraction-limited resolution. The optical response of fluid dynamics and MHD are practically instantaneous, enabling the optical technique to study details of turbulent flows and transition states. Coupled to a state-of-the art high-speed camera and the long interaction path length of a light beam with a field of view adjustable to arbitrary dimensions, the optical technique enables one to obtain the physical characteristics for the entire subject being investigated in a short period of time.

3.1.2 Development of optical diagnostic system

An optical diagnostic system is designed and constructed for imaging a free mercury jet interacting with a high intensity proton beam in a pulsed high-

field solenoid magnet. The optical imaging system employs a back-illuminated, laser shadow photography technique. Object illumination and image capture are transmitted through radiation-hard multi-mode optical fibers and flexible coherent imaging fibers. A retro-reflected illumination design allows the entire passive imaging system to fit inside the bore of the solenoid magnet. A sequence of synchronized short laser light pulses are used to freeze the transient events and the images are recorded by several high speed charge coupled devices.

3.1.2.1 *the optical imaging system and Viewports design*

Laser back-illuminated shadow photography technique is employed in experiment to capture the dynamics of the interaction of the proton beam with a moving free mercury jet. The design of the optical imaging system is based on a few essential criteria which are described below. The entire optical imaging head has to fit inside a small portion of a 1 meter long, 150 mm diameter bore magnet. Fig. 3.2(a), Fig. 3.2(b), and Fig. 3.2(c) show the conceptual back illuminated optics design, the installation of 4 Viewports on the primary containment vessel, and the schematic layout of optical components, respectively.

Note that all optics placed inside the interaction beam tunnel are required to be radiation-hard because of high radiation levels in the beam tunnel and the activation of the mercury after proton beam interactions. In our setup, all cameras, lasers, and all other associated electronics are placed in an adjacent beam tunnel controlled locally by several desktop computers. Remote control of the entire system is achieved through designated control desktops located

in the control room via MS Window XP remote desktop connections from the ethernet network (see Fig. 3.7).

A Viewport is located at the beam interaction center and two additional Viewports are located at ±152.4 mm up/down stream locations. Viewport 4 is positioned at +457.2 mm and is designed to capture the residual dynamics of the proton interaction. Because of limited space inside the magnet bore, object illumination and image capture are transmitted through multi-mode optical fibers and coherent imaging fibers, respectively, all positioned on one side exterior to the primary containment vessel. Fig. 3.3 shows the fabricated and assembled optical head containing the integration of ball lens, imaging lens, illumination fiber, and imaging fiber.

The arrangement resembles a compact endoscope design but with a different illumination scheme. Illumination light pulses are coupled into a 15 meter long multi-mode fiber (ThorLabs BFL22-200). It has a numerical aperture of 0.22, 25° cone angle, with a core diameter of 200 μm that matches that of the fiber-coupled lasers. To provide a $\sim$ 55 mm illumination area at the center of the primary containment vessel over a limited short working distance of $<$ 100 mm, the illumination cone angle has to be opened up to a 43° full cone angle. This is achieved by placing a tiny $\sim$ 0.5 mm diameter sapphire ball lens (Edmund Optics M46-117) at the tip of the illumination fiber and secured by a thin stainless steel plate. At the heart of the illumination arrangement is a 76 mm diameter Au-coated concave spherical retro-reflector that has a short radius of curvature of 124 mm (Rainbow Research Optics). When the much

diverged illumination fiber is placed at the radius of curvature and shined onto the optical axis of the reflector, a retro-reflected beam returns back to the illumination fiber providing the back-illumination scheme. Again, because of the tight environment inside the primary, a Au-coated 90° prism mirror turns the optical path from longitudinal to transverse onto the center of the primary. Two anti-reflection coated sapphire windows (Swiss Jewel Company) are mounted on the primary with airtight seals tested up to 1.4 bar pressure. The diameter and the thickness of the window is 100 mm and 6 mm respectively, sufficiently large enough for the observation of a 1 cm diameter jet and mechanically strong enough to withstand the momentum of a direct impact from mercury jet with a mean velocity of 20 m/s (Simos, 2005).

Based on this optical arrangement, a mercury jet in front of the reflector naturally makes a shadow on the retro-reflected beam. The shadow is collected by a 1 mm diameter AR-coated cylindrical grin objective lens (GrinTech, GT-IFRL-100-inf-50-CC) which has an optical path length of 2.43 mm. The grin lens is coupled onto a coherent image fiber. This flexible coherent imaging fiber is the key optical element of the imaging system. It is a 10 meter long Sumitomo IGN-08/30 fiber with 30,000 picture elements (pixels). Each individual fiber has a core diameter of ~ 4 μm with a total fiber diameter of merely 0.96 mm including coating. It has a bending radius of 40 mm, sufficiently small to allow curving and arching inside the primary containment vessel. All imaging fiber ends are hand polished in-house to optical finished quality to allow high quality images with maximum light intensity transmission. Fig. 3.4 shows

the final finished end of an imaging fiber after polishing with 0.3 μm lapping film (ThorLabs, LFG03P). The surface quality and the flatness of the imaging fibers are inspected under a microscope. The imaging fibers are jacketed in-house with reinforced furcation tubing (ThorLab FT030-BK). One end of the imaging fiber is finished with an SMA 905 fiber-optics connector to facilitate coupling to a CCD camera. The other ends of the illumination and imaging fibers are positioned next to each other with ~ 2 mm separation inserted inside a specially fabricated plastic ferrule. The integrated optical head is shown in Fig. 3.3, where a red laser diode is used to illuminate the optical head. The integrated all-in-one ferrule (ball lens, illumination fiber, objective lens, and imaging fiber bundle) is placed at the radius of curvature as well as on the optical axis of the reflector so that it allows both the illumination and the imaging collection to work on one side of the primary. The liquid mercury target is enclosed in a stainless steel primary containment vessel which is placed in the primary beam tunnel (TT2A). A total of four optical imaging heads for each Viewport are mounted on the exterior of the primary, designated as channels 1 to 4. All fibers are routed through a ~ 150 mm diameter, 2 meter long concrete passage to an adjacent beam tunnel (TT2), where radiation is much reduced. All electronics control for the optical diagnostic as well as all other electronics control for the solenoid magnet operation and hydraulic power unit used to generate the mercury jet are also placed in the adjacent tunnel. The exit end of each imaging fiber is coupled to an SMA fiber adaptor (ThorLabs SM1SMA) mounted on an x-y translator (ThorLab LM1XY). Four

40× infinitely corrected microscope objective (Newport M-40x) relay the ∼ 0.96 mm image outputs of each imaging fiber onto each corresponding CCD with appropriate lens tubes to fully expand the images onto a typical 10 × 10 mm CCD array. A non-rotating adjustable lens tube zoom housing (ThorLabs SM1ZM) provides fine and accurate adjustment of image focus on CCD.

3.1.2.2 *the consideration for focusing and tilting alignment of optics*

A retro-reflective mirror captures the output beam of the laser diode and focuses it through the field of view at the target onto the lens of the telescope. The CCD camera views the target through the telescope. Tilting alignment by using fine adjustments on the side of the retro-reflecting mirror can be made and the field of view can be adjusted by moving the imaging lens forwards or backwards. The system is designed to make 6 possible alignment adjustments. After the retro-reflecting mirror is moved forward or backward, the field of view can also be adjusted. The maximum field of view that we can obtain is ∼ 5.0 cm diagonally. The distance d from the objective lens to the imaging lens is related to the field of view at the target. For target to be in focus, one must obey the lens formula,

$$\frac{1}{f} = \frac{1}{c} + \frac{1}{d} \ , \tag{3.5}$$

where c is the distance from the target to the objective lens and d is the distance from the objective lens to the camera.

3.1.2.3 *high speed cameras and light sources*

Table 3.1 gives the specifications of high speed cameras in terms of some selected attributes. Two FastVision cameras with CCD size of 15.4 × 12.3 mm run with a full 1280 × 1000 pixel resolution at a 0.5 kHz frame rate. One Olympus Encore PCI 8000S camera with 1/3 inch CCD size runs with a 480 × 420 pixel resolution at a 4 kHz recording rate. A high speed "Silica Mountain Devices (SMD)" 64KIM camera with a CCD size of 13.4 × 13.4 mm runs with a reduced single frame size of (960 × 960)/4 pixel resolution at up to 1 MHz frame rate. For the three slower cameras, images collected by each individual imaging fiber overfill the CCD pixels by a factor of ~ 6 and ~ 3, respectively, i.e. one fiber projected onto 6 × 6 and 3 × 3 CCD pixel area, respectively. However, for the SMD camera, each imaging fiber slightly underfills the CCD pixels by a factor of 0.83, i.e. one fiber projected onto nearly a single CCD pixel area. Due to the nature of spatial superposition, an array of imaging fibers imaged by an array of CCD pixels, some images might compose of a honeycomb pattern caused by this pixelation artifact. However, the artifact can be minimized by slightly defocusing the image on the CCD. However, the FastVision and Olympus CCDs are capable of recording at a frame rate higher than 500 Hz, the architecture for binning at reduced resolution requires a change of the zoom ratio on the image head doom. The SMD camera has a different but fixed binning architecture so that the full field of view is taken at a high speed frame rate with reduced resolution. Except for the SMD camera where images are frozen by the short 150 ns illumination laser pulses, all other

images are arrested by the short adjustable electronic exposure time of 10 $\sim$ 50 μs set on the CCDs.

Synchronized short laser light pulses are used to illuminate the target and freeze the motion of the jet after the impact of the proton beam. For SMD camera, the mask reduces the photosensitive area to 0.03 of the nominal pixel area. The quantum efficiency of the photo-resistive area is 0.18 at 800 nm, and the pixel fill is 200000 electrons. Therefore, a full exposure of a frame of the CCD therefore requires $(960)^2 \times 200000/0.03/0.18 \approx 3.4 \times 10^{13}$ photons or 10 Watts for 800 nm photons. For FastVision camera, the sensor is 1280×1024 pixel (1.03 megapixel) of CCD of total area $15.36 \times 12.29 mm^2$ in 8 bits at 500 frames per second (10 bits at 400 frames per second). Maximum frame rate is 500,000 at 1×1280. The mask reduces the photosensitive area to 0.4 of the nominal pixel area. Based on the estimation of required photons, a full exposure of a frame of the CCD therefore requires $1280 \times 1024 \times 200000/0.4/0.18 \approx 3 \times 10^{12}$ photons or 1 Watts for 800 nm photons.

Optical light pulses are sent through 15 meters of multi-mode illumination fibers. The light sources used in the experiment are all Class 4 lasers, emitting at wavelengths of 808 to 850 nm. Three lasers are capable of emitting a peak optical power of 1 Watt (JDS Uniphase SDL-2300-L2) driven by three independent current drivers (ThorLabs LDC220C). These 1 Watt lasers can be operated from CW to a minimum programmable pulse width of 1 μs limited by the trigger logic pulse. The 4^{th} laser emits at a peak optical power of 25 Watt (Bright Solution BDL20-808-F6) limited by the pulsed current driver (Avtech

AXOZ-A1A-B). It provides a current pulse of 150 ns and is capable of running at the maximum 1 MHz repetition rate, i.e. a frame rate of 1 μs/frame.

The complete transmission of the imaging system is ~ 0.2 per Viewport channel, including 0.85 for the 15 meter long illumination fiber, 0.86 for the sapphire ball lens, 0.86 for each pass of the sapphire Viewport, 0.91 for the retro-reflector, 0.67 for the 10 meter long imaging fiber, and 0.86 for the grin lens and the relay lens. For the SMD camera, the imaging circle filled $\pi/4$ of the CCD array. A measured output energy of 3.5 μJ/pulse is obtained from the Bright Solution (BDL20-808-F6) laser illumination light source for Viewport 2. Therefore the calculated number of photons impinging on the SMD camera reaches 4.2×10^6 photons/pixel. After taking into account the 18% quantum efficiency of the CCD, 7.5×10^5 photoelectrons are generated at the full illumination intensity. Since the SMD camera has full well capacity of 2.2×10^5 e^- , there is a factor of ~ 3 on the optical power budget reserved for unanticipated optical power loss and for overcoming the possible attenuation due to ionization radiation. Similar calculations for Viewport channels 1 and 3 give a factor of ~ 10 on the optical power budget. This larger factor is mostly due to the long, 10 μs, exposure time set on the FastVision cameras. Overall, the imaging system is designed to have sufficient optical power budget for the illumination of each Viewport throughout the entire experiment.

3.1.2.4 *radiation-hardness*

Because of the high radiation level in the beam tunnel and the activation of the mercury after the proton beam interactions, all optics placed inside the interaction beam tunnel are required to be radiation-hard. One complete set of optics was selected for radiation resistance test done at CERN. This complete set of optics included an Au-coated reflector, sapphire window, illumination fiber, imaging fiber, and Grin objective lens. The experiment has anticipated a total of 200 proton pulses at 14 and 24 GeV with a total of $\sim 3 \times 10^{15}$ protons. The calculated total radiation reaches $\sim$ 1 Mrad equivalent radiation dose. Therefore, all optics except the grin objective lens were irradiated at CERN to a lower energy 1.4 GeV proton beam but up to an equivalent radiation dose of 5×10^{15} protons. Because we missed an opportunity to deliver the grin lens to the CERN irradiation facility, the grin objective lens was instead irradiated at BNL using a Co-60 source up to a total dose of $\sim$ 3 Mrad.

The reflectance of the Au-coated reflector and the transmittance of all other optics are measured at the wavelength of 830 nm before and after irradiation. Table 3.2 shows the effects of irradiation up to an equivalent radiation dose of 1 Mrad on the reflectance and transmittance of the components of the optical diagnostic system. No noticeable change in the reflectance was observed on the Au-coated reflector even though the substrate of the reflector has turned nearly opaque. The sapphire, 5 meter long of illumination fiber, and 0.3 meter long of imaging fiber do not show any additional insertion loss. They are all radiation hard up to a 1 Mrad dose. However, the small grin objective lens did suffer

radiation damage resulting in a 0.73 transmission. This tiny grin objective lens is made of silver-ion exchanged index modification internal to a glass substrate. Therefore it was not anticipated to have a high radiation resistance. However, it is well known that although glass (and silica fibers) lose its transmission in the visible wavelengths, near infrared (NIR) light can still has adequate light throughput for some applications (Kakuta, 1999). This is one of the reason we select NIR rather than visible laser light for back-illumination of the mercury jet. Since the back-illuminated NIR light passes the grin objective only once, the 0.27 transmission loss over the entire experiment is tolerable and can be recovered with the present designed laser capability. We should note that the integrity of the imaging properties of the grin lens was unchanged, i.e. no image distortion was observed after the 1 Mrad radiation resistance test.

3.1.2.5 *scintillating fiber channel*

A jacketed 2 meter long 1 mm diameter blue emitting scintillating fiber is attached along with the imaging head to register gamma emission during the proton beam and mercury jet interaction. A 12 meter long 1 mm diameter fiber patch-cord (ThorLabs BFH37-1000) carries the blue scintillated light signal and is fiber-coupled to an Avalanche photodiode (ThorLabs APD210), designated as channel 0. The overall transmission at the center wavelength of 480 nm of the fiber patch-cord is measured to be 0.77. The scintillating signal trace is displayed on an oscilloscope and data can be retrieved remotely from the control room. This scintillating signal serves to confirm the arrival of the

proton beam and has the potential to extract the proton intensity from the scintillating signal pulse level.

3.1.3 Schematic of electronic trigger and high speed camera control

Because we are using several high speed cameras from different vendors, we must use separate camera control software for each camera. The limitation on their exposure time also requires two different set of illumination laser pulse trains. A master trigger pulse, synchronized to the arrival of the proton bunch, is delivered to trigger the mercury loop system, the solenoid magnet system, and the optical diagnostic system together. The mercury jet reaches its steady state for 1 second when the solenoid magnet reaches the highest magnetic induction field of 15 T. However, there is a significantly long time lag of ~ 10 seconds for the solenoid system to power up to its full capacity. Therefore, the master trigger signal is first sent to a digital delay generator (Stanford Research DG535) to provide a sufficient long delay to synchronize with all other electronic components. These relative and absolute delays are measured by an oscilloscope. By adjusting each independent delay channel, complete synchronization of all cameras with the pulsing of the laser light sources can be achieved and verified by comparing the bright/dark image intensities of each frame of each CCD.

Fig. 3.5 shows the two sets of pulse sequences used to simultaneously trigger all cameras. The 25W infrared laser consisted of a 17 pulse sequence with a

pulse width of 150ns. This determines the exposure time of the SMD camera on the Viewport 2. The laser pulse period is set to match the frame rate of the images. The SMD camera collects 16 frames of image. Fig. 3.6 shows the traced signals on an oscilloscope when the beam and the beam triggering are delivered. After the master trigger from the synchrotron is delivered at time t = 0, the proton beam comes in $\sim$ 3 μs. The photodiode response from scintillating fiber has a 20 ns rise time and the level indicates the beam intensity and beam position. The scintillating fiber signal gives the beam arrival time. Therefore, it is possible to set the trigger timing for the cameras and laser driver inputs, which is $\sim$ 2 μs after the master trigger from the proton synchrotron.

Three 1 Watt lasers pulsed to a 0.5 second duration are used to independently illuminate Viewport 1, Viewport 3, and Viewport 4, respectively. Typically the FastVision and Olympus cameras continuously collect 220 frames of images. The exposure times on the cameras are set at 10 $\sim$ 50 μs respectively to give a sharp image quality. Although the sharpness of images increases with reduced exposure time, much more light is required for illumination. Therefore, a trade off between exposure time and laser intensity is made. On the contrary, the exposure time for SMD camera is determined by the laser pulse width. As the pulse width of the laser decreases, the laser intensity also decreases. In order to utilize the maximum allowable intensity of the 25W laser, the maximum pulse width of 0.15 μs is used. This pulse width should not seriously jeopardize the image quality even running at its highest frame rate

of 1 μs/frame. A schematic diagram linking all cameras, triggering electronics, and controlling computers is shown in Fig. 3.7. 2 desktops reside in the control room to master the optical diagnostics system. All other electronics and desktops are placed in the TT2 tunnel adjacent to the interaction beam tunnel TT2A.

3.2 Windows Consideration as Viewports for Observation

The mercury jet target is observed through four windows. These windows must contain any possible spray of mercury due to intense beam energy deposition, and remain transparent after a radiation dose from the interaction of beam and mercury.

3.2.1 Fiducial mark on windows

We put fiducial mark on each sapphire window to use the magnitude of the referenced length. The size of fiducial on the back and front windows is varying on images according to the changing field of view. i.e, the back fiducial looks smaller than the front fiducial. Fig. 3.8 shows the artificially marked fiducial on the sapphire window. It gives referencing length scale when we measure the size of jet, velocity, rotation of windows, and the location of magnetic axis on images.

3.2.2 Impact resistance test

We used sapphire windows to obtain enough strength and did surface coating on both sides for anti-reflection at 800nm wavelength. In order to check the survival from mercury droplet impact, we tested sapphire window using a paint ball gun. A paint ball is a 2.75 gram sphere of radius 8.6 mm containing a colored gel that readily "splats" on impact. The velocity of a paint ball was 95m/s. The ratio of the force from a paint ball to that due to the dispersal of the entire mercury jet by the proton beam is

$$\frac{F_{paintball}}{F_{mercury}} = \frac{m_{paintball} v^2_{paintball} r_{mercury}}{m_{mercury} v^2_{mercury} r_{paintball}} \ . \tag{3.6}$$

The momentum of the paint ball is the same as that of a 7 mm diameter mercury drop at 95 m/s. The sapphire window survived in the test.

3.2.3 Pressure leaking test of sapphire windows

The primary containment is mostly welded and the window ports are sealed with rubber gaskets (BUNA-N). Each window is sealed with two sheets of rubber gaskets per port. 21 psi is loaded inside the primary containment to check the sealing of the primary containment. To locate leaks, a Metheson 8850 flammable gas sniffer, which has a 5ppm sensitivity, and Ar/Methane (90 % / 10 %) was used. All of 8 windows survived the 21 psi pressure for over 17 hours.

3.3 Integrated Experimental Setup for High Power Target

3.3.1 Mercury loop system in solenoid magnet

The cross-section and actual equipment for the mercury system with high field solenoid magnet is shown in Fig. 3.9. The horizontal line in Fig. 3.9(a) represents the proton beam. The Hg jet, which is ejected from right to left in Fig. 3.9(a), co-propagates with the proton beam. Four Viewports are shown within the solenoid bore, which represent viewing locations for observation of the Hg jet within its primary containment vessel (see Fig. 1.3). Viewport 2 is positioned at the center of the solenoid and is the location where the center of the proton beam interacts with the Hg jet. The Hg system provides for double containment vessel of the hazardous liquid metal, and can be inserted or removed from the solenoid bore without disassembly. A hydraulic syringe pump, with a piston velocity of 3 cm/s was used to pulse the mercury jet. This pump minimizes the heat added to the Hg as opposed to a centrifugal pump. The syringe pump also reduces the discharge pressure which is the limitation of a centrifugal pump. The Hg system provides a jet duration of a ~ 3 seconds of constant velocity profile. A total of 180 kg of Hg is loaded in the system. A 30 KW, 200 bar hydraulic power unit drives the syringe pump.

The pulsed solenoid incorporates a magnetic induction field ramp up of 10 seconds and is capable of sustaining its peak field for a duration of approximately 1 second. A 5.5 MW, 700 V power supply delivers 7500 A of current

to pulse the solenoid. The magnet is cryogenically cooled to 77 K prior to operation and warms up by 30 K during pulsing due to 30 MJ coil heating. Therefore, a 30 minute cooling time is needed for each single shot. The magnetic axis is positioned at an angle of 67 milliradian to the proton beam, with the tilt provided by a common baseplate supporting all the equipment (see Fig. 3.9(a)). The applied magnetic induction field has been measured with a gaussmeter placed both perpendicular and parallel to the magnetic induction field. The relationship between the measured magnetic induction field and the applied solenoid current was mapped to deduce the maximum magnetic induction field at the center of the solenoid. It was found that the maximum magnetic induction field reached 15 T at Plasma Science and Fusion Center in Massachusetts Institute of Technology.

3.3.1.1 *the considerations in nozzle design*

Better yields of low energy pions are obtained from the mercury jet target when the proton beam and target are tilted with respect to the axis of the capture solenoid magnet. Monte Carlo simulations have indicated that a tilt angle of about 100 milliradian between the mercury jet and the proton beam is optimal (Mokhov, 2000). However, jet motion in a magnetic induction field behaves differently, depending on the angle between the axis of the magnet and that of the jet, as a result of the differences in the magnitude of the components of the magnetic induction field (Samulyak, 2006). As the crossing angle increases, the transverse component of the magnetic induction field increases,

but with no significant change in the longitudinal component. The increase in the transverse component of the magnetic induction field raises the induced current on the Hg jet. Therefore, the angle of the Hg jet is launched at 33 milliradian with respect to the axis of the magnet, resulting in an interaction region about 30 cm long in case of a 1 cm diameter mercury jet with a 1.5 mm RMS diameter of proton beam. Since the proton beam in TT2A beamline at CERN is horizontal, the mercury jet should make a 34 milliradian angle with respect to the proton beam axis, and the magnetic axis should make an angle of 67 milliradian with respect to the proton beam. The mercury will flow from the upstream end of the magnet to the downstream end of the magnet. The jet velocity is designed to be 20 m/s and the center of the jet to intersect the center of the proton beam at center of magnet.

3.3.2 Water jet observation for nozzle performance test

Prior to mercury injection in the primary at Oak Ridge National Laboratory(ORNL), extensive optical diagnostics were carried out by pulsing water jets in the system using 4 different types of nozzle configurations. One nozzle showed the most stable shape of jet motion with fairly uniform velocity, $\sim$ 10 mm diameter and 20m/s respectively.

Due to the spray and wetting of water on the interior of windows, only ambiguous shadow of the water jet was observed. A clear surface motion is required in order to obtain accurate velocity measurement. Therefore, only qualitative diagnostics was made on the water jet. The field of view of each Viewport is $\sim$

50 mm. The diameter of the jet is measured by overlaying a grid of referenced field of view onto the images. The time lapse of each frame is read from the camera frame rates. The trajectory of the jet between several frames can then be measured and the velocity of the jet surface motion is estimated.

These measurements of the water jet tests were done at ORNL. The observations led us to select the design of the final nozzle for the subsequent jet runs. It was fabricated from Titanium and the assembly was anodized for electrical insulation.

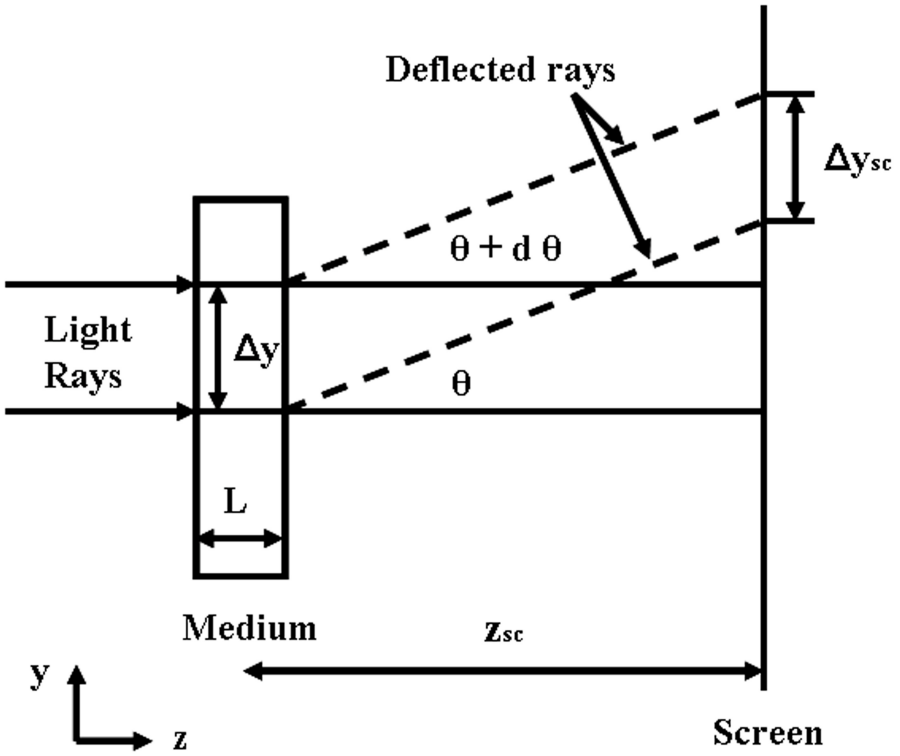

Figure 3.1: Displacement of light beam for shadowgraph.

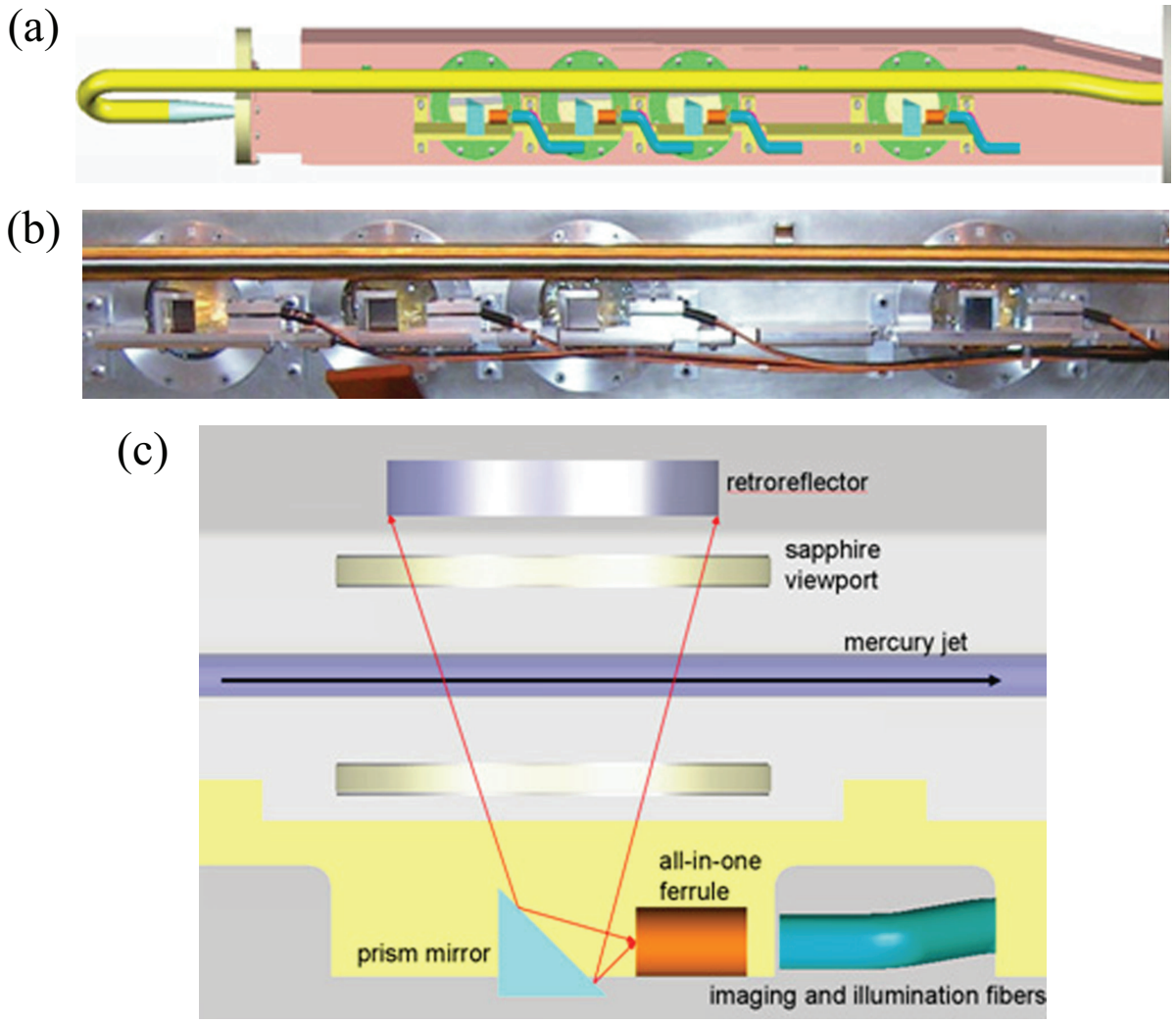

Figure 3.2: Design of optical layout and installation of 4 Viewports of primary containment vessel. a.) Conceptual integration of optics to primary containment vessel. b.) Photograph of installation of optics to primary containment vessel. c.) Schematic layout of optical components.

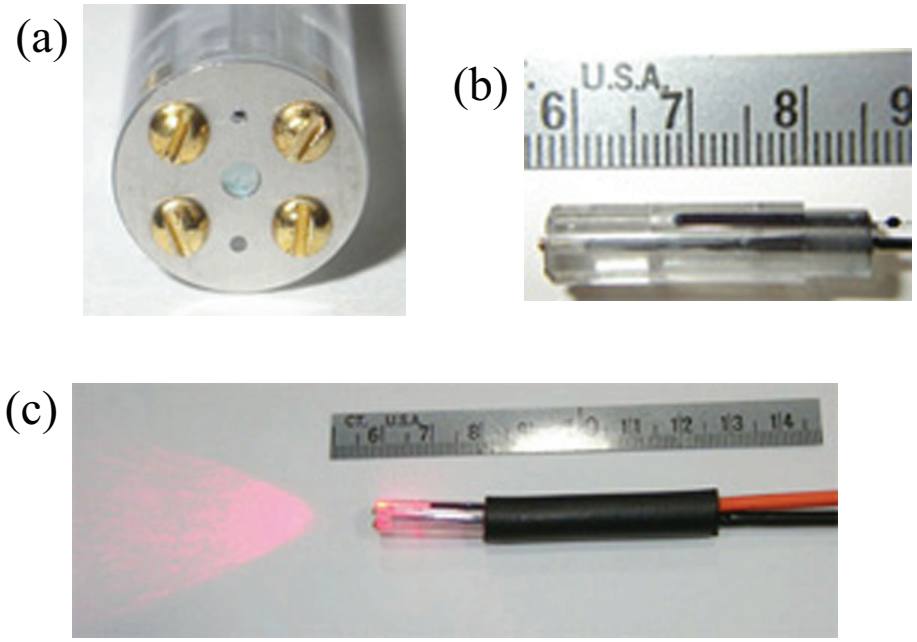

Figure 3.3: Photograph of optical head assembly and its illumination of laser. a.) Front view of optical head assembly. b.) Side view of optical head assembly. c.) Illumination of fiber-optics head assembly.

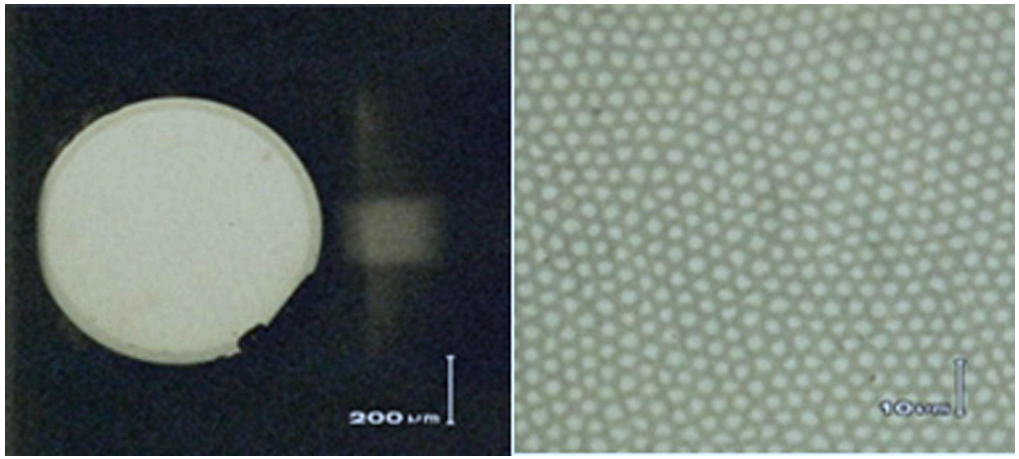

Figure 3.4: Polished fiber end, 50X and 800X magnifications, respectively

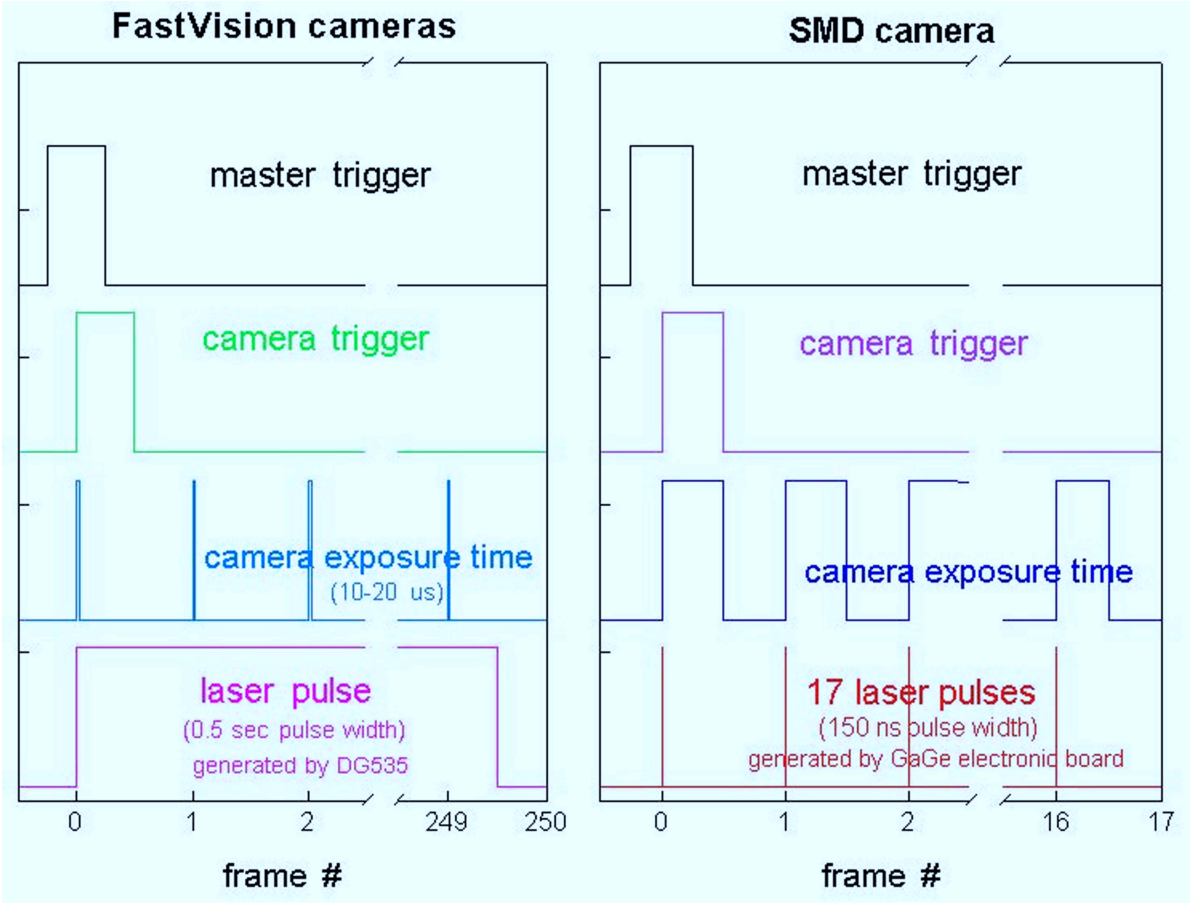

Figure 3.5: Schematic of synchronized signal of high speed camera and laser pulse.

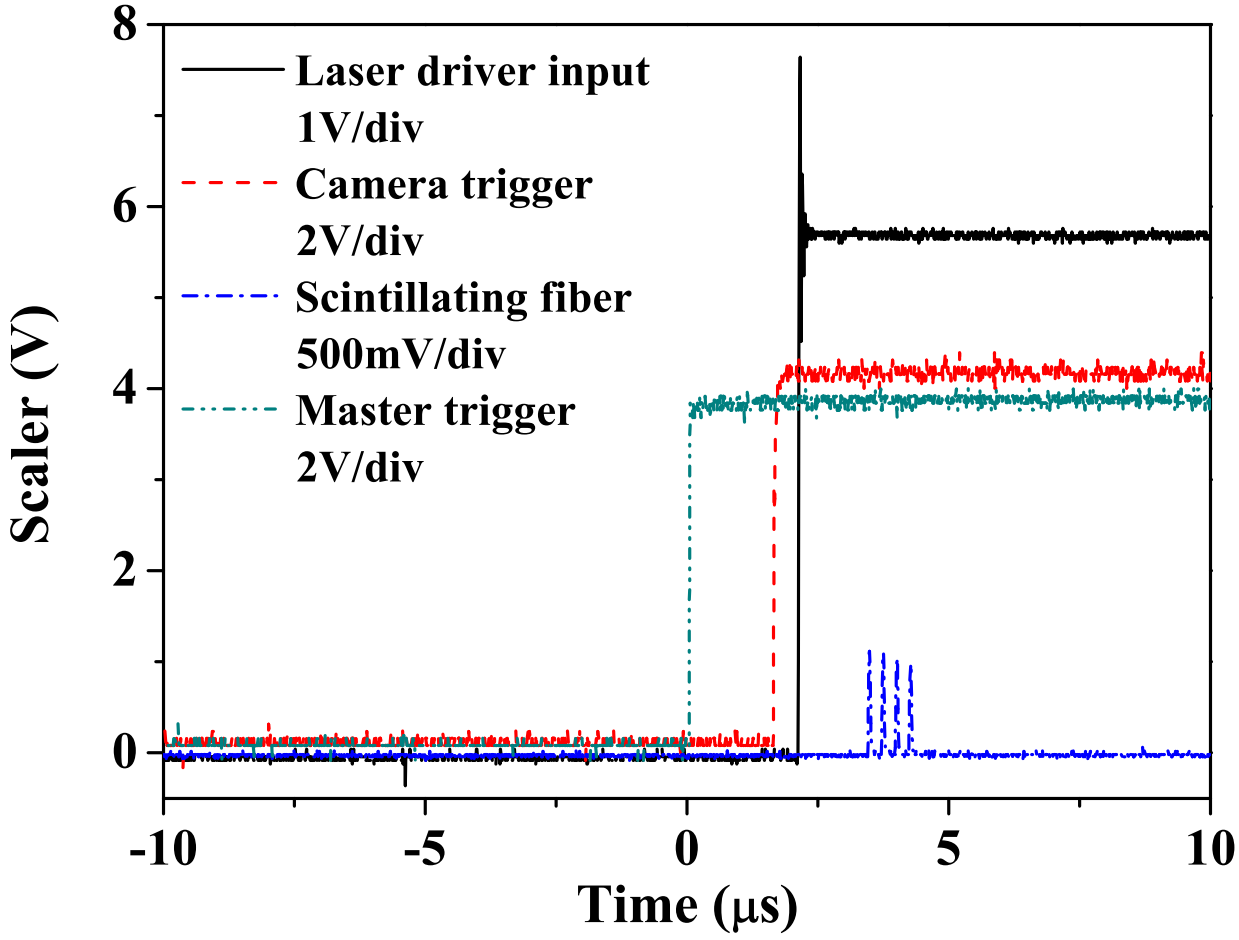

Figure 3.6: The triggering time for high speed camera upon beam arrival.

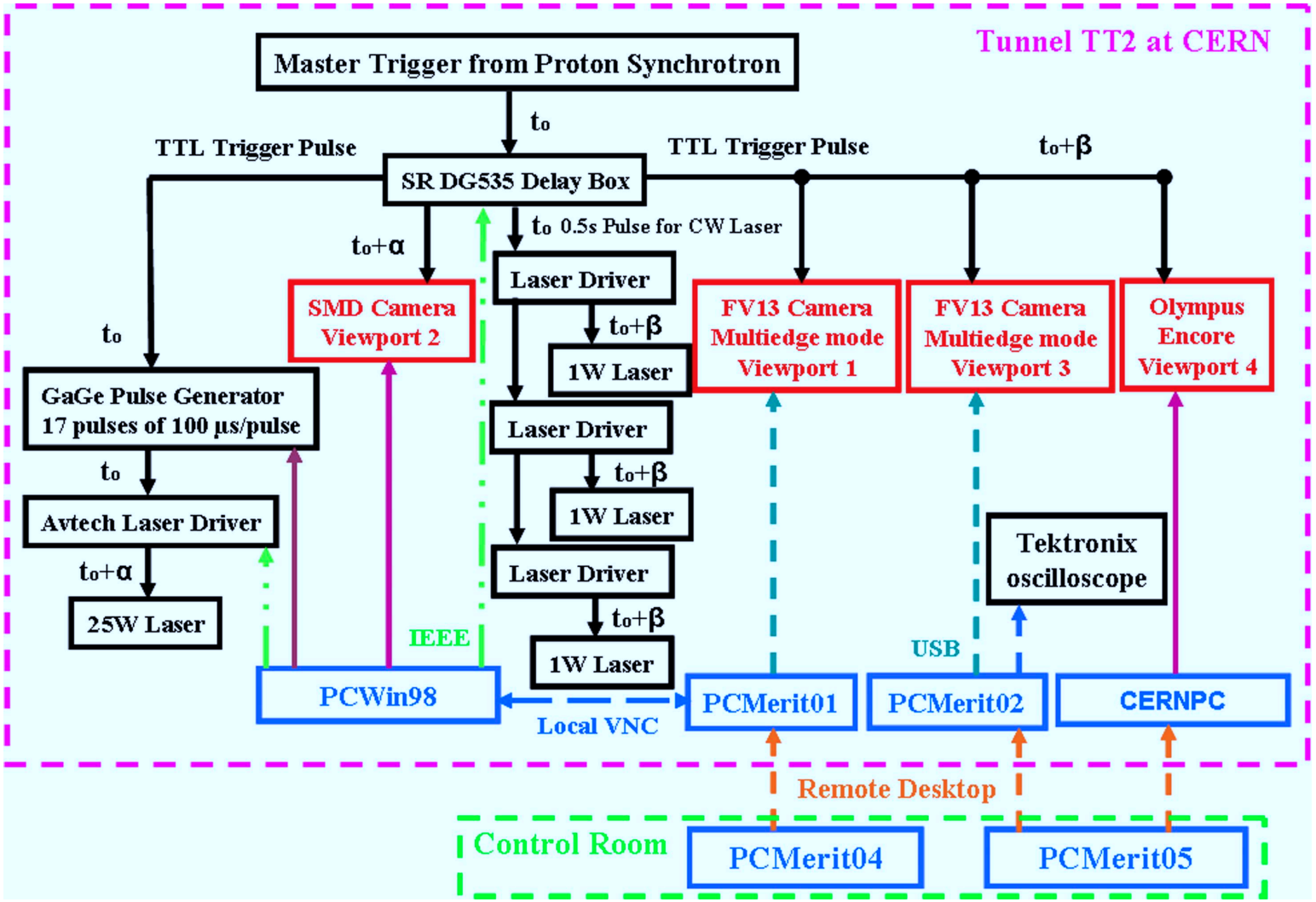

Figure 3.7: Schematic of electrical triggering and high speed camera control in tunnel for experiment.

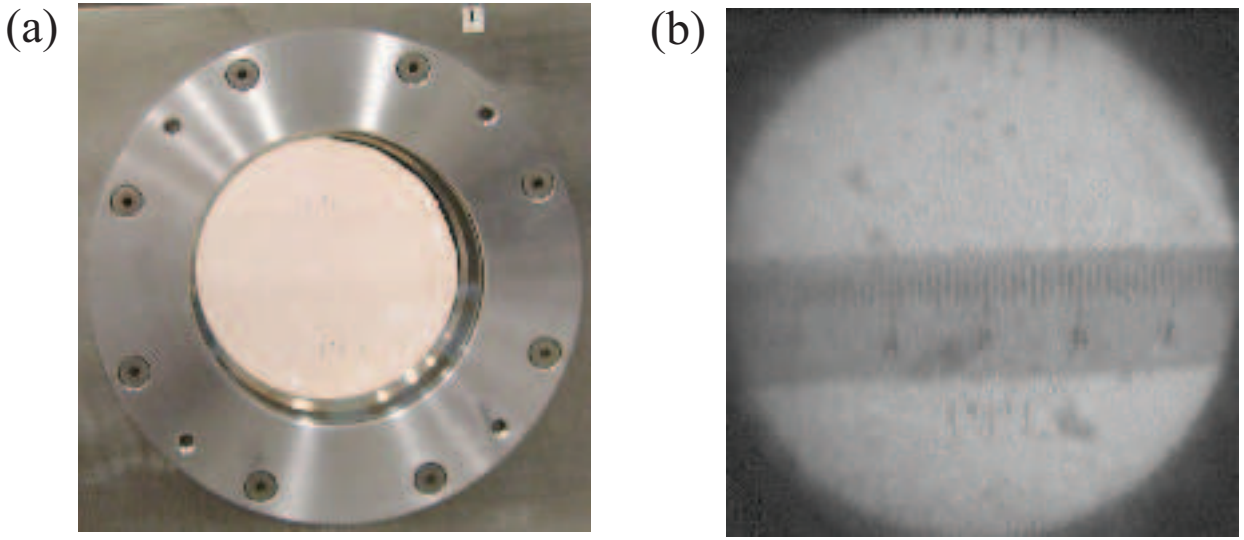

Figure 3.8: Top fiducial on the front window and bottom fiducial on the rear window. a.) Photo of fiducial on the sapphire window assembled in Viewport. b.) Image of fiducial captured by camera.

(a)

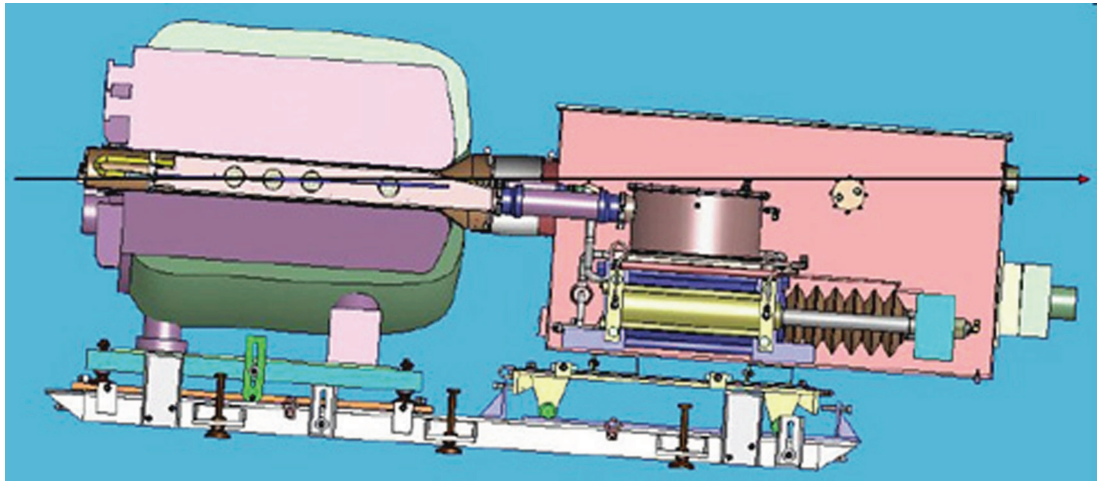

(b)

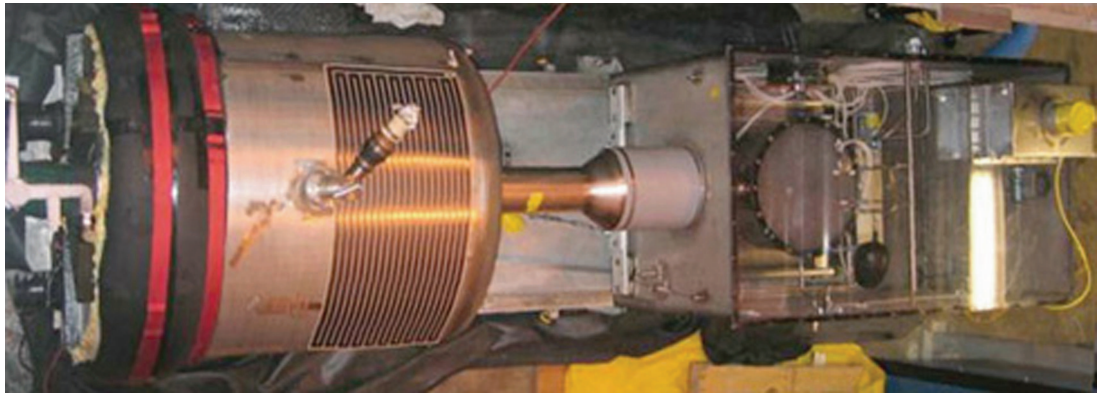

Figure 3.9: Photographs of the entire MERIT experiment. a.) Sectional side view of mercury loop system integrated with 15 T solenoid magnet. b.) Fabricated mercury loop system assembled with 15 T solenoid magnet (Top view).

Table 3.1: Specifications of high speed cameras.

Attributes	SMD 64KIM	FastVision	Olympus Encore PCI 8000S
CCD chip size	13.4 mm × 13.4 mm	15.4 mm × 12.3 mm	1/3 inch
Pixels	960 × 960	1280 × 1024	480 × 420
Pixel size	14 μm	12 μm	13 μm
Single frame	240 × 240	1280 × 1000	480 × 420
Maximum frame rate	1 MHz[1]	0.5 kHz[2]	4 kHz[3]
Full well Capacity	220,000 e^-	$\sim$ 1000 LSB/lux-sec	-
ADC	12 bit	8 bit	8 bit

[1] 16 frames.

[2] at full resolution.

[3] 12.5 μs electronic shutter, with reduced frame size.

Table 3.2: Effects of irradiation up to an equivalent radiation dose of 1 Mrad on the reflectance and transmittance of the components of the optical diagnostic system. Reflectance is inferred on the Au-coated mirror and transmittance is inferred on all other components.

Optical component	Before radiation	After radiation	% difference
Large Au-coated mirror	0.91	0.92	no change
Sapphire window(1-mm)	0.86	0.87	no change
Illumination fiber(5m)	1	1.02	no change
Imaging fiber (30 cm)	0.67	0.71	no change
Grin lens	0.90	0.66	73 %

Chapter 4

Experimental Investigation of Mercury Jet Flow in Magnetic Fields

In this chapter, the jet behavior in magnetic field are investigated. To do this, the collected images are read digitally and the characteristic jet parameters are evaluated based on the probability approach. It effectively diagnoses the jet condition on each collected image. Jet deformation such as the free jet surface deformation and surface stabilization is investigated by measuring the pixels on the collected images based on 2-D shadow photography. Aa a result, we will discuss the magnetic field effect to the dynamic behavior of freely moving jet in a solenoid magnetic field. The driving pressure of mercury flow entering inlet pipe is measured to monitor the effect of the magnetic field and assure if the input condition for driving the jet is affected. In order to diagnose the flow rate, the flow velocity in magnetic field is discussed and the deflection of jet size in various magnetic field is investigated. Based on the observed flow rate of jet, the shape of jet is suggested for the energy deposition calculation

by proton beam interaction with Hg jet target.

4.1 Image Analysis for Data Reduction

4.1.1 Image acquisition

$\sim$ 360 complete integrated tests (i.e., with magnet, proton beam, Hg loop system, and optical diagnostic system) were conducted at CERN (European Organization for Nuclear Research) with various values of the proton beam structure (8 harmonic and 16 hamonic) and the beam intensity up to 30 $\times 10^{12}$ protons and the beam energy (14 Gev/c and 24 GeV/c) and the the magnetic field (0T, 5T, 7T, 10T, and 15T) and two Hg jet velocities (15 m/s and 20 m/s). Fig. 4.4 and 4.5 are representative optical diagnostic results collected by the 3 cameras, with and without a magnetic induction field at Plasma Science and Fusion Center in Massachusetts Institute of Technology. Note that the Olympus Encore PCI 8000S camera for Viewport 4 was integrated in the beam interacting target study done at CERN.

The current in the magnet system generates heat, which is cryogenically removed using liquid nitrogen. As the magnet cools down, all Viewports become foggy up due to condensation. It was found out that $\sim$ 0.5 ℓ of water (from nozzle performance test at Oak Ridge National Laboratory) was not removed from the system prior to loading Hg. Flexible heater strips were installed both on the exterior of the primary containment vessel and on the snout in order to prevent the condensation of the humid air on the Viewports. Although residual Hg droplets in sizes less than 1 mm often adhere to the

sapphire Viewports after every shot, jet motion with adequate image quality could still be collected.

4.1.2 Image processing

To measure the shape of the jet, 8 and 12 bit grey scaled TIF images are converted into digital forms. Background images are subtracted to reject the noise in the image digitization process. The residual data is then transformed into a 2 bit scaled image. Fig. 4.1 shows the collected image and its transformed 2 bit scaled image. Only the black and white colored pixels in the 2 bit depth images are used to differentiate the shadow of the jet and the background. Due to the image quality caused by the Hg droplet on window and the quality in fiber optic system, the noise such as black dots exits. A threshold is adjusted according to Otsu's method to highlight the interface between the mercury and background (Otsu, 1979). Otsu's method selects the threshold by minimizing the within-class variance and maximizing the between-class variance of the two groups of pixels separated by the thresholding operator. Otsu's method, which relies on the assumption that all image pixels belong to one of two classes, background or foreground, has been shown to be efficient in image segmentation for bi-level thresholding.

Fig. 4.2 show the sensitivity of 2 bit scaled image conversion to the measurement of jet height using Otsu's method. As the threshold level increases, the mean value of the jet height as well as the σ value of the jet height in measurement is approaching an asymptotic level. The optimally selected threshold

value by the Otsu's method in this example is 0.35.

The Hg jet was observed at upstream (Viewport 1), midstream (Viewport 2), and downstream (Viewport 3) locations from the nozzle exit. 220 images are collected at each run for both the upstream and downstream locations, with an image size of 1280 $\times$ 1000 pixels. The most probable transverse jet height within the longitudinal pixel range of 300 to 1000 is shown in the histogram of Fig. 4.3(a). Note that within this range, the transverse jet height probability P is obtained by counting the number of longitudinal pixel events in the jet image. If z denotes the transverse direction (in terms of pixels), the histogram in Fig. 4.3(a) can be written as (Eqn. (4.1)) using the least square curve-fairing approach:

$$P(z) = P_1 \frac{1}{\sqrt{2\pi}\sigma_1} e^{-\frac{(z-\mu_1)^2}{2\sigma_1^2}} + P_2 \frac{1}{\sqrt{2\pi}\sigma_2} e^{-\frac{(z-\mu_2)^2}{2\sigma_2^2}} \quad , \tag{4.1}$$

where μ_1, μ_2 are the means, σ_1, σ_2 are the standard deviations, and P_1, P_2 are the a-priori count of the histogram distribution. Note that, in pixel units, μ_1=386, μ_2=401, σ_1=3.8, and σ_2=21.6. The number of background events (i.e., outside of the jet) is always larger than that within the jet because the portion of bright background on each image is larger than that of the black jet shadow. The distribution on the left in Fig. 4.3(a) (i.e., $0 < z < 200$) represents the background pixels and is not included in the faired curve in Fig. 4.3(b).

On the other hand, rather than using the fitting of the histogram of number of events, the number of pixels corresponding to the jet height is counted within

the longitudinal pixel range of 300 to 1000. Each counted pixel numbers are directly average to give a jet height measurement and then added up over $\sim$ 200 images for 1 jet shot, where the time elapse corresponds to $\sim$ 0.4 s at Viewport 1 and 3. Multiple shots are then used to add up all of the counted vertical jet height. The average of the individually counted vertical pixels is given to indicate the nominal jet height. In a mathematical form, the direct averaging method is described as Eqn. (4.2) and its measurement is shown at Fig. 4.7 (b).

$$D_{jet} = \frac{1}{i+j+k} \sum_{1}^{i} \sum_{1}^{j} \sum_{1}^{k} N_{vertical} \tag{4.2}$$

where D_{jet} and $N_{vertical}$ denote the averaged vertical jet height and a individually counted number of vertical pixels respectively. i, j, k represent the number of shots, images in a shot, and vertical lines in a image respectively.

On Viewport 2, 16 image files are collected at each run, with an image size of 316 $\times$ 316 pixels. The images are analyzed in the same manner as described above. Viewports 1 and 3 give the same resolution for the images: 1280 $\times$ 1000. Thus, no image re-scaling is needed when comparing the pixel size for these images. However, Viewport 2 gives a resolution of 316 $\times$ 316. Based on the 1 cm scale fiducial mark on the exterior of all Viewports, all images taken on this Viewport are re-scaled to match the resolution of Viewport 1 prior to comparison.

4.1.3 Study on the scaling length and the location of center of window

In order to relate the lengths on the collected images at each Viewport, the pixel length on the images has to be investigated. Since the image size corresponds to the CCD size, any discrepancy in horizontal and vertical pixel size is not considered. Viewports 1 and 3 give the same resolution for the images: 1280 × 1000. Thus, no image re-scaling is actually needed when comparing the pixel size for these images but did the scaling to see any difference on the image length of Viewport 1 and Viewport 3. The fiducial length on the top front window and the bottom back window is measured and then interpolated to get the length at the mid-span on the primary containment. The interpolated pixel length at the mid-span corresponds to 1 cm at the mi-span of primary containment. Thus, in Viewport 3, a pixel length at the mid-span where the jet is moving is approximated ~ 0.05 mm. Same scaling was done at images in Viewport 3. The ratio of the pixel length in Viewport 3 to Viewport 1 is 1.06.

Viewport 2 gives a resolution of 245 × 252. Based on the 1 cm scale fiducial mark on the exterior of all Viewports, all images taken on this Viewport are re-scaled to match the resolution of Viewport 1 prior to comparison. A pixel length at the mid-span is approximated ~ 0.21 mm. Viewport 4 gives a different resolution of images depending on the frame rate setting but typically the resolutions of 320 × 280 was used. A pixel length at the mid-span is approximated ~ 0.21 mm, which is same with Viewport 2.

The distance of the center position between the fiducial and the window is 0.75 inch apart. In order to locate the center of the window at the mid-span, the positions where 0.75 inch is apart from the top fiducial and bottom fiducial is found on each image and then the averaged difference in the located position is considered as the center of window.

Based on these scaling study, the measurement is performed for the following investigation. The measurement is averaged for ~ 200 images to give a result of the following investigation and the standard deviation is also calculated for the individual measurement respectively. Based on the standard deviation and the number of events, the error bar, $\sigma/\sqrt{N}$, is calculated to give error estimation for each measurement.

4.2 Motion of Mercury Jet and Stability in Magnetic Field

4.2.1 Jet deflection and surface flattening

When the jet is injected without an applied magnetic field, it is difficult to discern the jet surface because of blockage by Hg droplets on the window. Therefore, some errors in the measurement exists (see images Fig. 4.4(a) through Fig. 4.4(c) and 4.5(a) through 4.5(c)). On the contrary, when a magnetic field is applied, the measurement errors are significantly reduced,leading to significantly less intermittent jet boundaries.

The inertial forces appear to dominate the jet movement when the jet velocity is 15 m/s. The turbulent jet motion is unstable but becomes stabilized

as the magnetic field approaches 5 T. It has been reported that the radial force induced by the transverse component of magnetic field caused by the axially induced current due to the tilted jet angle can significantly increase the jet height (Gallardo *etal*, 2002). The phenomena of increasing jet thickness with high magnetic induction field is observed for the first time when the magnetic field exceeds 10T.

The Fig. 4.7 (a) shows the jet height variation by the magnetic field strength and the jet height is measured by fitting the histogram of number of events resulted from the image processing. The standard error is used to give the error bar, where the standard deviation is divided by the number of samples. The Fig. 4.7 (b) shows the jet height measurement by direct average of vertical jet height from scanned pixels on each image. The standard deviation is used to give the error bar. This two plot shows the extreme two conditions of evaluation of the measured jet height, but one can effectively observe the fluctuating amount relative to the nominal jet height according to the various magnetic fields.

At a jet velocity of 15 m/s, the relatively low inertial force reduces the extent of turbulent fluctuation. For this case, the magnetic field does not significantly affect the dynamics of the jet until the magnetic field strength of $\sim$ 5 T reaches. Consequently, the height of the jet decreases only slightly until 5T since the magnetic field reduces the fluctuating surfaces and the jet is more likely to elongate axially to the jet axis. The results shown in Fig. 4.4 and 4.5 clearly suggest that the magnetic field has constrained (stabilized)

the Hg jet flow by smoothing out the edges of the otherwise turbulent flow. At large number of the magnetic field (>10 T), stability is maintained at all Viewports. At 15 T, a larger height (cross sectional distortion) is observed on all Viewports.

The fact that the Hg jet size is relatively reduced from 0 T to 5 T but increases from 10 T to 15 T suggests that the Hg jet might encounter a different type of instability at high field, namely a quadrupole effect. The quadrupole effect would alter the jet's circular cross-section to become elliptical. From the data obtained with a 15 m/s jet, the jet height at a 10 T is smaller than that at 15 T, which is manifested in the vertical elongation of the jet. However, the height at a 10 T is smaller than that at 5 T. The issues for such a behavior have to be addressed. There are two possibilities. First, the jet is elongating axially up to 10 T. The equivalence of hydrodynamic pressure with magnetic pressure is more dominantly affecting to the axial elongation of jet than the transverse pressure. Eqn. (2.76) shows the magnetohydrodynamic stress tensor, which indicates the ration of the axial pressure and the transverse pressure. The increasing axial pressure of jet is more elongating from 0 T to 10 T. However, the transverse magnetic pressure becomes significant once the magnetic field exceeds 10 T. Thus, the jet at 15 T is experiencing the transverse deflection as well as axial deflection, but the the role of transverse deflection plays significantly on the behavior of jet. That can explain why the reduction of jet is appearing up to 10 T and then the expansion of jet is appearing at 15 T.

Second, the optical diagnostics depends only on the side sectional view of jet movement. The reduction of jet size on the minor axis of the elliptical core has to be accompanied by the gain in jet size on the major axis in order to satisfy the continuity condition in flow. In other words, the cross-sectional are in flow should be constant. Although the two dimensional nature of the image data does not distinguish between an elliptical cross section and a circular one, occasional observation of a smaller jet thickness at 15 m/s with 10 T field as opposed to a 5 T indicates that the jet cross section might vary between the major and minor axis of an elliptical core. It is important to note that within the axial distance of interest, the jet diameter is approximately constant. Therefore, references to "larger jet height" should be interpreted to mean larger distortions of the jet cross section. Since the jet and solenoid field are cylindrically symmetric, it is hard to estimate in what direction the jet is going to be distorted but the ratio of the deflection can be determined experimentally. The ratio also can be compared with the transverse magnetic pressure $B^2/2\mu$ considering the reversed direction of deflection on each plot. If then, the Fig. 4.7 (a) gives the deflection ratio with magnetic field in an increasing sequence from 0 T to 15 T approximately consistent with the ratio of magnetic pressure $B^2/2\mu$. Samulyak (2007) suggested that the deflection ratio of jet size $\triangle R/R_o$ is proportional to the magnitude $\mathbf{B}_o^2/U$. by using the developed MHD code, where the governing MHD equations and free jet boundary condition including Maxwell's equations using low magnetic Reynolds approximation are employed and calculated the Hg jet deflection in magnetic field

using a hybrid of Eulerian and Lagrangian method, so called Front tracking method. Fig. 4.8(a) shows the deflection ratio of Hg jet along the distance from nozzle at 10 T and 15 T magnetic field. As shown in Fig. 4.4 and Fig. 4.5, the magnetic field stabilizes the Hg jet surface so that the jet surface is getting flattened. In MHD simulation, constant 1 cm diameter of Hg jet is considered. Although the magnetic field causes the jet surface flattening, the nature of turbulence such as growth of jet size is observed in experiment. Therefore, in order to avoid such a turbulent nature between simulation and experiment, the ration of jet deflection ratio between 10 T and 15 T is evaluated to see the comparison of the magnetic field effect $\mathbf{B}_o^2/U$ between Fig. 4.8(a) and Fig. 4.7 (b), which is shown in Fig. 4.8(b). It shows somewhat consistency at upstream, but still the ratio diverges as the jet flows to downstream.

As expected, jet motion in a magnetic field behaves differently, depending on the angle between the axis of magnet and the axis of jet, as a result of the differences in the magnitude of components of magnetic field (Samulyak, 2006). Fig. 4.6(a) and 4.6(b) show the axial and radial components of the magnetic field in a solenoid. Fig. 4.6(c) and 4.6(d) show the transverse and longitudinal components of the magnetic field along the jet axis at different crossing angles. As the crossing angle increases, the transverse component of the magnetic field increases, but with no significant change in the longitudinal component of the magnetic field. An increase of the transverse component of the magnetic field raises the induced axial current on the Hg jet. Therefore, the angle of the Hg jet is launched at 33 milliradian with respect to the axis

of solenoid magnet.

The jet surface can readily be extracted from each collected image. The jet axis is approximated by fitting the averaged positions between top surface and bottom surface. This jet axis is moved with an offset until it interferes the top surface bottom surface. The amount of fluctuations of surface is measured by getting the difference between the fluctuation surfaces and the interfering jet axis on a RMS scale. Let $\delta(r,t)$ denotes the probability of turbulence at r, such that δ is 0 in the non-turbulent fluid, where the background is considered here, and is 1 in the turbulent fluid, where the jet is considered here. Time average of δ yields $\zeta(r)$, the intermittency factor at r. The turbulent fluctuations are produced by the intermittency effect and these fluctuations are significant for scalar quantities. The intermittency characteristics of the turbulence are the appropriate input to be used in defining rough surface for a scattering analysis. When the intermittency phenomenon is present, the conventional turbulent fluctuation is modified by the intermittency function and there is an additional contribution depending on the difference between the mean turbulent quantity and the non-turbulent quantity (Yen, 1967). However, the probability of the fluctuating jet surface area is introduced to define the intermittency in the following work. The pixel information along the jet axis by changing the translational offset is added to represent the intermittency of jet on the top/bottom surface. The intermittency within the jet represents 1 and it is gradually decrease to 0 at the background. The intermittency is between 0 and i at the jet surface depending on the surface fluctuations. Fig. 4.9

shows the intermittency as a function of magnetic field and time. Total evaluated time is 160 μs. Without magnetic field, the slope of intermittency at the jet surface is broad and it is oscillating as a function of time. With higher magnetic field, the slope of intermittency at the jet surface is more steep and it keeps same shape with respect to time. This result clearly tells that the magnetic field suppresses the fluctuation of jet surface.

The Fig. 4.10 shows the measured fluctuations on the jet surface. Surface fluctuations is monotonically decreasing and the surface is flattened approximately at 5 T. The fluctuations at Viewport 3 (downstream) is larger than that at Viewport 1 (upstream) since the tendency to be more turbulent grows. The amount of fluctuations at top surface and bottom surface of jet is almost same, though the magnetic field is varied. Thus, the symmetry on the jet surface in terms of the surface variations such as fluctuations and wave amplitude is valid. The amount of difference of surface fluctuations at Viewport 1 and Viewport 3 becomes same. It indicates that the jet surface becomes flattened at 5 T in flow velocity 15 m/s. The decreased amount of surface fluctuation at Viewport 1 and Viewport 3 is $\sim$ 0.5 and 1.5 mm RMS respectively. This explains why the jet height is reducing from 0 T to 5 T in Fig. 4.7 (a). The magnetic field makes the wavelength on the jet surface increases. Correspondingly, the wave propagation speed is increasing. Thus, it causes Re_{cr} to increase and the flow becomes laminar due to the stabilization by the magnetic field. The transverse component of magnetic field prevails more over the jet stabilization. Though there is some measurement errors due to the

saturation in image brightness, the measurement could show the field effect to the reduction of fluctuation on jet surfaces.

The these observations are supported by previous results. For example, several investigations have suggested that magnetic field suppresses turbulent fluctuations in conducting liquid by stabilizing the flow (Shercliff 1956, Gold 1962, Kozyrev 1981, Bernshtam 1982), where stabilization is judged by an increase in the characteristic wavelength of the flow.

4.2.2 Trajectory of mercury jet projectile in magnetic field

The Hg jet and the beam are launched at 33 and 67 milliradian with respect to the magnetic axis respectively. The trajectory of Hg jet projectile is acted upon by gravity, which is represented as follow:

$$
\begin{aligned}
t &= \frac{x}{v_o \cos\theta} \ , \\
y &= -\frac{g}{2}\, t^2 + v_o \sin\theta \ t + y_{nozzle} \ , \\
|v| &= \sqrt{v^2 - 2gx\tan\theta + (\frac{gx}{v\cos\theta})^2} \ ,
\end{aligned}
\tag{4.3}
$$

where x is the jet traveling distance, y is the height at x, y_{nozzle} is the vertical position of nozzle, v_o is the launched velocity, and θ is the launched angle of Hg jet.

The distance of jet elevation is determined by measuring the distance from the magnetic axis at center of each window to the jet axis, which is approximated by fitting the averaged positions between top surface and bottom sur-

face. The Fig. 4.11 shows the trajectory of Hg jet and it's effect by the magnetic field and gravity. The solid line represents the globally fitted value using the trajectory of projectile with different initial launching speed of jet for the case of 15 m/s and 20 m/s respectively. It shows that the trajectory of Hg flow approximately agrees well with the trajectory of projectile for both 15 m/s and 20 m/s shots. Experiment shows that the trajectory of the Hg jet is parabolic. The magnetic field caused some elevation of Hg jet closer to the center of magnetic field. As the jet moves to downstream, magnetic field effect is more clearly shown up since the jet is more likely to elongate to the axial direction (Davidson, 1999). The longitudinal magnetic force is more increasing as one can see the magnetic pressure term in the longitudinal direction increasing at Eqn. (2.76). Therefore, it is observed that the jet is behaving more like straight at Viewport 4 with higher magnetic field. At 15 T, the elevation of jet is observed from Viewport 1 to Viewport 4. It shows that the magnetic force is overcoming the inertia force at 15 T similarly as there is the increase in jet height at 15 T. The overall increase of the jet elevation in upstream, midstream, and downstream at 15 T may have been caused by the asymmetric change of jet height. Possibly the stable equilibrium between magnetic force and gravitational force could be varying according to the variation of magnetic field (Geim, 1999).

The beam trajectory is also given to show the overlap with the Hg jet. It is shown that the overlap length is $\sim$ 30 cm when we consider the height of jet at various position with various magnetic field.

Based on the result of the jet trajectory, the angle of jet axis at Viewport 2 (midstream) is determined by the trigonometric approach using the elevation of jet and the distance along the magnetic axis between Viewport 1 and Viewport 3. Fig. 4.12 shows the estimation of jet angle at centner of magnetic axis (Viewport 2), which is approximately $7 \sim 11$ milliradian. The jet angle is slightly decreasing with higher magnetic field, which indicates that the jet is more likely to move horizontally following the field line direction.

4.3 Dynamics of Liquid Jet Flow From Nozzle

4.3.1 Jet equations for analysis

Lee (1977) investigated the phenomenon of air wake caused by a cylindrical jet emerging from a nozzle and showed the boundary layer of jet by applying continuity of jet mass and matching the loss of jet momentum with air drag on the jet. Fig. 4.13 depicts schematically the boundary layer of jet emerging from a nozzle. The conservation of axial momentum and the rate of momentum loss to the skin friction on the jet and the continuity of the liquid jet are expressed as follows:

$$2\pi\rho_a \int_0^{\delta(x)} [a(x)+y]v^2(x,y)dy + \rho_l \pi a^2(x) v_l^2(x) = \rho_l \pi a_o^2 v_{lo}^2. \tag{4.4}$$

$$\frac{d}{dz}[\pi\rho_l a^2(x) v_l^2(x)] = 2\pi a(x)\mu_a \frac{\partial v}{\partial y}|_{y=0}. \tag{4.5}$$

$$\pi a^2(x)v_l(x) = \pi a_o^2 v_{lo}. \tag{4.6}$$

where velocity, density, and viscosity are denoted by v, ρ, and μ, respectively, with subscripts a and l for air and liquid, respectively. The subscripts o denotes the initial values at the nozzle. For boundary layer analysis of cylindrical objects, because of the diverging flux characteristics in radial direction, a logarithmic profile is the most appropriate (Stewartson, Glanert, 1955). Thus, the velocity profile of the air induced by the liquid jet is assumed to be as follow:

$$v(x,y) = v_l(z)\{1 - \frac{1}{\beta(x)}\ln[1 + \frac{y}{a(x)}]\}. \tag{4.7}$$

$$\frac{\delta(x)}{a(x)} = e^{\beta(x)} - 1. \tag{4.8}$$

Substitution of Eqns. (4.7) into Eqns. (4.4) Eqns. (4.6) results in

$$\bar{v}_l(barx) = \frac{v_l(barx)}{v_{lo}} = \frac{1}{1 - \bar{\rho}[1 + \frac{1}{\beta} - \frac{1}{2\beta^2}(e^{2\beta} - 1)]}, \tag{4.9}$$

$$\frac{d\beta(barx)}{dbarx} = \frac{\beta^2 - bar\rho[beta^2 + \beta - \frac{1}{2}(e^{2\beta} - 1)]}{\beta(1 + e^{2\beta}) - (e^{2\beta} - 1)}, \tag{4.10}$$

where $barx = \frac{4x}{\mathrm{Re}_e a_o}$, $\mathrm{Re}_e = \frac{2a_o\rho_a v_{lo}}{\mu_a}$, and $bar\rho = \frac{\rho_a}{\rho_l}$. For a given value of ρ, the stream velocity $barv_l(barx)$ and boundary layer thickness $bar\delta(x)$ are obtained. As seen in Fig. 4.14, the Reynolds number plays its role implicitly and this makes the density ratio $bar\rho$ to be varied. Since the cylindrical jet has

larger volumes, for the initial momentum of the jet to be maintained, the liquid density must be reduced and the value of the density parameter to be used must be modified to $bar\rho = \rho_a D^2/(\rho_l d_o^2)$, where D and d_o denote diameter of jet and nozzle, respectively.

4.3.2 Pressure loss and magnetic effect to the Hg delivery pipe

Fig. 4.15 (a) and 4.15 (b) show the pipe inlet pressure for driving jet in various magnetic field strength. The Hg jet is driven by the piston in syringe and the piston velocity is measured by position sensor. The piston velocity determines the flow rate so that the dynamic pressure head at pipe inlet is determined using the conservation of flow rate. The pressure sensor installed at the pipe wall measures the static pressure. No significant pressure drop is observed at the pipe inlet in magnetic field strength. It indicates that the driving pressure in pipe for nozzle is at same condition regardless of the magnetic field variation.

To obtain the jet velocity, the distance traveled by a fixed point on the jet surface is tracked over a given time period. Fig. 4.16 (a) shows the jet velocity measured at Viewport 1, Viewport 2, Viewport 3, and Viewport 4 in various magnetic field strength. Note that this velocity does not change with the imposition of a magnetic field. Therefore, considering the measurement error in Fig. 4.16 (a), the averaged flow velocity, regardless of magnetic fields, can reasonably indicate the flow velocity given in Fig. 4.16 (b). This explains

why the pressure is approximately constant in the pipe, consistent with the report (Graves, 2007).

Another interesting result is that the cross section of Hg jet is more likely to be elliptical since the longitudinal jet flow velocity is constant from upstream to downstream. Regardless of the magnetic field, the Hg jet does not show jet velocity change. Thus, the jet is changing its shape once it leaves the nozzle from circular to elliptical. Hence, the result in Fig. 4.7 (a) should be again interpreted by the result in Fig. 4.16 in the manner that the jet height at 5 T is elongated on the minor axis followed by the reduction of jet height on the major axis of the elliptical core, and the jet is deflecting further at 10 T. However, the jet height at 15 T is elongated on the major axis, which is manifested by the comparison between the ratio of the reduction of jet height and the increased ratio of the jet height at 15 T. This approach is already mentioned in the above, but it is examined again.

Considering that the driving pressure and the jet velocity are not significantly changed in various magnetic field, it is concluded that the longitudinal magnetic field does not affect to the pressure loss or velocity degradation while Hg passes the solenoid magnet two times along with the direction of magnetic field line. It is reported that the gradient of longitudinal jet velocity depends on the integration of gradient of longitudinal magnetic field along the magnetic axis plus it's multiplication to longitudinal magnetic field itself. (Gallardo *etal*,

2002) It is expressed as follow:

$$\Delta v(x) = \frac{\kappa}{\rho}\frac{r_o^2}{8}\left(\int_{x_1}^{x_2} \left(\frac{dB_x}{dx}\right)^2 + \frac{d}{dx}\left(B_x \frac{dB_x}{dx}\right)\, dx \right) , \tag{4.11}$$

where r_o is the radius of jet and κ is electrical conductivity. Since the gradient of magnetic field is increasing (plus) at entrance and decreasing (minus) at exit, it seems that there is an increasing velocity gradient (acceleration) at upstream and decreasing velocity gradient (deceleration) at downstream but it is ≤ 0.5 m/s due to the relatively high density comparing with the electrical conductivity only if we consider the effect by the magnetic field. The experimental result shows slight effect of magnetic field but is consistent with the reported result in terms of the gradient of longitudinal velocity in magnetic field.

4.3.2.1 *pressure loss in pipe flow*

Schematic pipe geometry is given in Fig. 1.3, where the pipe is connected from the syringe pump to nozzle and it is passing parallel with solenoid magnetic field line next to the primary containment. A loss coefficient is defined as follows:

$$\begin{aligned} (h_{loss}) &= K_1\frac{v_1^2}{2g} + K_2\frac{v_2^2}{2g} + \ldots + K_N\frac{v_N^2}{2g} \ , \\ A_1 v_1 &= A_2 v_2 = \ldots = A_N v_N = A_R v_R \ , \end{aligned} \tag{4.12}$$

where the subscript R signifies a reference location and K represents the loss coefficient.

The general thermodynamic loss, so called the head loss h_{loss} is defined as follow:

$$\int_1^2 \delta F = (h_{loss})_{1,2} = \frac{p_1 - p_2}{\rho g} + \frac{v_1^2 - v_2^2}{2g} + (z_1 - z_2) \ . \tag{4.13}$$

Darcy-Weisbach equation is given to express the head loss of wherever the density is constant, when the pipe diameter is constant and the pipe is horizontal.

$$\frac{\Delta p}{\rho g} = f \frac{L}{d} \frac{U^2}{2g} \ , \tag{4.14}$$

where f, L, d are friction factor, the pipe length, and the diameter of pipe respectively. Considering that the Re = 1800000 and $e/d = 0.002$ for commercial steel in terms of Nikuradse's sand grain scale, turbulent friction factor f via Moody plot or by Colebrook Eqn. (4.15) is approximated to 0.024. Colebrook simply combined the expressions for the friction factor for smooth and rough pipes into a single transition equation of the equivalent form.

$$\frac{1}{\sqrt{f}} = 1.74 - 2 \ log \ (\ 2\frac{e}{d} + \frac{18.7}{\mathrm{Re}\sqrt{f}} \ ) \ . \tag{4.15}$$

Note that Colebrook's expressions for the friction factor in the transition region reduces to Prandtl's smooth pipe equations when the relative roughness approaches zero, and reduce to von Karman's fully rough pipe equation at very high pipe Reynolds number.

The loss coefficients for elbows are presented as follows, where a and R represent the inside radius of the elbow and the radius of curvature of the

centerline of the elbow respectively. For $\mathrm{Re}(a/R)^2 > 91$, the loss coefficient is expressed as follow (Ito, 1960):

$$K_{elbow} = 0.00241\ \alpha\ \theta\ (\ \frac{R}{a}\ )^{0.84}\mathrm{Re}^{-0.17}\ , \tag{4.16}$$

where θ is the bend angle in degrees and α is an empirical factor given by Ito as,

$$\alpha_{\theta=90^\circ} = 0.95 + 17.2\ (\ \frac{R}{a}\ )^{-1.96}\ . \tag{4.17}$$

Inputting $R = 1.942$ and $a = 0.442$, $\alpha = 1.9$ and $K_{elbow} = 0.1232$.

A correction term is applied to the 90° elbow to determine the loss coefficient for arbitrary angle of elbow (SAE, 1960).

$$K_\theta = (\ C_\theta\ )_{elbow}\ K_{90^\circ}\ , \tag{4.18}$$

where C_{elbow} is given in the referenced manual (SAE, 1960). The C_θ is 0.28 at $\theta = 23^\circ$ and $K_\theta = 0.0345$.

The loss coefficient for the reducer or well-rounded inlet loss is $K_{reducer} = 0.05$ based on the flow area of the smaller piping section (Benedict, 1980).

The loss coefficient for the abrupt enlargement is determined by combining the momentum balance over the area of interest. Then, it yields the Carnot-Borda equation, which shows the head loss in the abrupt enlargement. By equating it to the head loss equation Eqn. (4.12), the loss coefficient is given

based on the inlet velocity as follow:

$$K_{enlargement} = (1 - \frac{v_2}{v_1})^2 = (1 - \frac{A_1}{A_2})^2 = (1 - \beta^2)^2 \ ,$$

$$\frac{p_1}{p_2} = 1 + (\frac{1 - G_1}{G_1})(2\beta^2 - 2\beta^4) \ , \tag{4.19}$$

where G_1 is the inlet pressure ratio of static pressure to total pressure, p_t/p_{t1}. The fluid experiences pressure loss when going from a piping system to a plenum, so called exit loss. According to Eqn. (4.19), the loss coefficient for exit K_{exit} is 1, where $\beta = 0$. It applies regardless of whether the pipe protrudes into the exit plenum, is well rounded at exit, or is flush.

Finally, the loss coefficient for the abrupt contraction is given based on the velocity at exit as follow (Benedict, 1980):

$$K_{contraction} = (\frac{1}{C_D^2} - 1)(1 - \beta^4) \ ,$$

$$C_D = \frac{Q_{acutal}}{Q_{ideal}} \ , \tag{4.20}$$

where the discharge coefficient C_D is given in reference (Benedict, 1980). The mean discharge coefficient is given as 0.815 based on the water tests in short pipes. According to Eqn. (4.20), this yields a maximum loss coefficient at $\beta = 0$ of 0.506. Assuming $\beta = A_2/A_1 = 0.9$, $K_{contraction}$ yields 0.1738.

The head losses and the contribution of each geometry are given in Table 4.2. Total length of pipe is 87.1 inch. The diameter of inside pipe is 0.884 inch. The diameter of inside nozzle is 0.4 inch. Total pressure head loss is

4.5344 m., which corresponds to $\sim$ 30 % of input pressure head. The main loss is caused by the exit from nozzle, which is over $\sim$ 50 %. The following loss is caused by the friction due to the large length, which is $\sim$ 27 %. The loss from pipe bend is somewhat low comparing with others.

Based on the calculated head loss, the jet velocity at nozzle is determined assuming the pressure right after the nozzle is atmospheric. The pipe inlet pressure is given in Fig. 4.15 (a) and 4.15 (b). The elevation of the pipe inlet and the nozzle is 2.9 inch. The calculated jet velocity from nozzle including the pressure loss in pipe is 13.4 m/s, which is consistent with the measured result in Fig. 4.16 where the jet velocity is $\sim$ 13.5 m/s. According to Eqn. (2.76), the magnetic field increases the fluid pressure by an amount $B^2/2\mu$, in directions perpendicular to the magnetic field, and decreases the fluid pressure by the same amount, in the parallel direction of the magnetic field. The fluid pressure including the magnetic pressure has to balance with the atmospheric pressure and surface tension of jet and satisfy the continuity condition. The fluid pressure will find equilibrium point since the fluid pressure perpendicular to the magnetic field line is mutually symmetric. Therefore, the jet is changing to be elliptical in Fig. 4.7 (a). Hence, the pressure drop is not occurred significantly and correspondingly the longitudinal jet velocity is not changed with magnetic field in Fig. 4.16.

4.3.2.2 *the measurement of wall tap pressure*

Wall taps is used in order to sense static pressure, wherein small pressure taps are located at a point on such surface as cylindrical pipe so that it does not disturb the fluid. Tap size error arises because of a local disturbances of the boundary layer.

$$\mathrm{Re}_d^* = \frac{v^* d_{tap}}{\nu} \ ,$$

$$\mathrm{Re}_d^* = \sqrt{\frac{f}{8}} \ (\frac{d_{tap}}{d}) \ \mathrm{Re} \ , \tag{4.21}$$

where d_{tap} is the tap diameter, Re_d^* is the tap Re number, and v^* is the friction velocity. The friction factor is 0.024. The tap inside diameter and pipe inside diameter are 0.5, 0.884 inch respectively, which yields $\mathrm{Re}_d^* = 55764$.

At tap Re greater than 385, the error in static pressure caused by the tap size is given as follow:

$$\frac{e_{tap}}{\tau} = 0.269 \ (\mathrm{Re}_d^*)^{0.353} \ , \tag{4.22}$$

where $\frac{e_{tap}}{\tau} = 12.74$.

Combining the Darcy friction factor with the wall shear stress yields

$$f = 4 \ (\frac{\tau}{\rho v^2 / 2g}) \ . \tag{4.23}$$

Therefore, the error in a static pressure can be expresses as non-dimensionalized

form by the dynamic pressure $p_{dynamic}$.

$$\frac{e_{tap}}{p_{dynamic}} = (\frac{e_{tap}}{\tau})\frac{f}{4} \ , \tag{4.24}$$

where $\frac{e_{tap}}{p_{dynamic}} = 0.0764$. The error of static pressure in Fig. 4.15 (a) is estimated to give 7.64 % uncertainty of the dynamic pressure in Fig. 4.15 (b).

Table 4.1: Error estimation of fiducial length at each viewport.

Viewport number	Fiducial length (cm)	Scaling factor
1	1.0 ± 0.095	1.0 (reference)
2	1.0 ± 0.091	4.3 ± 0.81
3	1.0 ± 0.062	1.0 ± 0.16
4	1.0 ± 0.067	4.3 ± 0.70

Table 4.2: Pressure head losses by geometry in pipe for mercury loop.

Geometry in pipe for mercury loop	Calculated pressure head loss	Percentage in total pressure head loss (%)
Friction by surface roughness	1.4176	60.7
Elbows in pipe bend (3 $\times 90^{\circ}$, 2 $\times 23^{\circ}$)	0.2629	11.3
Reducer, Contraction in nozzle	0.6553	28

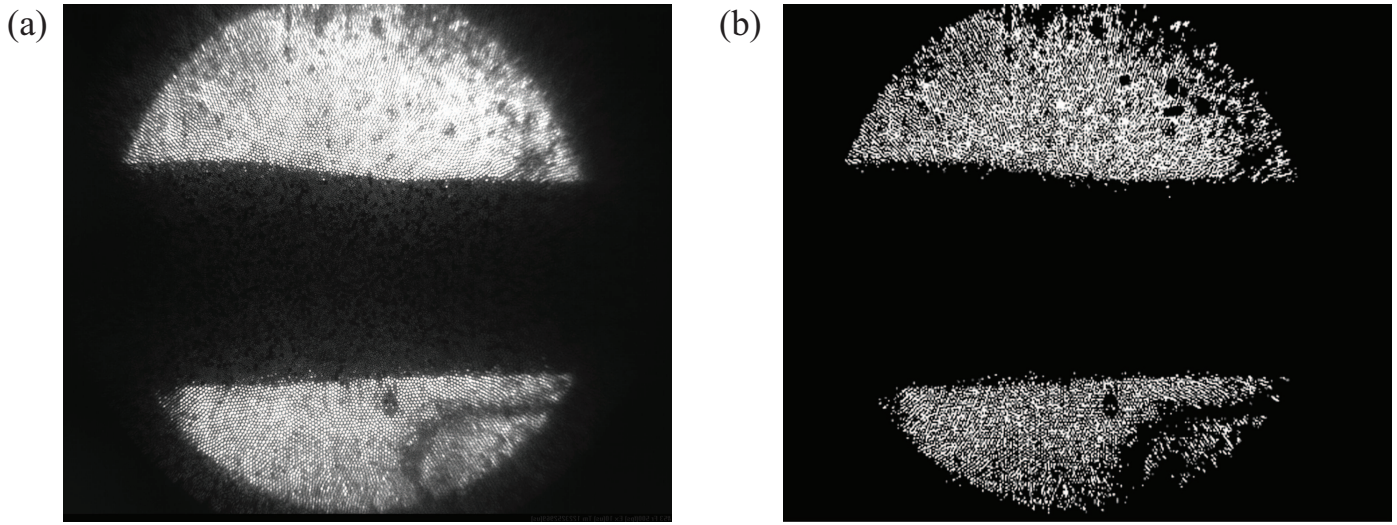

Figure 4.1: Image data conversion for image analysis. a.) Collected image data. b.) 2 bit scaled image data.

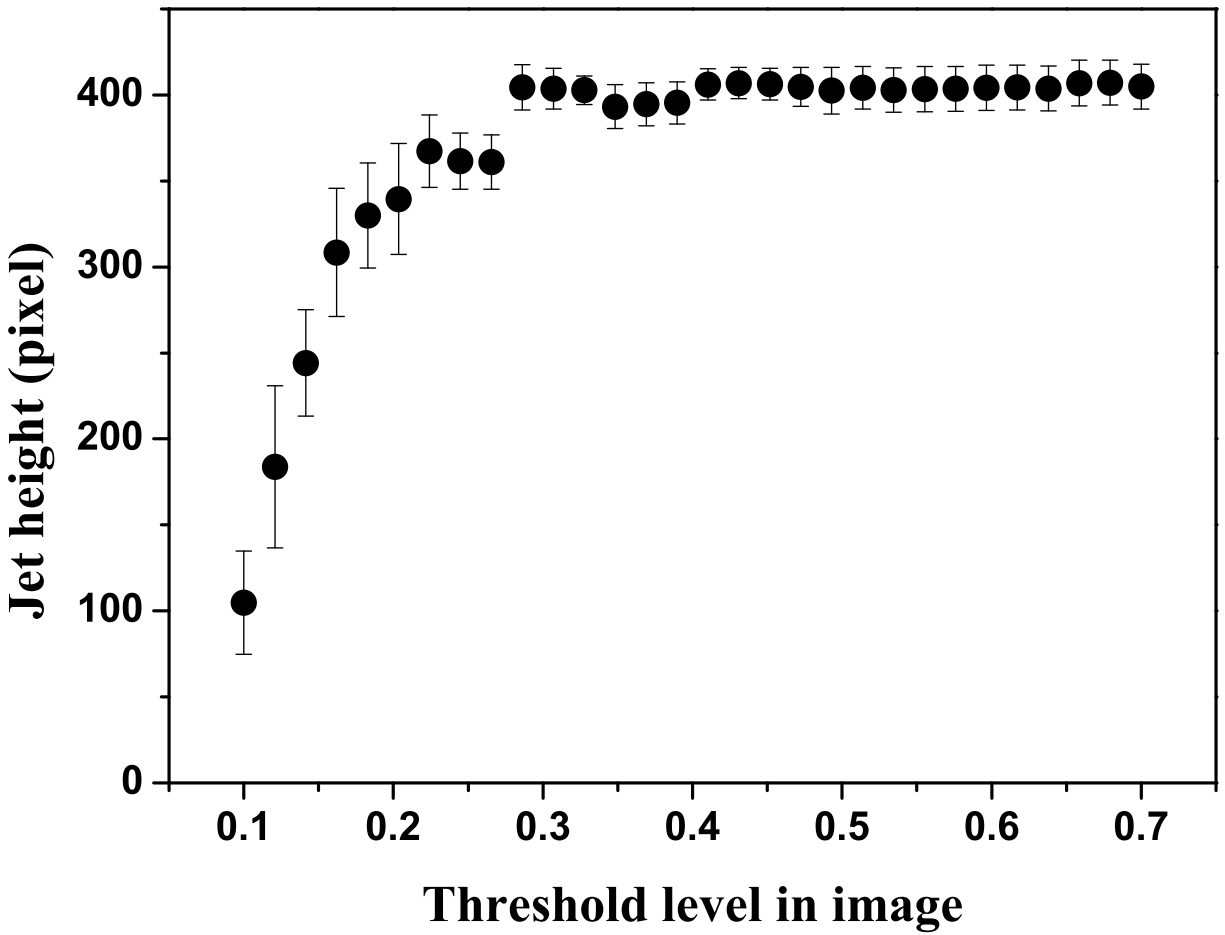

Figure 4.2: Sensitivity of threshold in a 2 bit scaled image conversion.

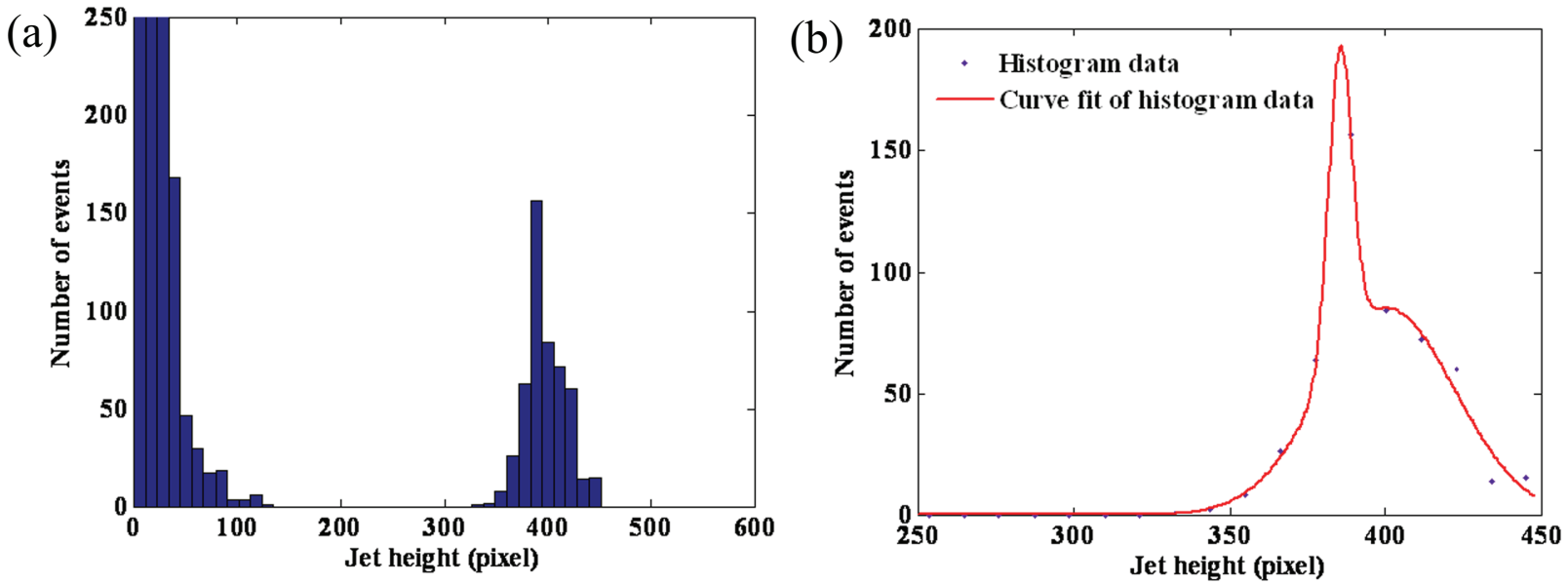

Figure 4.3: Jet height determination from image analysis. a.) Histogram of number of events in the jet height measurement. b.) Fitted histogram distribution.

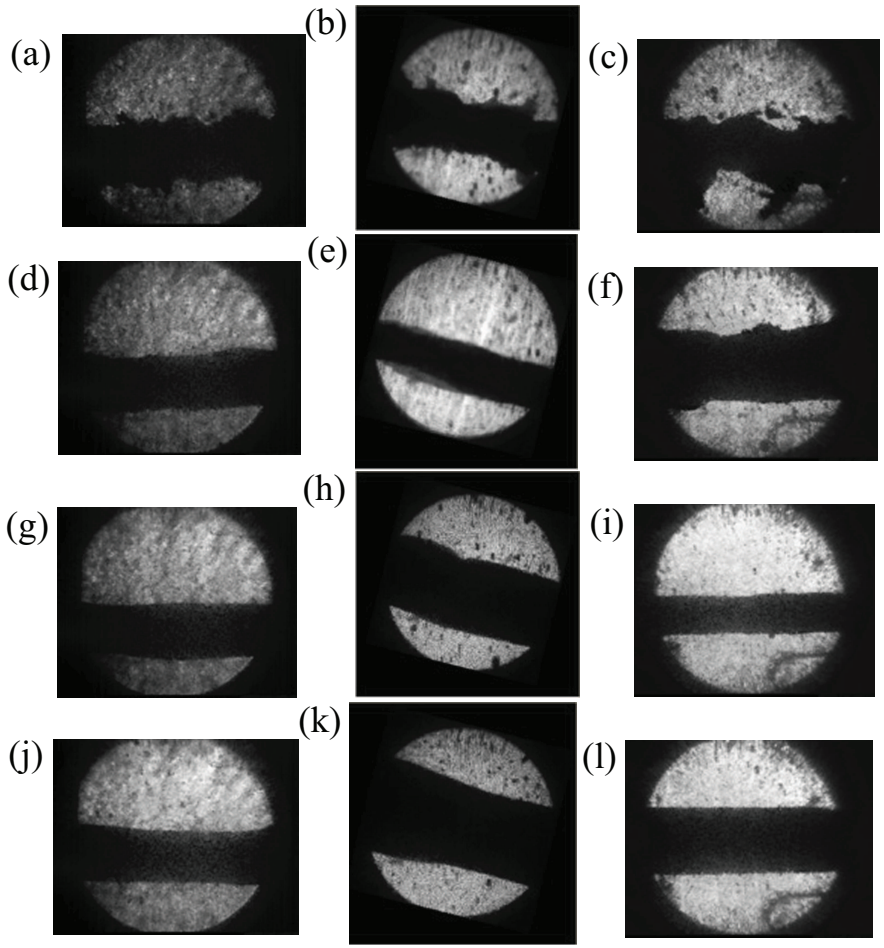

Figure 4.4: Mercury jet flows as observed from the 3 Viewports. The jet flows from left to right on each image. The first, second, and third columns represent Viewport 1, 2, and 3, respectively. The individual caption shows the applied magnetic induction field. The jet velocity is 15m/s. Images on Viewport 2 has a 14° clockwise rotation due to the SMD software. a.) B=0T. b.) B=0T. c.) B=0T. d.) B=5T. e.) B=5T. f.) B=5T. g.) B=10T. h.) B=10T. i.) B=10T. j.) B=15T. k.) B=15T. l.) B=15T.

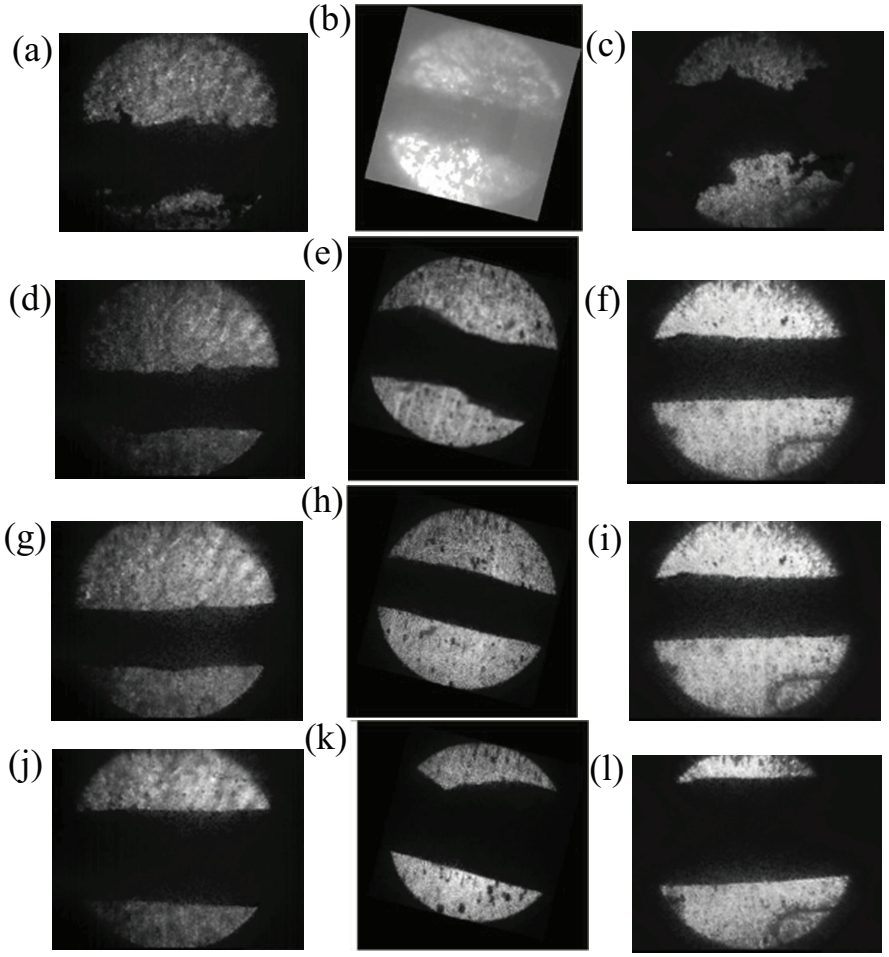

Figure 4.5: Same as Fig. 4.4 but with a jet velocity of 20 m/s. a.) B=0T. b.) B=0T. c.) B=0T. d.) B=5T. e.) B=5T. f.) B=5T. g.) B=10T. h.) B=10T. i.) B=10T. j.) B=15T. k.) B=15T. l.) B=15T.

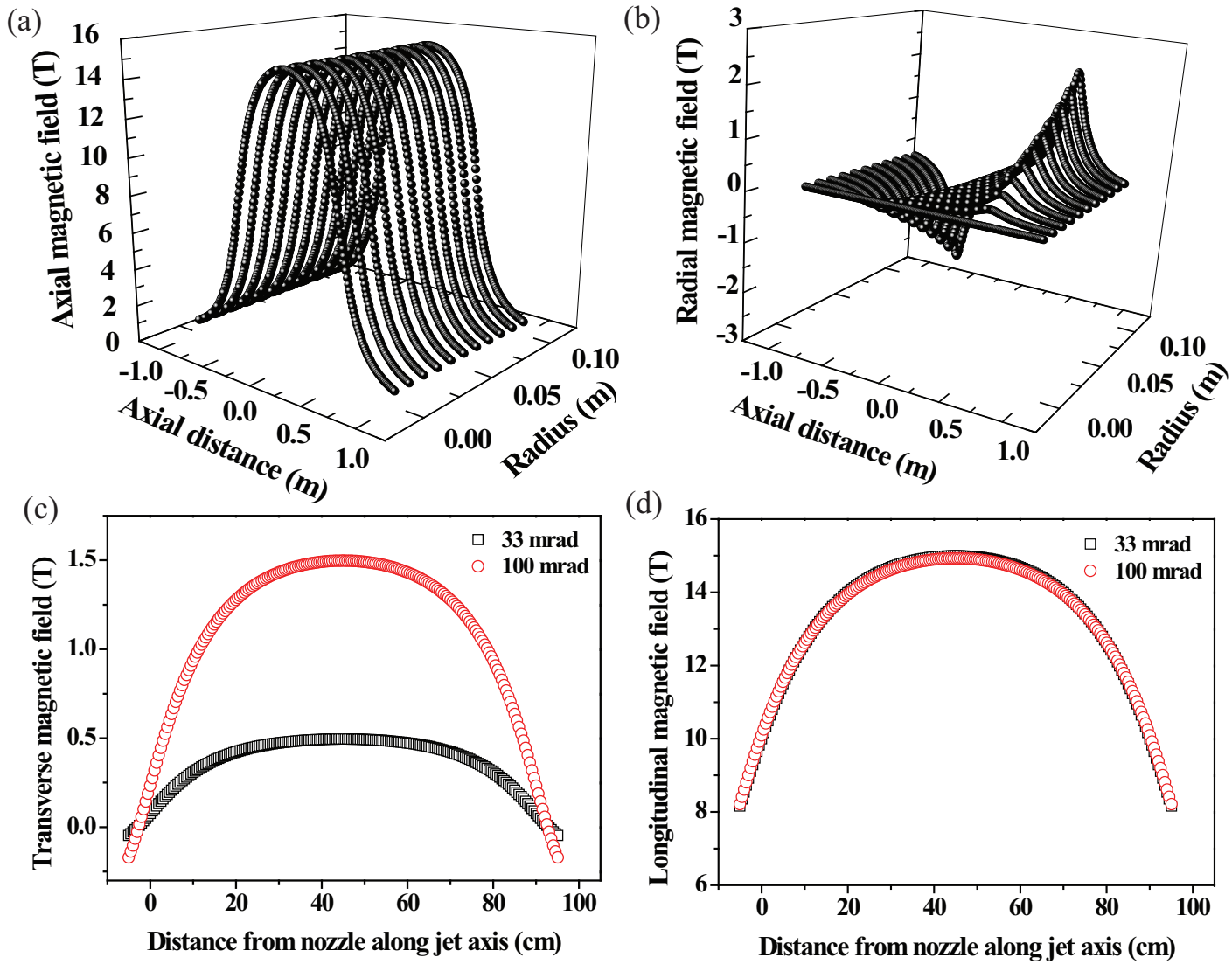

Figure 4.6: Calculated solenoid magnetic induction field map. a.) Radial field map. b.) Axial field map. c.) Transverse component of magnetic induction field along jet axis. d.) Longitudinal component of magnetic induction field along jet axis.

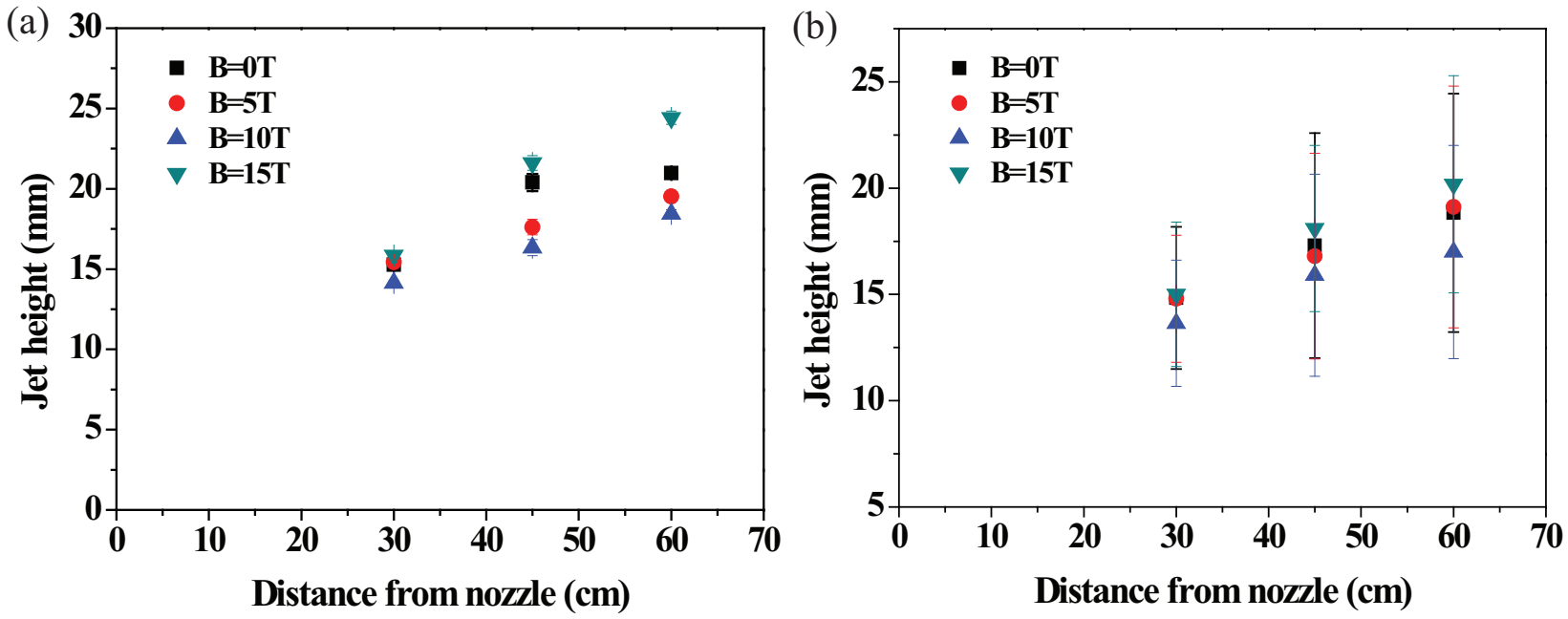

Figure 4.7: Hg jet height measurement in magnetic fields. a.) Histogram fitting of number of events. b.) Direct average of vertical height on each image.

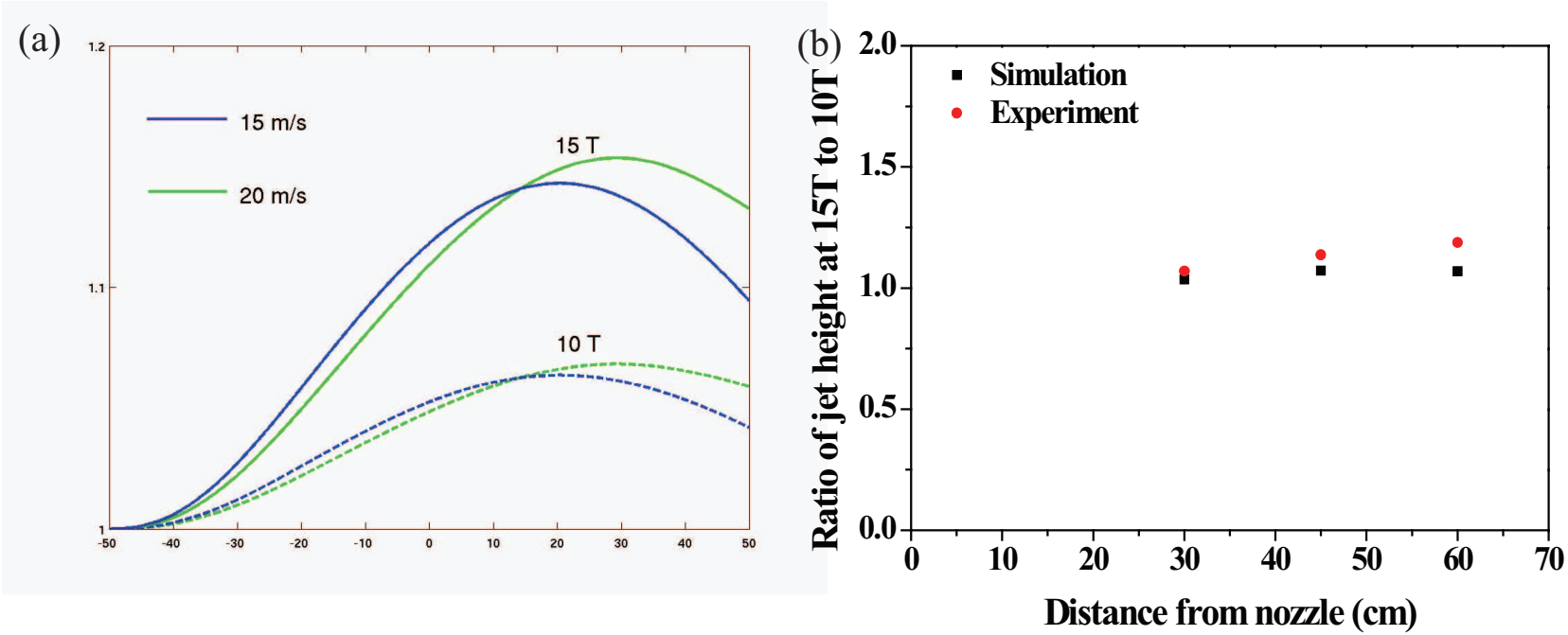

Figure 4.8: Comparison of Hg jet deflection ratio at 15 T to that at 10 T. a.) Numerical calculation of deflection ratio. b.) Comparison of ratio of jet deflection.

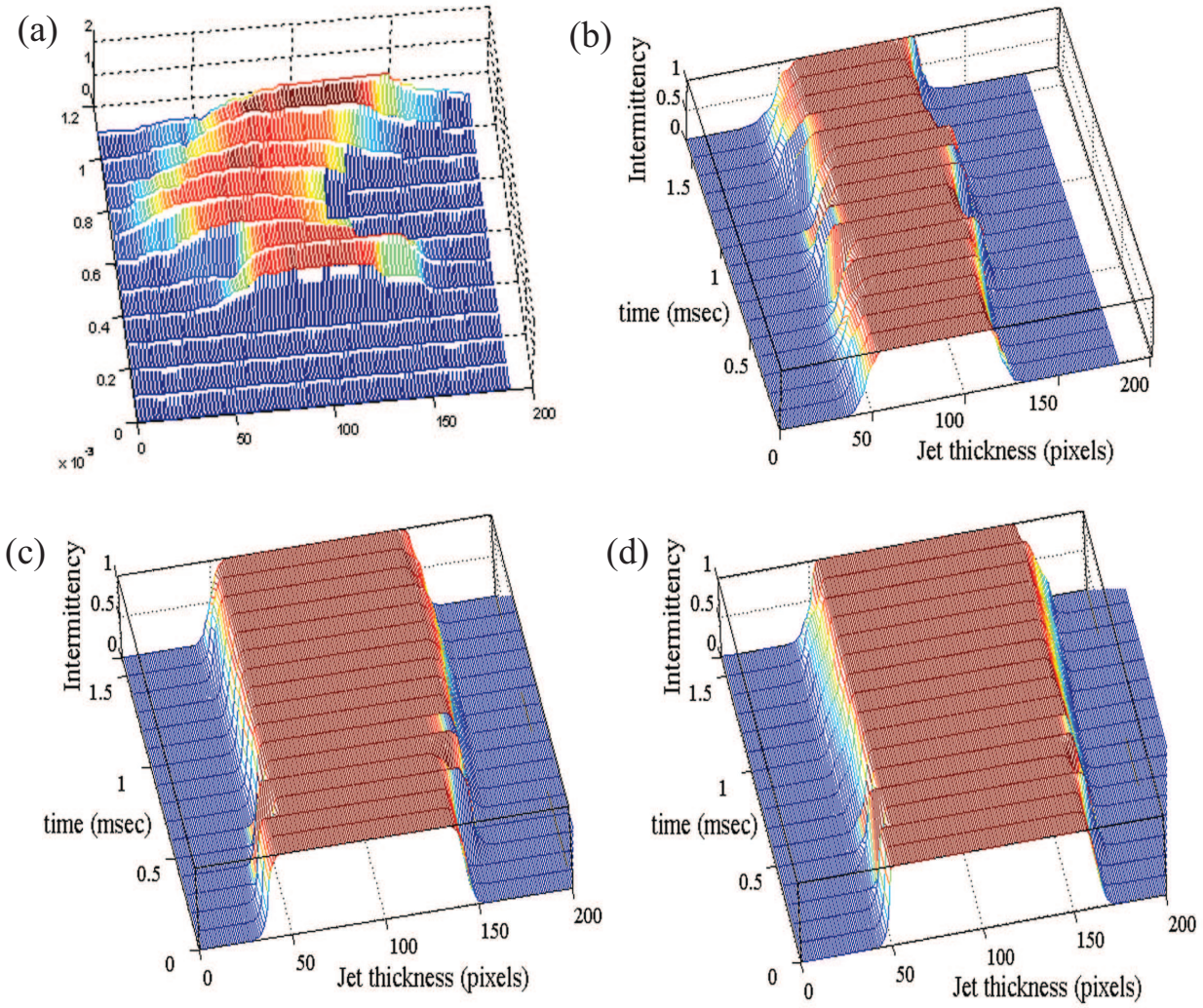

Figure 4.9: Intermittency of Hg jet at Viewport 2. The jet velocity is 15 m/s. a.) B=0T. b.) B=5T. c.) B=10T. d.) B=15T (continued).

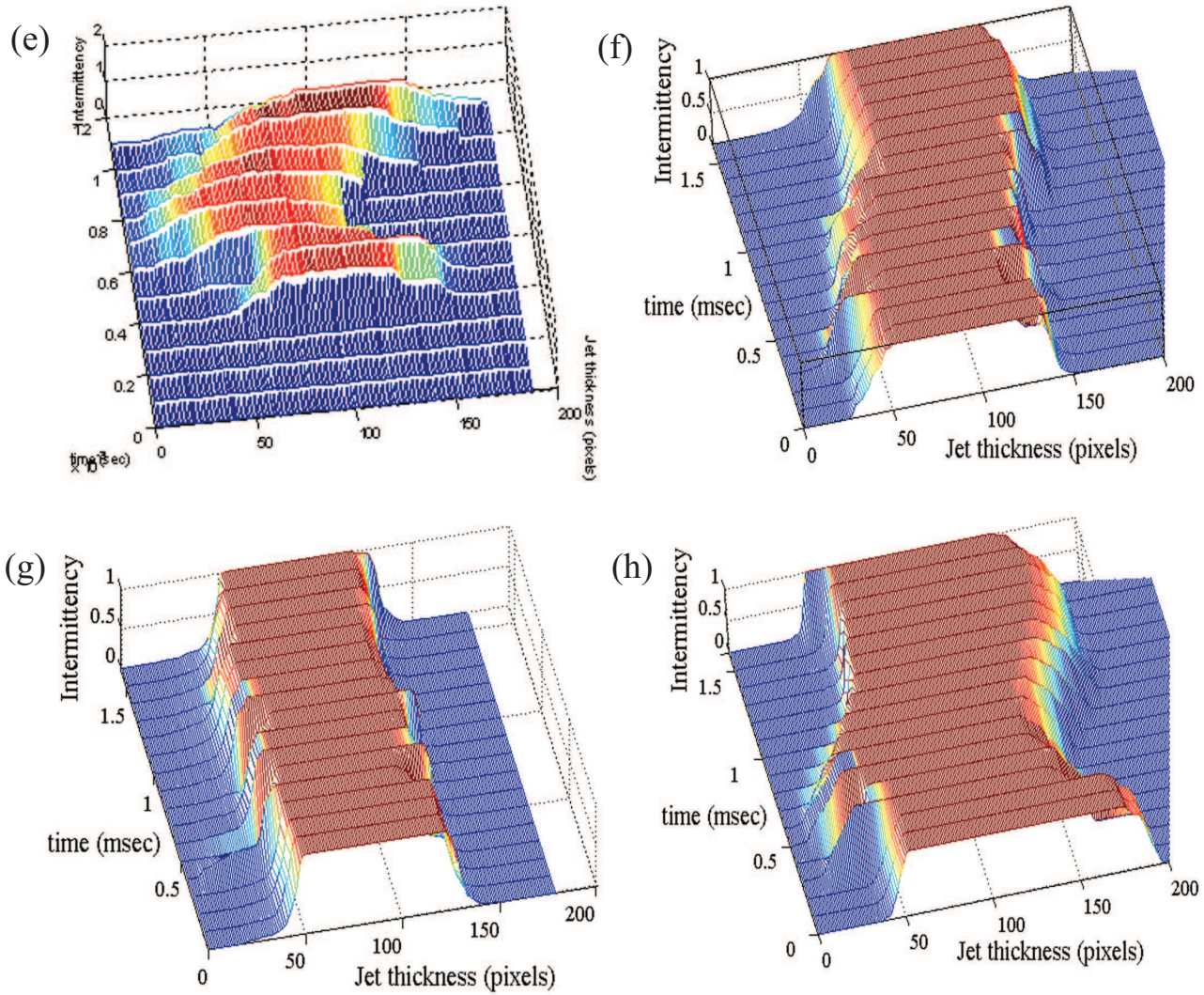

Figure 4.9: Intermittency of Hg jet at Viewport 2. The jet velocity is 20 m/s. e.) B=0T. f.) B=5T. g.) B=10T. h.) B=15T.

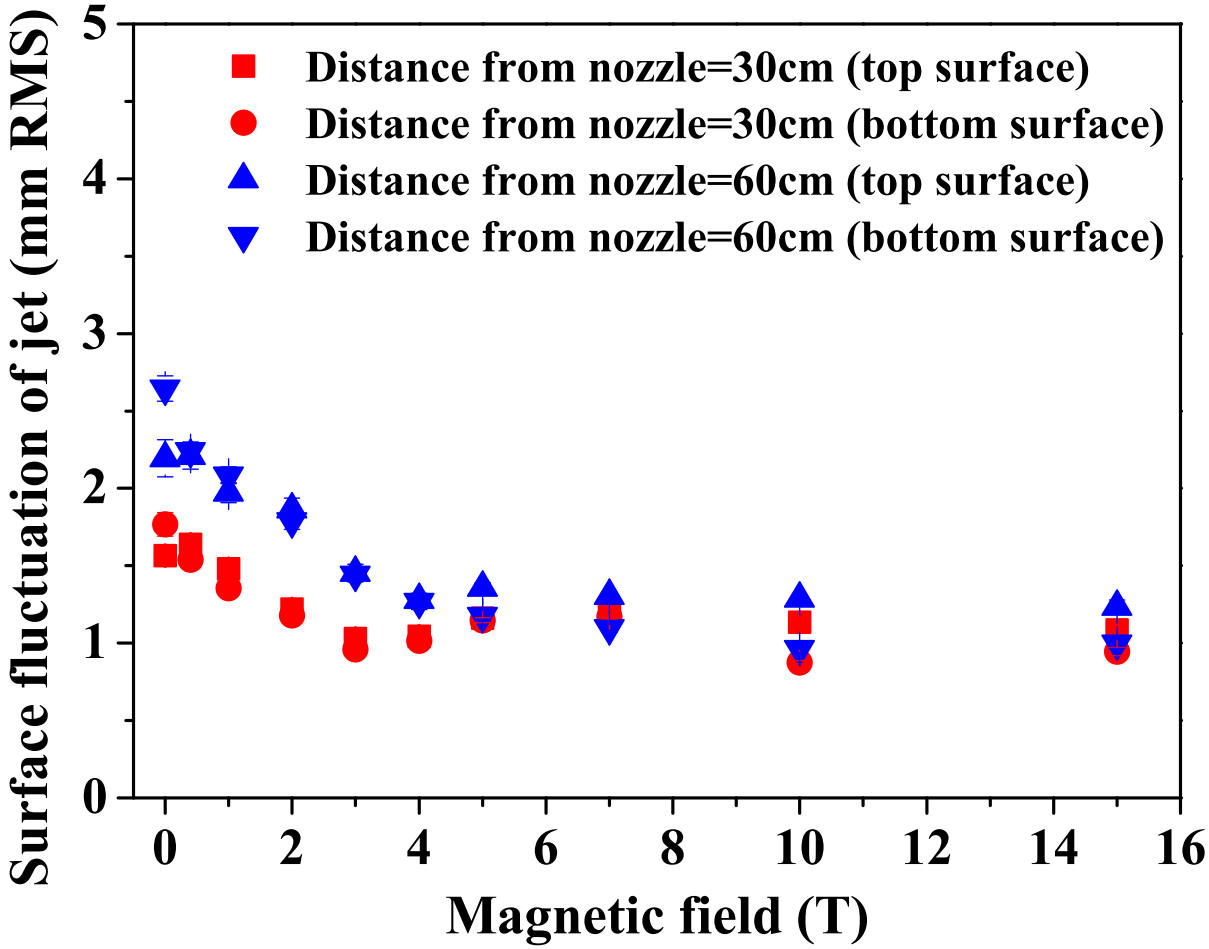

Figure 4.10: Surface fluctuations in a magnetic field.

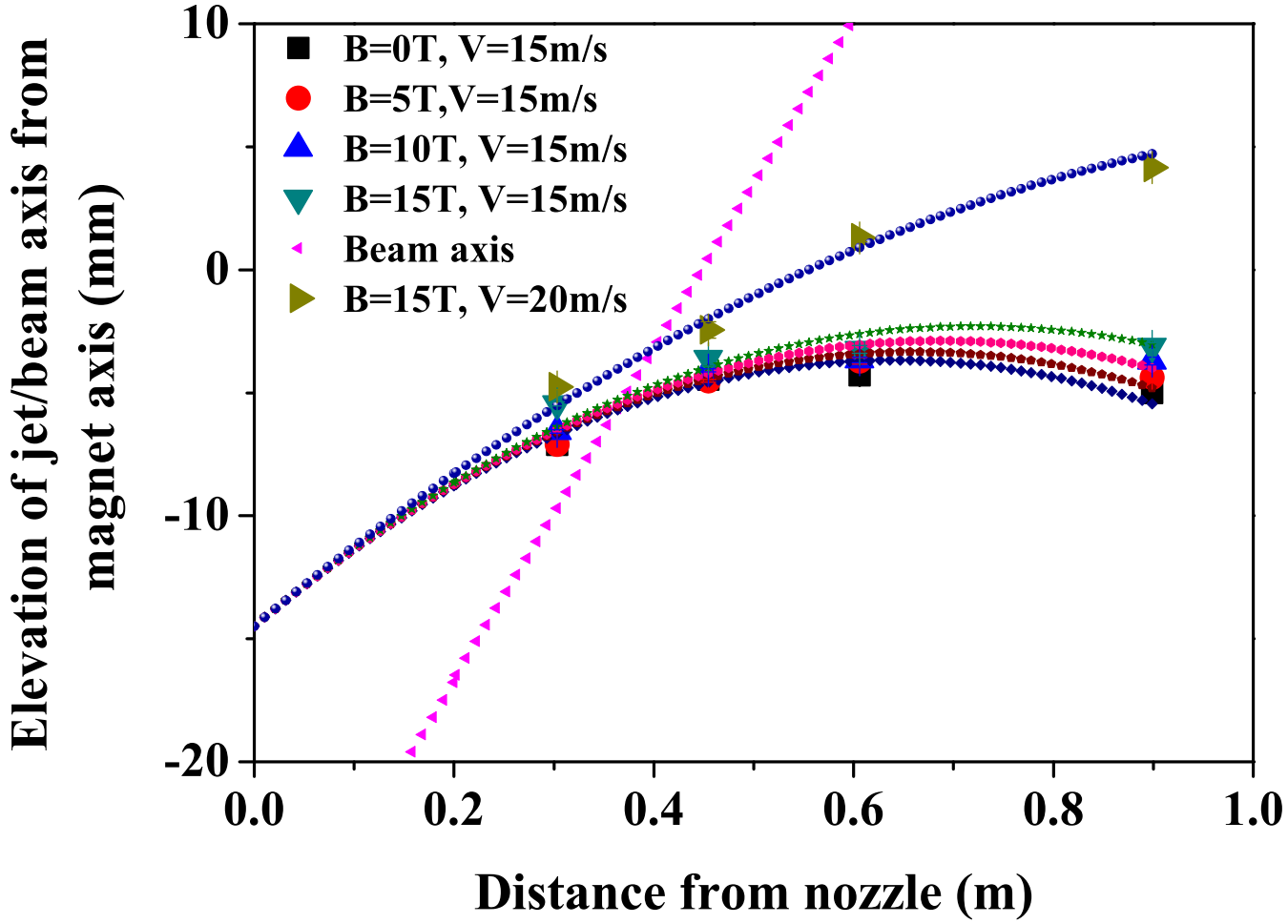

Figure 4.11: Trajectory of beam axis and Hg jet axis projectile with respect to magnetic axis in magnetic field. Solid line represents the simulated value using trajectory of projectile with different velocity.

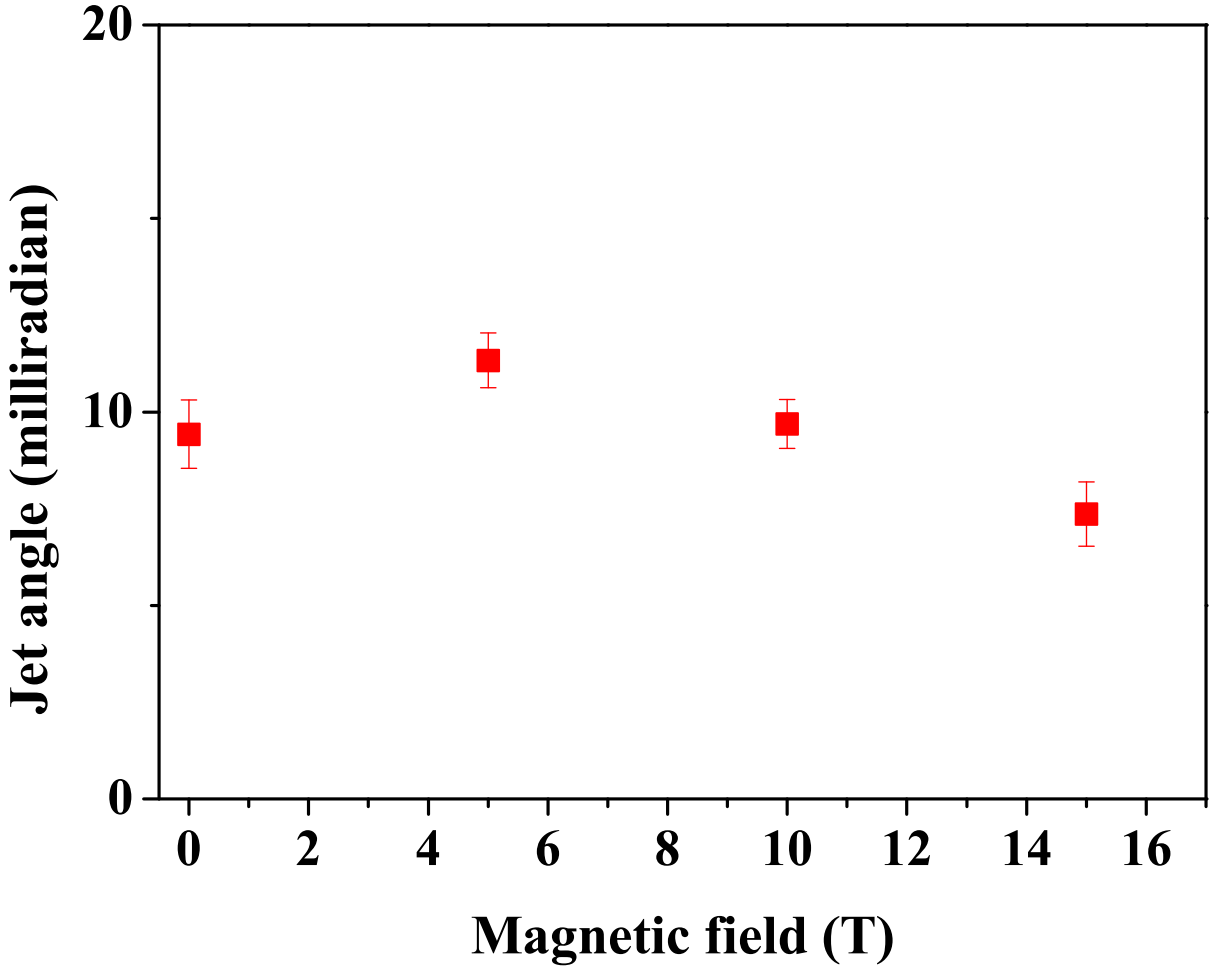

Figure 4.12: Hg jet angle at the center of magnetic axis (Viewport 2) as a function of magnetic field.

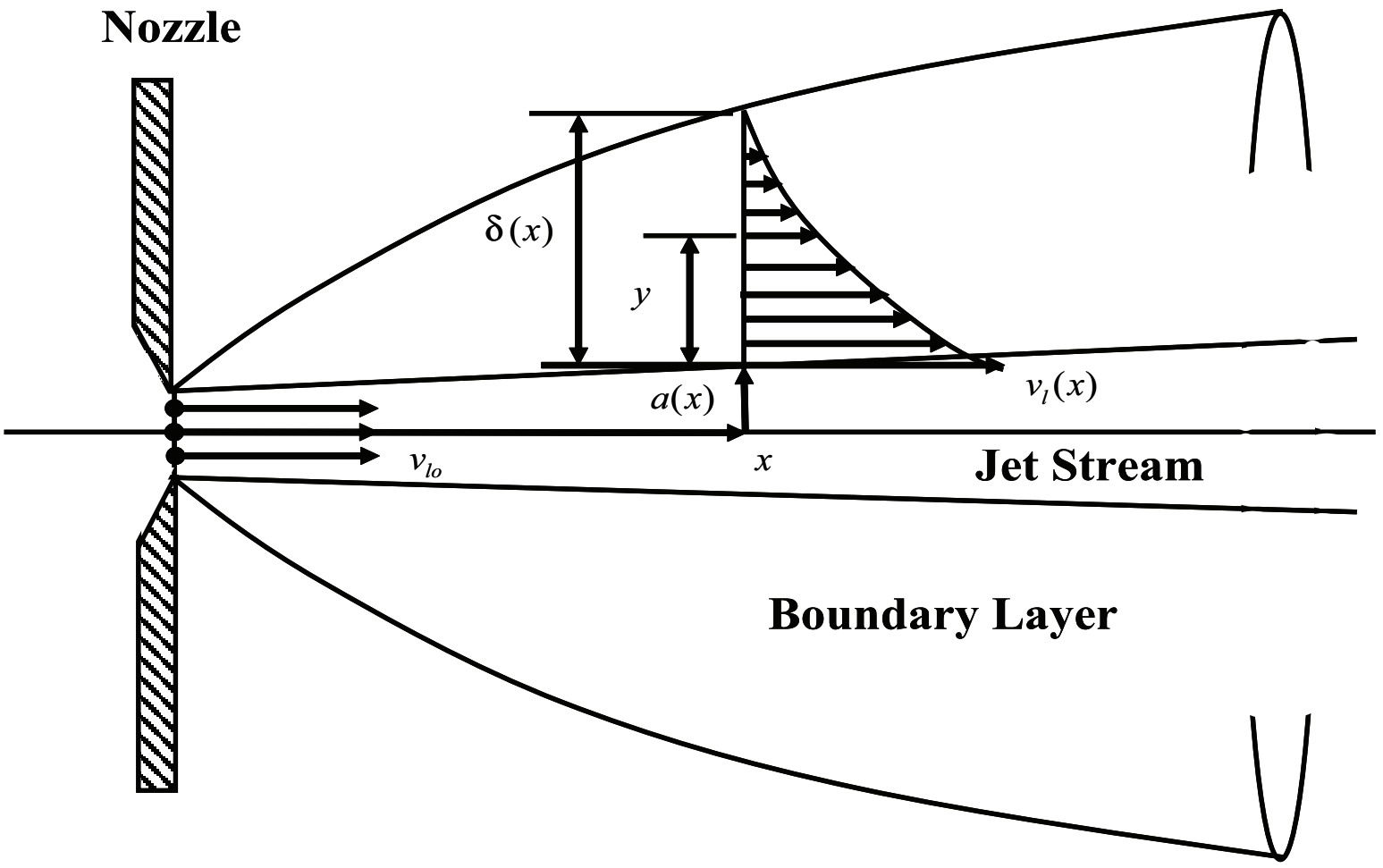

Figure 4.13: Boundary layer induced by a jet emerging from a nozzle.

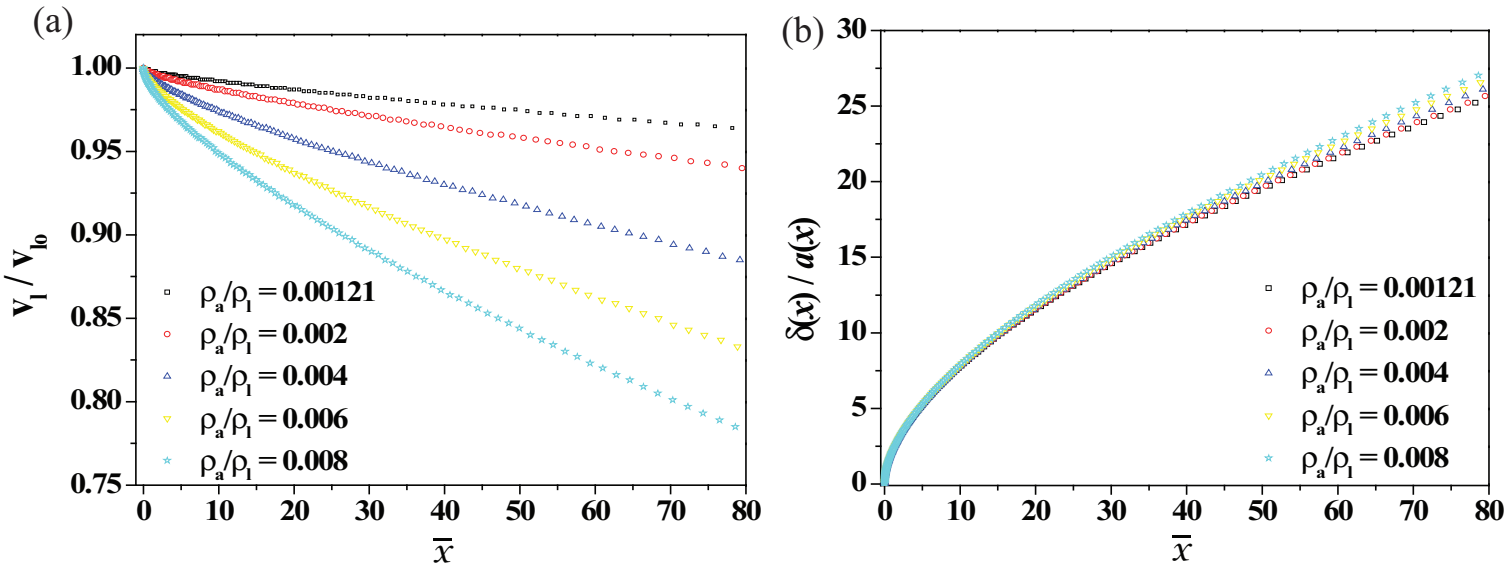

Figure 4.14: Stream velocity and boundary layer thickness for various values of density ratio.

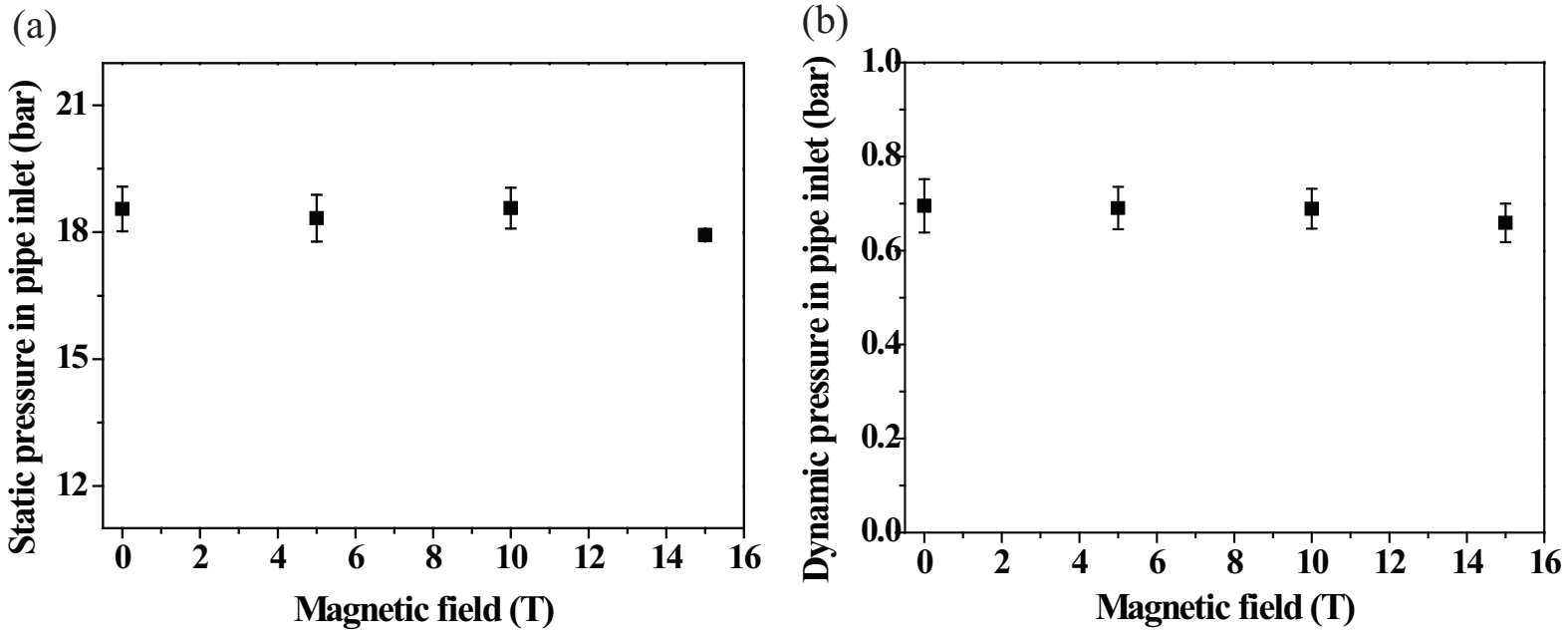

Figure 4.15: Pipe inlet pressure for the driving jet. a.) Static pressure. b.) Dynamic pressure.

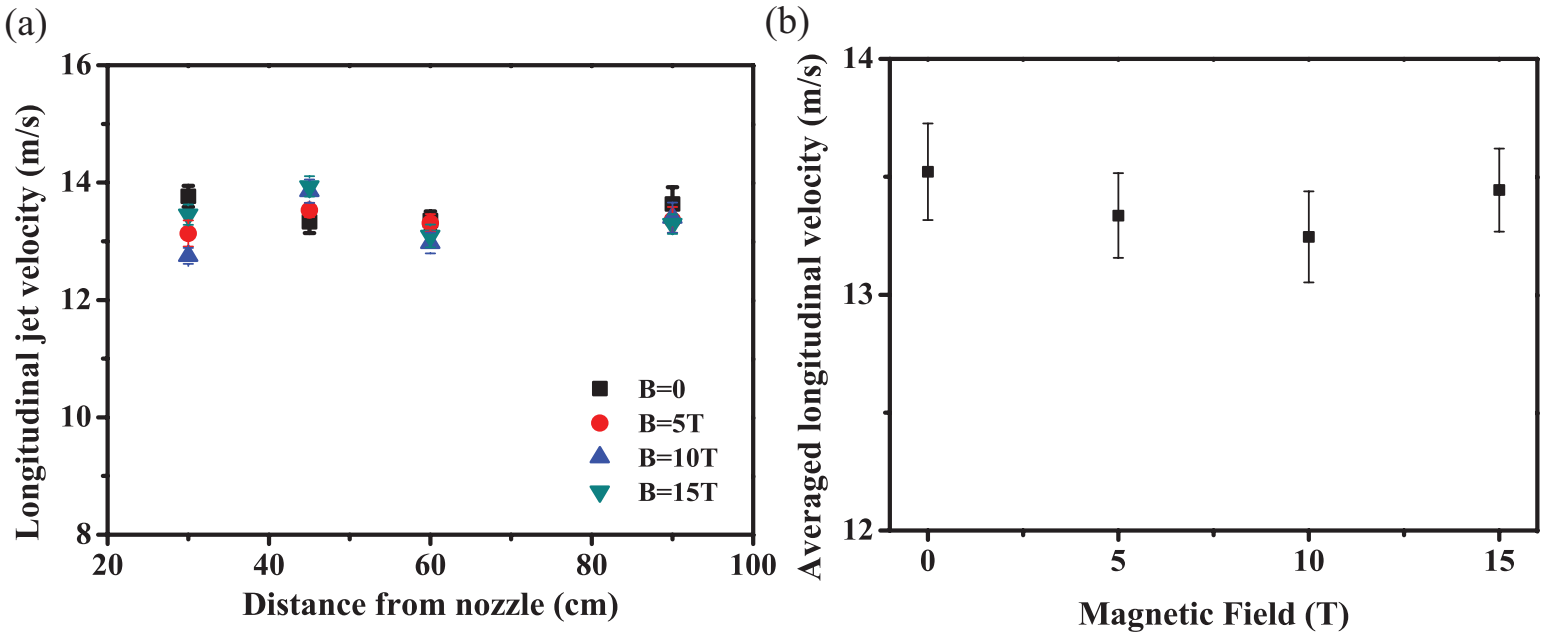

Figure 4.16: Longitudinal Hg jet flow velocity in magnetic field. a.) Velocity at each Viewport dependent of magnetic field. b.) Averaged velocity at each Viewport independent of magnetic field.

Chapter 5

Interaction of an Intense Proton Beam with Hg Jet in Magnetic Field

In this chapter, the jet's interacting characteristics in magnetic field are investigated. The disruption of the jet interacting with various beam intensities and beam energy is observed and the magnetic suppression to it is discussed. The captured images show the mechanism of the beam-jet interaction and the qualitative consistency with the distribution of calculated energy deposition is discussed. The energy deposition induced by the proton beam generates filaments on the Hg jet surface due to thermal stresses. The filaments velocity and its reduction by magnetic field are discussed. It explains that the joule damping dissipates the kinetic energy on a time scale of joule damping term.

5.1 High Energy Proton Beam Structure

5.1.1 Proton synchrotron machine

Neutrino factories requires a large number of muons, which are obtained from the decay of pions. Efficient production of pions can be achieved by

colliding an intense proton beam with a high-Z target. An important consideration is the problem of removing the power deposited by the proton beam without interfering with the process of extracting the end-product, which is the muon beam. The response of a liquid target in a high-magnetic induction field will have beam energy effects, which is investigated experimentally. Experiments on the interaction of a 14 GeV/c and 24 GeV/c proton beam with pulse structures of 4 to 16 bunches per pulse and the spot sizes in the order of 2 to 10 mm^2 RMS up to 30 tera-protons(TP) per pulse in magnetic field up to 15 T has been carried out at CERN. Fig. 5.1 (a) shows the infrastructures for experiment at CERN. All equipments for experiment are installed at tunnel TT2/TT2A and these are controlled remotely at control room. The proton beam is delivered from proton synchrotron ring and the beam setup is schematically shown in Fig. 5.1 (b). The PS machine is set up in harmonic 16 bunches and the extracted protons fill the machine in bunch pairs. A bunch in harmonic 8 mode is consisted of a bunch pair. Therefore, a bunch period in harmonic 8 mode is two times of a bunch period in harmonic 16 mode. Each bunch can fill protons up to 2 2.5 $\times 10^{12}$. Therefore, the maximum beam intensity can be achieved up to 32 $\times 10^{12}$ protons. Fig. 5.2 shows the layout of tunnel at CERN, where equipments for experiment are installed. Electronic equipments for optical diagnostics, hydraulic power unit, and cryogenic system are positioned at tunnel TT2. Hg loop system, solenoid magnet, and beam diagnostic system are positioned at tunnel TT2A. The fibers for optical diagnostics of Hg target in solenoid magnet and cables for controlling the Hg loop

system and solenoid magnet are connected between TT2 and TT2A passing through an artificially drilled hole.

5.1.2 Proton beam pulse length

In order to produce the design number of $10^{21} muons/year$ in the muon storage ring, 4MW of proton beam power is desired. For our experiment, the CERN PS ran typically in a harmonic 16 mode. Hence, it is possible to fill with 2×10^{12} protons/bunch and therefore up to 32×10^{12} protons/spill. One beam pulse consists of several beam bunches. The bunch lengths for harmonic 16 mode are 50 ns and 30 ns at full width at half maximum (FMWH) respectively. The bunch lengths for harmonic 8 mode are 70 ns and 40 ns at full width at half maximum (FMWH) respectively. The bunch-to-bunch differences for harmonic 16 mode and harmonic 8 mode are multiples of 131 ns and 262 ns respectively. The proton beam pulse structure of harmonic 8 and harmonic 16 in 14 GeV, 6 TP is shown in Fig. 5.17. The spot size at the experiment is in the order of 2 to 10 mm^2 RMS. This allows to place up to 32 $\times 10^{12}$ protons on the mercury target, generating a peak energy deposition of $\sim$ 150 J/g. Power consumption is dominated by the repetition rate. Thus, the capability to replace the disrupted jet determines the ultimate beam power. The optimal interaction length for the 24 GeV beam energy is in the region of 30 cm which corresponds to approximately 2 interaction length for mercury (Kirk *et al*, 2008). For a 20 m/s jet velocity, replacing two interaction lengths will be taken in 14 ms thus allowing for operations with a repetition rate of up to 70

Hz. The beam energy per pulse is 115 kJ for a beam of 30×10^{12} protons with 24 GeV beam energy. The disruption length at 30×10^{12} protons with 24 GeV beam energy in a magnetic field of 15 T is less than 20 cm at 24 GeV beam energy in Fig. 5.20, thus preserving the 70 Hz beam repetition rate option. It yields the key result that a target system capable of supporting proton beams with powers of up to 8 MW (Kirk *et al*, 2008).

5.1.3 Proton beam envelope by optics and camera screen

The proton beam with 14 GeV and 24 GeV beam energy is employed in the experiment. As the number of protons in a beam pulse increases, it is reported (Efthymiopoulos, 2008) that the beam spot size increases. The beam spot size is calculated by CERN using the measured beam emittance, dispersion, and the momentum spread of the beam particle. The emittance is measured by measuring the beam profile in a position of known beam parameters based on optics. Fig. 5.4 shows the estimated 1 σ beam spot size at the center of target based on optics (Efthymiopoulos, 2008). Fig. 5.5 shows the measured 1 σ beam spot size at the phosphor camera screen installed $\sim$ 4.2 m away from the center of magnet before entering the magnet (Skoro, 2008). It is also reported (Skoro, 2008) that the beam spot size increases as the number of protons increases. Due to the saturation of image, the measured size is shown as $\sim$ 2 times larger than the estimated beam spot size from optics. Fig. 5.6 (c) shows the beam sizes distribution measured by phosphor screen monitor as a function of time interval between beam shots, where the histogram for events

of beam size in horizontal plane is shown in Fig. 5.6 (a) and the histogram for events of beam size in vertical plane is shown in Fig. 5.6 (b). This plots show that the possible residual saturation of image by phosphor screen monitor is not related with time interval between each beam shot. The distribution of beam spot size is uniform regardless of the possible residual saturation by screen monitor.

5.2 MARS Simulation for Energy Deposition to Mercury Jet by Proton Beam

5.2.1 Physics model

MARS is a Monte Carlo code for inclusive and exclusive simulation of 3D hadronic and electromagnetic cascades, muon and heavy ion transport in accelerator, detector, and shielding components in the energy range from a fraction of an electronvolt up to 100 TeV. In MARS code, hadron production, neutrino interactions, electromagnetic interactions of heavy particles, and electromagnetic showers are considered. For hadron production, information on the nuclides generated in nuclear collisions is scored, or reported in the results of the simulation, which covers a hadron kinetic energy range up to 100 TeV. For neutrino interactions, the model permits the selection of the energy and angle of each particle (ν, e, μ)emanating from a simulated interaction. These particles, and the showers initiated by them, are then further processed in the code. Four types of neutrino interactions are distinguished ($\nu_\mu, \bar{\nu_\mu}, \nu_e, \bar{\nu_e}$) and the model identifies all possible types of neutrino interactions with nuclei. The

corresponding formulas for these processes as well as results of Monte Carlo simulations are considered. For electromagnetic interactions of heavy particles, electromagnetic interactions of muons and charged hadrons in arbitrary materials are simulated. Radiative processes and atomic excitation and ionization with energy transfer are considered. The electromagnetic showers are based on the physics of electromagnetic interactions and it gives electron and photon interactions in composite solid, liquid and gaseous materials (Mokhov, 2000).

5.2.2 Mercury jet modeling in MARS code

Using MARS code, Calculation of energy deposition is performed at Fermi National Accelerator Laboratory (Striganov, 2009). For the modeling of jet in MARS, the experimentally measured Hg jet size and trajectory in magnetic field with assumption of sectionally elliptic jet shape and circular jet shape with equivalent reduced mass density to the initial flow rate from nozzle. The proton beam is passing through the center of magnetic axis. For simplicity, the z coordinate of modeling in MARS defines as 0 at the center of magnetic axis along the direction of magnetic field. Accordingly, the x coordinate of modeling in MARS defines as the vertical direction perpendicular to the direction of magnetic field. The experimentally measured jet size and vertical position to the center of magnetic axis is shown at Fig. 4.7 and Fig. 4.11. The vertical distance in cm in MARS code between center of jet and magnetic axis is employed by using Eqn. (5.1). The experimental measurement of vertical

distance between magnetic axis and the center of jet is given in Table 5.1, where the experimentally measured jet size as well as approximated mass density for the simulation of circular jet case are also given.

$$x_{vert} = -1.4522 - 3.65 \times 10^{-2} \times zz - 3.1672 \times 10^{-4} \times zz^2 + 5.4206 \times 10^{-9} \times zz^4, \tag{5.1}$$

where $zz = z - 46$ in cm.

Fig. 5.7 (a), (b) show the sectional view of elliptic/circular jet and Fig. 5.7 (c) shows the side view of jet interacting with proton beam in magnetic field, which is indicated as arrows. Using MARS code, Calculation of energy deposition with various magnetic field strength and beam intensity is performed at Fermi National Accelerator Laboratory (Striganov, 2009).

5.2.3 Energy deposition to mercury jet

5.2.3.1 *energy deposition in magnetic field*

Fig. 5.8 shows the averaged energy deposition along the jet axis for the case of 3 Tp according to the variation of magnetic field. Calculated energy deposition in each meshed volume is averaged along the jet axis using Eqn. (5.2).

$$\frac{1}{N_\theta^r} \Sigma_r \Sigma_{\theta=0}^{2\pi} E_\theta^r, \tag{5.2}$$

where N_θ^r, E_θ^r represent the number of meshes along radial angle at each radial distance and its energy deposition respectively. As the magnetic field increases, the distribution of energy deposition over the jet increases. This

indicates interaction of charged particles with magnetic field, so that more atomic excitation and ionization with energy transfer occurs in higher magnetic field. Also, the electromagnetic shower produced by a particle that interacts via the electromagnetic force gives electron and photon interactions in mercury. From the equation of particle motion and Lorentz force in Eqn. (5.3), the momentum of charged particle has an influence of the intensity of magnetic field followed by Maxwell's equations.

$$\frac{d\mathbf{p}}{dt} = e[\mathbf{E} + \mathbf{v} \times \mathbf{B}], \tag{5.3}$$

where e is the charge on the particle and $\mathbf{v}$ is the particle velocity.

5.2.3.2 *geometric distribution of energy deposition in elliptic Hg jet cross section*

Fig. 5.9 (a) shows the radially averaged energy deposition over the orientation in sectional jet area along the jet axis for the case of 3 Tp in 5 T. Calculated energy deposition in each meshed volume is averaged along the jet axis using Eqn. (5.4).

$$\frac{1}{N_\theta^r} \Sigma_r E_\theta^r. \tag{5.4}$$

The larger distribution of energy deposition occurs at bottom ($\sim 270°$)of jet where the beam enters. Gradually the larger distribution moves to the top ($\sim 90°$) of jet where the beam leaves. It again gives the consistent result with Fig. 5.14 (a) and Fig. 5.15 (a), where the profile of energy deposition shows

its changes along with the beam path through Hg jet.

Fig. 5.9 (b) shows the axially averaged energy deposition over the variation of magnetic field along the orientation in sectional jet area for the case of 3 Tp. Calculated energy deposition in each meshed volume is averaged along the orientation in sectional jet area using Eqn. (6.2).

$$\frac{1}{N_z^r}\Sigma_z\Sigma_r E_z^r, \tag{5.5}$$

where N_z^r, E_z^r represent the number of meshes along axial jet axis at each radial distance and its energy deposition respectively. The larger axially averaged energy deposition is at bottom ($\sim 270^\circ$) of jet and the distribution of energy deposition increases as the magnetic field increases. The geometrical distribution of energy deposition depending on the applied magnetic field does not changes but keeps uniform profile of distribution, which indicates that the profile of distribution is most likely dependent to the shape of Hg jet.

5.2.3.3 *proton beam spot size to the energy deposition*

Fig. 5.10 shows the averaged energy deposition density along the jet axis using Eqn. (5.2) according to the variation of number of protons in 10 T. As shown in Fig. 5.4, the beam spot size increases as the number of protons increase. As a result, the energy deposition density (per proton) decreases due to the decrease of beam intensity caused by increasing beam spot size. Fig. 5.11 shows the variation of peak energy deposition density with respect to the beam sectional area and magnetic field. The total energy deposition

amounts to $\sim 6 \sim 8$ % of the incident beam energy and the total energy deposition is same regardless of the variation of beam spot size. However, the total energy deposition increases as the magnetic field increases. As discussed in Fig. 5.8, it again indicates interaction of charged particles with magnetic field, so that more atomic excitation and ionization with energy transfer occurs in higher magnetic field. Since the beam spot area increases parabolically, the peak energy deposition density decreases parabolically accordingly. The solid line represents the fit of calculation of peak energy deposition density using Eqn. (6.1).

$$E_{peak} = \frac{E_{peak,N=threshold} \quad A_{beam,optics,N=threshold}^{\frac{1}{x}}}{A_{beam,optics}^{\frac{1}{x}}}, \tag{5.6}$$

where $x = 2.6$ is used for fitting of calculated energy deposition in Fig. 5.11. The peak energy deposition density is estimated by fitting using the peak energy deposition density and the estimated beam cross sectional area at threshold beam intensity, so that the peak energy density can be estimated as a function of beam cross sectional area. Based on the result in Fig. 5.11, the number of protons is multiplied to the energy deposition density, which yields the result in Fig. 5.12. The peak energy deposition with respect to the number of protons increases parabolically due to the increase of parabolically approximated beam cross sectional area, which directly influences to the peak energy deposition to Hg jet. Also, the higher magnetic field again results in larger peak energy deposition to Hg jet. As expected, the smaller peak energy deposition is resulted when the beam spot size from camera is considered, since

the larger beam spot size reduces the beam intensity. This study is useful since it allows one to extrapolate the trend for estimation of profile of energy deposition, so that one can approximate the profile of energy deposition over all of the region of Hg jet based on the previous characteristics of relations in energy deposition to magnetic field, beam intensity, and Hg jet shape.

5.3 Observation of Interaction and Hg Jet Response to The Energy Deposition by Proton Beam

5.3.1 Hg jet pressurization by energy deposition of proton beam

The target material is mercury, whose ρ is 13.6 g/cm^3. The density of the energy deposition E_{dep} due to ionization losses of the protons is $\sim$ 33 J/g. Additional ionization due to secondary particles from interactions of the protons in the target raises this to a peak of $\sim$ 100 J/g at 10 cm into the target (McDonald, 2000). The energy deposition, E_{dep}, leads to peak pressure P that can be estimated as follow:

$$P \approx K\alpha_v \Delta T = \frac{\alpha_v K E_{dep}}{c_p} \ , \tag{5.7}$$

where α_v is the thermal volumetric expansion coefficient, which corresponds to 3 times of thermal linear expansion coefficient, K is the bulk modulus, E_{dep} is the energy deposition, and c_p is the specific heat capacity. For mercury, $\alpha_v = 180 \times 10^{-6}/K$, $E_v = 25GPa$, $c_p = 138J/(K\ kg)$. A peak value of

E_{dep}=100J/g corresponds to a peak stress of $\sim$ 3000 MPa. The mercury target will be disrupted by the proton beam, leading to a breakup into droplets. The strain energy is built up in the jet due to compression (Sievers and Pugnat, 2000). The strain energy per unit volume can be estimated as follow based on the relationship between pressure thermal expansion:

$$E_{strain} = \frac{K}{2}(\alpha \Delta T)^2. \tag{5.8}$$

This deposited strain energy will be released as kinetic energy such as the generation of filaments on the jet surface. Hence, it indicates that the thermal volumetric expansion is possibly proportional to the jet expansion velocity with the coefficient of compressibility of jet material.

5.3.2 Observation of proton beam interaction and jet breakup

Fig. 5.13 is the photographs of the typical Hg jet interacting mechanism with a 16 TP, 14 GeV/c proton beam at 5 T captured at Viewport 3 at a 500 μs frame rate, which shows clearly how the Hg jet is responding from the sudden energy deposition by the proton beam. The beam hits the Hg jet at the bottom surface, passing through the center of jet at Viewport 2, leaving the Hg jet on the top surface. The captured photos show the response of the Hg jet upstream, midstream, and downstream with the interaction of proton beam. There are filaments on the top surface of jet downstream, where the beam is leaving, and on the bottom surface of the jet upstream, where the

proton beam is hitting, entering the target. The jet break up voids midstream where the beam is passing through, possibly caused by the cavitations from energy deposition.

5.3.2.1 *energy deposition calculation with low intensity of proton beam and its observation*

Fig. 5.14 (a) shows the distribution of energy deposition by 24 GeV, 3 Tp intensity proton beam in 5 T. Calculated energy deposition in each meshed volume is averaged along the jet axis and vertical radius of jet using Eqn. (5.9).

$$\frac{1}{N_\theta^r}\Sigma_{\theta=0}^{2\pi}E_\theta^r, \tag{5.9}$$

where N_θ^r, E_θ^r represent the number of meshes along radial angle at each radial distance and its energy deposition respectively.

The spot size from optics is used. The energy density distribution is plotted depending on the radial position of Hg jet from jet center. Therefore, the peak of energy density exists respectively depending on the radial position in analysis. It shows that the maximum energy deposition density is obtained at the bottom surface of jet at $\sim$ 13 cm from the center of magnet, where Viewport 1 is actually positioned, and the peak energy deposition density moves to the center of the Hg jet followed by the larger energy deposition density is located at the top surface of the Hg jet. The peak energy deposition density is moving corresponding to the beam crossing trajectory in Hg jet. The most dense energy deposition is distributed at the center of Hg jet between upstream and midstream, where the Hg jet breaks. The collected photos in

Fig. 5.14 (b) clearly supports these simulation results, where the frame rate is 2 ms and measured disruption length at Viewport 3 is 11 cm.

5.3.2.2 *energy deposition calculation with high intensity of proton beam and its observation*

Fig. 5.15 (a) shows the distribution of energy deposition by 24 GeV, 10 Tp intensity proton beam in 5 T. Averaged energy deposition is also calculated using Eqn. (5.9). The distribution profile of energy deposition throughout Hg jet is similar with low intensity of beam. The collected photos in Fig. 5.15 (b) clearly supports these simulation results again, where the frame rate is 2 ms and measured disruption length at Viewport 3 is 17 cm. However, the jet breakup voids the midstream where the beam is passing through, which is different with comparing with the observation of low intensity beam. These voids are not observed at 3 Tp intensity of beam, possibly indicates threshold of the existence of cavitation induced by energy deposition.

5.3.3 Hg jet disruption and magnetic suppression of the disruption

The disruption length is determined by counting the number of frames at Viewport 3 where the complete disruption of the jet is observed. The time delay between Viewport 2 and Viewport 3 is 10 ms. Thus, the disruption generated at Viewport 2 by the beam could be observed at Viewport 3 after 10 ms, where the jet is moving with a velocity of 15 m/s. Each image is separated into 10 segments vertically in order to locate the position of disruption. Thus,

the accuracy of the measurement to define the location of starting(ending) disruption in measurement could be increased. The disruption length is given by multiplying the frame rate by the counted number of images and investigated with the beam energy, beam intensity, and magnetic field. 230 events out of 360 beam shots are evaluated for the disruption length. About 130 events out of 360 beam shots are evaluated for the detection of particles without Hg jet. Thus, the images for these events are not collected. Fig. 5.16 shows the standard deviation of the evaluated disruption lengths with respect to the disruption length. The solid line represents the curve fitted approximation of the reduced data distribution, where the line asymptote logarithmic. This curve fitted line is used for estimation of the standard deviation of the disruption length at respective disruption length. Correspondingly, the error bar is determined by dividing the the estimated standard deviation by the root square of the number of samples N for each data point.

5.3.3.1 *characteristics of beam structure in disruption length, harmonic 8 and 16*

The proton beam pulse structure of harmonic 8 and harmonic 16 in 14 GeV, 6 Tp is shown in Fig. 5.17. Fig. 5.18 shows the dependence of the disruption length of the Hg jet on the proton beam pulse structure with a 14 GeV beam in 5 T. A pulse contains same total protons. Doubled bunches shows doubled disruption length. It indicates that the energy deposition by the collision of Hg and protons is same, but the disruption of Hg jet is more likely affected by the number of protons in each bunch and time difference in a

pulse due to the different bunches, i.e, 8 bunches and 16 bunches, though there are same protons in a pulse. The disruption on the Hg jet surface disappears when the beam intensity is less than $\sim$ 4 Tp in Fig. 5.19. The threshold of beam intensity is $\sim$ 4 Tp at 14 GeV in 5 T. Fig. 5.18 also indicates that the harmonic 8 pulse structure can increase the threshold of disruption for a bunch of beam intensity. Considering that the different beam pulse structure results in different disruption to Hg due to the time difference of bunches in a pulse structure, we consider only harmonic 16 pulse structure for the following experiment.

5.3.3.2 *disruption length with 14 GeV proton beam*

Fig. 5.19 shows the disruption length with beam intensities up to 30 Tp for a 14 GeV beam. The peak energy deposition to Hg with 14 GeV beam energy at 30 Tp is $\sim$ 70 J/g by approximating it from Fig. 5.12 and the ratio of energy deposition by 14 GeV and 24 GeV respectively, where the disruption length corresponds to $\sim$ 23 cm $\pm$ 5 cm for 10 T to $\sim$ 18 cm $\pm$ 5 cm for 15 T respectively. At high intensities of beam, the disruption length appears to be approaching an asymptotic level. The magnetic field reduces effectively weak disruption such as the generation of the filaments on the jet surface. The threshold of the disruption for beam intensity is around 4 Tp at 5 T and the magnetic field can increases it, though the effect is not clear in Fig. 5.19 due to the difficulty in quantifying and measuring the small amount of the disruption length.

5.3.3.3 *disruption length with 24 GeV proton beam*

Fig. 5.20 shows the disruption length with the beam intensities up to 30 Tp for a 24 GeV proton beam. The estimated disruption of Hg jet is also determined by using the threshold level from experimentally measured beam intensity as follow :

$$L^{disruption} \quad for \quad E \geq E_{threshold}, L^{disruption}_{E^{peak}_{threshold}} = 0, \tag{5.10}$$

where $L^{disruption}$, $E^{peak}_{threshold}$ represent the length of disruption and peak energy level of thresholding beam intensity experimentally determined for jet disruption.

According to Fig. 5.12, the peak energy deposition to Hg with 24 GeV beam energy at 30 Tp in 10 T is $\sim$ 130 J/g, where the disruption length corresponds to $\sim$ 22 cm $\pm$ 5 cm for 10 T to $\sim$ 17 cm $\pm$ 5 cm for 15 T respectively. The results show that the magnetic field suppresses the disruption length. The disruption length appears to be approaching an asymptotic level. If there is no magnetic field, the disruptions are always generated by proton beam regardless of the beam intensities, though very weak disruptions on the Hg jet surface are observed with low beam intensities. The threshold of the disruption for beam intensity is $\sim$ 2 Tp at 5 T but the higher magnetic field increases it. The estimation of disruption length in 10 T based on the calculation of energy deposition using the beam spot size from optics is well agreed with the experimental measurement, but the estimation in 0 T based on the beam spot size from optics underestimates the experimental results. Possibly, the difference

in MARS model may cause the difference of energy deposition calculation and the beam spot size is more likely to be larger at 0 T. Therefore, possibly the estimation by energy deposition from larger beam spot size is more likely to be fit to the experimental measurement. However, the estimation in 0 T based on the beam spot size from camera screen is well agreed with the experimental measurement at 0 T. For theses estimations, the independent threshold of beam intensity is chosen individually from the experimental results depending on the conditions of individual cases for estimation. Therefore, the energy for threshold is differently used for the case of estimation using the beam size from optics and camera. For the case of estimation of 0 T and 10 T, 1 Tp and 3 Tp of threshold beam intensity is chosen respectively.

5.3.3.4 *validation of measurements of Viewport 3 through comparison with Viewport 4*

In order to validate measurements of the disruption length at Viewport 3, measurements of disruption lengths at Viewport 4 are also performed. Fig. 5.21 (a) shows the disruption length at Viewport 3 for 23 events with a harmonic 16 beam structure, 16 Tp, 14 GeV beam energy in 5 T. Fig. 5.21 (b) shows the disruption length at Viewport 4 for the same events. Fig. 5.21 (c) shows the difference of disruption length between Viewport 3 and Viewport 4 for the same events. The solid line represents the average and distribution of the disruption length difference. The difference of measured disruption length between Viewport 3 and Viewport 4 is 1.3 ± 3.5 cm. The reason for the difference of the disruption length measurement between Viewport 3 and Viewport

4 is mainly caused by the fluctuation of the proton beam and the Hg jet in a magnetic field. The reduction of surface instabilities by the presence of a static magnetic field is a consequence of magnetic damping. Also, surface structure is frozen by magnetic field. Therefore, the same disrupted shape on the jet surface at Viewport 3 is observed at Viewport 4 without variation of the disruption length.

Table 5.1: Measurement of vertical distances of center of jet from magnetic axis and jet size for modeling in MARS code for the cases of elliptic and circular jet sectional shape.

1 (T)	**2** (mm)	**3** (mm)	**4** (mm)	**5** (mm)	**6** (mm)	**7** (mm)	**8** (g/cm^3)
Elliptic jet shape							
0	7.11	4.46	4.28	5.01	8.65	2.9	13.55
5	7.1	4.52	3.7	4.38	8.4	3.0	13.55
10	6.57	4.08	3.66	3.71	7.95	3.15	13.55
15	5.45	3.6	3.24	3.11	9.05	2.76	13.55
Circular jet shape							
0	7.11	4.46	4.28	5.01	8.65	8.65	4.50
5	7.1	4.52	3.7	4.38	8.4	8.4	4.77
10	6.57	4.08	3.66	3.71	7.95	7.95	5.32
15	5.45	3.6	3.24	3.11	9.05	9.05	4.11

1. Magnetic field

2. Vertical distance at Viewport1

3. Vertical distance at Viewport2

4. Vertical distance at Viewport3

5. Vertical distance at Viewport4

6. Vertical radius of jet

7. Horizontal radius of jet

8. Hg density

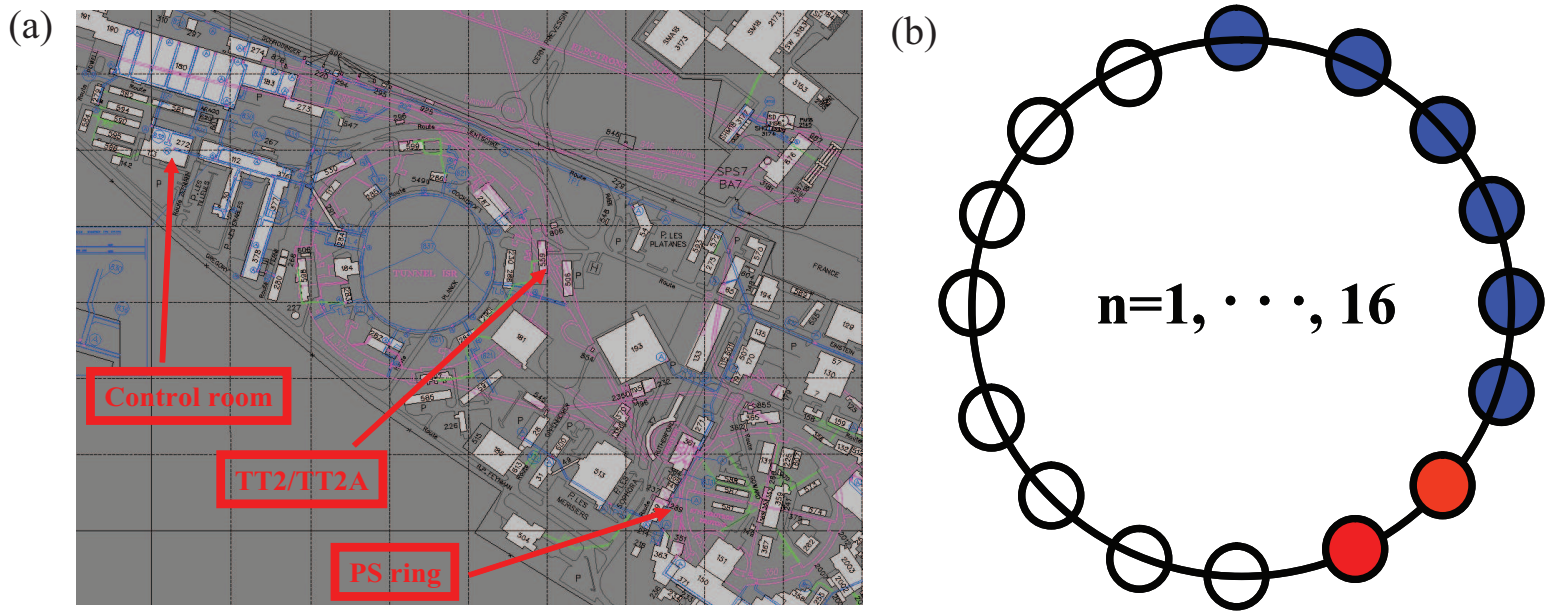

Figure 5.1: Infrastructures for experiment at CERN. a.) Proton synchrotron and TT2 tunnel for experiment. b.) 16 harmonics of beam extraction in proton synchrotron.

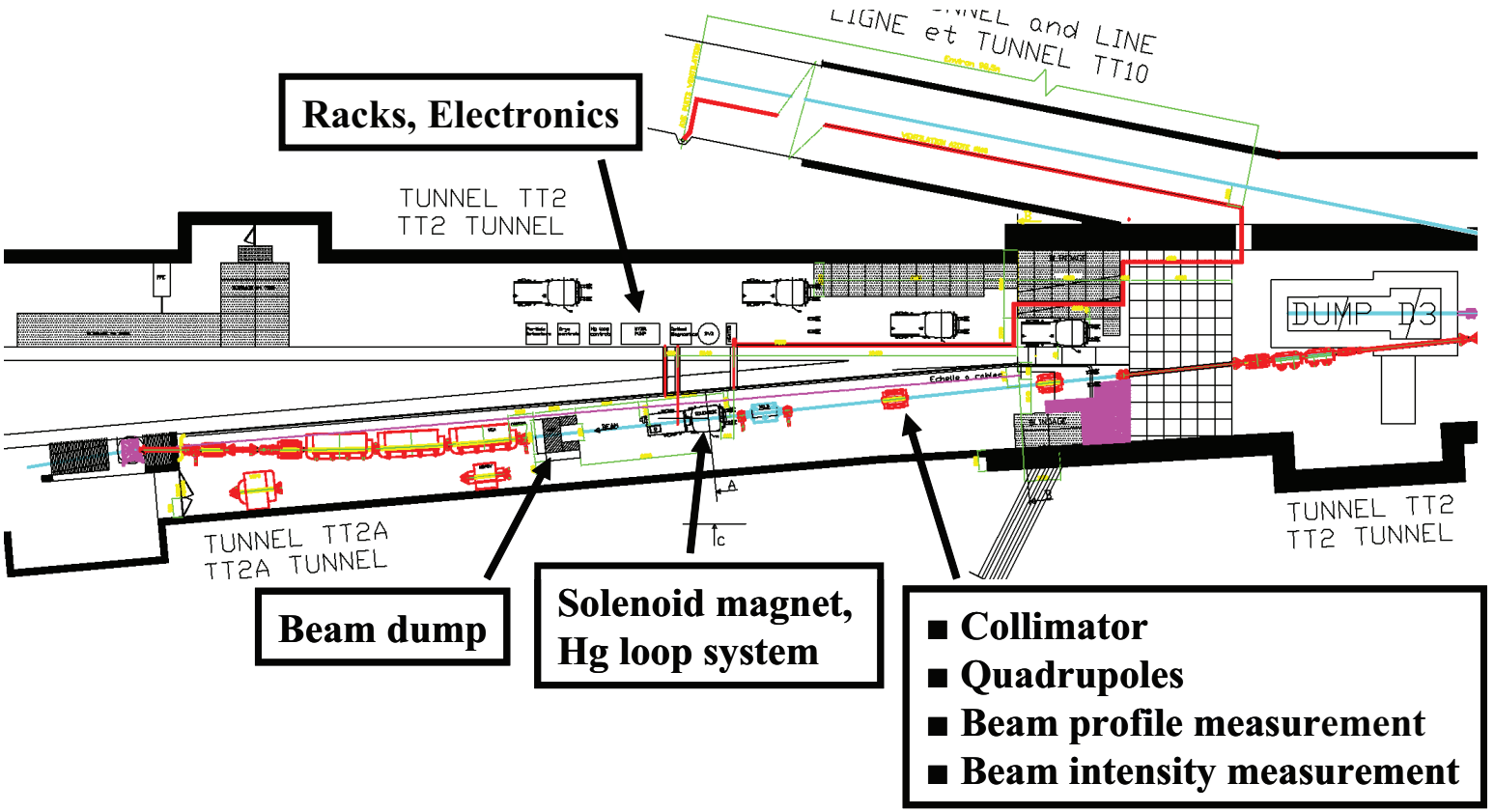

Figure 5.2: Installation of integrated experimental components in tunnel TT2/TT2A for high power target experiment. Extracted proton beam comes from right to left in tunnel TT2A.

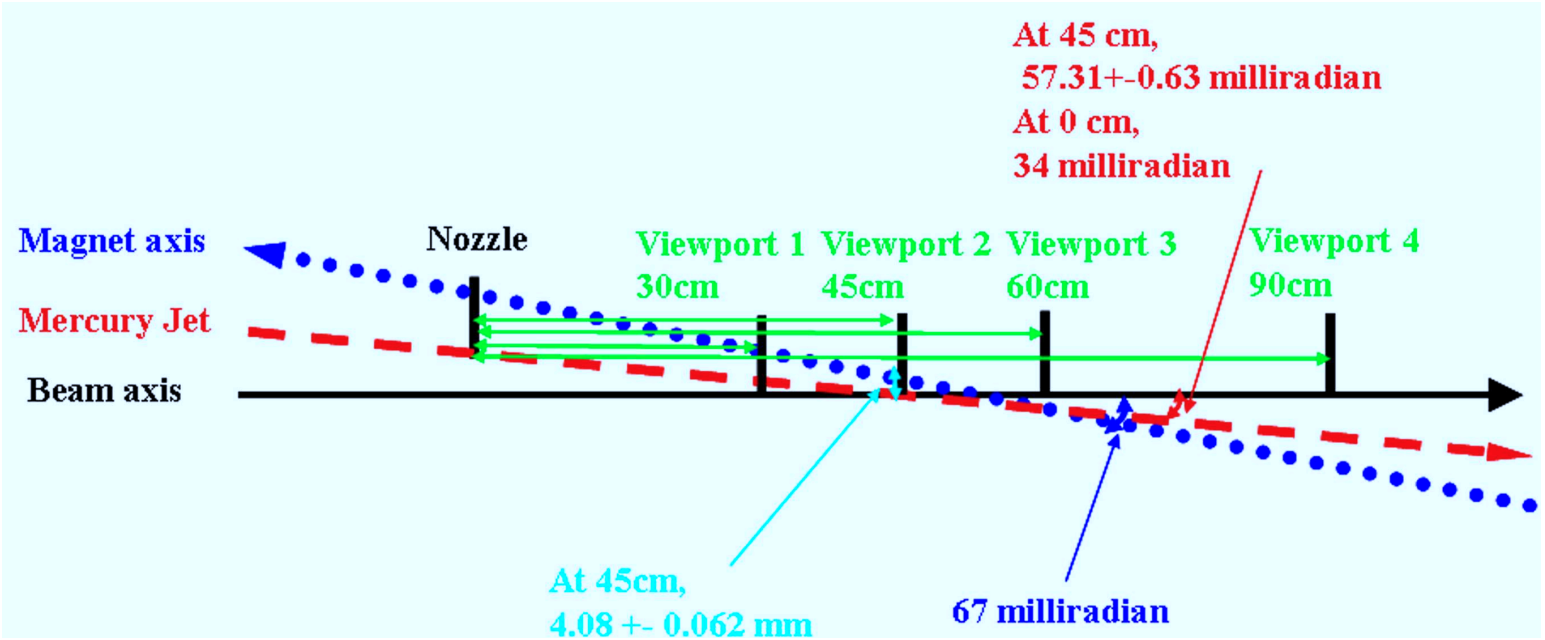

Figure 5.3: Schematics of beam to jet interaction in magnetic field and the location of each Viewport.

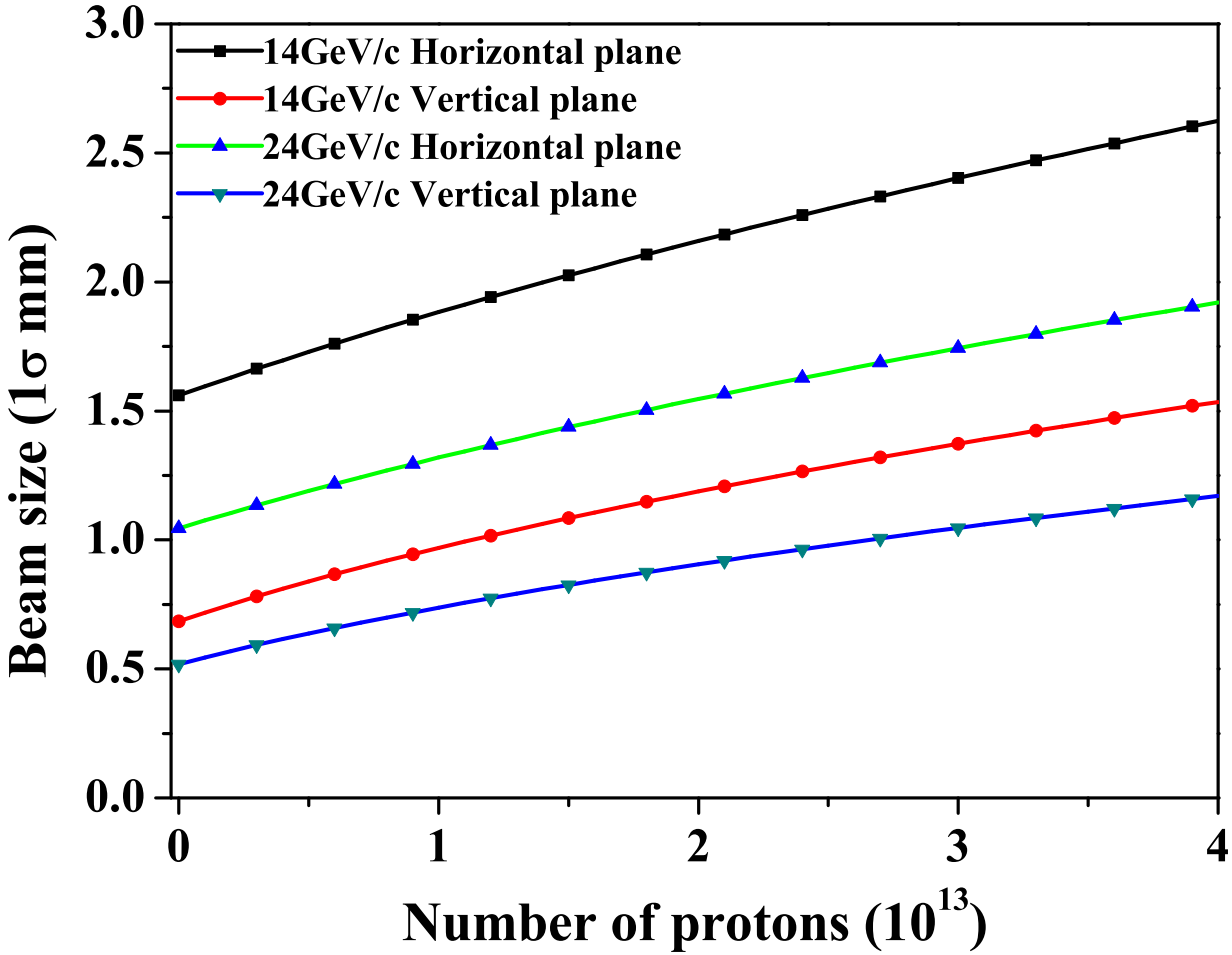

Figure 5.4: 1 σ proton beam size at the center of magnet by optics (Efthymiopoulos, 2008).

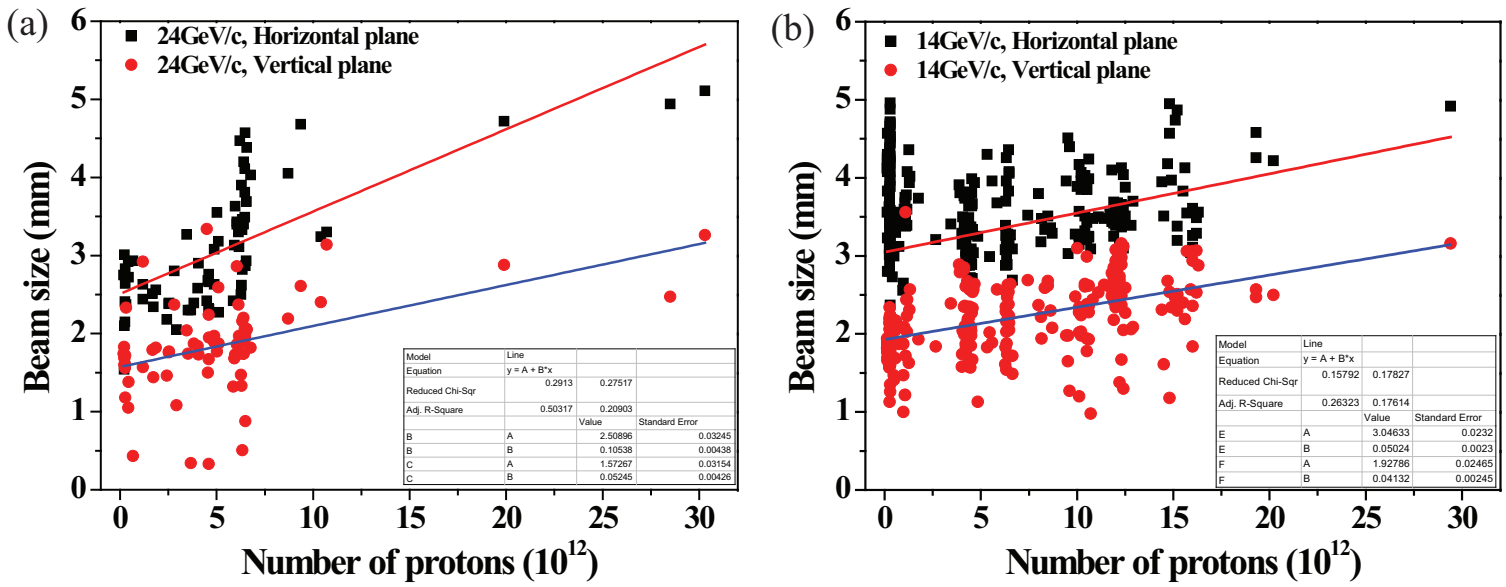

Figure 5.5: 1 σ proton beam size by camera screen (Skoro, 2008). a.) 14 GeV beam. b.) 24 GeV beam.

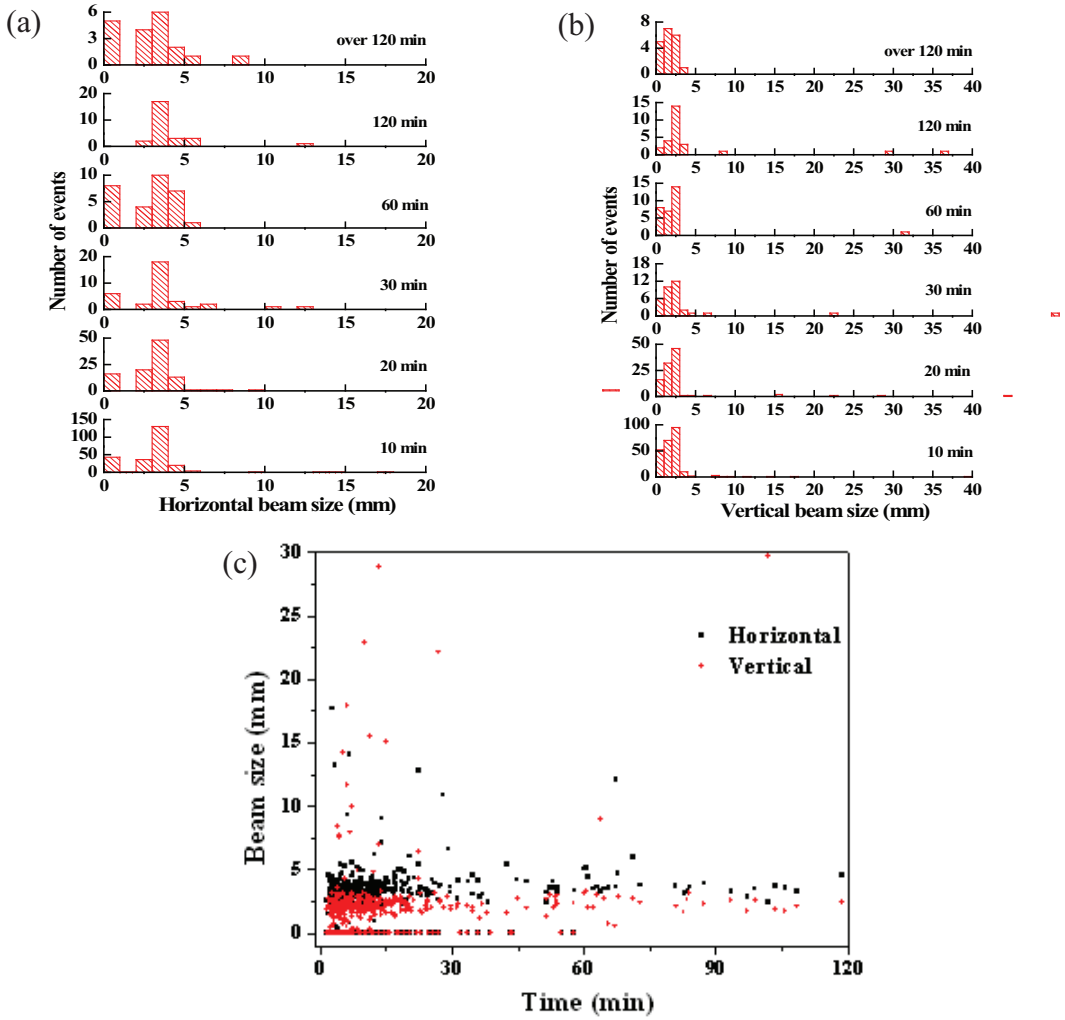

Figure 5.6: Beam size measured by phosphor screen monitor as a function of time interval between beam shots. a.) Histogram of beam size in horizontal plane. b.) Histogram of beam size in vertical plane. c.) Beam sizes distribution.

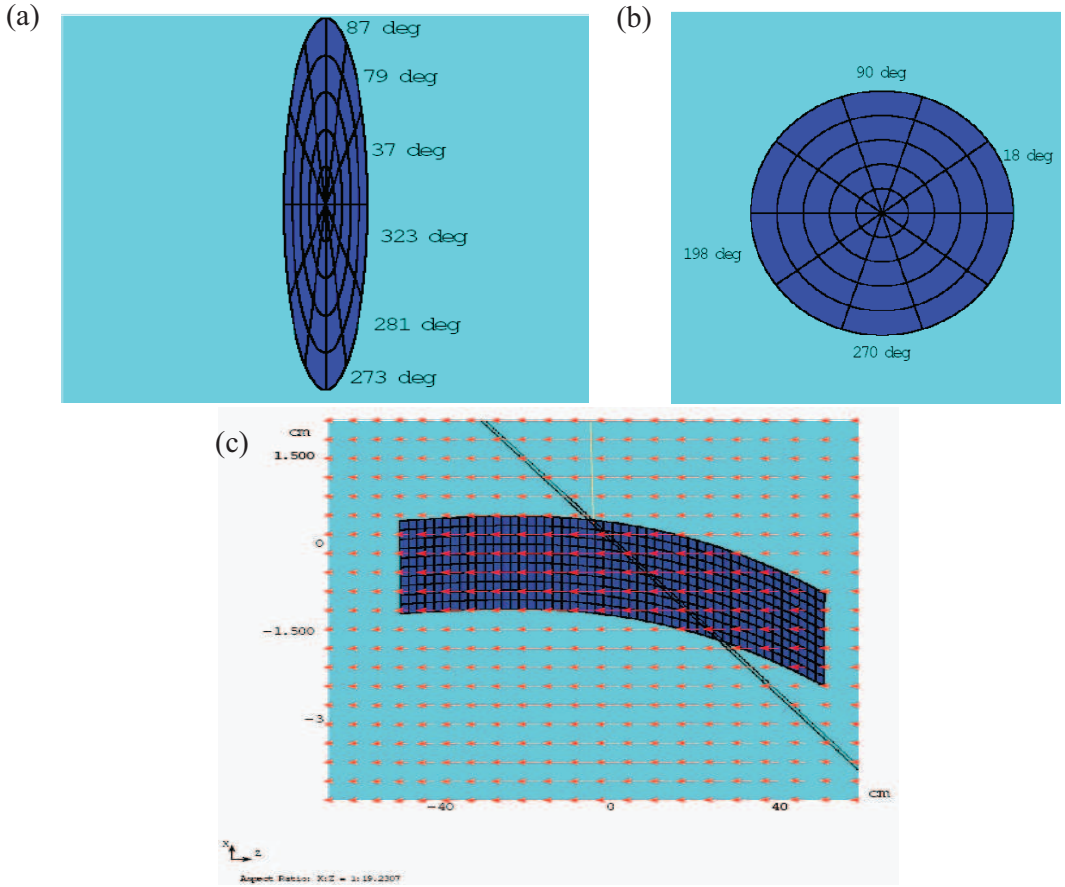

Figure 5.7: Modeling in MARS code for energy deposition calculation (Striganov, 2009). a.) Sectional view of elliptic jet. b.) Sectional view of circular jet. c.) Side view of mercury jet.

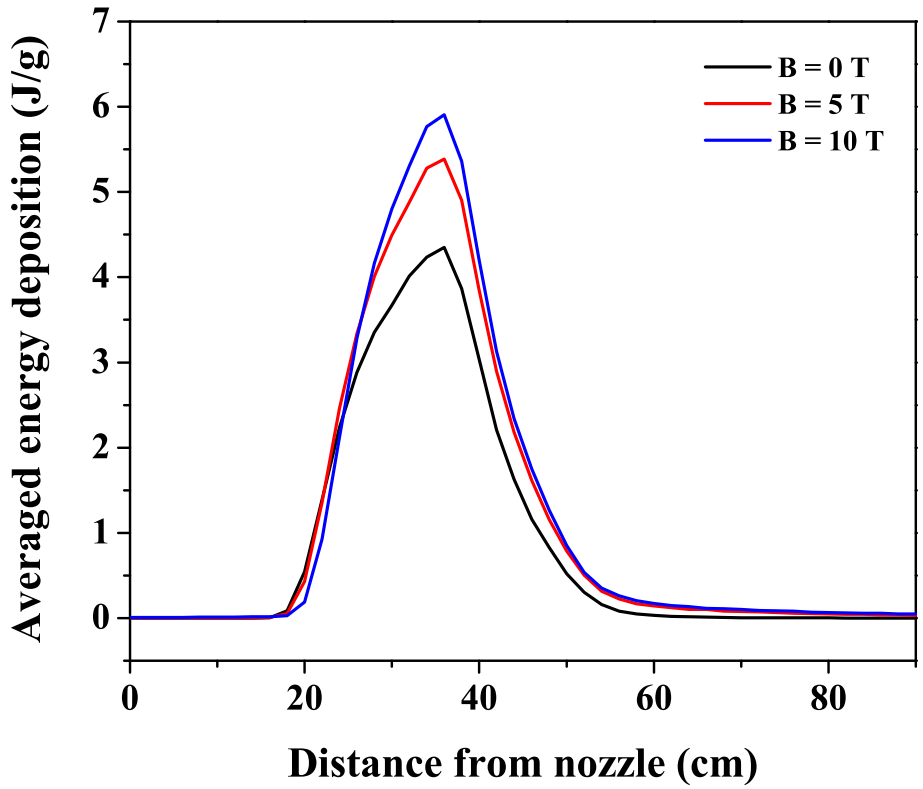

Figure 5.8: Influence of magnetic field to the energy deposition distribution to Hg jet considering experimentally measured jet parameters.

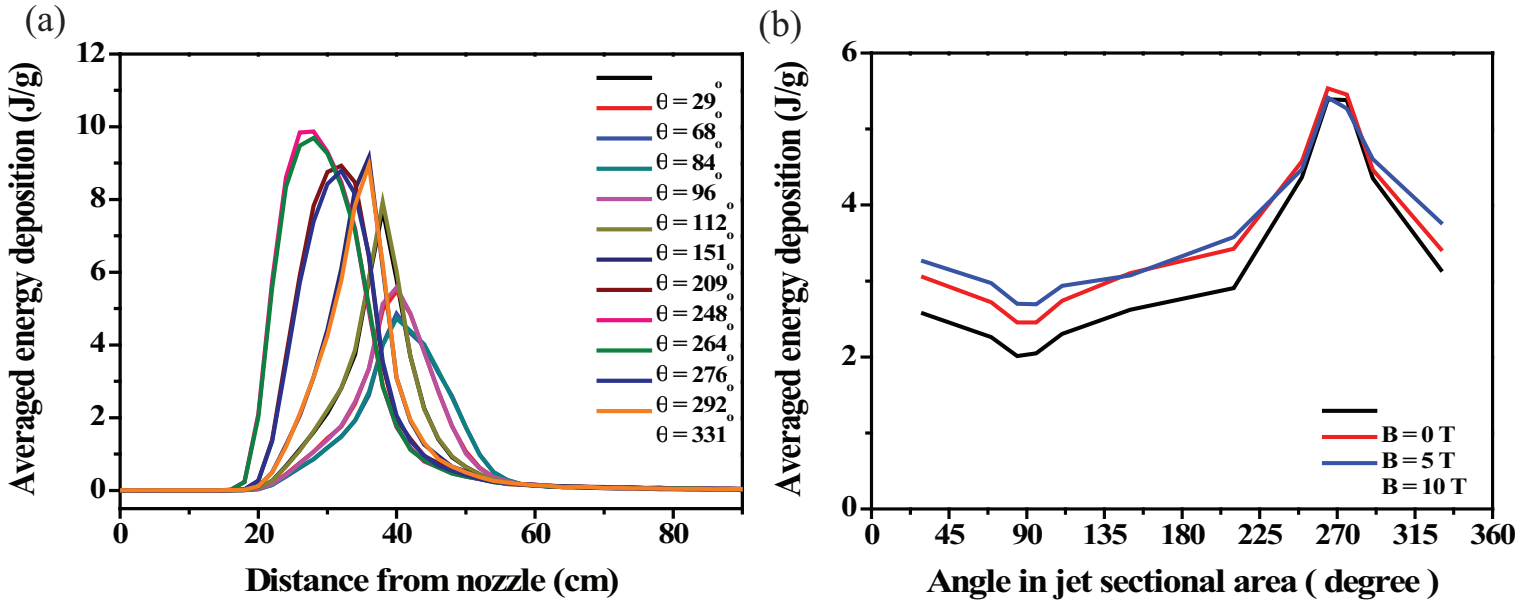

Figure 5.9: Radial energy deposition distribution along jet axis. a.) Along jet axis. b.) Along radial angle in jet cross section.

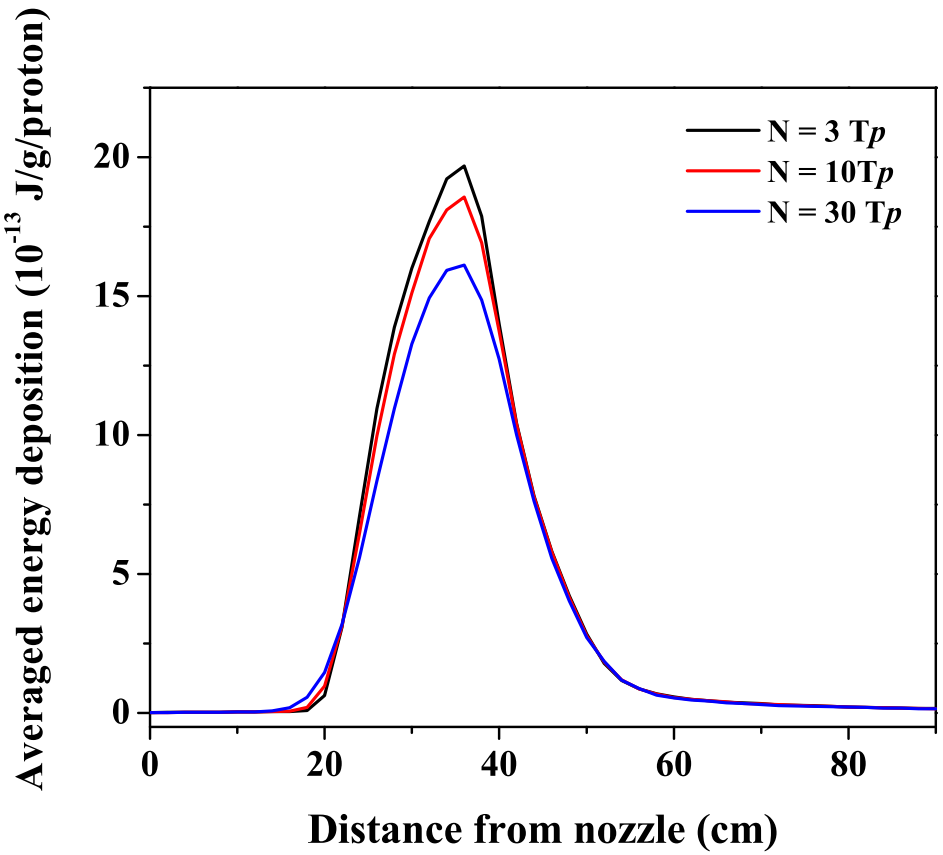

Figure 5.10: Energy deposition distribution per proton according to the variation of beam spot size along jet axis.

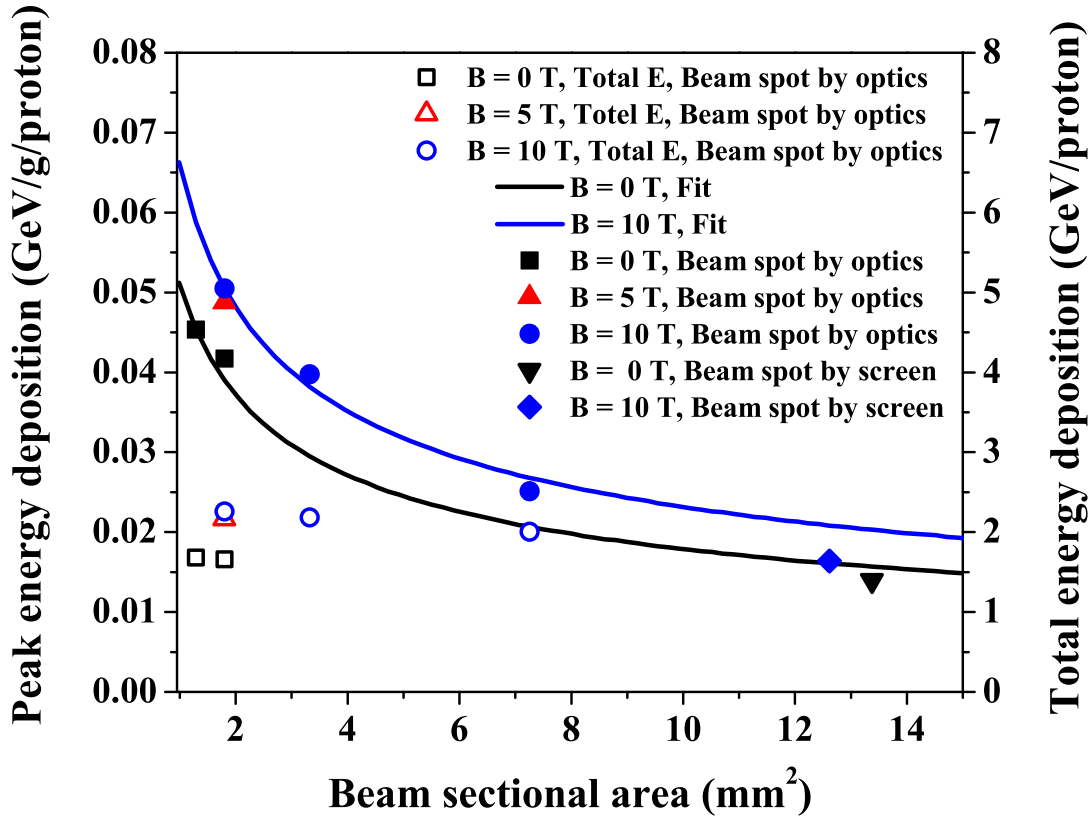

Figure 5.11: Peak energy deposition and total energy deposition per proton according to the beam spot sizes by beam intensities.

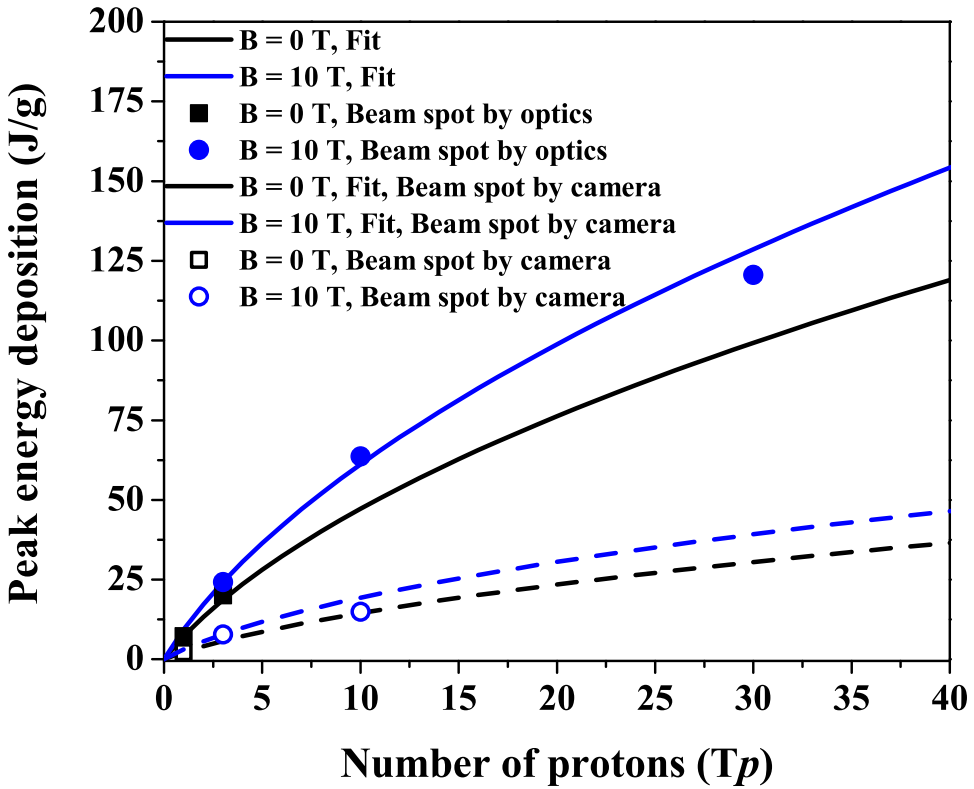

Figure 5.12: Peak energy deposition of total number of protons.

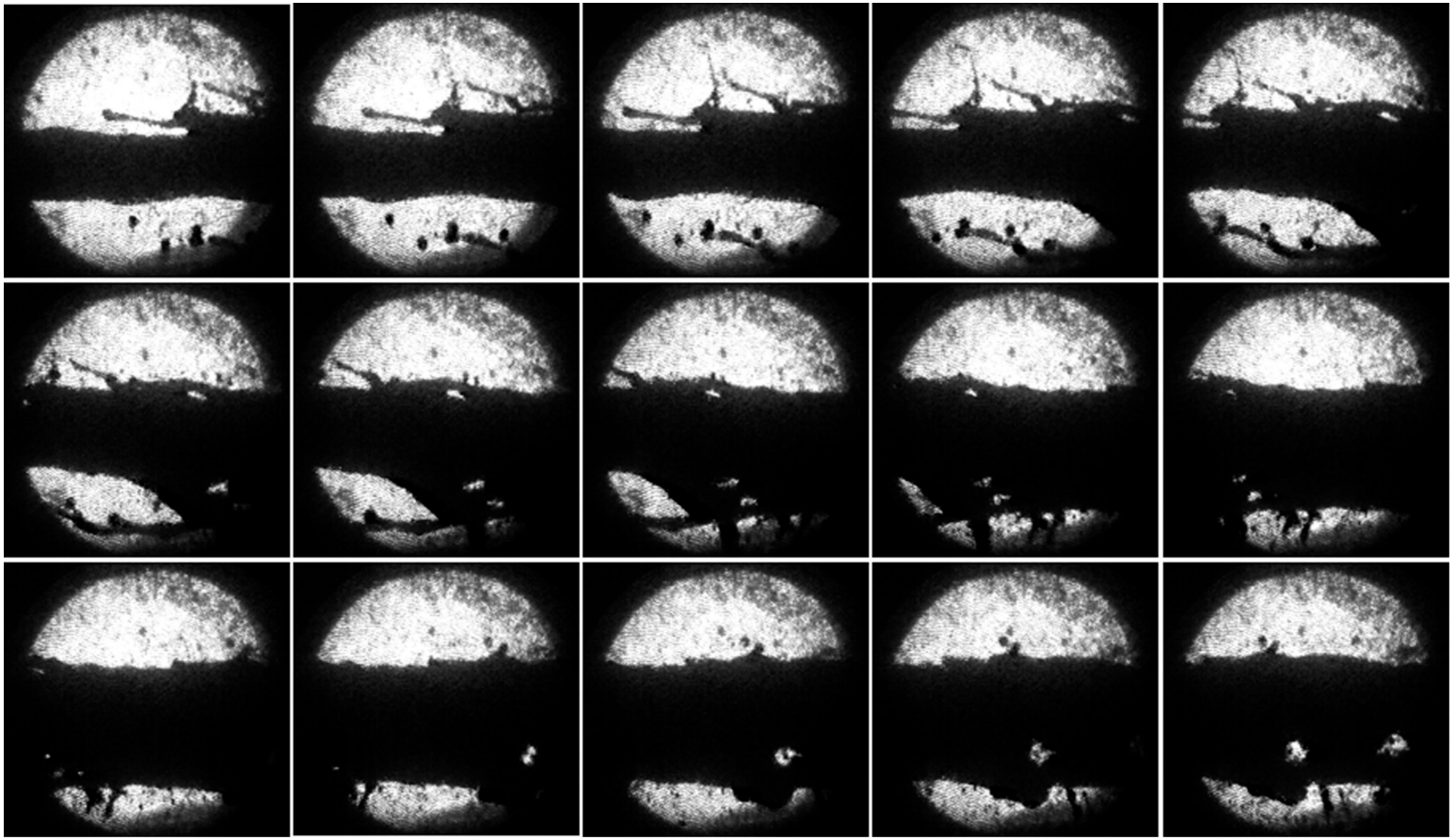

Figure 5.13: Photographs of the Hg jet interaction with 16 TP, 14 GeV proton beam at 5 T. Captured at Viewport 3 at 500 μs frame rate (continued).

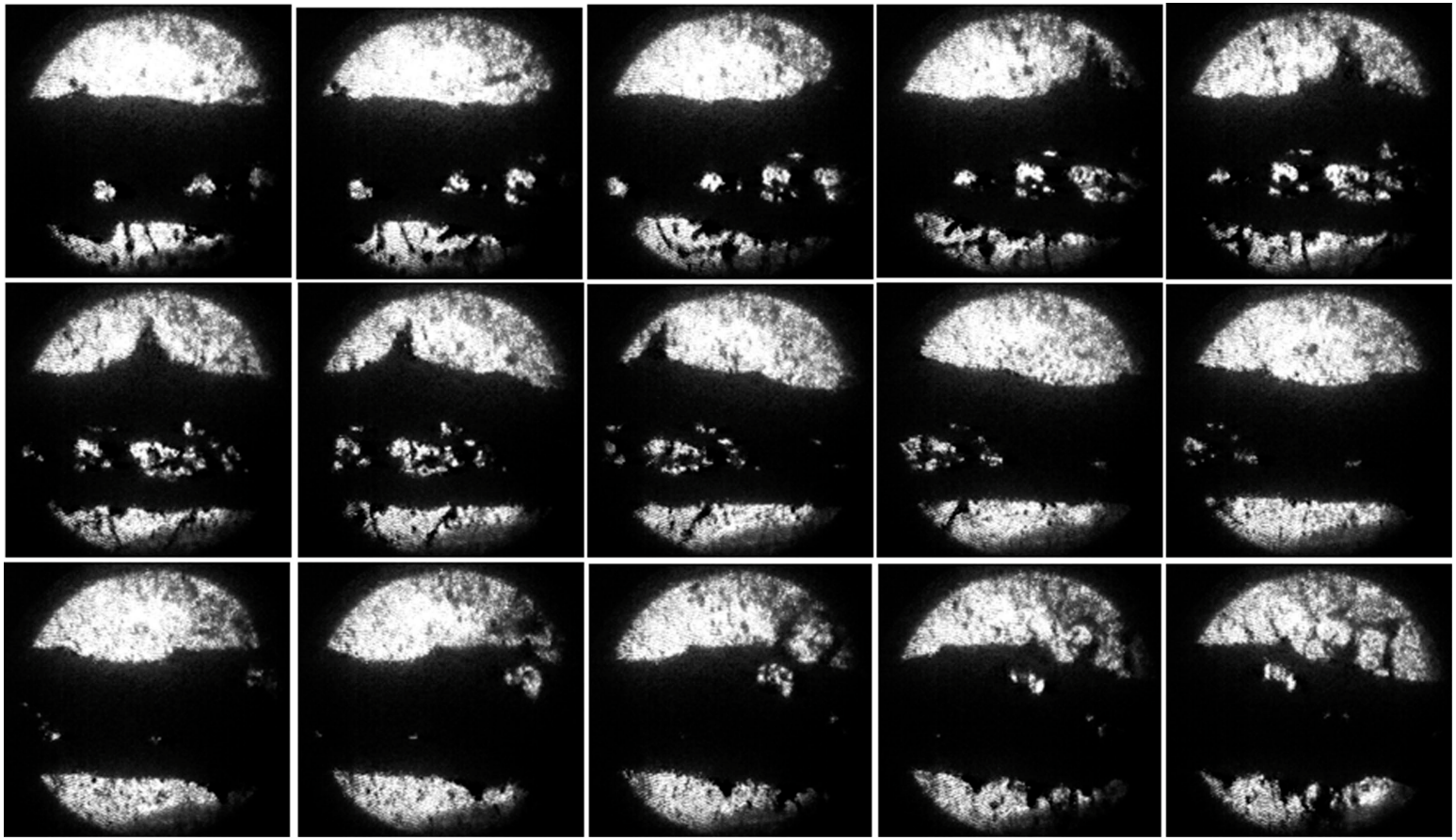

Figure 5.13: Photographs of the Hg jet interaction with 16 TP, 14 GeV proton beam at 5 T. Captured at Viewport 3 at 500 μs frame rate (continued).

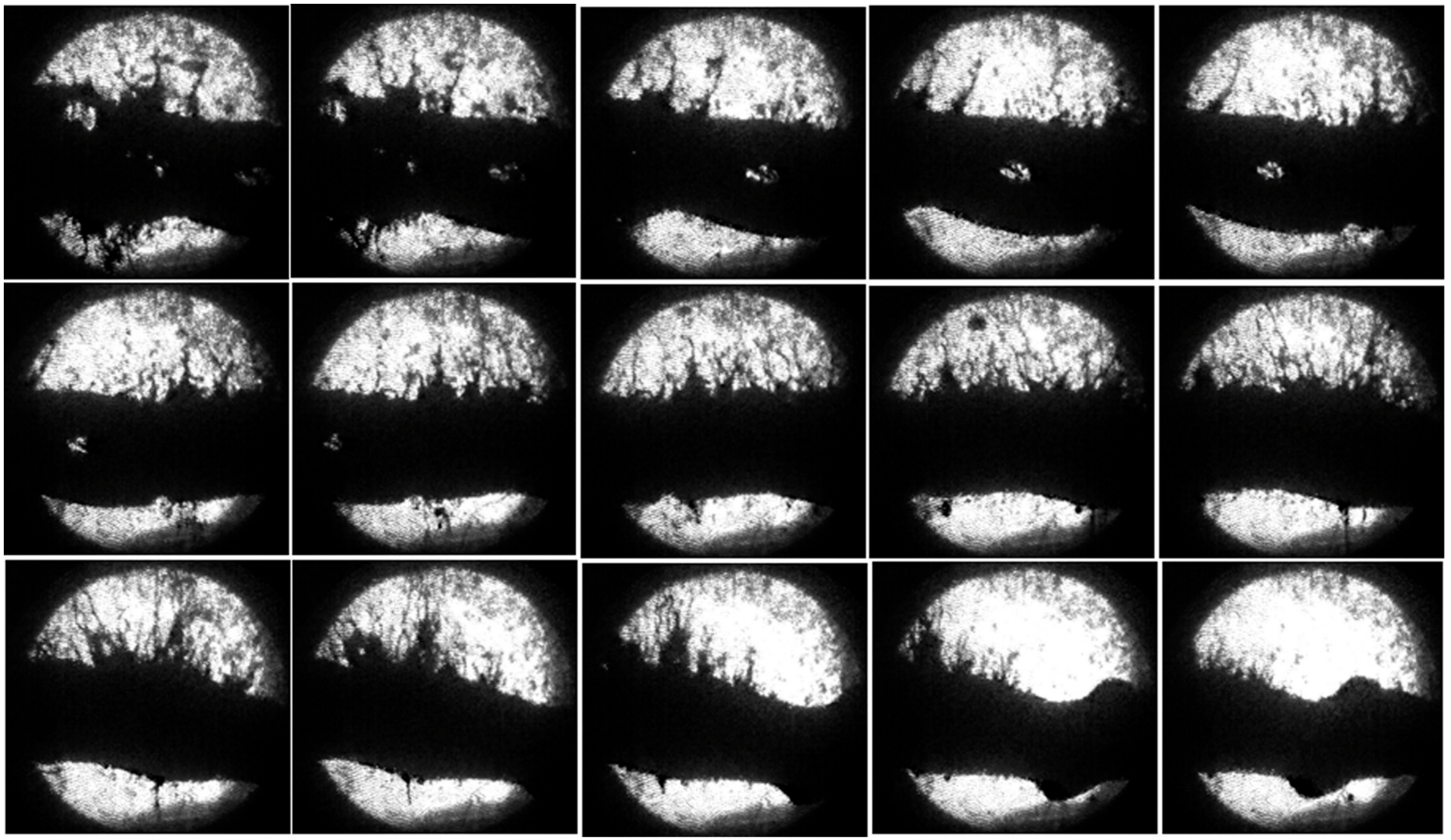

Figure 5.13: Photographs of the Hg jet interaction with 16 TP, 14 GeV proton beam at 5 T. Captured at Viewport 3 at 500 μs frame rate.

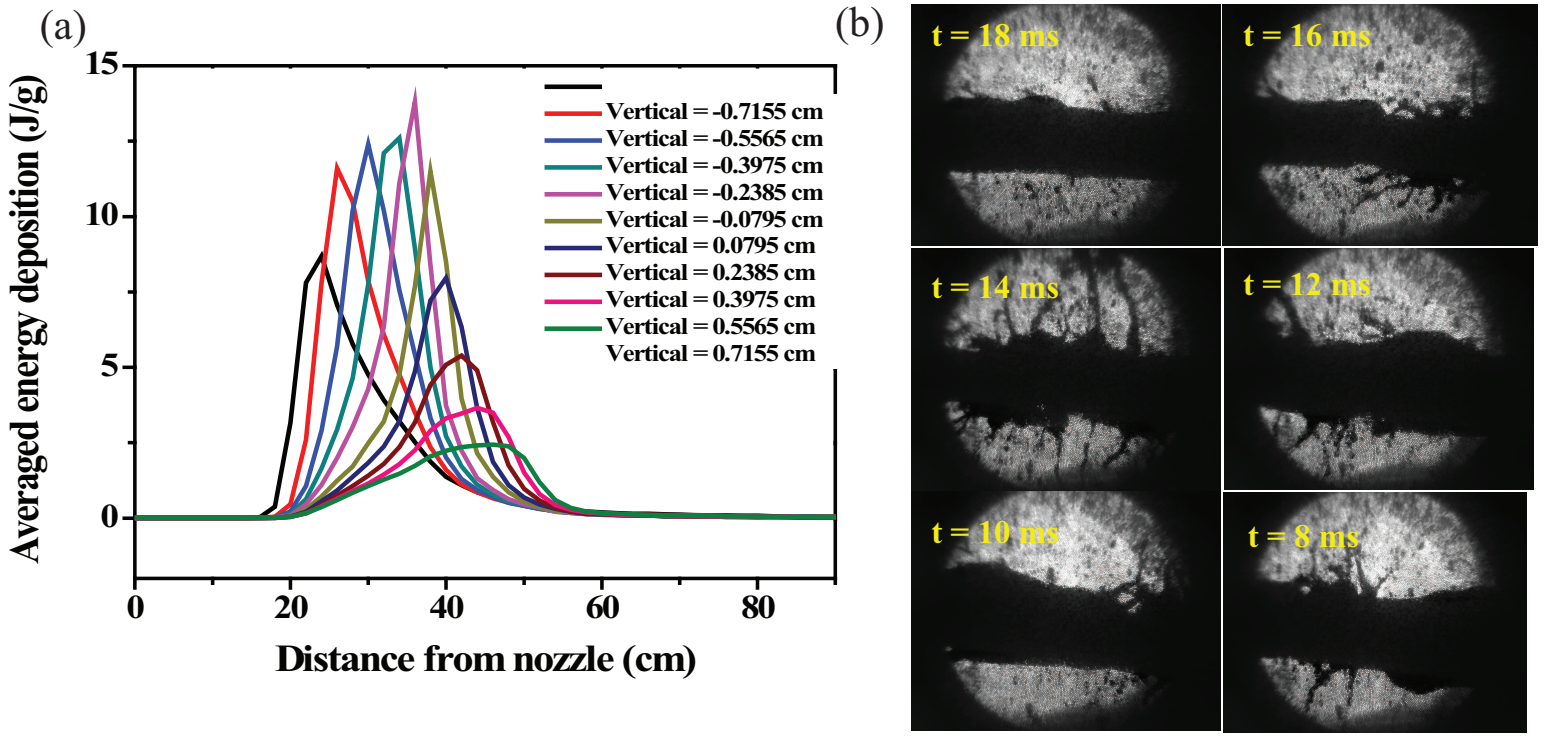

Figure 5.14: Qualitative comparison of the jet response incident by interaction of low intensity (3 Tp) of beam at 5 T. a.) Calculated averaged energy deposition profile to mercury jet according to the distance from jet center. b.) Jet response by captured image.

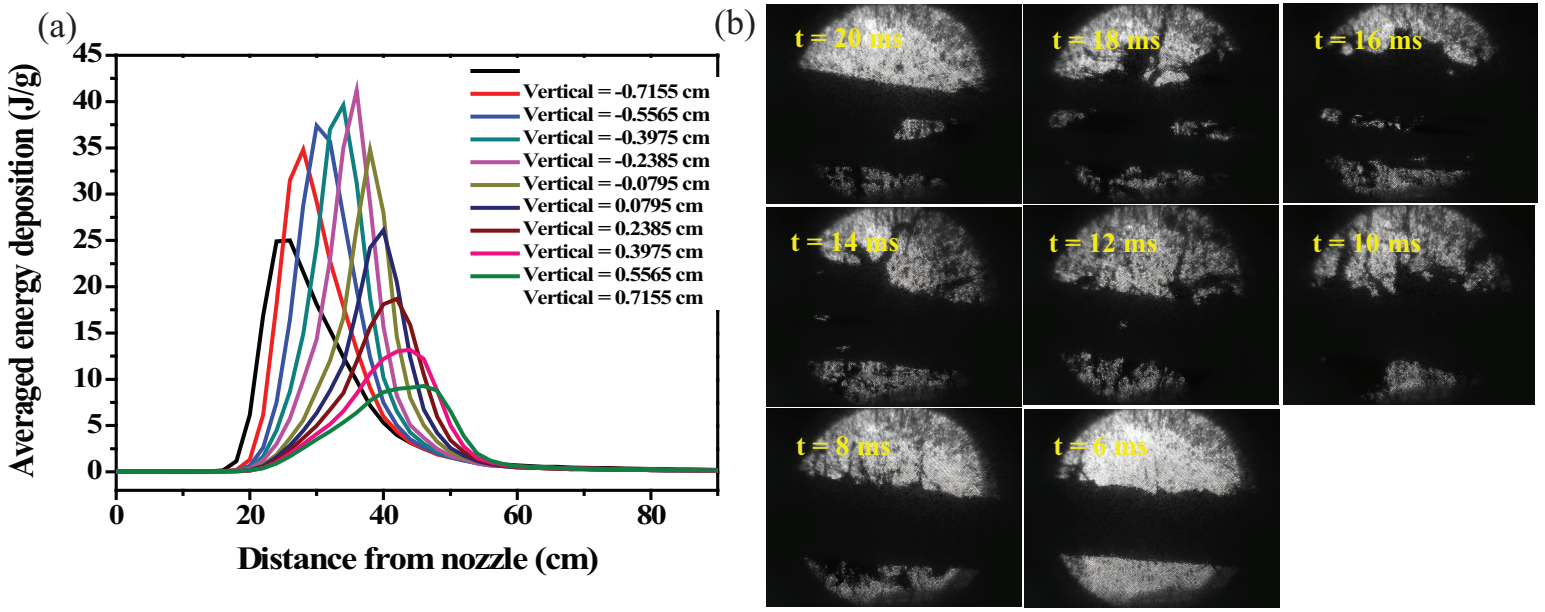

Figure 5.15: Qualitative comparison of the jet response incident by interaction of high intensity (10 Tp) of beam at 10 T. a.) Calculated averaged energy deposition profile to mercury jet according to the distance from jet center. b.) Jet response by captured image.

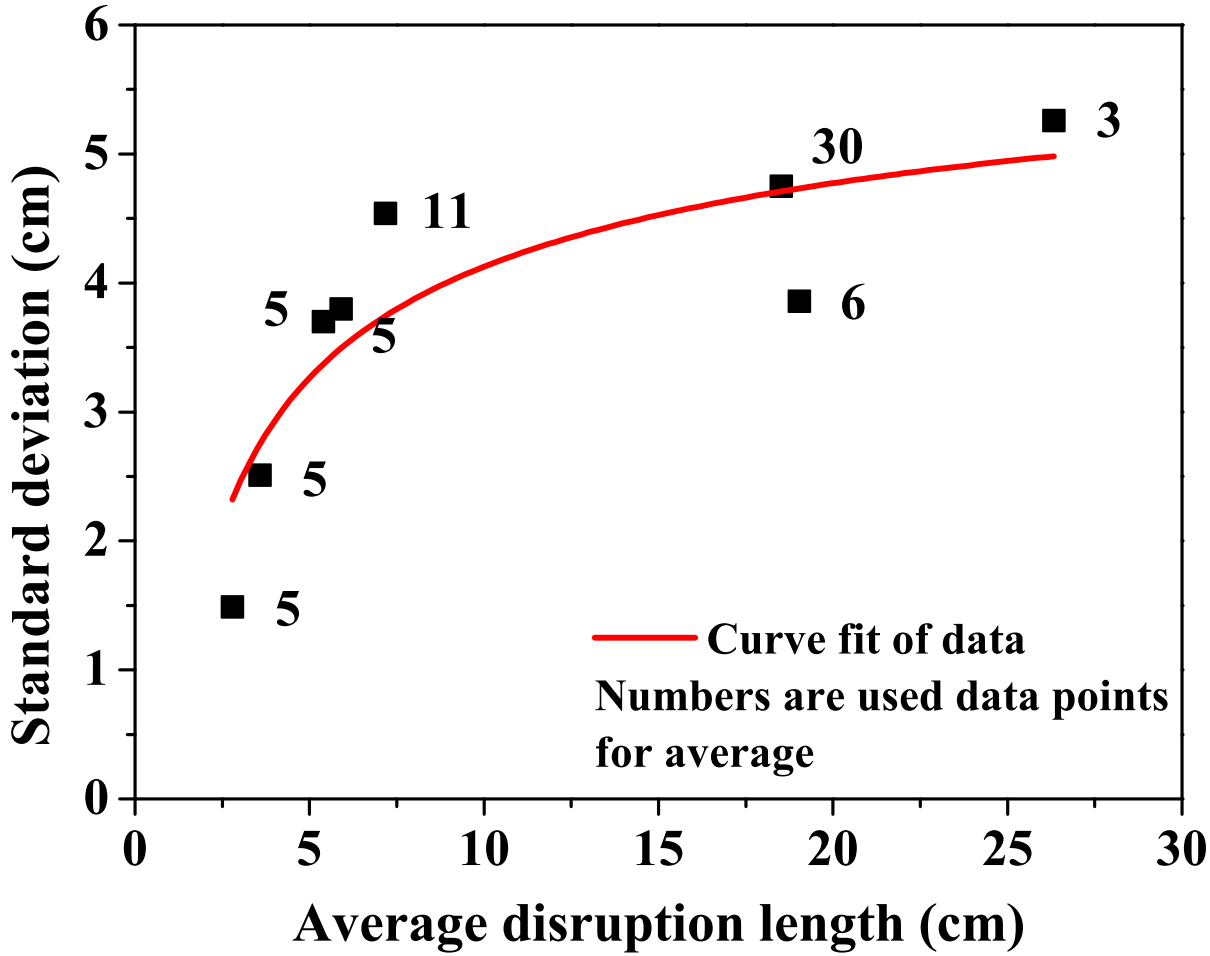

Figure 5.16: Standard deviation of disruption length as a function of disruption length and the function of fitted curve. The fitted curve is $\sigma_{disruption} = 6.7921(1 - L_{disruption}^{-0.4124})$.

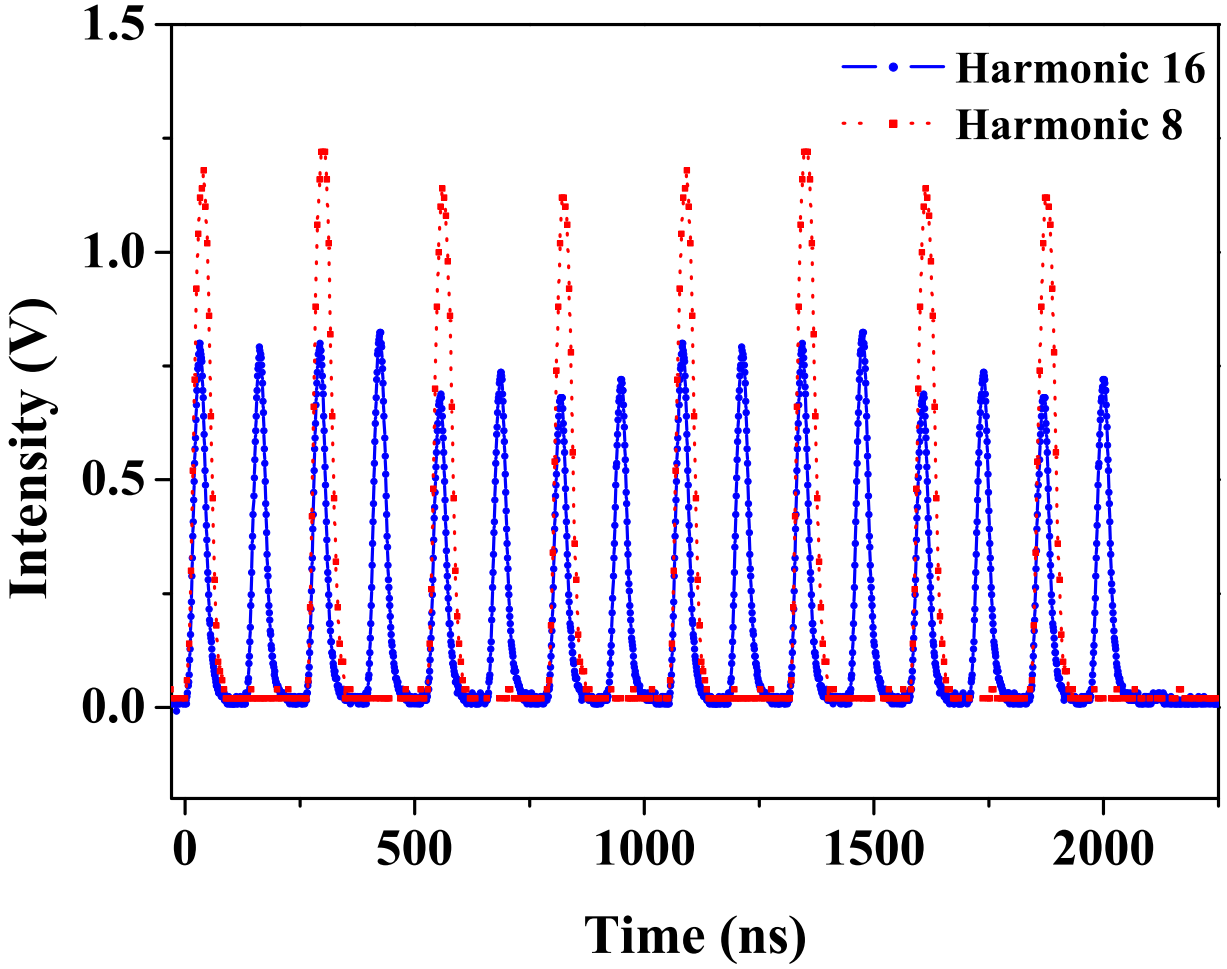

Figure 5.17: Proton beam pulse structure of harmonic 8 and harmonic 16 in 14 GeV and 6 TP.

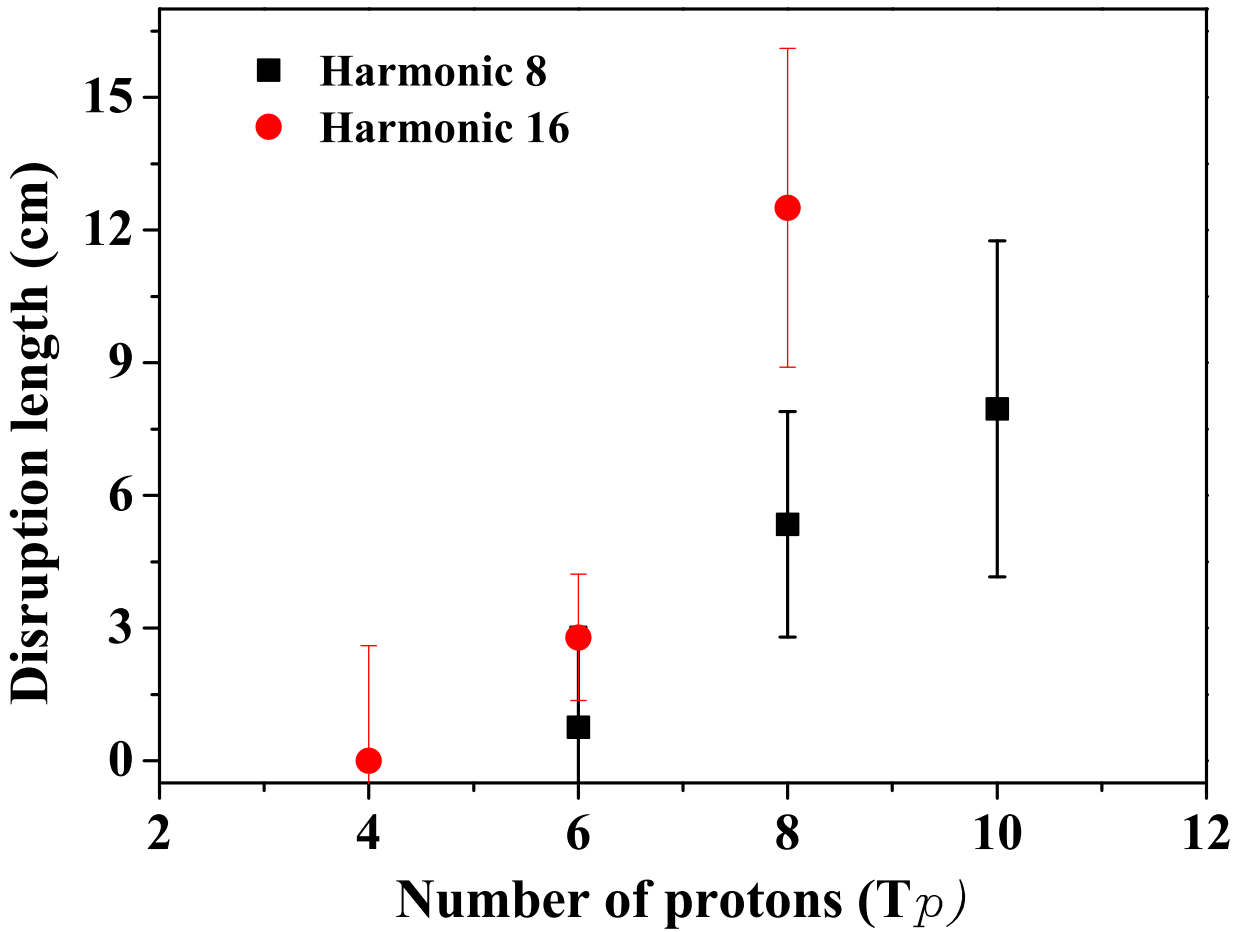

Figure 5.18: Disruption length of Hg jet depending on the beam pulse structure as a function of 14 GeV beam intensity in 5 T. T$p = 10^{12}$ protons. The error bars are estimated by using the formula given in Fig. 5.18 divided by $\sqrt{N}$.

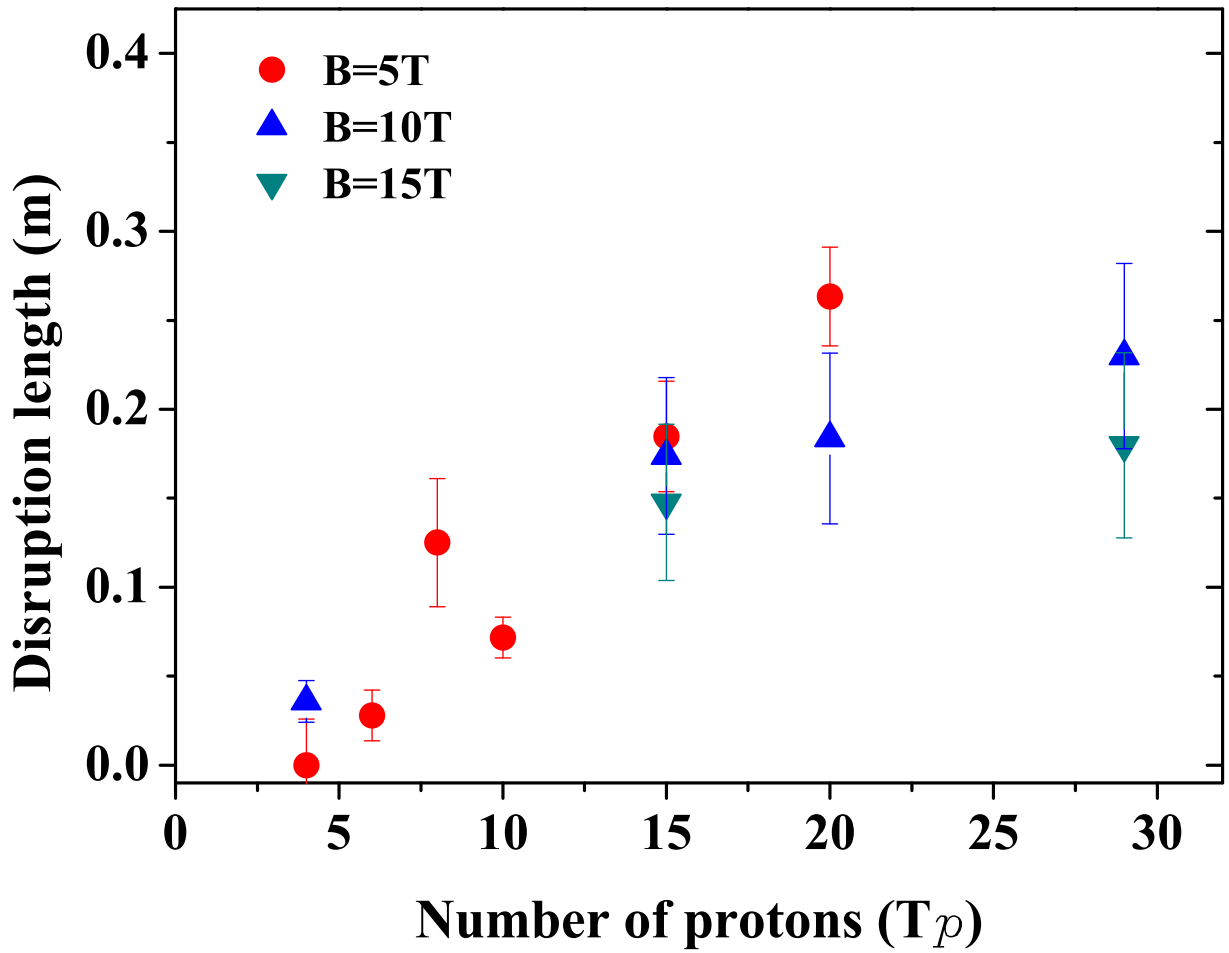

Figure 5.19: Disruption length of Hg jet as a function of 14 GeV beam intensity and magnetic field. Harmonic 16 with 16 bunches is used. The error bars are estimated by using the formula given in Fig. 5.18 divided by $\sqrt{N}$.

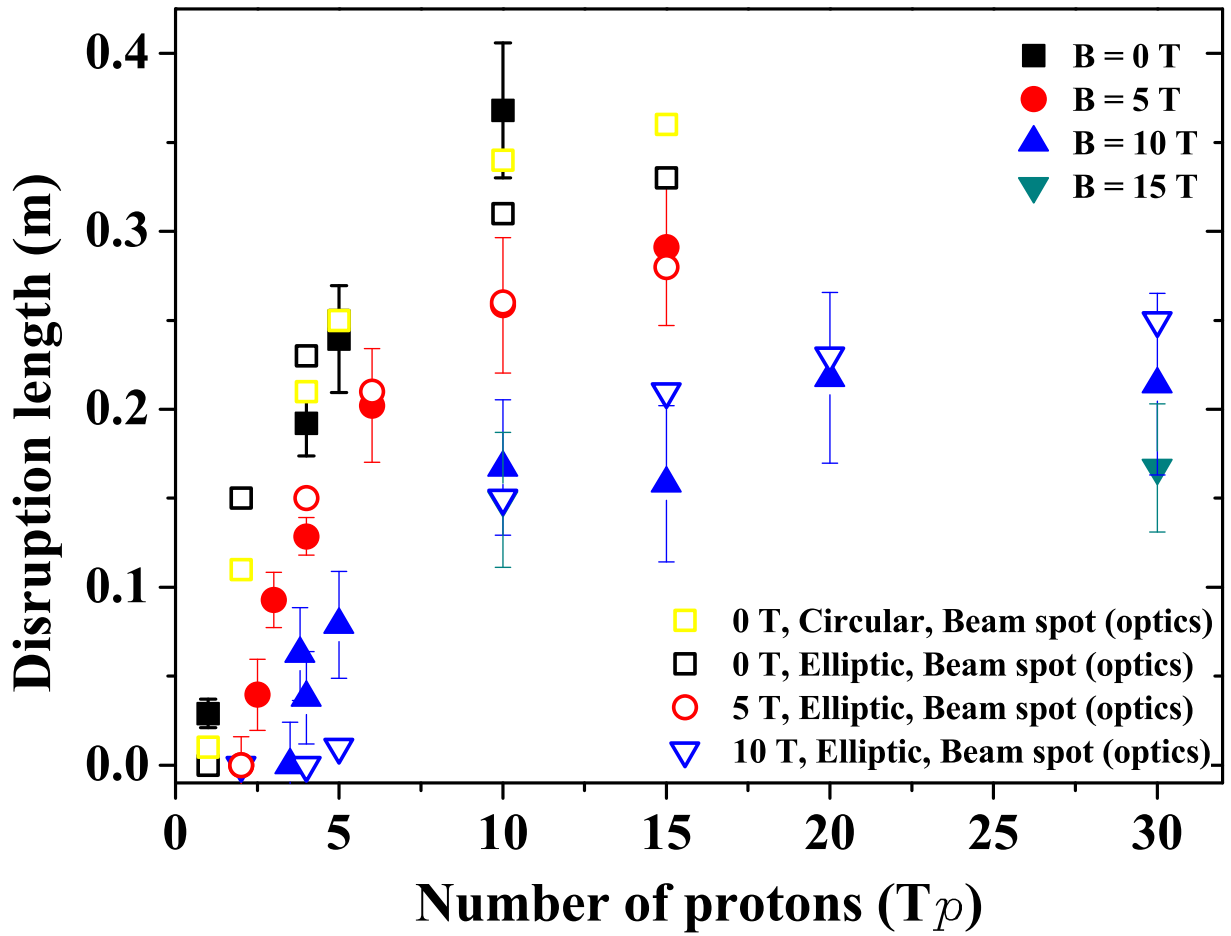

Figure 5.20: Disruption length of Hg jet and its estimation as a function of 24 GeV beam intensity and magnetic field. The error bars are estimated by using the formula given in Fig. 5.18 divided by $\sqrt{N}$.

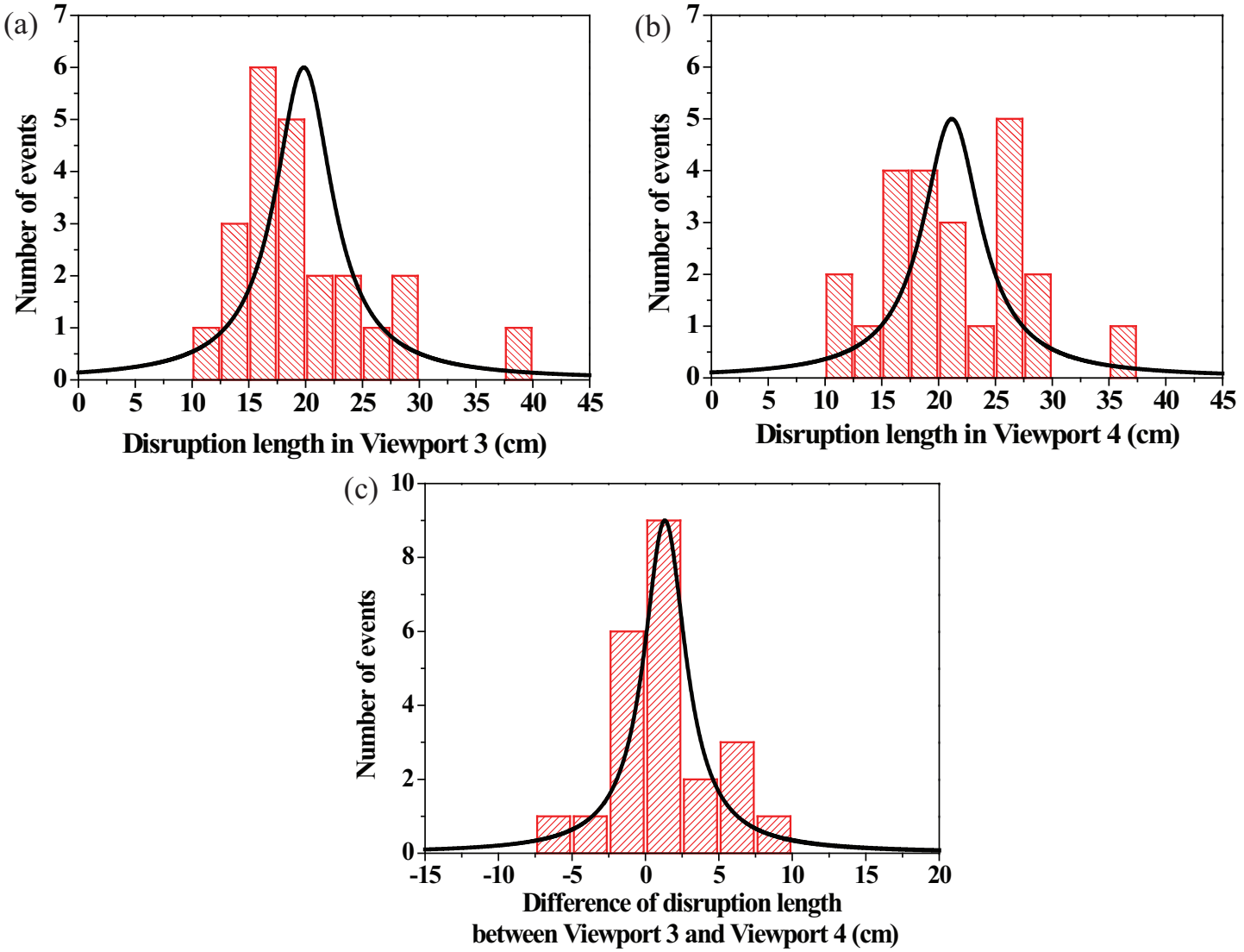

Figure 5.21: Validation of disruption measurement for the evaluation of evolution of disruption length from Viewport 3. a) Disruption length at Viewport 3. b.) Disruption length at Viewport 4. c.) Difference of the disruption length at Viewport 3 and Viewport 4.

Chapter 6

Mercury Jet Surface Development in Magnetic Field

In this chapter, the motions of filaments emanating from jet surface caused by disruption in magnetic field are investigated. The energy deposition induced by the proton beam generates filaments on the Hg jet surface due to thermal stresses. The filaments velocity leaving from the jet surface and the effect of magnetic field to it are discussed. It explains that the joule damping dissipates the kinetic energy on a time scale of joule damping term.

6.1 Filament Model on Jet Surface

6.1.1 Geometry of viewing mercury filaments

It is investigated (McDonald, 2009) that the observed motion of filament by images has geometric relation with the viewing angle by focal length in optics. The filaments ejected from mercury jet by the proton beam interaction are viewed via shadow photography from a focal length $f = 9.15$ cm from the center of the jet. The jet is supposed to have elliptical cross section. The

schematic geometry of viewing mercury filaments is shown in Fig. 6.1. The measurements describes the projection $y_m(t)$ onto the y axis of a ray from the observer to the surface. McDonald (2009) assumes that the filaments leave perpendicularly as shown in Fig. 6.1. The elliptic expression is given as Eqn. (6.1).

$$\frac{x^2}{a^2} + \frac{y^2}{b^2} = 1, \tag{6.1}$$

where the jet is circular with radius b if $a = b$. Suppose a filament leaves the surface with velocity v_o at time t_o from point (x_o, y_o), at time $t > t_o$, the travel distance d is then $v_o(t - t_o)$ assuming that the velocity is constant. The position of the filament is $x_d = x_o + d\sin(\theta)$, $y_d = y_o + d\cos(\theta)$. Using the trigonometric notation of slope at point (x_o, y_o), the position of the filament, y_m, as projected onto the y axis is

$$\begin{aligned} y_m &= y_d \frac{f}{f - x_d} \approx y_d(1 + \frac{x_d}{f}) \\ &= b\cos\theta + v_o(t - t_o)\cos\theta + \frac{[a + v_o(t - t_o)][b + v_o(t - t_o)]}{2f}\sin 2\theta. \end{aligned} \tag{6.2}$$

Thus, the apparent velocity of the filament along y axis is

$$v_m = \frac{dy_m}{dt} \approx v_o[\cos\theta + \frac{a + b + 2v_o(t - t_o)}{2f}\sin 2\theta]. \tag{6.3}$$

The earliest time t_{om} that a filament can be seen vis projected shadow

photography when $y_m = b$ is given as

$$t_{om} \approx t_o + \frac{b(1 - \frac{v_m}{v_o})}{v_m} \tag{6.4}$$

and

$$v_m \approx \frac{v_o}{1 + v_o \frac{(t_{om} - t_o)}{b}}. \tag{6.5}$$

6.1.2 Distribution of filaments on jet surface

McDonald (2009) suggested three cases of possible distribution of filaments on the jet surface, which can indicate the probable existence of filaments in observation depending on the assumed orientation of the filaments. First, in case that the filaments are distributed uniformly in angle θ, the probability of the existence of the filaments is

$$P(\theta)d\theta = \frac{d\theta}{2\pi}. \tag{6.6}$$

Second, in case that the filaments are distributed uniformly in angle θ, the probability of the existence of the filaments is

$$P(\theta)d\theta = \frac{d\phi}{2\pi} = \frac{ab}{a^2 \sin^2\theta + b^2 \cos^2\theta} \frac{d\theta}{2\pi}. \tag{6.7}$$

Third, in case that the filaments are distributed uniformly in position s around the circumference C of the ellipse, the probability of the existence of

the filaments is

$$P(\theta)d\theta = \frac{ds}{C} \approx \frac{2\sqrt{a^2\cos^2\theta + b^2\sin^2\theta}}{3(a+b) - \sqrt{(3a+b)(a+3b)}}\frac{d\theta}{2\pi}. \tag{6.8}$$

6.1.3 Approximation of filaments velocity

6.1.3.1 *first order approximation*

Sievers and Pugnat (2000) reported the response of solid and liquid target to rapid heating by the incident proton beam. The parabolic radial energy deposition density E_{beam} is considered, dropping to 0 at the outer radius $a =$ 1 cm as follow :

$$E_{beam} = E_o[1 - (r/a)^2]. \tag{6.9}$$

The increase in temperature causes pressure rise. It is assumed that the rise time for the temperature is of the same order of magnitude with the beam energy deposition, 10^{-9} s, thermal expansion is initially prevented by the mass inertial of the material. From the definition of bulk modulus K, the resulting instantaneous thermal pressure for mercury is

$$\Delta p(r) = K\alpha_v \Delta T(r). \tag{6.10}$$

If the thermal heating occurs very slowly comparable to the material's dynamic frequency, it would correspond to quasi-static thermal expansion. It is believed that the energy stored in the material due to the initial thermal

expansion may be converted into kinetic energy bombarding the liquid flow away. Corresponding to the thermal expansion caused by the pressure rise, strain energy is stored in the liquid flow due to the compression, which is expressed as

$$\frac{E_c}{V} = \frac{K(\alpha_v \Delta T(r))^2}{2}, \tag{6.11}$$

where E_c represents the converted beam energy. The order of the velocity with which the boundary of the liquid material is given by the thermal expansion at the boundary divided by the time over which the sound travels across the radius of the jet, which is in units of $c\alpha_v T_o$. The pressure and the velocity at the boundary are reduced by extending the time of heating, which depends on the compressibility like

$$p \sim \frac{1}{\kappa} \quad , \quad v \sim \frac{1}{\sqrt{\kappa}}, \tag{6.12}$$

where κ is the compressibility of material.

6.2 Observation of Filaments Development on Mercury Jet Surface

6.2.1 Image calibration

6.2.1.1 *image calibration with proton beam arrival signal*

In order to investigate the time response of filaments, we need to establish the accuracy and calibration of the measurement based on the experimental

setup. Fig. 3.6 shows the traced signals on an oscilloscope when the beam and the beam triggering are delivered. The scintillating fiber signal gives the beam arrival time. Therefore, it is possible to set up the trigger timing for the cameras and laser driver inputs, which is ~ 2 μs after the master electronic triggering signal from the proton synchrotron. Therefore, the first image of the SMD camera tells the status of jet for the time before the beam arrives since the exposure time of SMD camera is 150 ns. All of the electronic delays including the cable delays are less than 1 μs. The maximum frame rate of SMD camera is up to 1 MHz. The accuracy of camera frame rate is checked by using laser pulses. Laser pulses with certain periods are generated and then monitored at oscilloscope through photodiode. The frame rate of camera is set at the corresponding values of laser pulse period. The frame rate is checked by monitoring the variation of intensity of image captured from camera, which is judged as negligibly uniform.

6.2.1.2 *time delay structure of proton beam to light source triggering*

Fig. 6.2 shows the time structures between freezing image after laser enabling and proton beam arrival. Fig. A.1 shows the specifications of 25 W laser, where the response time to reach the peak laser, wavelength of laser, and optical power for various pulse rates are shown (Tsang, 2006). Laser emits ~ 250 ns after receiving the 16 pulse trigger from the pulse generator. The time of flight of light to the primary vessel is ~ 60 ns. Once the light source arrives at the primary vessel, the freezing image of mercury jet flow

is instantaneously generated and it is then transmitted through the optical fiber corresponding to the light speed $\sim$ 4 ns/m, where $\sim$ 60 ns is taken for the used imaging fiber length. From the traced signals in Fig. 3.6, the proton beam arrival time is measured. Considering the time of flight from primary vessel through scintillating fiber, $\sim$ 60 ns delay is estimated, so that the time delay between the 1^{st} acquired image and the actual proton beam arrival is given as $T_3 - T_2$ in Fig. 6.2, which is considered for the velocity analysis of filaments.

6.2.2 Parameter optimization with uncertainty

6.2.2.1 *linear curve fit for estimation of model*

Selecting a model of the right form to fit a set of data requires the use of empirical evidence in the data, knowledge of the process and some trial-and-error experimentation. Much of the need to iterate stems from the difficulty in initially selecting a function that describes the data well. Some scientific theory describing the mechanics of a physical system provide a functional form for the process, which type of function makes an ideal starting point for model development. So, a practical approach is to choose the simplest possible functions that have properties ascribed to the process. Complex models are fine, but they should not be used unnecessarily. Fitting models that are more complex than necessary means that random noise in the data will be modeled as deterministic structure. This will unnecessarily reduce the amount of data available for estimation of the residual standard deviation, potentially increas-

ing the uncertainties of the results obtained when the model is used. Numerical methods for model validation, such as R^2 statistic, are useful. Graphical methods have an advantage over numerical methods for model validation because they illustrate a broad range of complex aspects of the relationship between the model and the data. Numerical methods tend to be focused on a particular aspect of the relationship between the model and the data and try to compress that information into a single descriptive number. The residuals from a fitted model are the differences between the responses observed at each combination values of the explanatory variables and the corresponding prediction of the response computed using the regression function.

The linear regression model is

$$\mathbf{Y} = f(\mathbf{X}, \Theta) + \epsilon, \tag{6.13}$$

where $\mathbf{X} = (x_1, x_2, \ldots, x_m)$ are independent variables and $\Theta = (\Theta_1, \Theta_2, \ldots, \Theta_k)$ are parameters and ϵ is the random error assuming the mean is equal to 0 with normal distribution, where k is the degree. A measure of the quality of non-linear fitting parameters is the chi-square value :

$$\chi^2 = \sum_{i=1}^{n} w_i (y_i - \hat{y}_i)^2, \tag{6.14}$$

where w_i is the weighting coefficient, y_i are the experimental data points, and $\hat{y}_i$ are the theoretical points. To fit the model, the residual is defined as

$$r_i = y_i - \hat{y}_i. \tag{6.15}$$

It conforms to a normal distribution with the mean equal to 0 and the variance equal to σ_i^2. Then the maximum likelihood estimates of the parameters Θ_i can be obtained by minimizing the chi-square value , defined as

$$\chi^2 = \sum_{i=1}^{n} \frac{(y_i - \hat{y}_i)^2}{\sigma_i^2}. \tag{6.16}$$

If the error is treated as weight, $w_i = \frac{1}{\sigma_i^2}$ can be defined in the chi-square minimizing equation, where σ_i are the measurement errors. The quality of regression can be measured by the coefficient of determination, R^2, which is defined as

$$R^2 = 1 - \frac{w_i(y_i - \hat{y}_i)^2}{\sum_i^n (y_i - \bar{y})^2}. \tag{6.17}$$

In order to express the relationship between independent variables and dependent variables and a degree of confidence in regression model, the adjusted R^2 for validation of goodness of fit measurement is defined as

$$\bar{R}^2 = 1 - \frac{\frac{w_i(y_i - \hat{y}_i)^2}{n^* - k}}{\frac{\sum_i^n (y_i - \bar{y})^2}{n^*}}. \tag{6.18}$$

Note that if intercept is included in the model, the degree of freedom is $n^* = n - 1$. Otherwise, $n^* = n$. The adjusted R^2 will avoid the effect of the degrees of freedom by adding variables in the model, which results in rising of R^2. Therefore, the adjusted R^2 overcomes the rise in R^2 when fitting a small sample size by multiple predictor model.

The covariance value indicates the correlation between two variables, and

the matrices of covariance in regression show the inter-correlations among all parameters. The correlation matrix rescales the covariance values. The covariance matrix of the regression and correlation between parameters are defined as

$$Cov\ (\Theta_i, \Theta_j) = \sigma^2 (X'\ X)^{-1} \tag{6.19}$$

and

$$Cor\ (\Theta_i, \Theta_j) = \frac{Cov\ (\Theta_i, \Theta_j)}{\sqrt{Cov\ (\Theta_i, \Theta_i)}\sqrt{Cov\ (\Theta_j, \Theta_j)}}. \tag{6.20}$$

Parameter errors are equal to the square root of the covariance matrix diagonal values.

6.2.2.2 *Levenberg-Marquardt minimization*

To estimate the $\hat{\Theta}$ value with the least square method, we need to solve the normal equations which are set to be zero for the partial derivatives of χ^2 with respect to each $\hat{\Theta}_p$:

$$\frac{\partial \chi^2}{\partial \hat{\Theta}_p} = 0. \tag{6.21}$$

Employing an iterative strategy to estimate the parameter values, it starts with some initial values Θ_o. With each iteration, χ^2 value is computed and then the parameter values are adjusted to reduce the χ^2. When χ^2 values computed in two successive iterations are small enough compared with the tolerance, the fitting is converged. The Levenberg-Marquardt algorithm is employed for an

iterative technique that locates a local minimum of a multivariate function that is expressed as the sum of squares of nonlinear function. Levenberg-Marquardt is considered as a combination of steepest descent and the Gauss-Newton method. When the solution is far from a local minimum, the algorithm behaves like a steepest descent method. When the solution is close to a local minimum, it becomes a Gauss-Newton method and exhibits fast convergence.

Given the residuals r_i ($i = 1, \ldots, n$) of parameters $\Theta = (\Theta_1, \Theta_2, \ldots, \Theta_p)$, with $n \geq k$, the Gauss-Newton algorithm finds the minimum of χ^2 given in Equation (6.16). Starting with an initial guess Θ_o for the minimum, the method proceeds by the iteration $\Theta^{s+1} = \Theta^s + \delta\Theta$ with an increment $\delta\Theta$ satisfying the normal equation given as Equation (6.22) using Equation (6.21).

$$(\mathbf{J}_r^T \mathbf{J}_r)\delta\Theta = -\mathbf{J}_r^T \mathbf{r}, \tag{6.22}$$

where $\mathbf{r}$ is the vector of r_i and $\mathbf{J}_r$ is the Jacobian of $\mathbf{r}$ with respect to Θ. The residuals r_i are defined as $r_i(\Theta) = y_i - f(x_i, \Theta)$. In order to find the parameters Θ that a given model function $y = f(x, \Theta)$ fits best data points, the increment $\delta\Theta$ can be expressed in terms of Jacobian of the function as follow:

$$(\mathbf{J}_f^T \mathbf{J}_f)\delta\Theta = \mathbf{J}_f^T \mathbf{r}, \tag{6.23}$$

The Levenberg-Marquardt iteration is a variation on the Newton iteration. The normal equations $\mathbf{N}\delta\Theta = \mathbf{J}_f^T \mathbf{J}_f = \mathbf{J}_f^T \mathbf{r}$ are augmented to $\mathbf{N}'\delta\Theta = \mathbf{J}_f^T \mathbf{r}$ where $N'_{ij} = (1 + \delta_{ij}\ \lambda)\ N_{ij}$ with δ_{ij} the Kronecker delta. The λ is initialized

to a small value, e.g. 10^{-3}. If the value obtained for $\delta\Theta$ reduce the residuals, the increment is accepted and λ is divided by 10 before the next iteration. If the residuals increase then λ is multiplied by 10 and the augmented normal equations are solved again until an increment is obtained that reduces the residuals. For large λ, the iteration approaches a steepest descent.

6.2.3 Filaments distribution and uncertainty of measurement

6.2.3.1 *onset of filamentation on jet surface*

Fig. 6.3 shows photographs of filament evolution on the Hg jet surface at 25 μs frame rate, where the beam is 10 Tp, 24 GeV and the magnetic field is 10 T. Fig. 6.4 shows the locations of filaments where the individual velocity is measured as a function of time, shown in Fig. 6.6, Fig. 6.7 (a), (b). The first collected image among 16 images is brighter than the rest of 15 images. It indicates that the radiation generated by the interaction of Hg with proton beam affects the transmittance and/or reflectance of optical components, resulting in the production of darker images as one sees at the rest of collected 15 images.

6.2.3.2 *measurement of traveled distance of filament*

To obtain the vertical filament velocity, the distance traveled by a fixed point on the jet surface is tracked over a given time period. The jet volume, where the maximal energy is deposited, results in the initial generation of the filaments. The higher jet velocity occurs when the filaments is initially

protruded out of the jet surface and then the jet velocity decreases due to the magnetic damping and viscous dissipation. So, the velocity at steady state is obtained in order to evaluate the relationship with the beam intensity and magnetic field.

The quality of optical images varies from shot to shot since the radiation or jet dispersion may make image quality varies. The most difficulty in measurement is to discern the edge of filaments as it moves somewhat far away from surface because the initial jet filament edge is dense(clearly black) but it looks like dissipating, dilute, disappearing (grey or similar with background) as it moves further. Because measurement is done in several points, there may be some error in measurement after some steady velocity(constant peak velocity) at weak filament velocity measurement.

The image size at Viewport 2 is 240 by 240. Using graphic software, pixels on image is picked to locate the edge of filament. Therefore, the uncertainty while locate the position y_m is reported to be $\pm$ 2 pixels, which corresponds to the difference of $\sim \pm$ 17 m/s filaments velocity. This uncertainty can occur randomly uniformly. The peak strong filament which gives constant velocity within $\pm$ 2 pixels until the end of 15 frames is assumed to be considered as there is constant uncertainty, $\pm$ 2 pixels. The weak filament which gives constant velocity within $\pm$ 2 pixels until the filament reaches some frames, for example, 3 $\sim$ 7 frames, is also assumed to be considered as there is constant uncertainty, $\pm$ 2 pixels, where the black edge of filament is clearly observed. However, after the some frames, for example, 3 $\sim$ 7 frames, because the original edge

of filament dilute or dissipates or disappear, the uncertainty in measurement may not be constant. In this case, measurement is stopped at that frames.

6.2.4 Linear regression with the first order polynomial

6.2.4.1 *curve fit function*

The heaviside step function is defined as the integral of the Dirac delta function as follow:

$$H(t) = \int_{-\infty}^{t} \delta(\xi) d\xi. \tag{6.24}$$

The ramp function is the antiderivative of the Heaviside step function:

$$R(t) = \int_{-\infty}^{t} H(\xi) d\xi = tH(t). \tag{6.25}$$

In discrete form, it is now defined as an alternative form for our linear regression model as follow:

$$R(t) = \begin{cases} y_m = s, & t \leq t_o \\ y_m = s + v(t - t_o), & t > t_o \end{cases}, \tag{6.26}$$

where y_m, s, v, t_o denote the measured position of the filament as projected onto the y axis in image, the position of jet surface before the filaments developed, the apparent velocity of the filament along the y axis, and onset time delay of filaments respectively.

6.2.4.2 *parameter estimation using multiple data points*

Shot 11019 is chosen for illustration. Using Equation (6.26) for linear regression model with measured data points y_m and t, minimizing R^2 yields s, v, and t_o. Fig. 6.5 (a) shows the illustration of multiple data points where the intercept of x axis and slope approximate the onset time of filament and apparent velocity projected on y axis in image, which are $t_o = 43.6 \pm 4.5$ μs and $v = 55.5 \pm 0.8$ m/s respectively. The reduced R^2 value and adjusted $\bar{R}^2$ values are 1.749 and 0.998 respectively. In case of larger velocity of filaments, maximally measurable data points are limited to $\sim 2 \sim 3$ points due to the limited field of view in optical diagnostic image. Fig. 6.5 (b) shows the illustration of 3 data points. The onset time from regression model yields underestimated value such as negative time delay because the data point is equal or smaller than the number of data points. Thus, we assumed the real onset time should be between typical onset time 50 μs and 0 μs, which yields the onset time of 25 ± 25 μs. Therefore, the slope of fit curve is determined by fixing the assumed onset time accordingly, which yields the filament velocity of 148 ± 24.5 m/s. The error is determined directly by dividing approximated filament velocity of the cases of $t_o = 0$ and $t_o = 50$ μs by 2. The shot 10008 is chosen for the illustration of parameter estimation of 3 data points.

6.2.4.3 *filaments velocity distribution on jet surface*

Fig. 6.6 (a) shows the approximated velocity distribution of filaments over the jet surface shown in Fig. 6.3. Fig. 6.6 (b) shows the approximated onset

time distribution of filaments according to the approximated velocity of filaments. As the approximated apparent velocity of filaments projected on y axis in image increases, the approximated onset time of filaments decreases. This shows the evidence of the evidence of the geometric effects of viewing of filaments. Assuming the filaments are generated perpendicular to the jet surface, as the filaments leaves farther from the jet surface, it takes more time to make an initial observation in images. Thus,it is possible to consider the low velocity of filaments with large onset time leaves from more close to the center of jet normal to the side view shown in images. Note that the velocity of each filament is approximated with uncertainty by doing linear regression using the fit function in order to give one representative velocity according to each filament. Low velocity of filaments close to 0 showed larger error of approximation of onset time due to the uncertainty of the very small traveled distance of filaments.

Each filament used for measurement of velocity in Fig. 6.3 has been numbered in Fig. 6.4 for particular indication of each filament. According to the notation in Fig. 6.4, Fig. 6.7 (a) shows the velocity of filaments on the upper free surface of jet as a function of time and Fig. 6.7 (b) shows the velocity of filaments on the lower free surface of jet as a function of time. Note that the instantaneous velocity as defined in Equation (6.28) is used for measurement in Fig. 6.7. The onset time of filament increases as the peak velocity of filament decreases, which indicates the possible evidence of the geometric effect of viewing of filaments.

6.3 Velocity of Filaments on Mercury Jet Surface

6.3.1 Magnetic dissipation of energy

As a conducting liquid moves through a static magnetic field, electric currents are generated. This, in turn, leads to ohmic heating such as Joule dissipation. As the thermal energy of the fluid rises, there is a corresponding filament in its kinetic energy, and so the fluid decelerates. This results in a suppression of the motion of liquid jets. According to P. A. Davidson's approximation (1999), the Eqn. (2.42) shows the energy decay with respect to time depending on the magnetic damping time constant, where $\tau = \rho/\sigma B^2$. This implication is that the filaments decelerates on a time scale of τ. Fig. 2.3 (a) shows the decay of the normalized energy of flow in magnetic fields with respect to time due to the magnetic damping. Higher magnetic field dissipates energy faster. Fig. 2.3 (b) shows the integral calculation of energy with respect to time. Thus, it represents the total energy of flow by the certain time.

6.3.2 Time response of filaments in magnetic field

6.3.2.1 *averaged time response of filament in magnetic field*

Since the camera is triggered before beam arrives at the Hg jet and the laser pulse width is 150 ns, the first collected image shows the status of Hg jet before beam comes. Thus, the velocity of filament can always be judged as 0 m/s in the following Fig. 6.8. Fig. 6.8 represents the time response of filament

average velocity as a function of magnetic field with 14 GeV, 20 TP beam and 24 GeV, 10 TP beam respectively. The expression for the calculation of average velocity is

$$v_n^{avg} = \frac{1}{T_n - T_o} \int_{T_o}^{T_n} v(t)dt = \frac{y_m(T_n) - y_m(T_o)}{T_n - T_o}, \tag{6.27}$$

where T_n, T_o denotes the time taken in each framed image and the initial time of the first image respect to the proton beam arrival time respectively. Since the joule damping dissipates the energy with an exponential factor, the energy dissipation arises rapidly in the beginning depending on the magnetic field term B^2. Thus, higher magnetic field will have higher damping effect so that it takes more rising time. Therefore, the slope of rising velocity in Fig. 6.8 is varying depending on the magnetic field proportional to B^2 in exponential function. The magnitude of steady peak velocity is reduced by increased applied magnetic field strength, which is possible indication of the magnetic damping role induced by the joule damping dissipation. Again, in Fig. 6.8 (a), the delay of onset time of filament causes reduced steady peak velocity in same 5 T, which again indicates the fluctuation of jet flow in magnetic field and the geometric effect of viewing of filaments in shadow photography as well.

6.3.2.2 *instantaneous time response of filament in magnetic field*

Fig. 6.9 represents the time response of instantaneous filament velocity as a function of magnetic field with 14 GeV, 20 Tp beam and 24 GeV, 10 Tp beam respectively, which are reinterpretation of Fig. 6.8 in terms of instantaneous

velocity analysis. The expression for the calculation of instantaneous velocity assuming ΔT_n is small enough is

$$v_n = \frac{y_m(T_n) - y_m(T_{n-1})}{\Delta T_n}. \tag{6.28}$$

Comparing with Fig. 6.8, the velocity of filaments are fluctuating.

6.3.3 Beam induced filaments velocity in magnetic field

6.3.3.1 *filaments velocity with 14 GeV beam in magnetic field*

Fig. 6.10 (a) shows the filament velocity as a function of 14 GeV beam intensity and magnetic field corresponding to the observed onset time of filaments shown in Fig. 6.10 (b). The filament velocity increases with the beam intensity. However, the magnetic field suppresses the filament velocity. At relatively low magnetic field of 5 T, the jet flow and/or the charged beam may be fluctuating depending on the initial conditions at experiment. Thus, there are scattering distributions over the resulting data points. The slope of the data points at higher magnetic fields are less than that associated with lower magnetic field. All velocities are less than 30 m/s regardless of the magnetic field. The filament velocity at 14 GeV, 20 Tp, 10 T is $\sim$ 13 m/s.

6.3.3.2 *filaments velocity with 24 GeV beam in magnetic field*

Fig. 6.11 (a) shows the filament velocity as a function of 24 GeV beam intensity and magnetic field corresponding to the observed onset time of filaments shown in Fig. 6.11 (b). The filament velocity increases with the beam

intensity. The slope of the increase is $\sim 4 \times$ larger than that for the 14 GeV case, which indicates that parameters such as beam spot size may be affecting the energy deposition density since the ratio of peak energy deposition is $\sim$ 1.5 at 0 T assuming the beam spot sizes for 14 GeV and 24 GeV are $\sim$ 1.6 mm RMS. However, the magnetic field suppresses the filament velocity. At relatively low magnetic field up to 5 T as in the 14 GeV case, the jet flow and/or the charged beam is unstably fluctuating depending on the event conditions at experiment. Thus, there are distributions of the resulting data points. All velocities are less than 130 m/s regardless of the magnetic field, and the filament velocity for the 24 GeV, 20 Tp, 10 T case is $\sim$ 70 m/s.

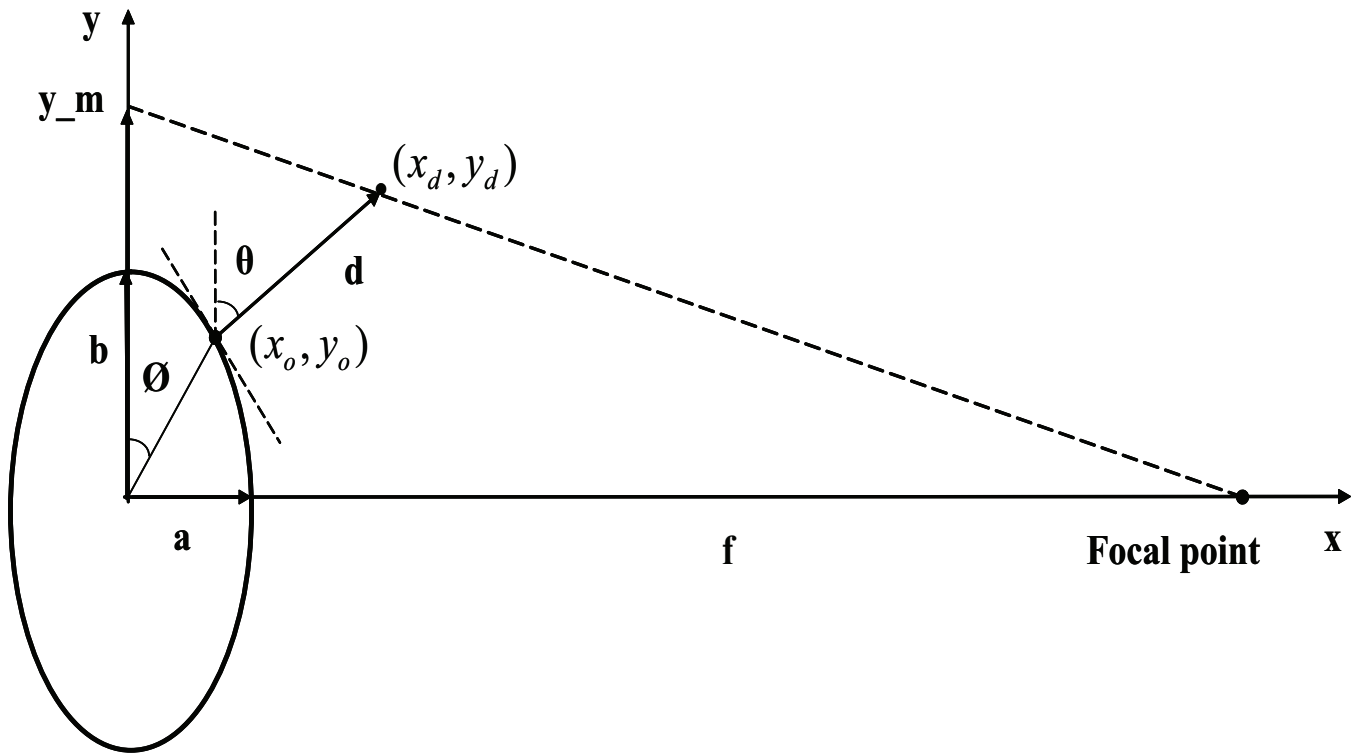

Figure 6.1: Schematic geometry of viewing mercury filaments.

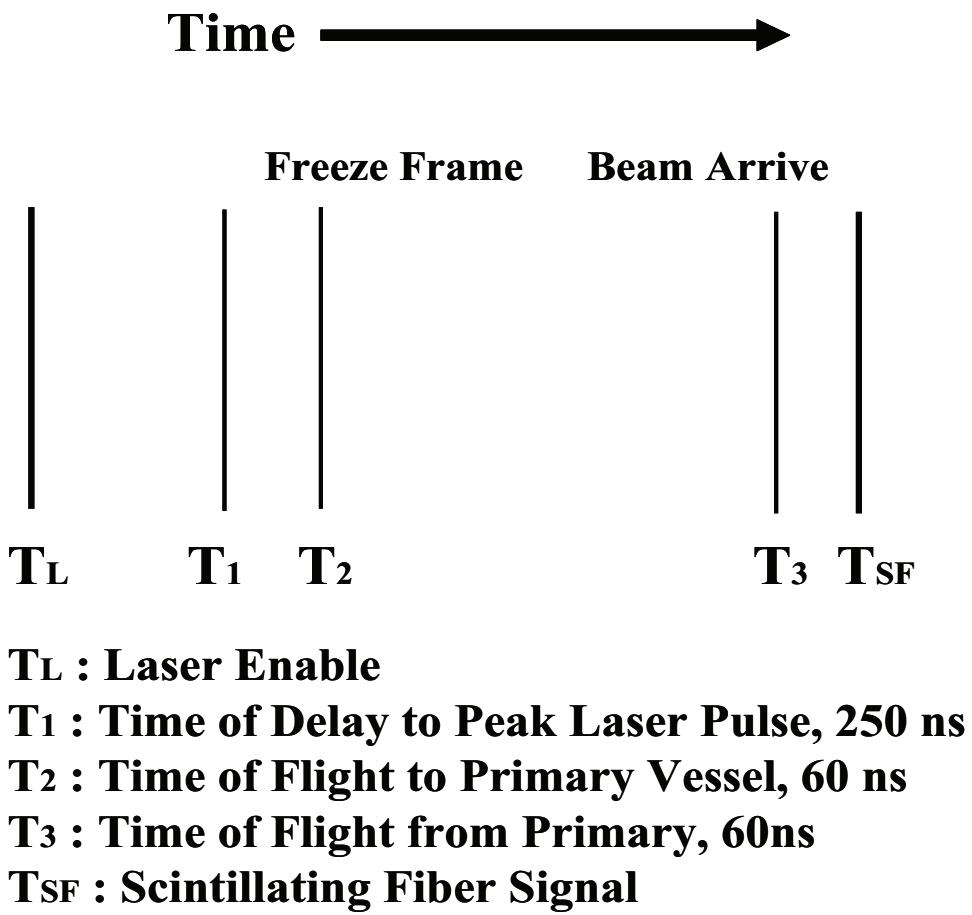

Figure 6.2: Time structures between light source enabling and proton beam arrival.

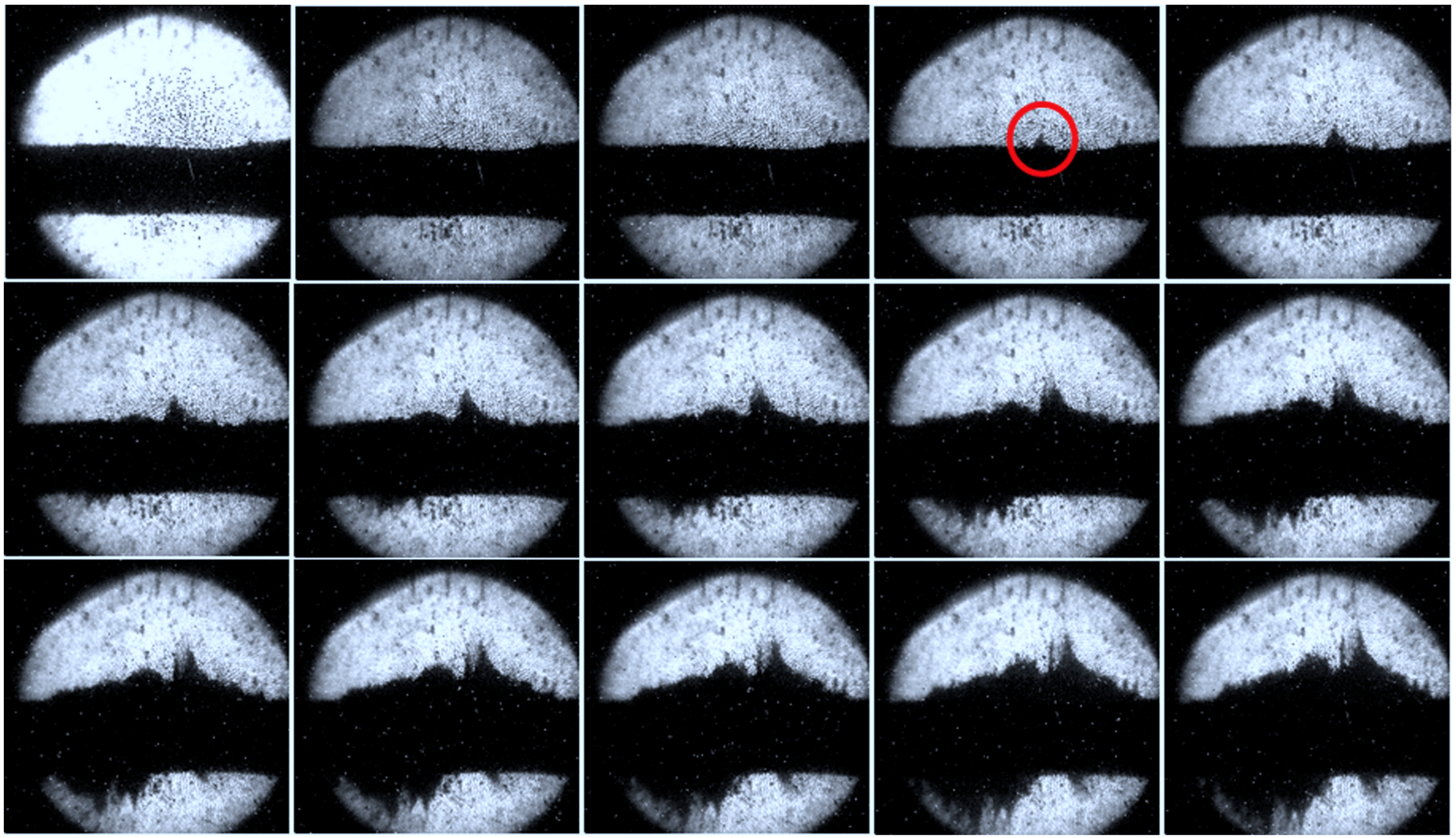

Figure 6.3: Photographs of filament evolution on the Hg jet surface as a function of time at 25 μs frame rate. The beam is 10 Tp, 24 GeV. The magnetic field is 10 T. The red circle on the 4^{th} image of the top row points the filament that is used for velocity measurement in Fig. 6.8 (b) and Fig. 6.9 (b).

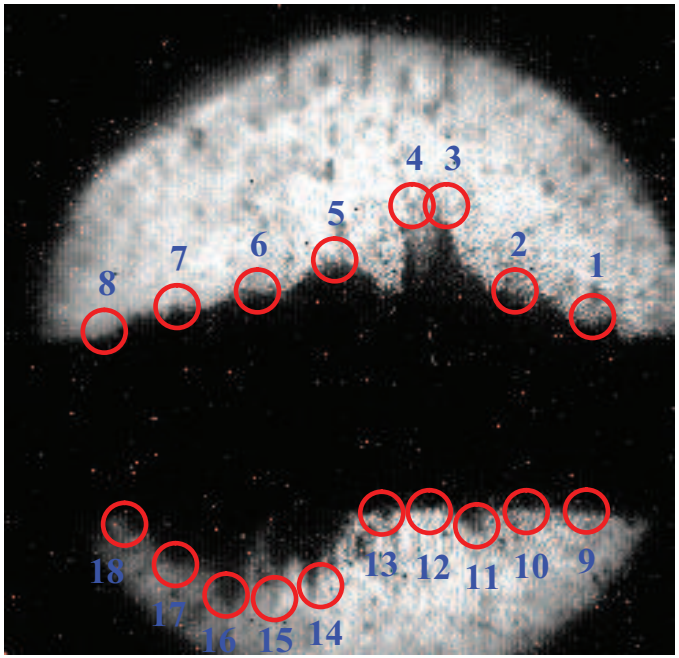

Figure 6.4: Location on the Hg jet surface for velocity measurement of 14 points of filament. The shot condition same with Fig. 6.3. The numbers above red circles points the filament that is used for velocity approximation in Fig. 6.6 and Fig. 6.7.

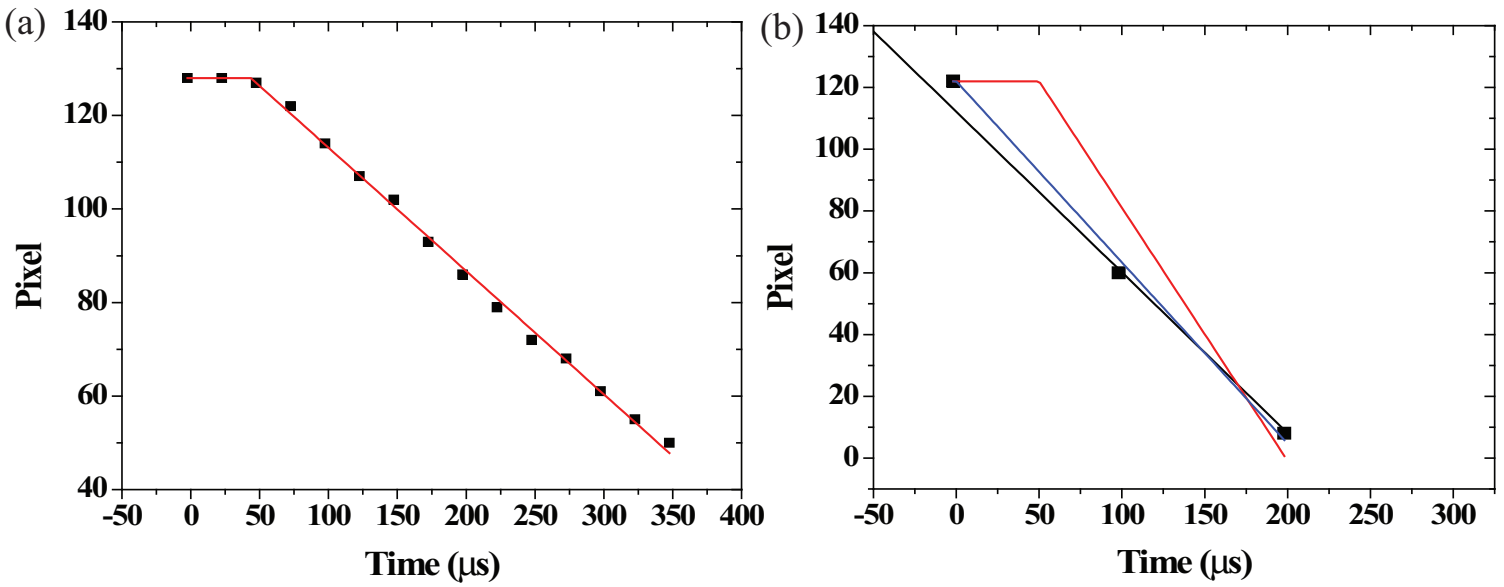

Figure 6.5: Illustration of curve fit for parameters estimation. a.) Multiple data points. b.) 3 data points.

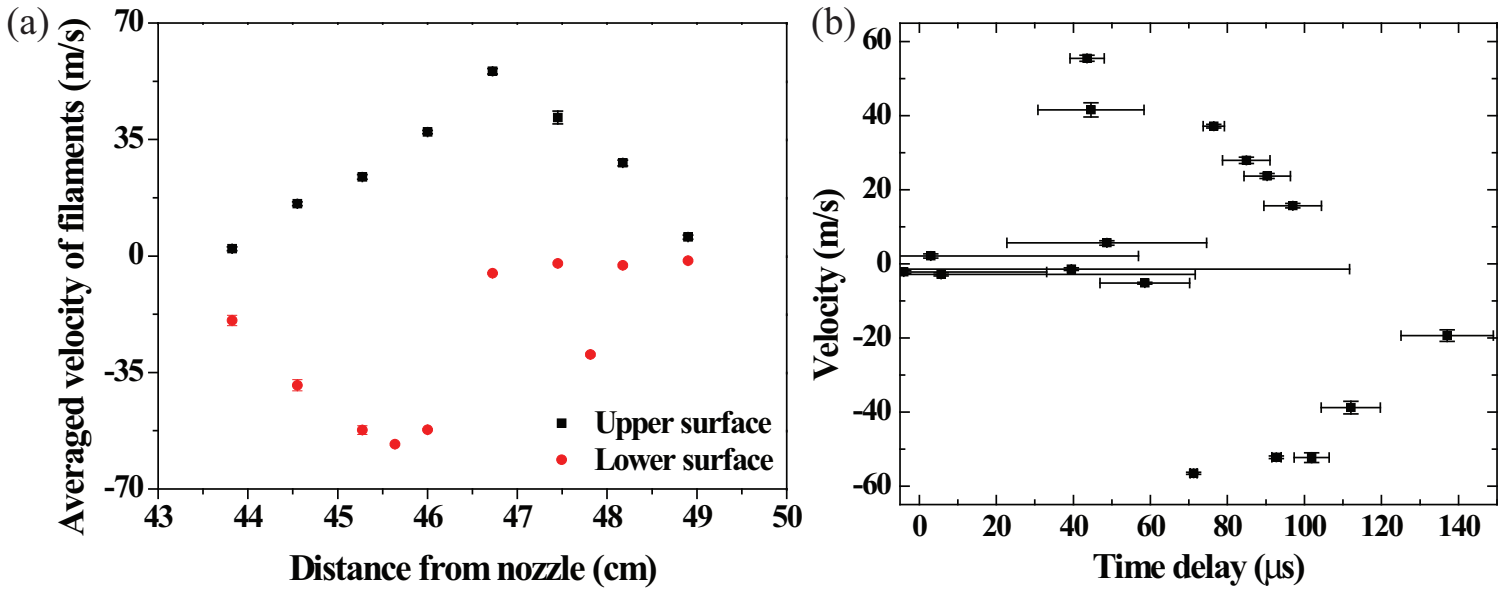

Figure 6.6: Approximation of velocity and onset time of filaments shown in Fig. 6.3. The beam is 10 Tp, 24 GeV. The magnetic field strength is 10 T. a.) Approximation of velocity of filaments. b.) Approximation of onset time of filaments.

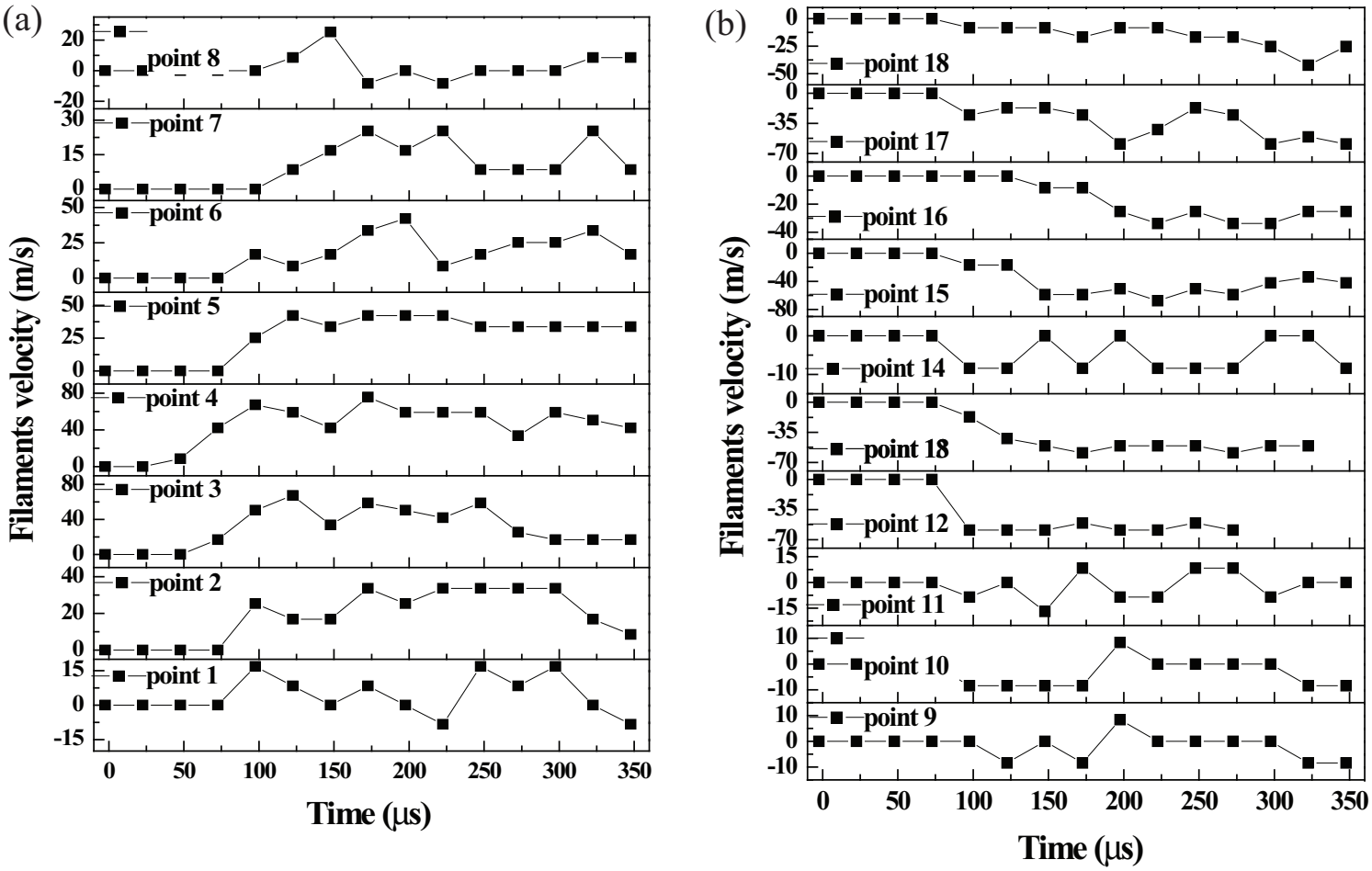

Figure 6.7: Time response of instantaneous filament velocity at jet surface in Fig. 6.3 as a function of distance from magnet center. The beam is 10 Tp, 24 GeV. The magnetic field is 10 T. a.) Upper surface. b.) Lower surface.

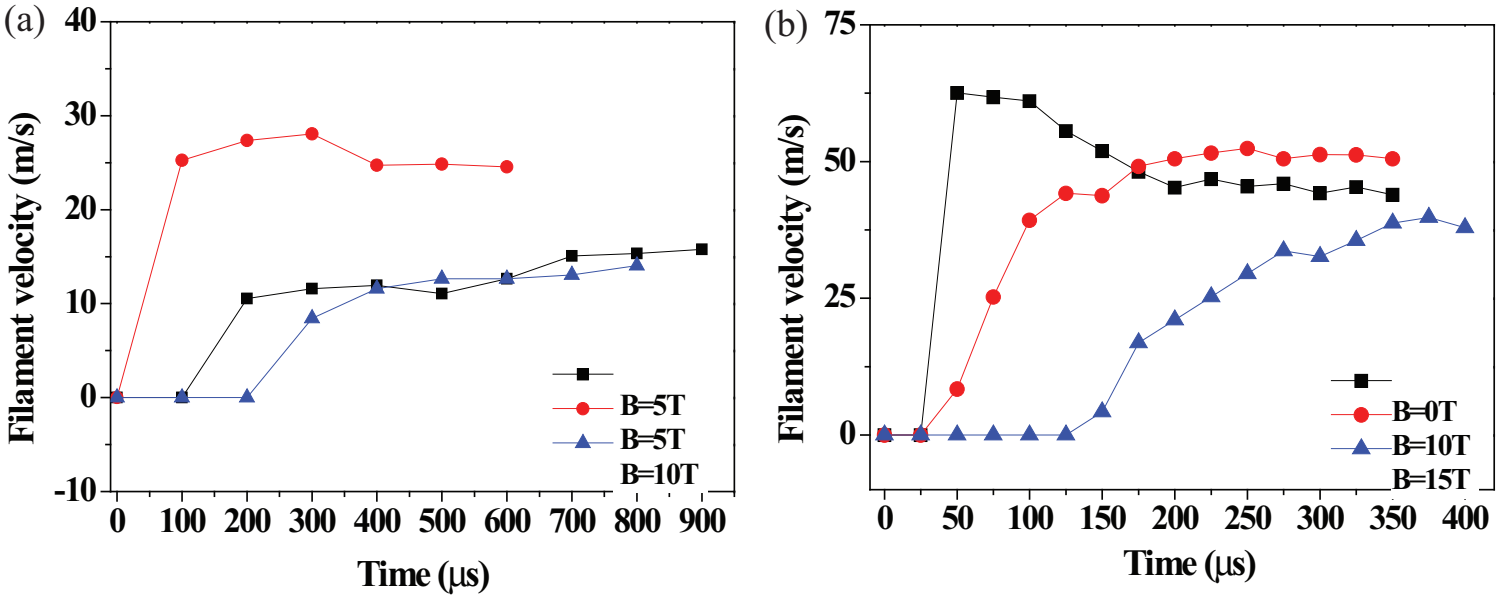

Figure 6.8: Time response of averaged filament velocity as a function of magnetic field. a.) 14 GeV, 20 Tp beam. b.) 24 GeV, 10 Tp beam.

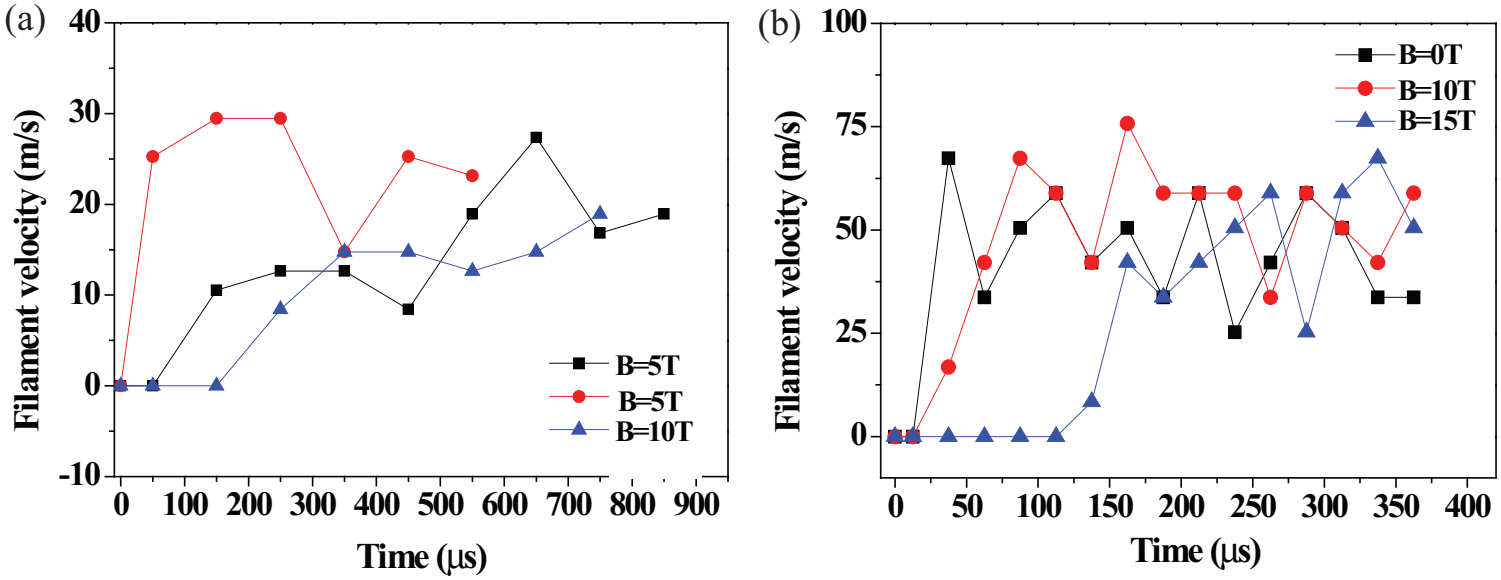

Figure 6.9: Time response of instantaneous filament velocity as a function of magnetic field. a.) 14 GeV, 20 Tp beam. b.) 24 GeV, 10 Tp beam.

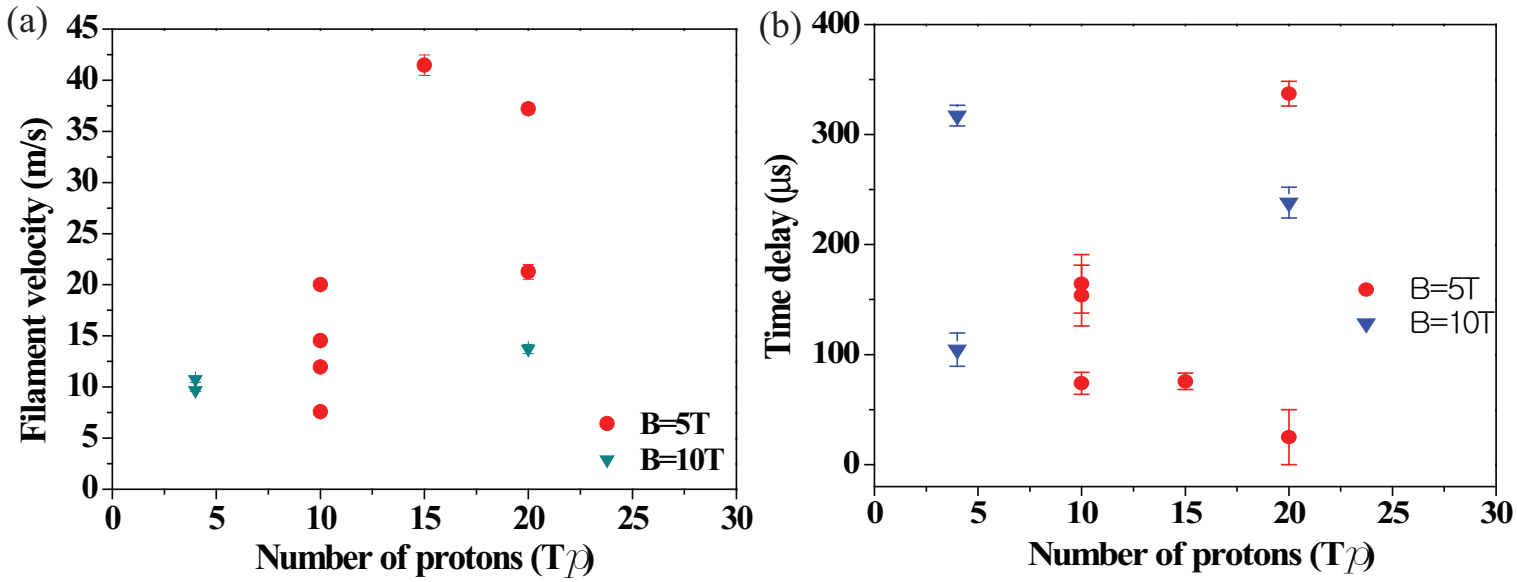

Figure 6.10: Filament velocity as a function of 14 GeV beam intensity and magnetic field.

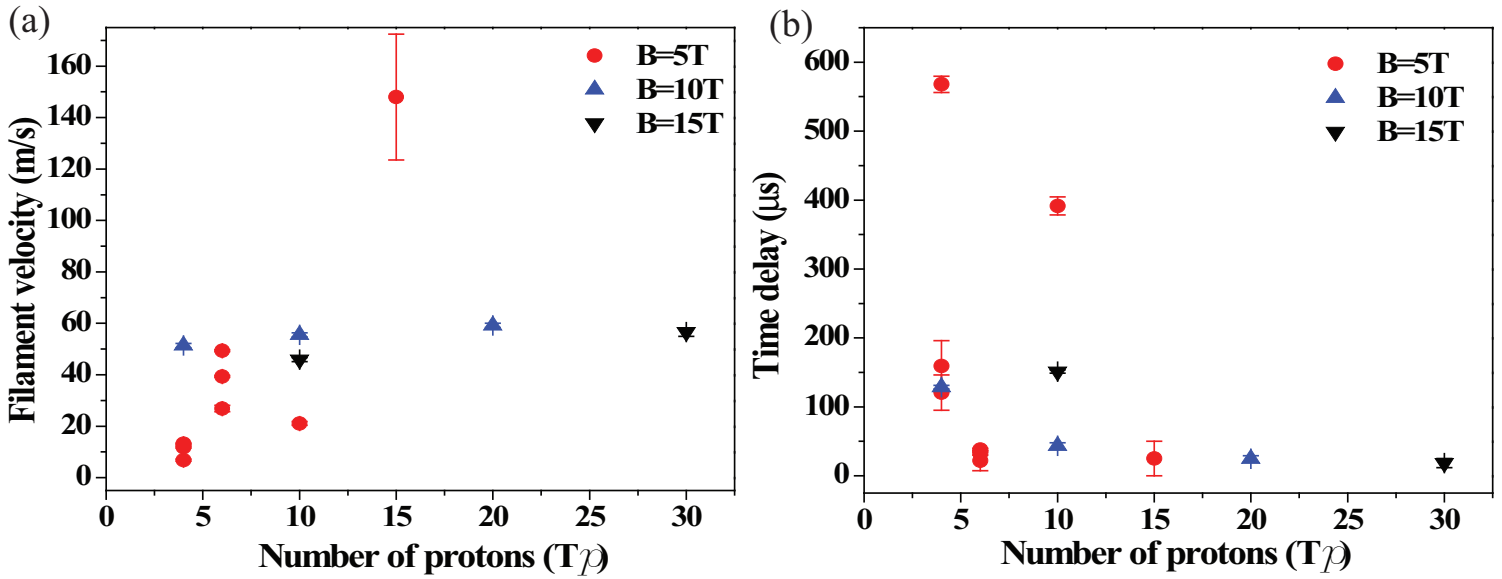

Figure 6.11: Filament velocity as a function of 24 GeV beam intensity and magnetic field.

Chapter 7

Conclusions

The experiment is a proof-of-principle test for a target system capable of accepting a high-intensity 4 MW proton beam. The system allows for the production of copious pions which subsequently decay into muons. These muons are magnetically captured, accelerated and inserted into storage rings. An experiment at the CERN Proton Synchrotron that combines a free mercury jet target with a 15 T solenoid magnet and 14 GeV and 24 GeV proton beam was performed. It validates the target concept for producing an intense secondary source of muons. When combined with a beam bunch of 30×10^{12} protons on the mercury target, this will generate a peak energy deposition of ~ 100 J/g. For this experiment, a pulsed solenoid was designed, which is capable of delivering a peak field of 15 T. The Hg jet loop system generates a mercury jet from 1 cm diameter nozzle with velocities up to 15 m/s. An optical diagnostic system based on back-illuminated laser shadow photography is employed to investigate the mercury jet flow. Synchronized short laser light pulses are used to illuminate the target and freeze the motion of the jet. A total of four optical imaging heads for each Viewport are mounted on the exterior of the

primary containment vessel. Three high speed cameras are used to simultaneously collect images on three Viewports. Integrated all-in-one compact optical heads, consisting of ball lens, illumination fiber, objective lens, and imaging fiber bundle, are placed at the radius of curvature of a retro-reflector allowing for the illumination and imaging collection on one side of the mercury primary containment vessel. Due to the short time of frame rate, the time delay from the light source to the image arrival at the camera CCD is adjusted considering the delay from the electronics as well as the fiber-optics. The optimum timing delay is judged by the uniformity of consecutive collected image brightness as well as the triggering signal pulse on the oscilloscope for each component of device. The trigger timing is adjusted using the response of the scintillating fiber on the oscilloscope with respect to the beam triggering timing. The motions of mercury jet for 0.4 s at Viewport 1, 3, and 4 and for 1.6 ms at Viewport 2 are collected, respectively, which enables us to give both the overall jet condition at upstream (downstream) and the accurate motion of jet at midstream, where the magnetic induction field is maximum and the center of beam-jet interaction is positioned. Image processing provides some information on the mercury jet thickness at various magnetic induction field strengths and velocities, i.e.,the optical diagnostic observation shows the effects of the magnetic force on the cross-sectional distortion of mercury jet caused by the Lorentz force. In addition, the image analysis reveals the jet instability which might be caused by the strong induced axial magnetic induction field, which is possibly the onset of a quadrupole effect. Nevertheless, the experimental

results clearly show that the magnetic induction field stabilizes the mercury jet by smoothing out the edges of the otherwise turbulent mercury flow, as previously reported in the literatures (Shercliff 1956, Gold 1962, Kozyrev 1981, Bernshtam 1982). The comprehensive optical diagnostic method allows us to have a better understanding of the behavior of a conducting jet moving in a high magnetic induction field environment. It plays a key role as a primary diagnostic of free mercury jet interacting with an intense proton beam under high-magnetic induction field. The optical diagnostics will allow us to interpret the beam-jet interaction length caused by the energy deposition from the proton beam as well as the splash velocity on the mercury jet surface with the aid of the high speed camera.

In order to achieve an understanding of liquid metal flow in a magnetic field, magnetohydrodynamic equations considering Lorentz force effect based on the Navier-Stokes equations as well as Maxwell equations are presented. The jet height is measured as a function of the magnetic field strength. The suppression of vorticity by the perpendicular magnetic field is introduced and the Stuart number gives the magnetic field effect.

Such a reducing effect in rotational motion on the jet surface is observed qualitatively. As a result, the rotational motion of jet on the surface becomes more two dimensional motion of flow and thus the jet surface is more stabilized.

For magnetohydrodynamic flow investigation, the mercury jet behavior is observed for various magnetic field strengths and then the jet deformation is measured. The fluctuation on the jet surface decreases as the magnetic field

increases and the jet height increases slightly with magnetic field assuming the major and minor axis of Hg jet is reversed. Gravity affects the jet trajectory so that the jet bends down as it goes downstream. But this deflection of the jet by gravity is reduced at higher magnetic field. The jet axis becomes more straight toward the direction of magnetic field line.

The stabilizing effect of the magnetic field on a turbulent jet is observed. It is well known that the turbulent fluctuation is suppressed by magnetic field and we could observe that the wave length on the jet surface increases. Thus, the jet surface is getting flattened as the magnetic field increases. Also, the critical Reynolds number increases due to the magnetic field. Therefore, the jet is getting more stabilized. The measured intermittency shows the fluctuating surface of jet is getting more flattened as the magnetic field increases. The transverse magnetic field is more dominant to the jet stabilization though the longitudinal magnetic field is also influential. However, the jet has a different type of instability at magnetic fields larger than 10 T. The jet height becomes larger at larger magnetic field than 10 T. This is induced by the longitudinal current due to the tilted jet axis with respect to the magnet axis. Thus, the induced current generates a Lorentz force. As a result, additional anisotropic magnetic force is changing the jet height. As the magnetic field increase up to 5 T, the jet fluctuation decreases and the jet is more elongating to the flow direction. Thus, the jet height decreases from 0 T to 5 T. However, the magnetic pressure is influencing at larger than 5 T. Since the optical diagnostics depends on the side view of jet flow, it is hard to tell in which direction the jet deflects

since the jet and the magnetic field line is axially symmetric. However, the jet height clearly increases at 15 T, which indicates that the magnetic pressure apparently affects the jet height at 15 T.

The longitudinal jet velocity is not varied. Again, the jet elongation to the field direction by the magnetic field is indicated from this result. The longitudinal magnetic field does not influence the jet flow velocity. The transverse magnetic field will change the jet velocity. This is known as the Hartmann flow. The longitudinal magnetic field does not influence the longitudinal jet flow as it is shown in the governing MHD equation.

The pipe pressure driven by the syringe piston was measured. It shows that the Hg driving pressure is the same regardless of the magnetic field variation. The driving pressure at the Hg pipe inlet is independent of the magnetic field strength. Therefore, the mercury delivery is not influenced by the longitudinal magnetic field. However, there may be some pressure loss or jet velocity profile change due to the pipe bend. According to the velocity measurement at upstream, mid-stream, and downstream, it is not significantly different but it is same comparing with the flow velocity at 0 T. Therefore, the field effect at the pipe bend is expected to be somewhat negligible. To support this result, the pipe loss due to the geometry and friction is estimated.

The most interesting result is the observation of the interaction of the proton beam with the jet, for provides clue to validate the performance of high power target for future accelerator. The disruption as manifested by the jet break up is caused by the energy deposition of proton beam. The filaments

begins on the bottom surface of Hg jet where the proton beam enters. The filaments ends on the top surface of Hg jet where the proton beam leaves. The jet breakup is occurring at the center of jet where the maximum energy is deposited. This phenomenon is consistent with the beam trajectory across the jet as well as the results of energy deposition by the proton beam. However, Hg jet breakup is influenced by the magnetic field. In order to validate the measured disruption length, circular jet shape with reduced mass density and elliptic jet shape are modeled in MARS code for calculation of energy deposition. Deposition of peak energy density to Hg jet according to the beam intensities and magnetic field strengths are analyzed. Based on the hypothesis of threshold of beam intensity causing the disruption of Hg jet at various magnetic field strength, the disruption length is estimated, which gives good agreement with experimentally measured disruption length.

The filamentation velocity increases as the beam intensity increases due to the increased energy deposition but the magnetic field reduces the filamentation velocity. The disruption length increases with both beam energy and intensity because the energy deposition to Hg jet increases as the beam energies and the beam intensities increase. However, the disruption length is also suppressed by the magnetic field because of the magnetic damping. As a result, the intensity threshold for breakup is lower at higher energy. The time scale of magnetic damping indicates the rate of decay of global kinetic energy due to the magnetic field strength. Thus, the energy decreases faster as the magnetic field increases. Therefore, the rising time to the maximum velocity

increases as the magnetic field increases. It indicates that the magnetic damping is getting larger by the magnetic field in terms of the transient response time.

Finally, the performance and feasibility of utilizing liquid metal jet as a target for an intense proton beam is explored. The liquid jet target concept is based on the target being recycled after each pulse. Therefore, the power of the target has to be evaluated in terms of the replacing capability. The optimal interaction length for the 24 GeV beam energy is in the region of 30 cm which corresponds to approximately 2 interaction length for mercury (Kirk *et al*, 2008). For a 20 m/s jet velocity, replacing two interaction lengths will be taken in 14 ms thus allowing for operations with a repetition rate of up to 70 Hz. The beam energy per pulse is 115 kJ for a beam of 30×10^{12} protons with 24 GeV beam energy. The disruption length at 30×10^{12} protons with 24 GeV beam energy in a magnetic field of 15 T is less than 20 cm at 24 GeV beam energy, thus preserving the 70 Hz beam repetition rate option, which corresponds to a beam power of 8 MW. It is validated that a target system capable of supporting proton beams with powers of up to 8 MW (Kirk *et al*, 2008).

Bibliography

[1] J. Alessi *et al*, 1998, "A proposal for an *R&D* program for targetry and capture at a muon collider source," *Approved as BNL E951*

[2] M. M. Alsharoa *et al*, 2003, "Recent progress in neutrino factory and muon collider research within the muon collaboration," *submitted to Phys. Rev. ST Accel. Beams.*, *http* : *//www.cap.bnl.gov/mumu/pubs/prstab* − 030422/*prstab.pdf*

[3] C. M. Ankenbrandt *et al*, 1999, "Status of muon collider research and development and future plans" *Phys. Rev. ST Accel. Beams 2*, **081001**

[4] Robert P. Benedict, 1980, *Fundamentals of pipe flow*, John Wiley & Sons, Inc.

[5] V. A. Bernshtam, S. V. Kozyrev, A. I. Él'kin, 1982, "Stability of flow of films of a conducting viscous liquid in longitudunal magnetic field," *Magnetohydrodynamics*, **18**, pp.132

[6] Herman Branover, 1978, *Magnetohydrodynamic flow in ducts*, John Wiley & Sons, Inc.

[7] Michael P. Brenner, 2002, "Single bubble sonoluminescence," *Reviews of Modern Physics*, **74**, pp.425-440

[8] G. A. Carlson, 1975, "Dynamic tensile strength of mercury," *J. Appl. Phys.*, v.46, pp.4069-4070

[9] Donald Chang, Thomas Lundgren, 1961, "Duct flow in magnetohydrodynamics," *Z. angrew. Math. Phys.*, **12**, pp.100-114

[10] I. G. Currie, 1993, *Fundamental Mechanics of Fluids*, Marcel Dekker, Inc.

[11] P. A. Davidson, 1999, "Magnetohydrodynamics in materials processing," *Annu. Rev. Fluid Mech.*, **31**, pp.273-300

[12] G. F. D. Duff, D. Naylor, 1966, *Differential equations of applied mathematics*, John Wiley & Sons, Inc.

[13] I. Efthymiopoulos, A. Fabich, J. Lettry, 2005, "CERN installation," *http://cern.ch/proj-hiptarget*

[14] I. Efthymiopoulos, 2008, "The MERIT experiment or nToF11," *MUTAC review*, *http* : *//www.hep.princeton.edu/ mcdonald/mumu/target/Ilias/ie*$_0$80408*.pdf*

[15] A. Fabich, 2005, "nToF11: Multi-MW target experiment in TT2A," *http://cern.ch/proj-hiptarget*

[16] A. G. Fedin, 1973, "Use of optical methods in investigating MHD processes" *Magnetohydrodynamics (English translation of Magnitaya Gidrodinamika)*, **9**, pp.301-308

[17] T. A. Gabriel *et al*, 2001, "Targets for high-intensity particle production," *Part. Accel. Conf.*, Chicago, pp.737

[18] T.A. Gabriel, J.R. Haines, T. J. McManamy, P. Spampinato, B. W. Riemer, 2001, "Targets for high intensity particle production," *Part. Accel. Conf.*, Chicago, pp737-741

[19] J. Gallardo *et al*, 2001, "Calculation for a mercury jet target in a solenoid magnet capture system," *Part. Accel. Conf.*, Chicago, pp627-629

[20] J. Gallardo *et al*, 2002, "First order perturbative calculations for a conducting liquid jet in a solenoid," *MUC-NOTE-TARGET-242, MU-047*

[21] D. Gao, N. B. Morley, 2002, "Equilibrium and initial linear stability analysis of liquid metal falling film flows in a varying spanwise magnetic field," *Magnetohydrodynamics*, **38**, No.4, pp. 359-375

[22] A. K. Geim, M. D. Simon, M. I. Boamfa, M. J. Lighthill, 1999, "Magnetic levitation at your finger tips," *Nature*, **400**, pp. 323

[23] M. B. Glanert, M. J. Lighthill, 1955, "The axissymmetric boundary layer on a long thin cylinder," *Proc. Roy. Soc. Ser.*, **A 230**, pp. 188

[24] Richard R. Gold., 1962, "Magnetohydrodynamic pipe flow: Part 1.," *J. Fluid Mech.*, **13**, pp.505-512

[25] R. J. Goldstein, 1991, *Optical systems for flow measurement*, McGraw-Hill, Inc.

[26] Andrew Gray and G. B. Mathews, 1966, *A treatise on Bessel functions and their applications to physics*, Dover, Inc.

[27] V. Graves, 2007, "MIT testing results" *MUTAC review*, *http* : *//www.hep.princeton.edu/ mcdonald/mumu/target/graves/VGraves−*070418*.pdf*

[28] J. Hartmann, 1937, "Hg dynamics I," *Kgl. Danske Videnskab Selskabs Math. Fys.*, Medd. 15, No.6

[29] H. Ito, 1960, "Pressure losses in smooth pipe bends," *Trans. ASME., J. Basic Eng.*, **82**, pp.131

[30] Uhlenbusch J., Fishcer E., 1961, "Hydromagnetische strömung im kreiszylindrischen rohr," *Z. Phys.*, **165**, pp.190-198

[31] Colin Johnson, 2002, "A self focusing mercury jet target," *CERN-NUFACT-113*

[32] T. Kakuta, T. Shikama, M. Marui, 1999, "Optical fibers and their applications for radiation measurement," *Seventh Int. Conf. on Nuclear Engineering*, Tokyo, Japan, pp.19

[33] H. G. Kirk *et al*, 2001, "Target studies with BNL E951 at the AGS," *Part. Accel. Conf.*, Chicago, pp.1531-1537

[34] H. G. Kirk *et al*, 2008, "The MERIT high power target experiments at the CERN PS," *European Part. Accel. Conf.*, Genoa, Italy, *WEPP169*

[35] B. A. Kolovandin, 1965, "Stability of flow of conducting liquid with free surface in the presence of magnetic and electric fields," *Prikl. Mekh.*, **1**, No. 11, pp.95

[36] S. V. Kozyrev, A. I. Él'kin, 1981, "Stability of flow of thin films of electrically conducting liquid in crossed magnetic and electric fields," *Magnetohydrodynamics*, **17**, No. 4, pp.353

[37] H. C. Lee, 1977, "Boundary layer around a liquid jet," *IBM J. Res. Develop.*, pp.48

[38] J. Lettry *et al*, 2003, "Thermal shocks and magnetohydrodynamics in high power mercury targets," *J. Phys. G: Nucl. and Part. Phys.*, **29**, pp.1621

[39] Junwoo Lim *et al*, 1998, "Control of streamwise vortices with uniform magnetic fluxes," *Physics of Fluids*, **10**, 8, pp.1997

[40] S. P. Lin, D. J. Kang, 1987, "Atomization of a liquid jet," *Physics of Fluids*, **30**, pp.2000-2006

[41] K. T. McDonald *et al.*, 2001, "The primary target facility for a neutrino factory based on muon beams," *Proc. Part. Accel. Conf.*, Chicago, IL, pp.1583

[42] K. T. McDonald, 2000, "Cooling of a target by helium gas," *Princeton /μ/μ/00-25*

[43] K. T. McDonald, 2000, "Damping of radial pinch effects," *Princeton /μ/μ/00-26*

[44] K. T. McDonald, 2000, "Magnetohydrodynamics of a continuous mercury jet coaxially entering a solenoid," *Princeton /μ/μ/00-29*

[45] K. T. McDonald, 2000, "Magnetohydrodynamics of a pulsed mercury jet entering a solenoid at an angle," *Princeton /μ/μ/00-30*

[46] K. T. McDonald, 2000, "Optics for E951 target tests in the A3 beamline," *Princeton /μ/μ/00-28*

[47] N. V. Mokhov, 2000, "Paricle production for a muon storage ring: I. Targetry and π/μ yield" *MUC0169*, http://www-mucool.fnal.gov/mcnotes/muc0169.pdf

[48] N. V. Mokhov, O. E. Krivosheev, 2000, "MARS code status," *FERMILAB-Conf-00/181*

[49] Neil B. Morley *et al*, 2000, "Liquid megnetohydrodynamics - recent progress and future directions for fusion," *Fusion Engineering and Design*, **51**, pp.701-713

[50] Neil B. Morley, Sergey Smolentsev, Donghong Gao, 2002, "Modeling infinite/axisymmetric liquid metal magnetohydrodynamic free surface flows," *Fusion Engineering and Design*, **63**, pp. 343-351

[51] S. Osaki, R. Palmer, M. Zisman, J. Gallardo, 2001, "Neutrino factory feasibility study 2," *BNL-52623*, Ch.3, *http* : *//www.cap.bnl.gov/mumu/studii/FS2 − report.html*

[52] N. Otsu, 1979, "A threshold selection method from gray-level histograms," *IEEE Trans. Sys., Man., Cyber.*, **9**, pp. 62-66

[53] SAE, 1960, "Aero-space thermodynamics manual," pp. A18-A20

[54] R. Samulyak, 2006, "Target simulations" *MUTAC review*, *http* : *//www.hep.princeton.edu/ mcdonald/mumu/target/samulyak/ mutac*06*_samulyak_targetsimulations.pdf*

[55] R. Samulyak, J. Du, J. Glimm, Z. Xu, 2007, "A numerical algorithm for MHD of free surface flows at low magnetic Reynolds numbers," *Jorunal of Computational Physics*, **226**, pp.1532-1549

[56] N. Simos, 2005, "MERIT experiment window study," *BNL Review*, *http* : *//www.hep.princeton.edu/ mcdonald/mumu/target/simos/ Simos_*121205*.pdf*

[57] P. Sievers, P. Pugnat, 2000, "Response of solid and liquid targets to high power proton beams for neutrino factories," *Report CERN LHC/2000-4, CERN-NuFACT Note 035*

[58] K. Stewartson, 1955, "The asymtotic boundary layer on a circular cylinder in axial incompressible flow," *Q. Appl. Math.*, **13**, pp. 113

[59] Sergei Striganov, 2009, Private communication

[60] Shuzo Oshima, Ryuichiro Yamane, Yoshihiro Mochimaru, Toshihiro Matsuoka, 1987, "The shape of a liquid metal jet under a non-uniform magnetic field," *JSME International Journal*, **30**, No.261, pp.437-448

[61] R. B. Palmer, 1998, "Muon collider design," *Report BNL-65242, CAP-200-MUON-982C*

[62] Mark A. Pinsky, 1991, *Partial differential equations and boundary value problems with applications*, McGraw-Hill, Inc.

[63] R. D. Reitz, F. V. Bracco, 1982, "Mechanism of atomization of a liquid jet," *Physics of Fluids*, **25**, pp.1730-1742

[64] Uflyand Y. S., 1960, "Hartmann problem for a circular tube," *Soviet Phys.*, **5**, pp.1194-1196

[65] Roman Samulyak, 2006, "Target simulations," *MUTAC Review*, *http* : *//www.hep.princeton.edu/ mcdonald/mumu/target/samulyak/ mutac*06*_samulyak_targetsimulations.pdf*

[66] J. A. Shercliff, 1953, "Steady motion of conducting fluids in pipes under transverse magnetic fileds," *Proc. Camb. Phil. Soc.*, **49**, pp.136-144

[67] J. A. Shercliff, 1956, "The flow of conducting flows in circular pipes under transverse magnetic fields," *J. Fluid Mech.*, **13**, pp.644-666

[68] J. A. Shercliff, 1962, "Magnetohydrodynamic pipe flow: Part 2 High Hartmann number," *J. Fluid Mech.*, **13**, pp.513-518

[69] J. A. Shercliff, 1965, *A textbook of magnetohydrodynamics*, Pergamon Press

[70] P. T. Spampinato *et al*, 2005, "A free jet mercury system for use in a high power target experiment," *Part. Accel. Conf.*, Knoxville, TN, pp.1637

[71] P. Thieberger, H. G. Kirk, R. J. Weggel, K. T. MacDonald, 2003, "Moving solid metallic targets for pion production in the muon collider/neutrino factory project," *Proc. Part. Accel. Conf.*, Portland, OR, pp.1634

[72] N. Tsoupas *et al*, 2003, "Injection acceleration and extraction of high intensity proton beam for the neutrino facility project at BNL," *Part. Accel. Conf.*, Portland, OR, pp.1637

[73] C. D. West, 2000, "Cavitation in a mercury target," *ORNL/TM-2000-/263*

[74] H. Q. Yang, 1992, "Asymmetric instability of a liquid jet," *Physics of Fluids*, **30**, pp.681-689

[75] K. T. Yen, 1967, "Role of intermittency in free turbulent flows," *American Institute of Aeronautics and Astronautics*, **5**, No. 12 pp.2187-2192

[76] W. M. Yao *et al*, 2006, "Accelerator physics of colliders" *Journal of Physics*, **33**, No.1, pp.35-62

Appendix A

Tabular Data for Chapter 3 and Chapter 5

A.1 Specifications of Optics

Table A.1: Specifications of optical components in optical diagnostics.

Item	Value
Right angle prism mirror	Gold coated, 25 × 25 × 35.4, Surface flatness $\lambda/10$
Gradient index lens	
Size	d=1.0 mm, L=2.48 mm
Numerical aperture	0.5
Working distance	Infinity
Coating	AR coated at 800 ∼ 960 nm
Sapphire ball lens	D=0.5 mm, Al_2O_3, Index of refraction=1.77
Retro-reflecting Parabolic mirror	
Diameter	76.2 mm
Thickness	12.7 mm
Focal length	444 mm
Coating	Gold
Microscope objective	
Magnification	40 ×

Continued on next page

Table A.1: *Continued from previous page*

Item	**Value**
Numerical aperture	0.65
Working distance	0.6 mm
Clear aperture	5.0 mm
Power	160 mm (tube length) / f
Optical fiber	
Number of picture elements	30000
Jacketing diameter	800 μm
Picture elements area diameter	720 μm
Coating diameter	960 μm
Core material	GeO_2 containing Silica
Coating material	Silicone
Numerical aperture	0.35
Allowable bending radius	40 mm
Core diameter	200 μm

A.2 Characteristic Response of 25 W Laser

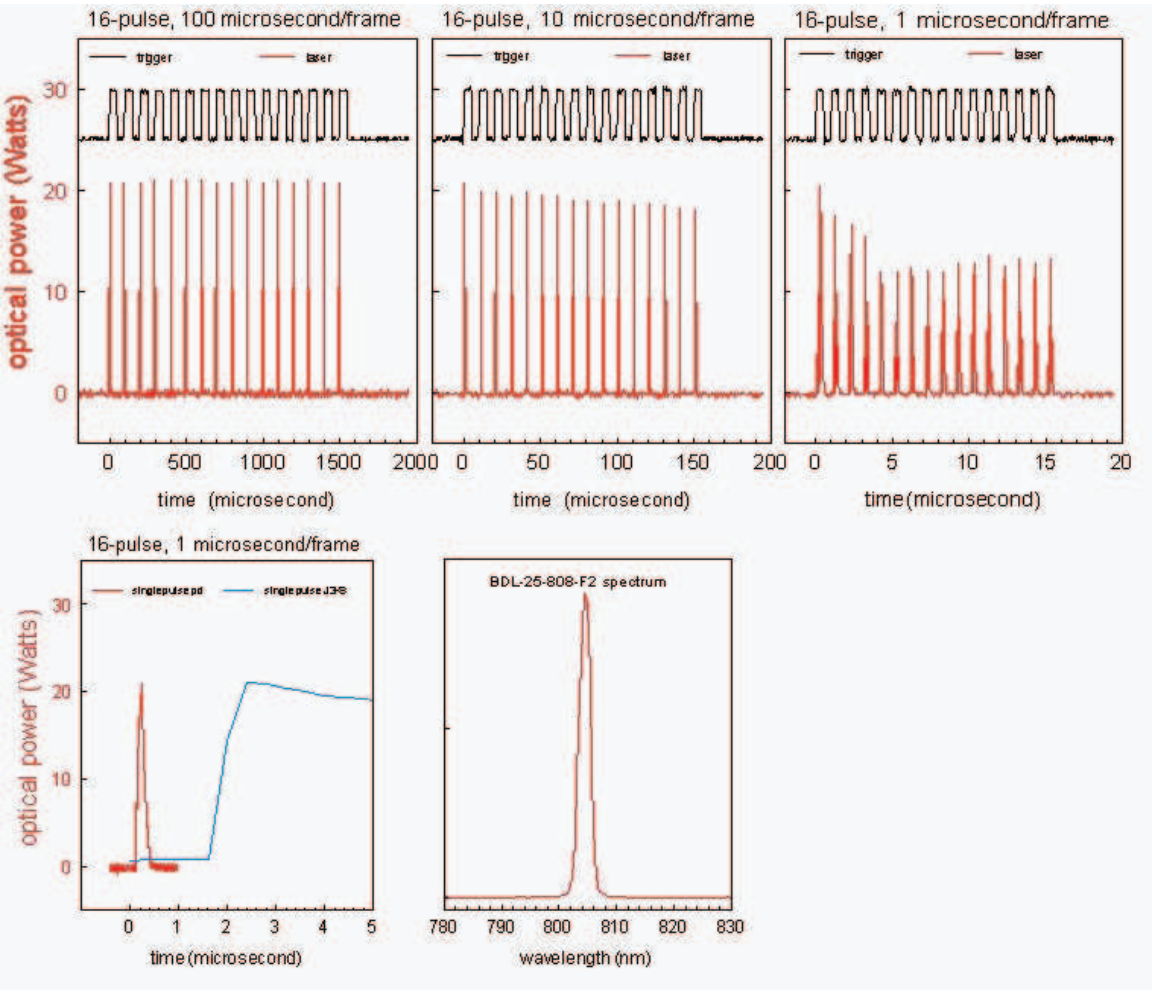

Figure A.1: Measurement of characteristic response of 25 laser used for high speed camera at Viewport 2 (Tsang, 2006).

A.3 Mercury Properties

Table A.2: Properties of mercury.

Property	**Value**	**Unit**
Atomic number	80	-
Atomic mass	200.59	-
Number of protons/electrons	80	-
Number of neutrons	121	-
Classification	Transition metal	-
Melting point	-38.87	°C
Boiling point	356.58	°C
Density	13.456 at 25 °C	g/cm^3
Naturally occurring isotopes	Hg-194 Hg-206	-
Group in periodic table	12	-
Period in periodic table	6	-
Electrical conductivity	1.06×10^6 at 25 °C	$\Omega^{-1}m^{-1}$
Thermal conductivity	8.34	$W\ m^{-1}\ K^{-1}$ at 27 °C
Specific heat	0.139	$J\ g^{-1}\ K^{-1}$
Heat of vaporization	59.229	kJ/mol
Heat of fusion	2.295	kJ/mol
Electrical resistivity	961 at 25 °C	$n\Omega \cdot m$
Speed of sound	1451.4 at 20 °C	m/s
Coefficient of thermal expansion	60×10^{-6} at 20 °C	K^{-1}
Bulk modulus	25	GPa
Dynamic viscosity	1.552	$kg\ m^{-1}\ s^{-1}$
Kinematic viscosity	1.145×10^{-4}	$m^2\ s^{-1}$
Dielectric constant	1.00074	-
Surface tension	485.5 (Hg-Air) at 25 °C	mN/m °C
Magnetic permeability	$4\pi \times 10^{-7}$	H/m

A.4 Beam Program List and Disruption Length Measurements

1. Shot number
2. Number of bunches
3. Number of protons (Tp)
4. Magnetic field (T)
5. Jet velocity (m/s)
6. Disruption length (m)
7. Error ($\pm$ cm)

Table A.3: Measured disruption length and beam shot program.

1	2	3	4	5	6	7
2002	1	0.25	0	0	-	-
2003	1	0.25	0	0	-	-
2004	1	0.25	0	0	-	-
2005	1	0.25	0	0	-	-
2006	1	0.25	0	0	-	-
2007	1	0.25	0	0	-	-
2008	1	0.25	0	0	-	-
2009	1	0.25	0	0	-	-
2011	1	0.25	0	0	-	-
2012	1	0.25	0	0	-	-
2013	1	0.25	0	0	-	-
2014	1	0.25	0	0	-	-
2015	1	0.25	0	0	-	-
2016	1	0.25	0	0	-	-
2017	1	0.25	0	0	-	-
2018	1	0.25	0	0	-	-
2019	1	0.25	0	0	-	-
2020	1	0.25	0	0	-	-
2021	1	0.25	0	0	-	-
2022	1	0.25	0	0	-	-

Continued on Next Page...

Table A.3 – Continued

1	2	3	4	5	6	7
2023	1	0.25	0	0	-	-
2026	1+1	0.50	0	15	0.085	4.0
3003	1+1	0.50	0	0	-	-
3005	1+1	0.50	0	0	-	-
3006	12+4	4.00	0	0	-	-
3007	12+4	4.00	0	0	-	-
3008	12+4	4.00	0	0	-	-
3011	12+4	4.00	0	0	-	-
3012	12+4	4.00	0	0	-	-
3014	1	0.25	0	0	-	-
3015	1	0.25	0	0	-	-
3016	1	0.25	0	15	No image	-
3017	1	0.25	0	15	0	0.0
3018	1	0.25	0	15	0	0.0
3019	1	0.25	0	15	0.013	0.7
3020	1	0.25	0	15	0	0.0
3021	1	0.25	0	15	0.005	0.5
3022	1	0.25	0	15	0.029	2.4
3023	1	0.25	0	15	0	0
3024	1	0.25	0	15	No image	-
3025	1	0.25	5	15	0	0
4001	1	0.25	0	15	0.018	1.5
4002	1	0.25	5	15	0	0
4003	1	0.25	5	15	0	0
4004	1	0.25	5	15	0	0
4005	1	0.25	5	15	0.054	3.4
4006	1	0.25	5	15	0.019	1.6
4007	1	0.25	5	15	0	0
4008	1	0.25	5	15	0	0
4009	1	0.25	5	15	No image	-
4010	1	0.00	5	0	-	-
4011	1	0.30	0	0	-	-
4012	1	0.30	5	0	-	-
4013	1	0.30	0	0	-	-
4014	1	0.30	5	15	0.007	0.7
4015	16	10.00	5	15	0.031	2.5

Continued on Next Page...

Table A.3 – Continued

1	2	3	4	5	6	7
4016	16	10.00	5	0	-	-
4017	16	10.00	0	15	0.038	2.9
4019	16	10.00	0	15	0.062	3.6
4020	2	0.50	0	0	-	-
4021	2	0.50	0	0	-	-
4023	2	0.50	0	0	-	-
4024	2	0.50	0	0	-	-
4025	2	0.50	0	0	-	-
4026	2	0.50	0	0	-	-
4028	16	10.00	0	0	-	-
4030	16	10.00	0	15	0.143	4.5
4031	16	10.00	5	15	0.080	3.9
5003	4	1.00	5	15	0	0
5004	16	10.00	5	15	0.111	4.3
5005	16	10.00	5	15	No image	-
5006	16	10.00	5	15	No image	-
5007	16	10.00	5	15	0.024	2.1
5008	16	10.00	5	15	0.031	2.5
5009	8	5.00	5	15	0.033	2.6
5010	8	5.00	5	15	0.022	1.9
5011	8	5.00	0	15	0.084	4.0
5012	16	10.00	5	15	No image	-
5014	16	15.00	0	15	No image	-
5015	16	15.00	5	15	0.189	4.8
5016	16	15.00	5	15	0.180	4.7
5017	16	20.00	5	15	0.303	5.1
5018	16	20.00	5	15	0.283	5.1
5019	16	20.00	5	15	0.204	4.8
5020	16	20.00	10	15	0.184	4.7
6001	16	4.00	0	15	0	0
6002	16	4.00	0	15	0.027	2.3
6003	16	10.00	5	15	0.105	4.2
6004	16	10.00	5	15	0.105	4.2
6005	16	10.00	5	15	0.035	2.7
6006	16	10.00	5	15	0.173	4.7
6007	16	10.00	5	15	0.028	2.3

Continued on Next Page...

Table A.3 – Continued

1	2	3	4	5	6	7
6008	16	10.00	5	15	0.052	3.3
6009	16	10.00	5	15	0.079	3.9
6010	16	10.00	5	15	0.074	3.8
6011	16	10.00	5	0	-	-
6012	1	0.25	0	0	-	-
6013	1	0.25	0	0	-	-
6014	1	0.25	0	0	-	-
6015	1	0.25	0	0	-	-
6016	1	0.30	0	0	-	-
6017	1	0.30	0	0	-	-
6018	1	0.30	0	0	-	-
6019	1	0.30	0	0	-	-
6020	1	0.30	0	0	-	-
6021	1	0.30	0	0	-	-
6022	1	0.30	0	0	-	-
6023	1	0.30	0	0	-	-
6024	16	4.00	0	0	-	-
6025	16	4.00	0	0	0.092	4.1
6026	16	4.00	0	15	0.101	4.2
6027	16	4.00	0	15	0.095	4.1
6028	16	4.00	5	15	0.005	0.5
6029	16	4.00	5	15	0.038	2.9
6030	16	4.00	10	15	0.044	3.1
6031	16	4.00	10	15	0.058	3.5
7001	16	4.00	0	0	-	-
7002	16	4.00	5	0	-	-
7003	16	4.00	10	0	-	-
7004	16	4.00	0	15	0.019	1.5
7005	16	4.00	0	15	0.036	2.8
7006	16	4.00	10	15	0.014	0.8
7008	16	4.00	0	0	-	-
7009	16	4.00	0	0	-	-
7010	16	4.00	0	0	-	-
7011	16	4.00	0	0	-	-
7012	16	4.00	0	0	-	-
7013	16	4.00	0	0	-	-

Continued on Next Page...

Table A.3 – Continued

1	2	3	4	5	6	7
7014	16	4.00	0	0	-	-
7015	16	4.00	0	0	-	-
7016	16	4.00	10	15	0	0
7017	16	4.00	10	0	-	-
7021	16	4.00	0	0	-	-
7022	16	4.00	0	0	-	-
7023	16	4.00	10	15	0.082	3.9
7024	16	4.00	10	0	-	-
7025	16	4.00	10	0	-	-
8001	16	4.00	0	0	-	-
8002	16	4.00	0	15	0.016	1.1
8003	16	4.00	0	15	0.024	2.1
8004	16	4.00	0	0	-	-
8005	16	4.00	0	15	0.051	3.3
8006	16	4.00	0	0	-	-
8007	16	4.00	0	15	0.147	4.6
8008	16	4.00	0	0	-	-
8009	16	4.00	0	15	0.132	4.5
8010	16	4.00	0	15	0.419	5.3
8011	16	4.00	0	0	-	-
8012	16	4.00	0	15	0.041	3.0
8013	16	4.00	0	0	-	-
8014	16	4.00	0	15	0.107	4.2
8015	16	4.00	0	0	-	-
8016	16	4.00	5	15	0	0.0
8017	16	4.00	5	0	-	-
8018	16	4.00	5	15	0.027	2.2
8019	16	4.00	5	0	-	-
8020		0.00	5	15	0	0
8021	16	4.00	5	15	0	0
8022	16	4.00	5	0	-	-
8029	16	4.00	7	15	No image	-
8030	16	4.00	7	15	0	0
8031	16	4.00	7	0	-	-
8032	16	4.00	7	15	0	0
8033	16	4.00	7	0	-	-

Continued on Next Page...

Table A.3 – Continued

1	2	3	4	5	6	7
8034	12+4	15+5	7	15	0.208	4.8
8035	12+4	15+5	7	15	0.152	4.6
8036	12+4	15+5	0	0	-	-
8037	12+4	15+5	7	15	0.160	4.6
8038	0	0.00	7	0	-	-
8039	-	-	0	0	-	-
8040	-	-	0	0	-	-
8041	12+4	15+5	7	15	0.203	4.8
8042	12+4	15+5	7	0	-	-
8043	12+4	15+5	7	0	-	-
8044	12+4	15+5	7	15	0.253	5.0
8045	12+4	15+5	7	15	0.165	4.7
8046	12+4	15+5	0	0	-	-
8047	12+4	15+5	7	0	-	-
9003	1	0.25	5	15	0	0
9004	16	4.00	5	15	0.064	3.6
9005	16	4.00	5	15	0.082	3.9
9006	16	4.00	5	15	0.215	4.9
9008	16	4.00	5	15	0.080	3.9
9009	12	3.00	5	15	0.108	4.2
9010	8	2.00	5	15	0	0
9011	-	-	-	-	0.068	3.7
9012	10	2.50	5	15	0.040	2.9
9013	-	-	-	-	0.040	3.0
9014	12	3.00	5	15	0.078	3.9
9015	16	6.00	7	15	0.162	4.6
9016	16	4.00	7	15	0.109	4.3
9017	12	3.32	7	15	0.005	0.5
9018	12	3.64	7	15	0	0
9019	12	3.78	7	15	0.040	3.0
9020	12	5.10	10	15	0.079	3.9
10001	16	4.00	0	0	No image	-
10002	16	4.00	0	0	No image	-
10003	16	4.00	0	15	0.188	4.8
10004	16	4.00	5	15	0.202	4.8
10005	16	4.00	5	15	0.128	4.4

Continued on Next Page...

Table A.3 – Continued

1	2	3	4	5	6	7
10006	18	4.00	10	15	0.038	2.9
10007	16	10.00	5	15	0.258	5.0
10008	16	15.00	5	15	0.291	5.1
10009	4	6.00	5	15	0.154	4.6
10010	2+2	6.00	5	15	0.184	4.7
10011	2+2	6.00	5	15	0.294	5.1
10012	4	6.00	5	15	0.228	4.9
10013	4	6.00	5	15	0.182	4.7
10014	4	6.00	5	0	-	-
10015	2+2	6.00	5	15	No image	-
10016	8	6.00	5	15	0.155	4.6
10017	8	6.00	5	0	-	-
10018	4+4	6.00	5	15	0.250	5.0
10019	4+4	6.00	5	0	-	-
11001	4	1.0	0	15	0.029	2.4
11002	16	6.0	5	15	0.202	4.8
11004	4	6.0	5	15	0.260	5.0
11005	4	6.0	5	15	0.246	5.0
11006	4	6.0	5	15	0.239	5.0
11007	4	6.0	5	15	0.174	4.7
11008	4	6.0	5	15	0.122	4.4
11010	4	6.0	5	15	0.194	4.8
11019	16	10.0	10	15	0.167	4.7
11020	16	3.5	10	15	0	0
11021	16	3.8	10	15	0.062	3.6
11022	16	15.0	10	15	0.158	4.6
11032	16	20.0	10	15	0.218	4.9
11033	16	30.0	10	15	0.214	4.9
11034	16	30.0	15	15	0.164	4.7
12001	4	5.0	0	15	0.201	4.8
12003	4	5.0	0	15	0.238	5.0
12004	4	5.0	0	15	0.273	5.1
12005	4	5.0	0	15	0.245	5.0
12007	-	-	0	15	0.039	2.9
12006	4	4.0	0	15	0.149	4.6
12008	4	4.0	0	15	0.252	5.0

Continued on Next Page...

Table A.3 – Continued

1	2	3	4	5	6	7
12009	4	4.0	5	0	-	-
12010	4	4.0	5	15	0.103	4.2
12011	4	4.0	5	15	0.079	3.9
12012	4	4.0	5	15	0	0
12013	4	4.0	5	0	-	-
12014	4	4.0	0	0	-	-
12015	4	4.0	5	15	0.105	4.2
12016	4	4.0	5	0	-	-
12029	8	15.0	15	15	0.046	3.2
12031	8	10.0	0	15	0.368	5.3
12032	8	10.0	15	15	0.149	4.6
12033	16	30.0	15	20	0.170	4.7
13001	2	2.5	0	15	0.042	3.0
13002	4	5.0	0	15	0.129	4.4
13003	4	5.0	0	15	0.138	4.5
13004	4	8.0	0	15	0.156	4.6
13007	6+2	16.0	5	15	0.157	4.6
13008	6+2	16.0	5	15	0.202	4.8
13009	6+2	16.0	5	15	0.196	4.8
13010	6+2	16.0	5	15	0.157	4.6
13011	6+2	16.0	5	15	0.170	4.7
13012	6+2	16.0	5	0	-	-
13013	6+2	16.0	5	15	0.221	4.9
13014	6+2	16.0	5	0	-	-
13015	6+2	16.0	5	15	0.167	4.7
13016	6+2	16.0	5	0	-	-
14008	6	6.0	5	15	0.061	3.6
14009	6	6.0	5	15	0.103	4.2
14010	6	6.0	5	15	0	0
14011	6	10.0	5	15	0.174	4.7
14012	6	10.0	5	0	-	-
14013	6	10.0	5	0	-	-
14014	6	10.0	5	15	0.151	4.6
14015	6	10.0	5	15	0.261	5.0
14017	6+2	16.0	5	15	0.290	5.1
14018	6+2	16.0	5	15	0.239	5.0

Continued on Next Page...

Table A.3 – Continued

1	2	3	4	5	6	7
14019	6+2	0.0	5	15	0.127	4.4
14020	6+2	16.0	5	0	-	-
14021	6+2	16.0	5	0	-	-
14022	6+2	16.0	5	15	0.233	4.9
14023	6+2	16.0	5	0	-	-
14024	6+2	16.0	5	15	0.119	4.3
14025	6+2	16.0	5	0	-	-
14026	6+2	16.0	5	15	0.215	4.9
14027	6+2	16.0	0	0	-	-
14028	6+2	16.0	5	15	0.186	4.8
14029	6+2	16.0	5	15	0.283	5.1
14030	6+2	16.0	5	0	-	-
14031	6+2	16.0	5	15	0.138	4.5
14032	6+2	16.0	5	0	-	-
14033	6+2	16.0	5	15	0.189	4.8
14034	6+2	16.0	5	15	0.383	5.3
14035	6+2	16.0	5	0	-	-
14036	6+2	4.0	5	15	0.032	2.6
14037	8	4.0	5	15	0	0
15001	8	4.0	5	15	0.014	0.8
15002	6+2	16.0	5	15	0.228	4.9
15003	6+2	16.0	5	15	0.117	4.3
15004	6+2	16.0	5	15	0.259	5.0
15005	6+2	16.0	5	0	-	-
15006	6+2	16.0	5	15	0.245	5.0
15007	6+2	16.0	5	0	-	-
15008	6+2	16.0	5	15	0.200	4.8
15009	6+2	16.0	5	0	-	-
15010	6+2	16.0	5	15	0.103	4.2
15011	6+2	16.0	5	15	0.188	4.8
15012	6+2	16.0	5	15	0.260	5.0
15013	6+2	16.0	5	0	-	-
15014	6+2	16.0	5	15	0.195	4.8
15015	6+2	16.0	5	0	-	-
15016	6+2	16.0	5	15	0.173	4.7
15017	6+2	16.0	5	0	-	-

Continued on Next Page...

Table A.3 – Continued

1	2	3	4	5	6	7
15018	6+2	16.0	5	15	0.157	4.6
15019	6+2	16.0	5	15	0.132	4.4
15020	8	16.0	5	15	0.341	5.2
15021	8	16.0	5	15	0.165	4.7
15022	8	16.0	5	15	0.236	4.9
15023	8	16.0	5	15	0.260	5.0
15024	8	16.0	5	0	-	-
15025	8	16.0	5	15	0.175	4.7
15026	8	16.0	5	0	-	-
15027	8	16.0	5	15	0.313	5.2
15028	8	16.0	5	15	-	-
15029	8	6.0	5	15	0.066	3.7
15030	8	6.0	5	0	-	-
15031	8	6.0	5	15	0.068	3.7
15032	8	6.0	5	0	-	-
15033	8	6.0	5	15	0.026	2.2
15034	8	6.0	5	0	-	-
15035	8	6.0	5	15	0.021	1.8
15036	8	6.0	5	0	-	-
15037	8	6.0	5	15	0.115	4.3
15038	8	10.0	5	15	0.080	3.9
15039	8	8.0	5	15	0.053	3.4
15040	8	8.0	5	15	0.054	3.4
15041	8	6.0	5	15	0.008	0.8
15042	8	6.0	5	15	0.007	0.7
15043	16	6.0	5	15	0.027	2.3
15044	4	12.0	5	15	0.043	3.1
15045	4	12.0	5	15	0.027	2.3
16001	4	2.0	0	15	0.082	3.9
16002	4	10.0	4.1	15	0.068	3.7
16003	4	12.0	4.1	15	0.205	4.8
16004	4	14.0	6	15	0.222	4.9
16005	8	12.0	5	15	0.136	4.5
16006	8	12.0	5	15	0.208	4.9
16007	8	12.0	5	15	0.189	4.8
16008	4+4	6+6	5	15	0.212	4.9

Continued on Next Page...

Table A.3 – Continued

1	2	3	4	5	6	7
16009	4+4	6+6	5	15	0.071	3.8
16010	4+4	6+6	5	15	0.164	4.7
16011	4+4	6+6	5	15	0.215	4.9
16012	4	14.0	5	15	0.229	4.9
16013	4	14.0	10	15	0.188	4.8
16014	4	12.0	10	15	0.172	4.7
16015	4	12.0	15	15	0.144	4.5
16016	4	10.0	5	15	0.131	4.4
17001	16	6.0	5	15	0.015	1.0
17002	16	8.0	5	15	0.125	4.4
17003	16	6.0	5	15	0.037	2.8
17004	16	6.3	5	15	0.048	3.2
17005	16	6.0	5	15	0.013	0.7
17006	16	6.0	7	15	0.093	4.1
17007	16	4.2	7	15	0	0
17008	16	8.0	7	15	0.101	4.2
17009	8+8	8.0	7	15	0.074	3.8
17010	8+8	8.0	7	15	0.062	3.6
17011	8+8	8.0	7	15	0.155	4.6
17012	8+8	8.0	7	15	-	-
17013	8+8	8.0	7	15	0.047	3.2
17014	8+8	8.0	7	15	0	0
17015	8+8	7.5	7	15	0.016	1.2
17016	8+8	7.4	7	15	0.086	4.0
17017	8+8	8.4	7	15	0.111	4.3
17018	8+8	6.0	7	15	0.057	3.5
17019	8+0	4.0	7	15	0.007	0.7
17020	8+0	6.0	7	15	0.059	3.5
17021	16	15.0	10	15	0.174	4.7
17022	16	15.0	15	15	0.148	4.6
17023	16	29.0	15	15	0.180	4.7
17024	16	29.0	10	20	0.230	4.9

3405

Appendix B

Image Data for Chapter 6

B.1 Images for filament velocity measurement at Viewport 2

1. Shot number
2. Camera frame rate (μ s)
3. Beam energy (GeV)
4. Number of bunches
5. Number of protons (Tp)
6. Magnetic field (T)
7. Jet velocity (m/s)
8. Lag time between peak laser emittance and proton beam arrival (μ s)

Table B.1: Properties of shots used for filaments velocity analysis.

1	2	3	4	5	6	7	8
11004	25	24	4	6	5	15	-4.03
11007	25	24	4	6	5	15	-3.97
11010	25	24	4	6	5	15	-3.99
11019	25	24	16	10	10	15	-2.43
11021	25	24	16	3.8	10	15	-2.43
11032	25	24	16	20	10	15	-2.03
12031	25	24	8	10	0	15	-1.93
12032	25	24	8	10	15	15	-1.83
12033	25	24	16	30	15	20	-1.85

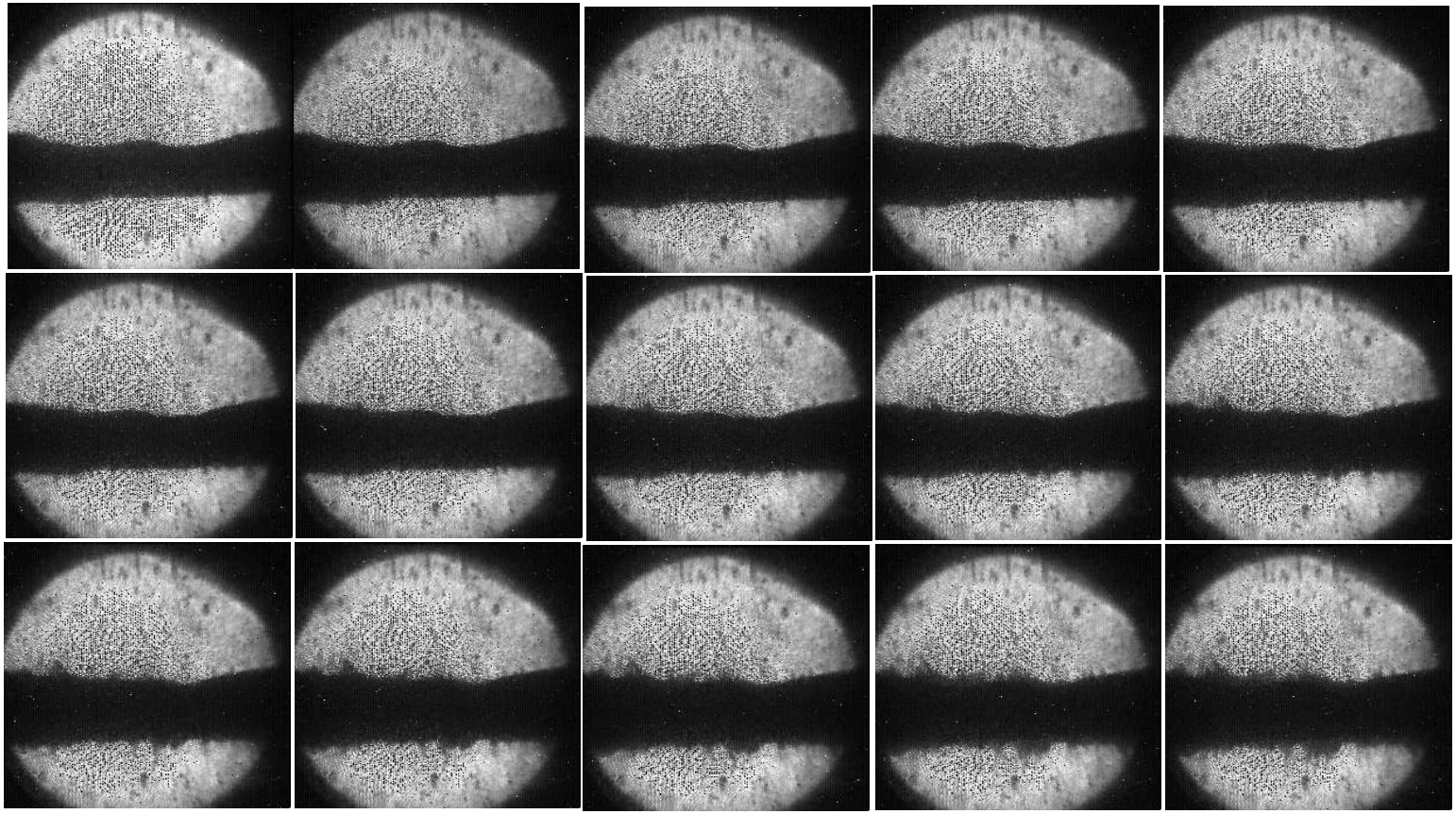

Figure B.1: Photo of continuous 15 frames of captured image. The timing for the 1^{st} image is given in Table B.1. Shot number is 11004.

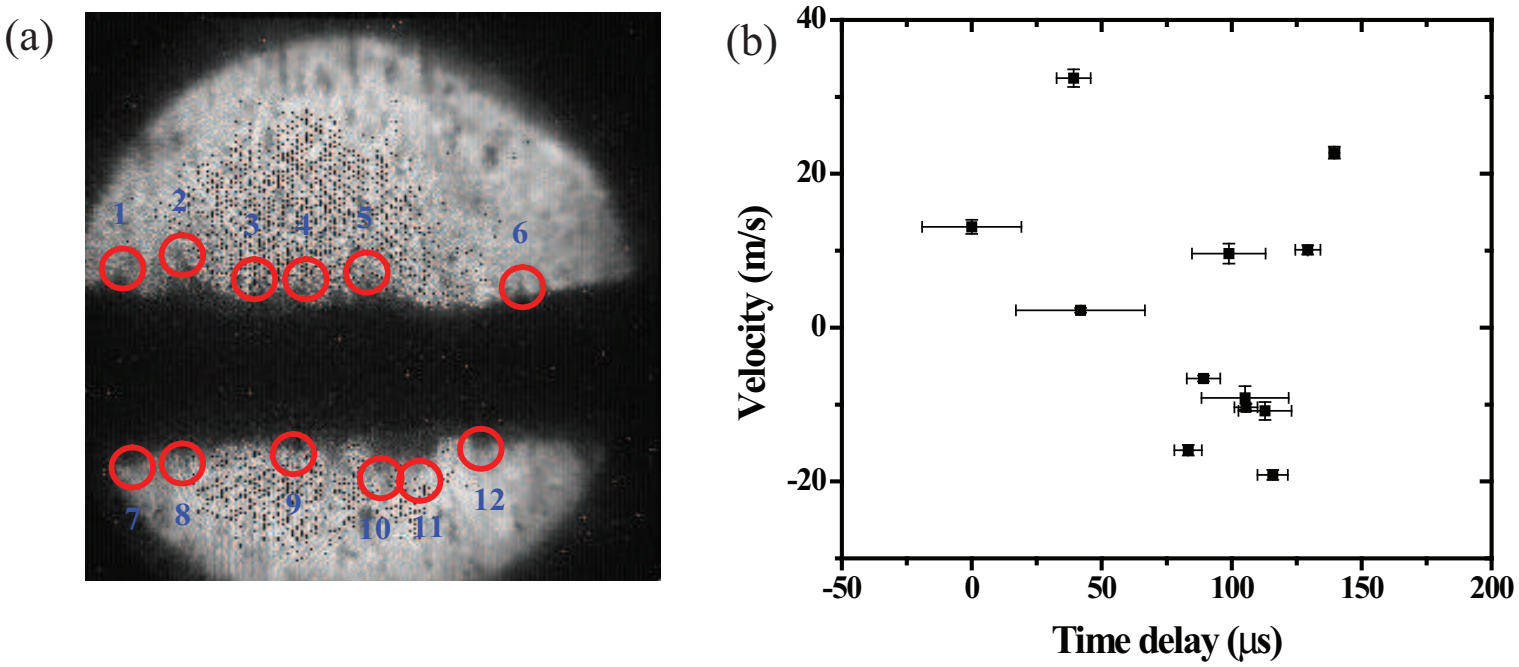

Figure B.2: Location on the Hg jet surface for velocity measurement of filaments. The numbers above red circles points the number of filaments that is used for velocity approximation. Shot number is 11004. a.) Illustration of measured filaments. b.) Velocity of filaments with it's onset time.

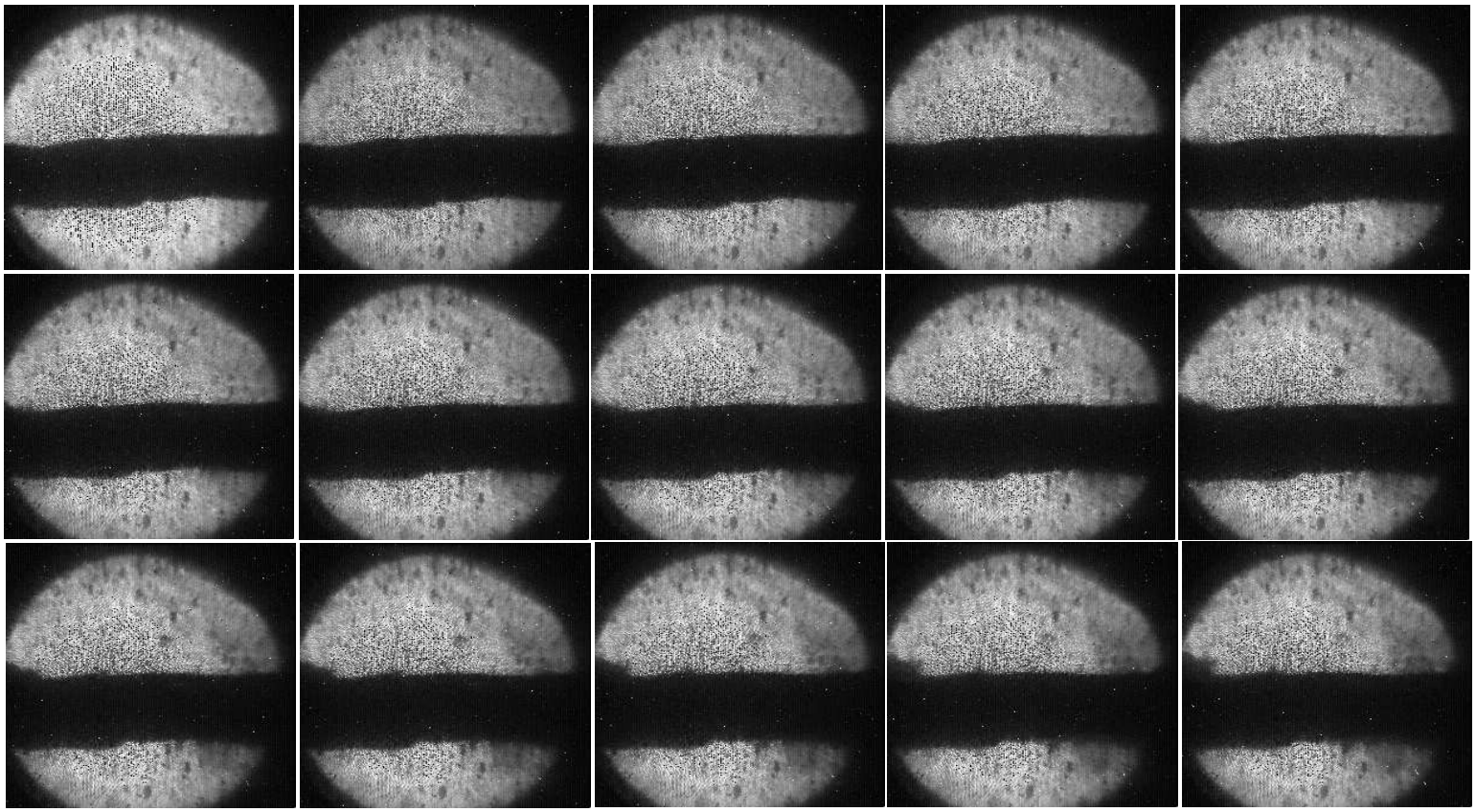

Figure B.3: Photo of continuous 15 frames of captured image. The timing for the 1^{st} image is given in Table B.1. Shot number is 11007.

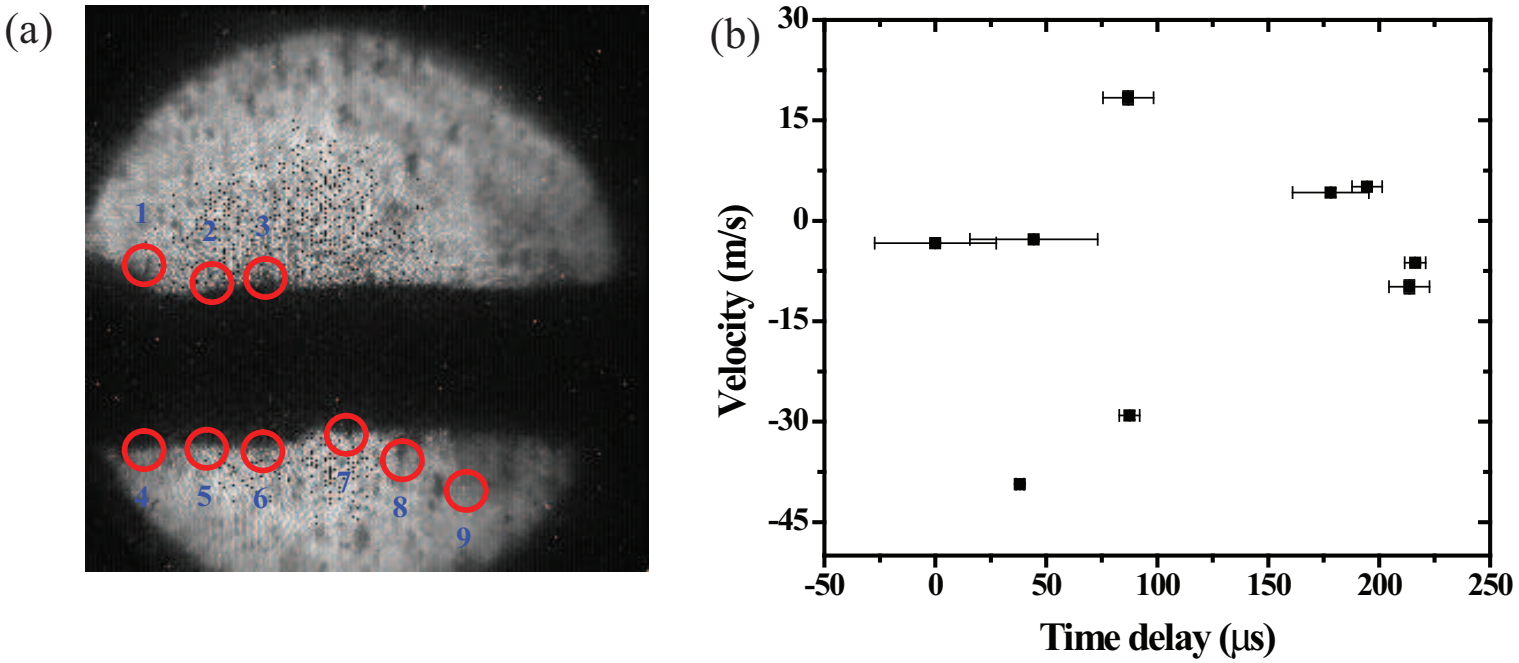

Figure B.4: Location on the Hg jet surface for velocity measurement of filaments. The numbers above red circles points the number of filaments that is used for velocity approximation. Shot number is 11007. a.) Illustration of measured filaments. b.) Velocity of filaments with it's onset time.

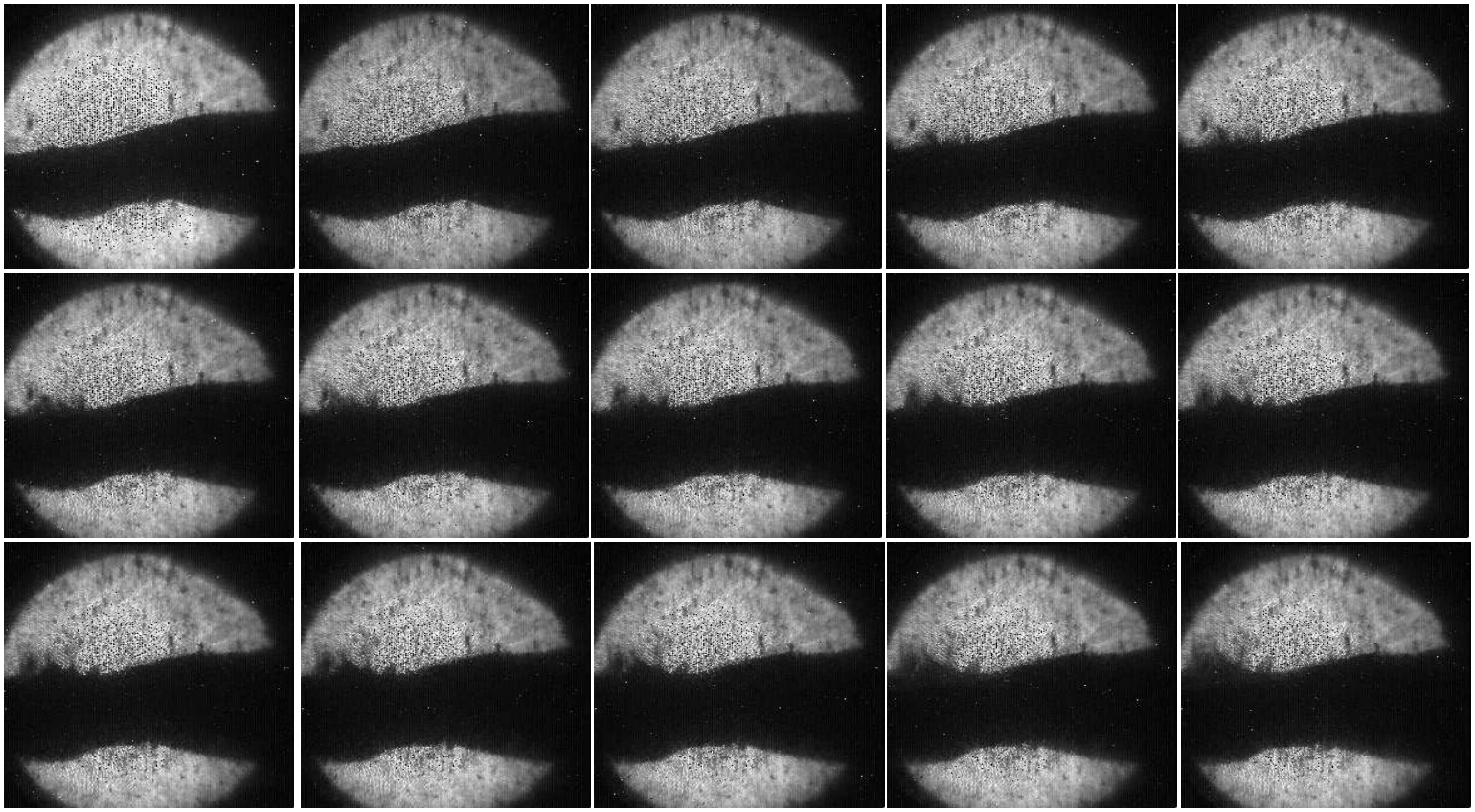

Figure B.5: Photo of continuous 15 frames of captured image. The timing for the 1^{st} image is given in Table B.1. Shot number is 11010.

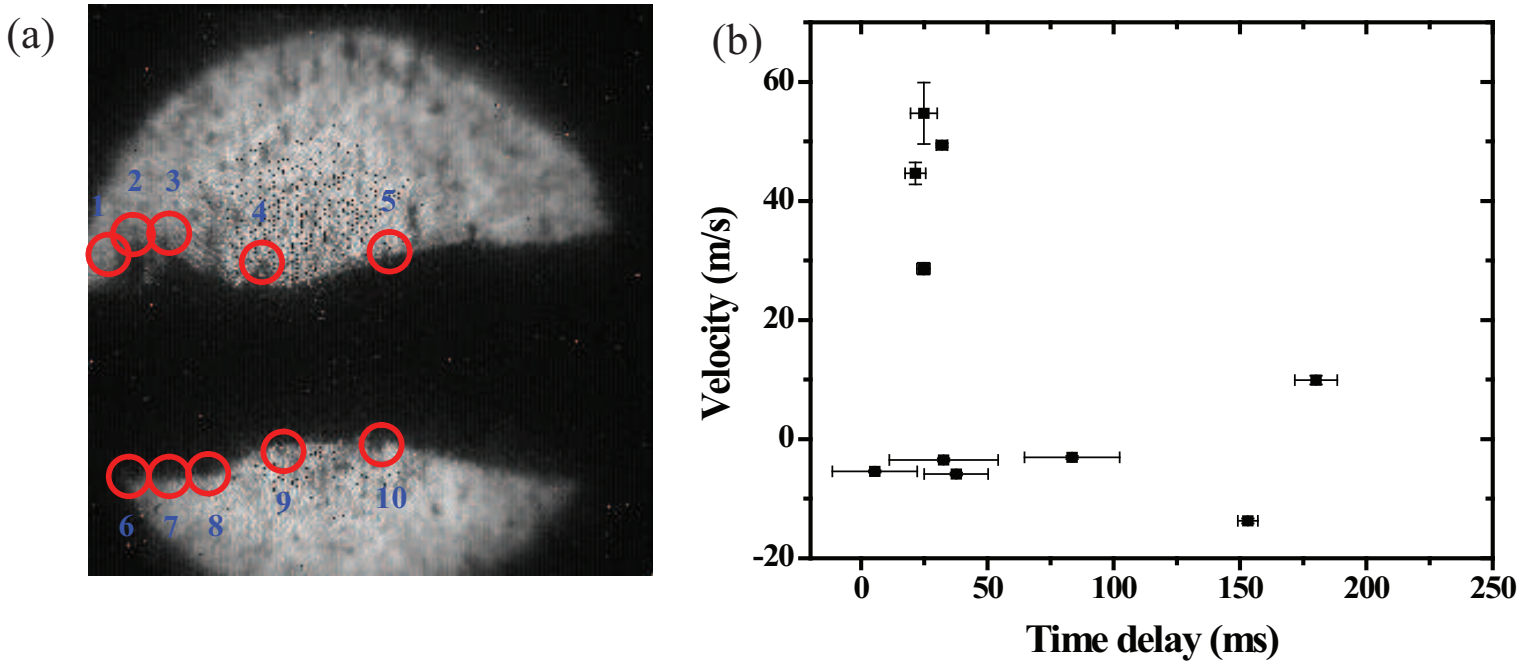

Figure B.6: Location on the Hg jet surface for velocity measurement of filaments. The numbers above red circles points the number of filaments that is used for velocity approximation. Shot number is 11010. a.) Illustration of measured filaments. b.) Velocity of filaments with it's onset time.

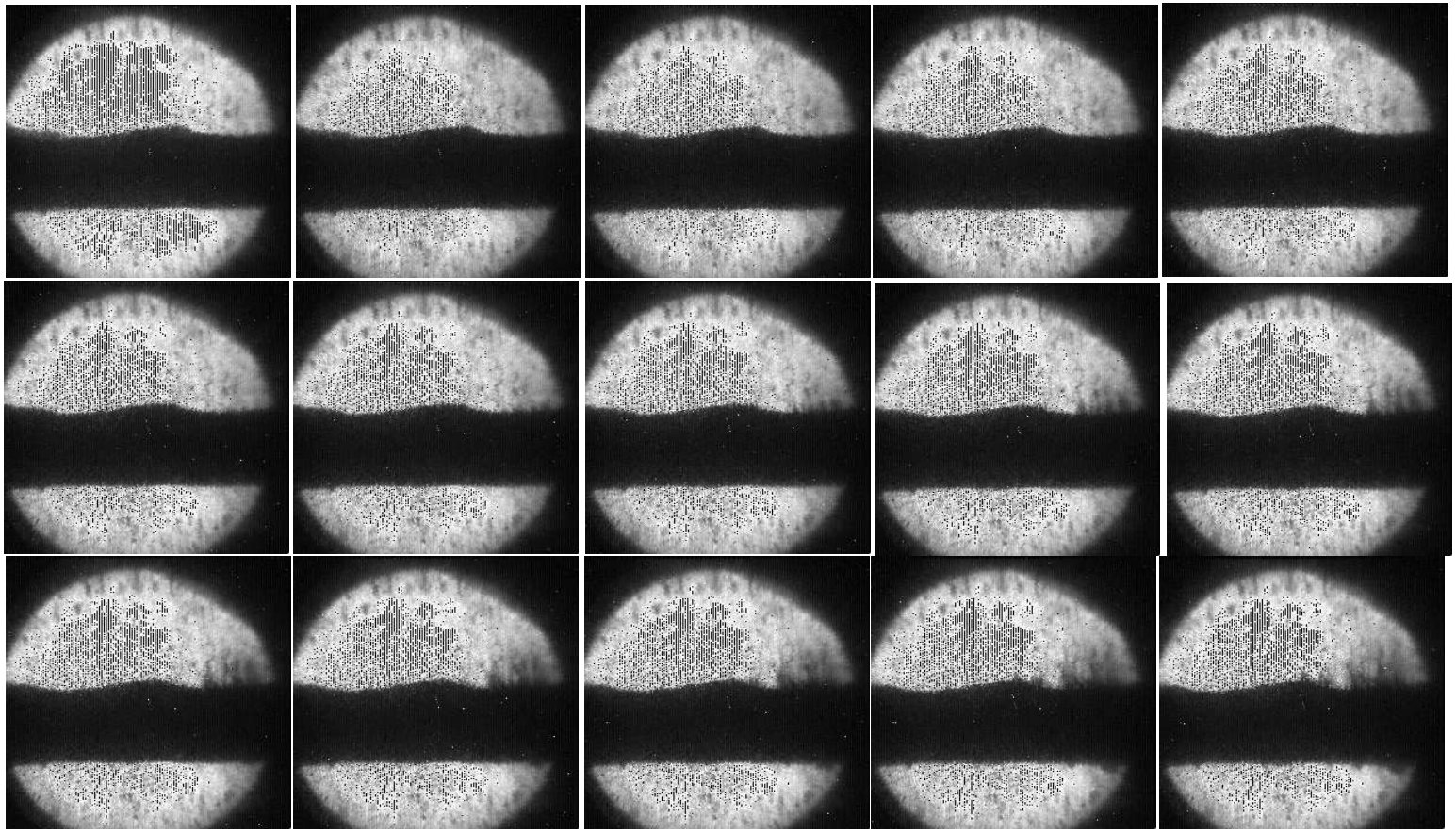

Figure B.7: Photo of continuous 15 frames of captured image. The timing for the 1^{st} image is given in Table B.1. Shot number is 11021.

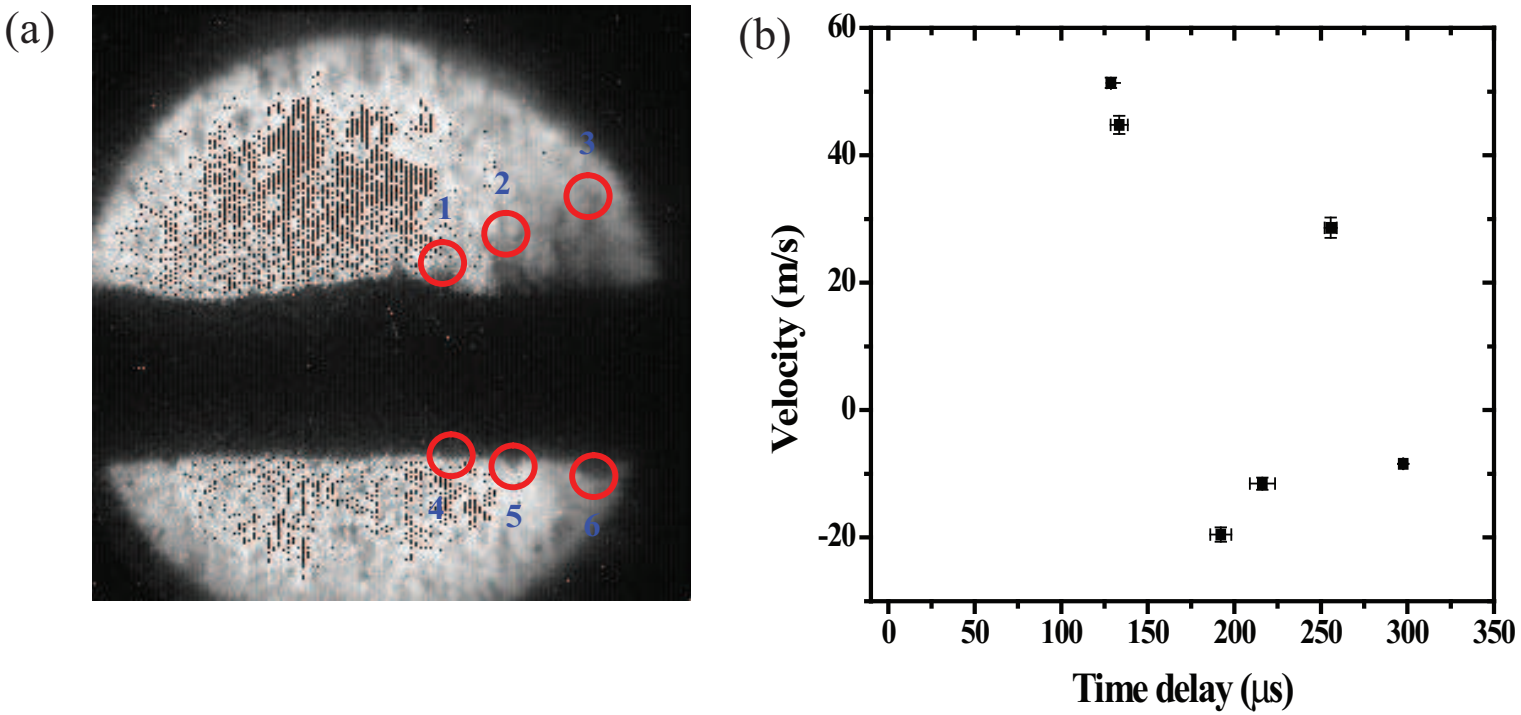

Figure B.8: Location on the Hg jet surface for velocity measurement of filaments. The numbers above red circles points the number of filaments that is used for velocity approximation. Shot number is 11021. a.) Illustration of measured filaments. b.) Velocity of filaments with it's onset time.

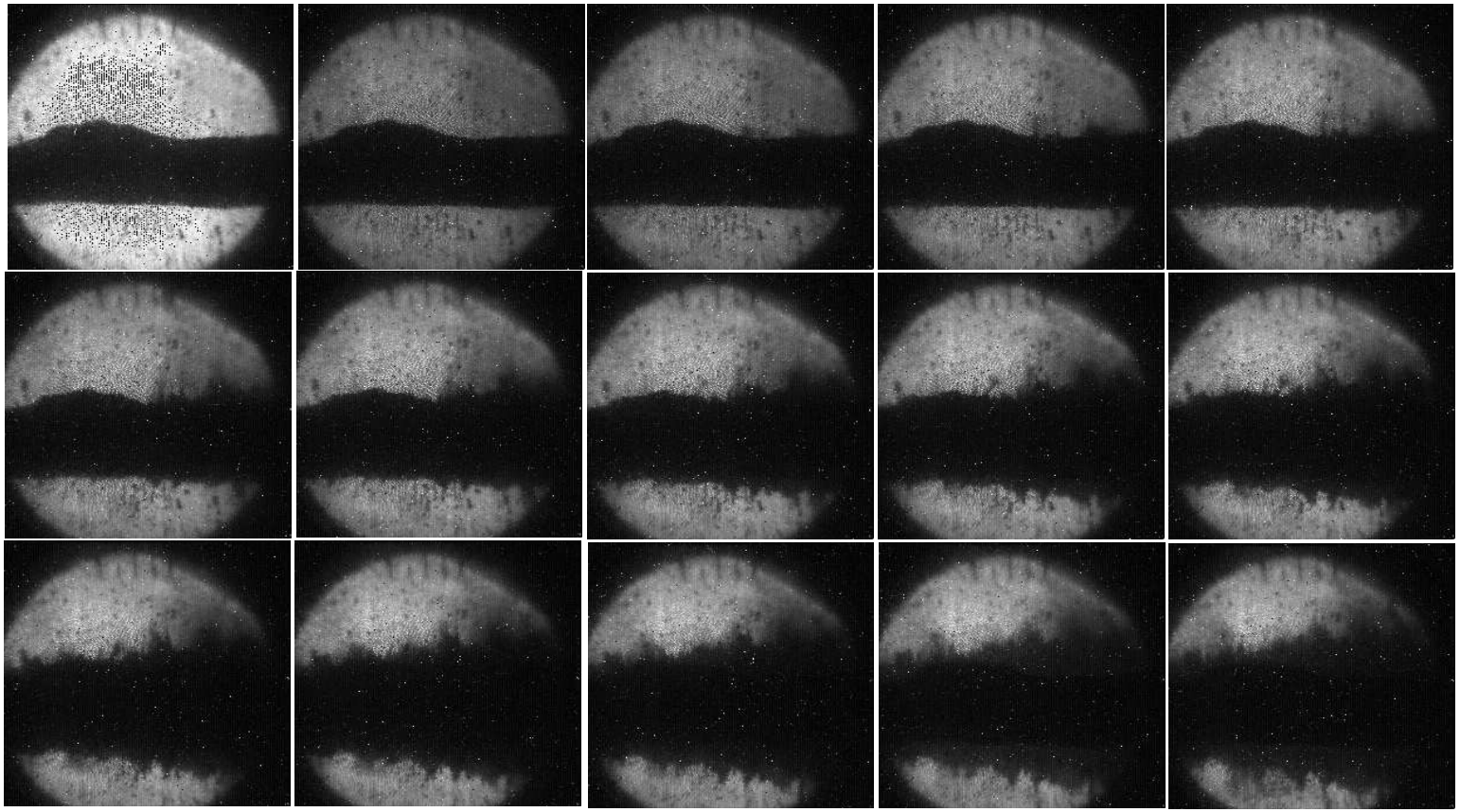

Figure B.9: Photo of continuous 15 frames of captured image. The timing for the 1^{st} image is given in Table B.1. Shot number is 11032.

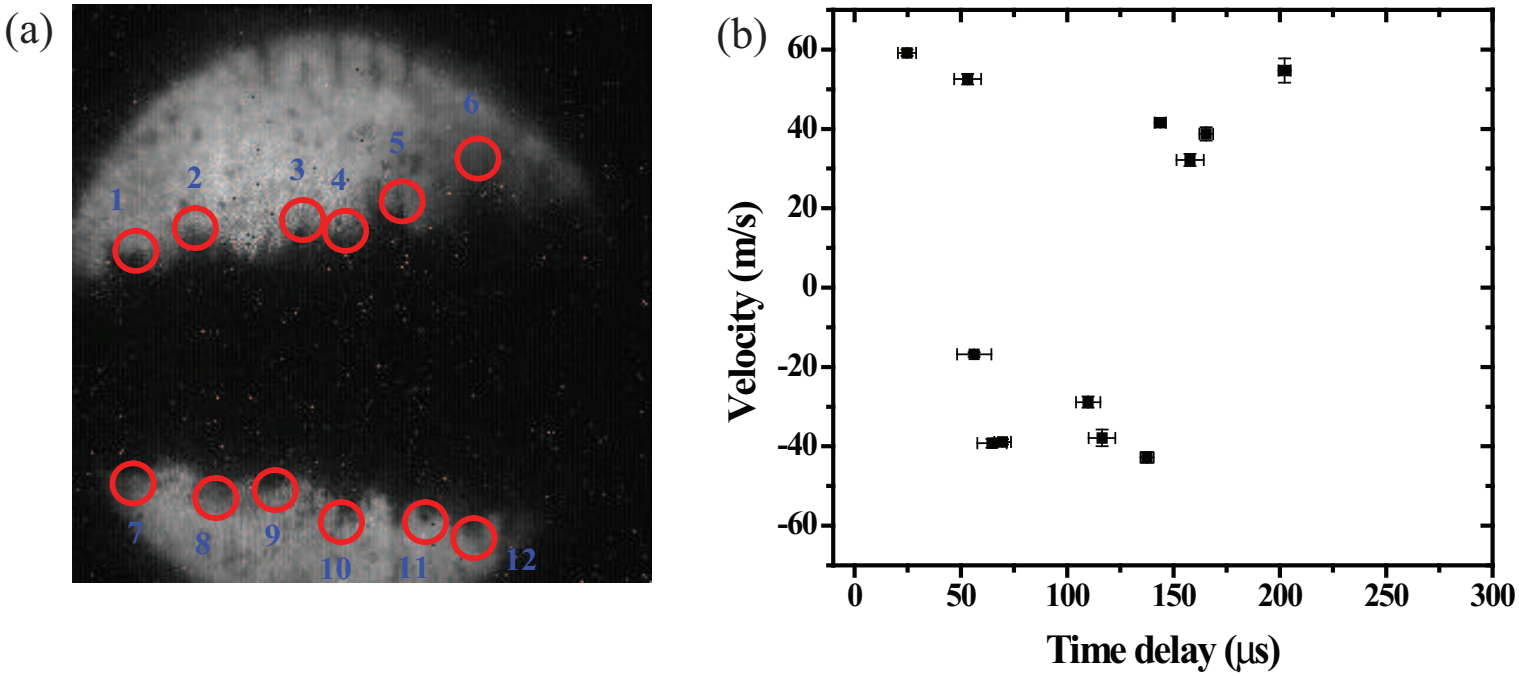

Figure B.10: Location on the Hg jet surface for velocity measurement of filaments. The numbers above red circles points the number of filaments that is used for velocity approximation. Shot number is 11032. a.) Illustration of measured filaments. b.) Velocity of filaments with it's onset time.

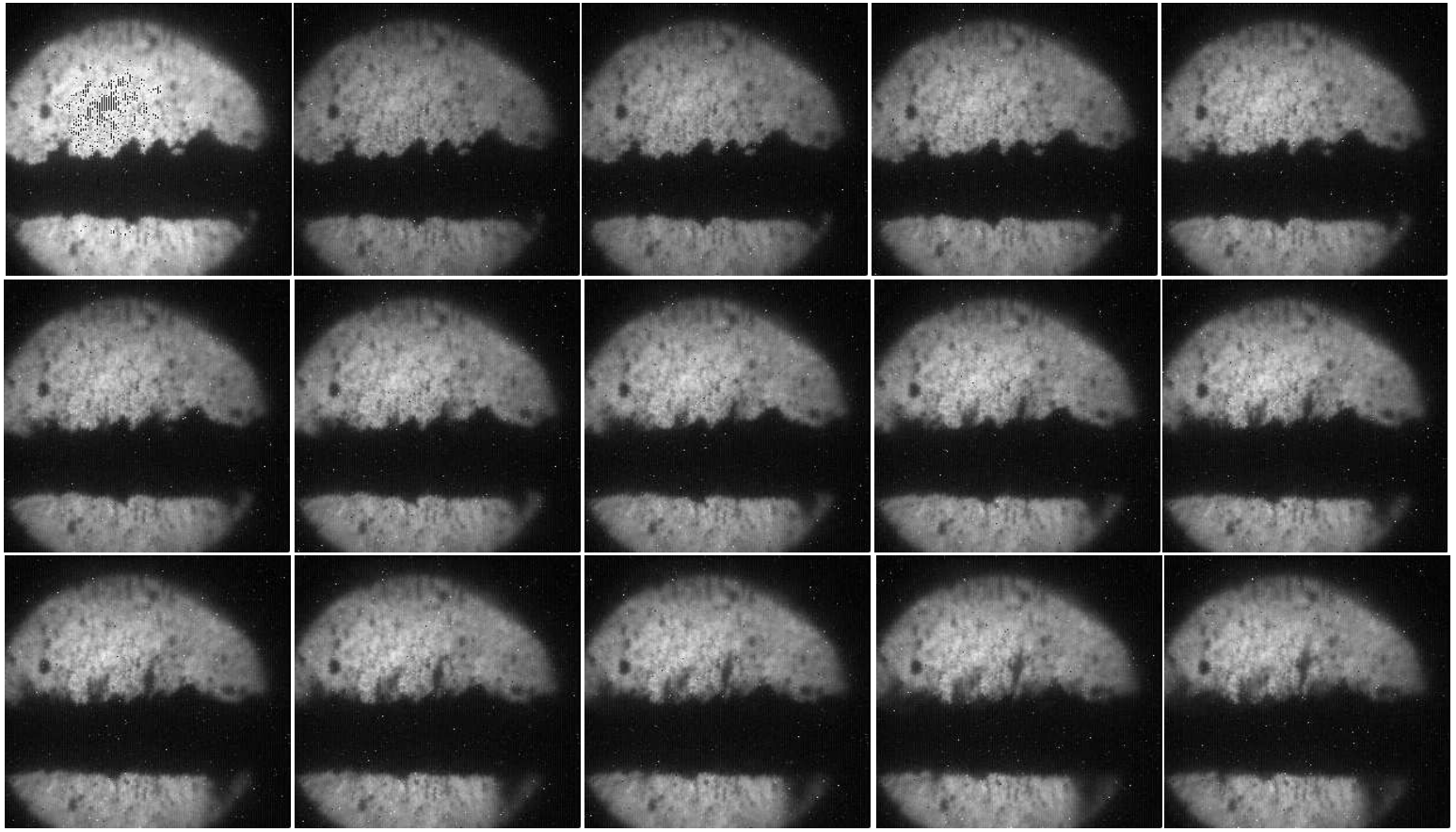

Figure B.11: Photo of continuous 15 frames of captured image. The timing for the 1^{st} image is given in Table B.1. Shot number is 12031.

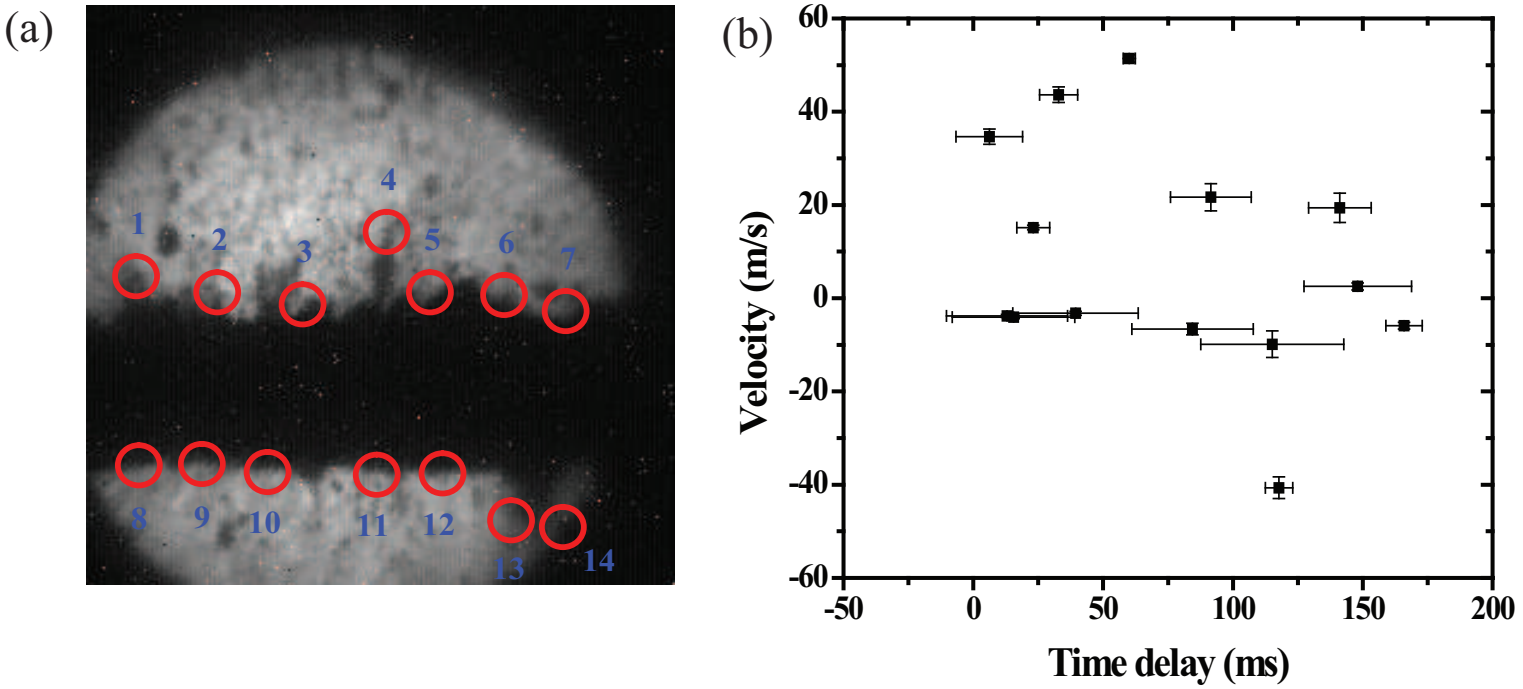

Figure B.12: Location on the Hg jet surface for velocity measurement of filaments. The numbers above red circles points the number of filaments that is used for velocity approximation. Shot number is 12031. a.) Illustration of measured filaments. b.) Velocity of filaments with it's onset time.

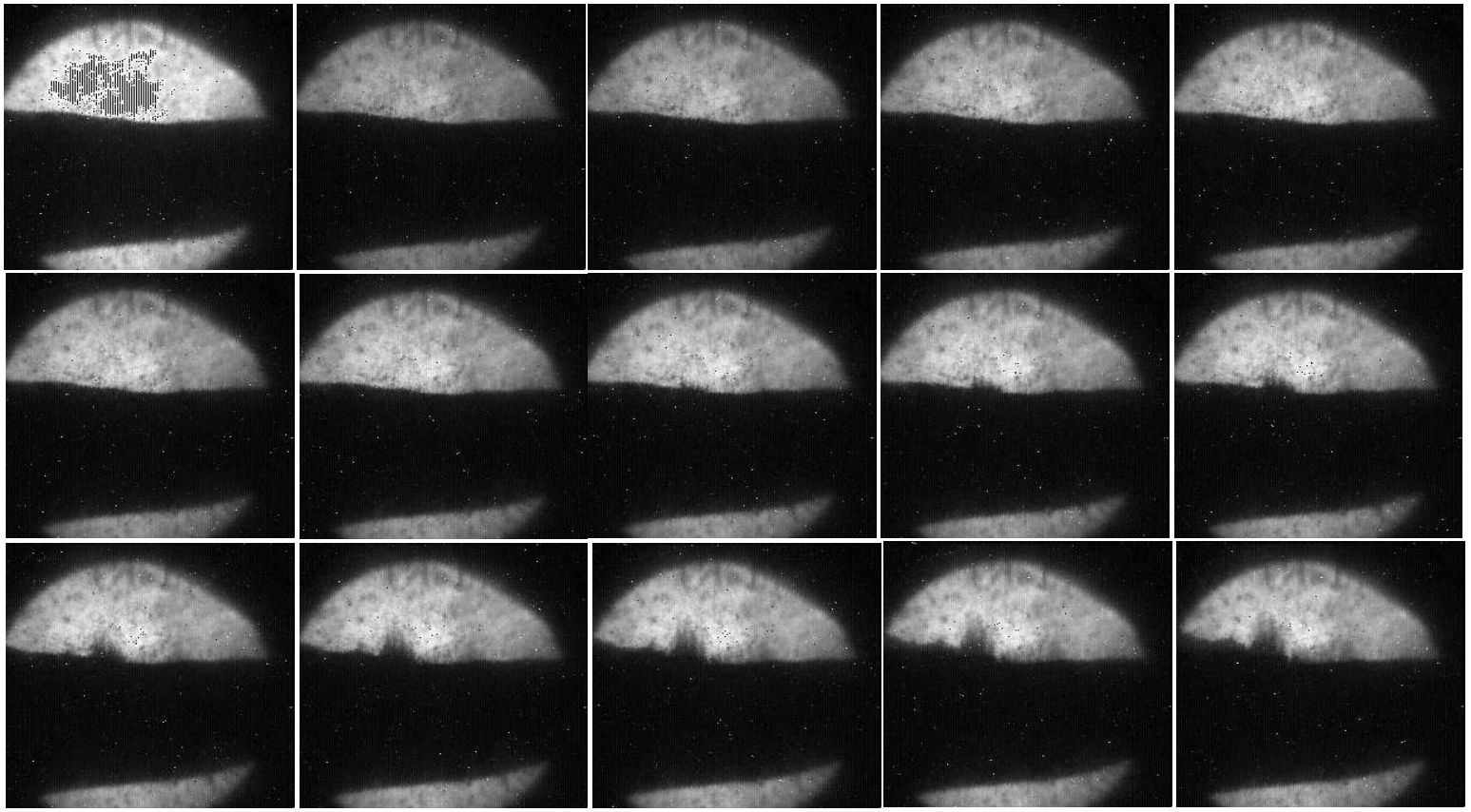

Figure B.13: Photo of continuous 15 frames of captured image. The timing for the 1^{st} image is given in Table B.1. Shot number is 12032.

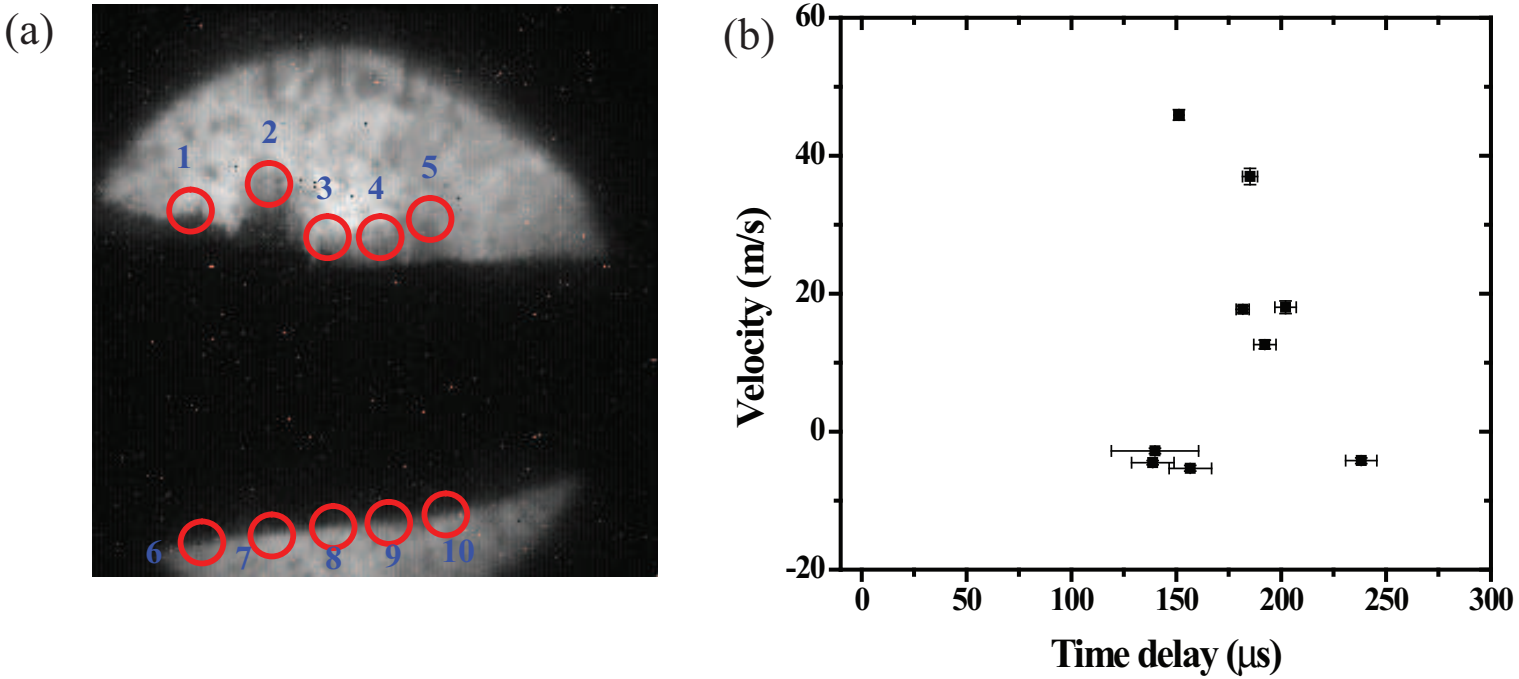

Figure B.14: Location on the Hg jet surface for velocity measurement of filaments. The numbers above red circles points the number of filaments that is used for velocity approximation. Shot number is 12032. a.) Illustration of measured filaments. b.) Velocity of filaments with it's onset time.

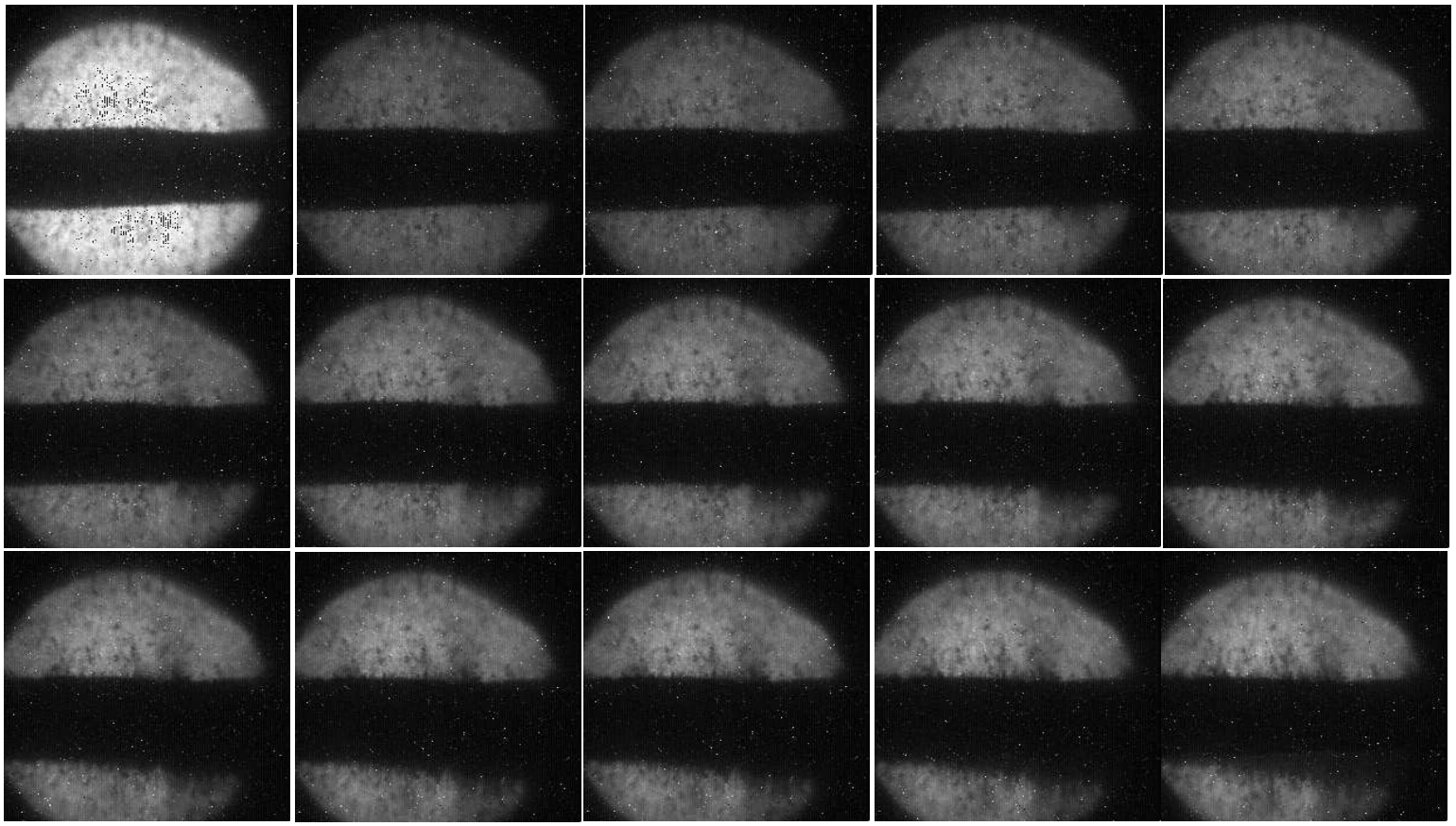

Figure B.15: Photo of continuous 15 frames of captured image. The timing for the 1^{st} image is given in Table B.1. Shot number is 12033.

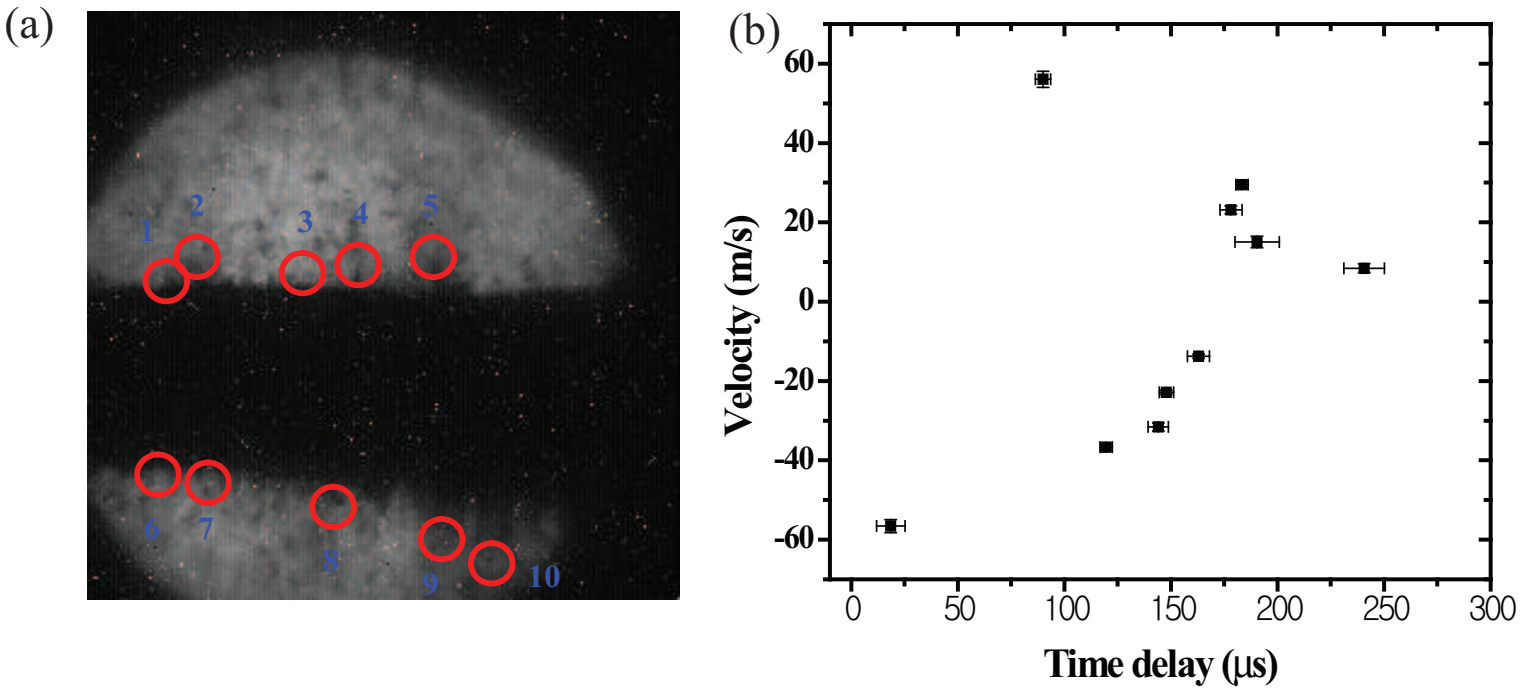

Figure B.16: Location on the Hg jet surface for velocity measurement of filaments. The numbers above red circles points the number of filaments that is used for velocity approximation. Shot number is 12033. a.) Illustration of measured filaments. b.) Velocity of filaments with it's onset time.

Appendix C

Mathematical Derivation for Chapter 2

C.1 The governing equations for MHD in cylindrical coordinates

The momentum equations in the (r, θ, z) coordinates in Fig. 2.2 can be written as follows:

$$-\rho(v_r\frac{\partial v_r}{\partial r}+\frac{v_\theta}{r}\frac{\partial v_r}{\partial \theta}+v_z\frac{\partial v_r}{\partial z})-\frac{\partial p_t}{\partial r}-\rho g\cos\theta+\eta(\frac{\partial^2 v_r}{\partial r^2}+\frac{1}{r}\frac{\partial v_r}{\partial r}+\frac{1}{r^2}\frac{\partial^2 v_r}{\partial \theta^2}+\frac{\partial^2 v_r}{\partial z^2})$$
$$+\frac{1}{\mu}(B_r\frac{\partial B_r}{\partial r}+\frac{B_\theta}{r}\frac{\partial B_r}{\partial \theta}+B_z\frac{\partial B_r}{\partial z})=\rho\frac{\partial v_r}{\partial t}\ , \tag{C.1}$$

$$-\rho(v_r\frac{\partial v_\theta}{\partial r}+\frac{v_\theta}{r}\frac{\partial v_\theta}{\partial \theta}+v_z\frac{\partial v_\theta}{\partial z})-\frac{1}{r}\frac{\partial p_t}{\partial \theta}+\rho g\sin\theta+\eta(\frac{\partial^2 v_\theta}{\partial r^2}+\frac{1}{r}\frac{\partial v_\theta}{\partial r}+\frac{1}{r^2}\frac{\partial^2 v_\theta}{\partial \theta^2}+\frac{\partial^2 v_\theta}{\partial z^2})$$
$$+\frac{1}{\mu}(B_r\frac{\partial B_\theta}{\partial r}+\frac{B_\theta}{r}\frac{\partial B_\theta}{\partial \theta}+B_z\frac{\partial B_\theta}{\partial z})=\rho\frac{\partial v_\theta}{\partial t}\ , \tag{C.2}$$

$$-\rho(v_r\frac{\partial v_z}{\partial r}+\frac{v_\theta}{r}\frac{\partial v_z}{\partial \theta}+v_z\frac{\partial v_z}{\partial z})-\frac{\partial p_t}{\partial z}+\eta(\frac{\partial^2 v_z}{\partial r^2}+\frac{1}{r}\frac{\partial v_z}{\partial r}+\frac{1}{r^2}\frac{\partial^2 v_z}{\partial \theta^2}+\frac{\partial^2 v_z}{\partial z^2})$$
$$+\frac{1}{\mu}(B_r\frac{\partial B_z}{\partial r}+\frac{B_\theta}{r}\frac{\partial B_z}{\partial \theta}+B_z\frac{\partial B_z}{\partial z})=\rho\frac{\partial v_z}{\partial t}\ , \tag{C.3}$$

where $p_t = p + \frac{\mathbf{B}^2}{2\mu}$. The magnetic induction equation in the (r, θ, z) coordinate directions can be written as follows:

$$\frac{1}{\mu\sigma}[\frac{\partial^2 B_r}{\partial r^2}+\frac{1}{r}\frac{\partial B_r}{\partial r}+\frac{1}{r^2}\frac{\partial^2 B_r}{\partial \theta^2}+\frac{\partial^2 B_r}{\partial z^2}]+\frac{1}{r}B_r(r\frac{\partial v_r}{\partial r})+\frac{1}{r}B_\theta\frac{\partial v_r}{\partial \theta}+B_z\frac{\partial v_r}{\partial z}$$
$$-\frac{1}{r}v_r(r\frac{\partial B_r}{\partial r})-\frac{1}{r}v_\theta\frac{\partial B_r}{\partial \theta}-v_z\frac{\partial B_r}{\partial z}=\frac{\partial B_r}{\partial t}\ , \tag{C.4}$$

$$\frac{1}{\mu\sigma}[\frac{\partial^2 B_\theta}{\partial r^2}+\frac{1}{r}\frac{\partial B_\theta}{\partial r}+\frac{1}{r^2}\frac{\partial^2 B_\theta}{\partial \theta^2}+\frac{\partial^2 B_\theta}{\partial z^2}]+\frac{1}{r}B_r(r\frac{\partial v_\theta}{\partial r})+\frac{1}{r}B_\theta\frac{\partial v_\theta}{\partial \theta}+B_z\frac{\partial v_\theta}{\partial z}$$
$$-\frac{1}{r}v_r(r\frac{\partial B_\theta}{\partial r})-\frac{1}{r}v_\theta\frac{\partial B_\theta}{\partial \theta}-v_z\frac{\partial B_\theta}{\partial z}=\frac{\partial B_\theta}{\partial t}\ , \tag{C.5}$$

$$\frac{1}{\mu\sigma}[\frac{\partial^2 B_z}{\partial r^2}+\frac{1}{r}\frac{\partial B_z}{\partial r}+\frac{1}{r^2}\frac{\partial^2 B_z}{\partial \theta^2}+\frac{\partial^2 B_z}{\partial z^2}]+\frac{1}{r}B_r(r\frac{\partial v_z}{\partial r})+\frac{1}{r}B_\theta\frac{\partial v_z}{\partial \theta}+B_z\frac{\partial v_z}{\partial z}$$
$$-\frac{1}{r}v_r(r\frac{\partial B_z}{\partial r})-\frac{1}{r}v_\theta\frac{\partial B_z}{\partial \theta}-v_z\frac{\partial B_z}{\partial z}=\frac{\partial B_z}{\partial t}\ . \tag{C.6}$$

The Ampère's law can be written as

$$j_r=\frac{1}{\mu}(\frac{1}{r}\frac{\partial B_z}{\partial \theta}-\frac{\partial B_\theta}{\partial z})\ ,$$
$$j_\theta=\frac{1}{\mu}(-\frac{\partial B_z}{\partial r}+\frac{\partial B_r}{\partial z})\ ,$$
$$j_z=\frac{1}{\mu}(\frac{\partial B_\theta}{\partial r}-\frac{1}{r}\frac{\partial B_r}{\partial \theta})\ , \tag{C.7}$$

and the equation of continuity and the solenoidal condition for the magnetic field are

$$\frac{1}{r}\frac{\partial}{\partial r}(rv_r) + \frac{1}{r}\frac{\partial v_\theta}{\partial \theta} + \frac{\partial v_z}{\partial z} = 0 \ , \tag{C.8}$$

$$\frac{1}{r}\frac{\partial}{\partial r}(rB_r) + \frac{1}{r}\frac{\partial B_\theta}{\partial \theta} + \frac{\partial B_z}{\partial z} = 0 \ . \tag{C.9}$$

C.2 Derivation of Rayleigh's instability at an interface separating two flows in magnetic field

C.2.1 *kinematic boundary condition at interface*

We consider the (x, y, z) coordinate system in Fig. 2.1. A particle of fluid that is at some time on the free surface will always remain on the free surface. Then, since the equation of the free surface is $y - (\xi + a) = 0$, it follows that

$$\frac{D}{Dt}(y - (\xi + a)) = 0 \ . \tag{C.10}$$

Neglecting quadratically small terms, Eqn. (C.10) yields at the interface($y = \pm a$),

$$\frac{\partial \xi}{\partial t} + U_i \frac{\partial \xi}{\partial x} = \frac{\partial \phi_i}{\partial y} \tag{C.11}$$

In the region $(-a < y < a)$, the velocity potential ϕ_i must satisfy $\frac{\partial^2 \phi_1}{\partial x^2} + \frac{\partial^2 \phi_1}{\partial y^2} = 0$, $|\nabla \phi_1|$=finite. In the region $y > a$, $y < -a$, the velocity potential must satisfy $\frac{\partial^2 \phi_2}{\partial x^2} + \frac{\partial^2 \phi_2}{\partial y^2} = 0$, $|\nabla \phi_2|$=finite. In view of the shape of the interface, the solutions should be trigonometric in x, then the y dependence will be exponential. In view of the finite conditions of velocity potentials, the negative

exponential should be rejected for ϕ_1 and the positive exponential should be rejected for ϕ_2. Therefore, the general solutions are

$$\phi_1(x,y,t) = A_1 e^{(2\pi/\lambda)y} e^{i(2\pi/\lambda)(x-ct)} \ ,$$
$$\phi_2(x,y,t) = A_2 e^{-(2\pi/\lambda)y} e^{i(2\pi/\lambda)(x-ct)} \tag{C.12}$$

Imposing the kinematic conditions on these solutions, the coefficients are determined at $y = a$ and $y = -a$ respectively.

$$\phi_1(x,y,t) = -i\epsilon(c-U_1) e^{i(2\pi/\lambda)(x-ct)} \ ,$$
$$\phi_2(x,y,t) = i\epsilon(c-U_2) e^{i(2\pi/\lambda)(x-ct)} \tag{C.13}$$

,where $U_1 = U_1(a),\ U_2 = U_2(a)$.

$$\phi_1(x,y,t) = i\epsilon(c-U_1) e^{i(2\pi/\lambda)(x-ct)}$$
$$\phi_2(x,y,t) = -i\epsilon(c-U_2) e^{i(2\pi/\lambda)(x-ct)} \tag{C.14}$$

,where $U_1 = U_1(-a),\ U_2 = U_2(-a)$.

Since the perturbed surface at $y = a$ and $y = -a$ are supposed to be symmetric, half of the jet section for the surface stability is considered in the following work.

C.2.2 *hydrodynamic stability in magnetic field*

Substituting the perturbed expressions into the equations of motion, neglecting second order terms in the perturbed quantities, and making use of the fact that U, P satisfy the flow equations and the current density in Lorentz force term can be represented using Ohm's law, we have the linearized equations governing the motion of disturbance.

$$\frac{\partial v'_{xi}}{\partial t} + U_i \frac{\partial v'_{xi}}{\partial x} + v'_{xi} \frac{dU_i}{dy}$$
$$= -\frac{1}{\rho_i}\frac{\partial p'_i}{\partial x} - \frac{\sigma_i}{\rho_i} \mathrm{B}_y^2 v'_{xi} + \frac{\sigma_i}{\rho_i} \mathrm{B}_x \mathrm{B}_y v'_{yi} \tag{C.15}$$

$$\frac{\partial v'_{yi}}{\partial t} + U_i \frac{\partial v'_{yi}}{\partial x} = -\frac{1}{\rho_i}\frac{\partial p'_i}{\partial y} - \frac{\sigma_i}{\rho_i} \mathrm{B}_x^2 v'_{yi} + \frac{\sigma_i}{\rho_i} \mathrm{B}_x \mathrm{B}_y v'_{xi} \tag{C.16}$$

,where $p'_i = f_i(c, \lambda, y) e^{i(2\pi/\lambda)(x-ct)}$.

The perturbed velocity v'_x, v'_y are given

$$v'_x = \frac{\partial \phi_1}{\partial x} = i(\frac{2\pi}{\lambda}) A_1 e^{(2\pi/\lambda)y} e^{i(2\pi/\lambda)(x-ct)}$$
$$v'_y = \frac{\partial \phi_1}{\partial y} = (\frac{2\pi}{\lambda}) A_1 e^{(2\pi/\lambda)y} e^{i(2\pi/\lambda)(x-ct)} \tag{C.17}$$

Putting Eqn. (C.17) into Eqn. (C.15)and Eqn. (C.16), equate the hydrodynamic pressures since it is isotropic, which leads to Rayleigh's stability equation for the flow in magnetic field.

$$\sigma_1 B_x B_y + i\sigma_1 B_x^2 = \sigma_1 B_y^2 i - \sigma_1 B_x B_y + \rho_1 (\frac{\lambda}{2\pi}) \frac{d^2 U_1}{dy^2} \tag{C.18}$$

,where $U_1 = U_1(y)$.

In the same manner, the Rayleigh's stability equation for the upper flow in magnetic field is be derived.

$$\sigma_2 B_x^2 + \sigma_2 B_x B_y i = \sigma_2 B_y^2 - i\sigma_2 B_x B_y - \rho_2 i (\frac{\lambda}{2\pi}) \frac{d^2 U_2}{dy^2} \tag{C.19}$$

,where $U_2 = U_2(y)$.

C.2.3 *dynamic boundary condition at interface*

The difference of the normal stresses must be balanced by the normal stress induced by surface tension at the interface.

$$(P_1 + \frac{\partial P_1}{\partial y}\xi + \frac{\partial^2 P_1}{\partial y^2}\xi + \ldots + p'_1) - (P_2 + \frac{\partial P_2}{\partial y}\xi + \frac{\partial^2 P_2}{\partial y^2}\xi + \ldots + p'_2) + \Gamma \frac{\partial^2 \xi}{\partial x^2} = 0 \tag{C.20}$$

, where Γ is surface tension.

Considering the gravity force in the free surface waves, Eqn. (C.20) can be rewritten as follows.

$$
\begin{aligned}
&(\rho_2-\rho_1)g\cos\theta+\rho_1(c-U_1)^2(\frac{2\pi}{\lambda})+\rho_2(c-U_2)^2(\frac{2\pi}{\lambda})\\
&+\rho_1(c-U_1)\frac{dU_1}{dy}-\rho_2(c-U_2)\frac{dU_2}{dy}+iB_y^2(\sigma_1(c-U_1)+\sigma_2(c-U_2))\\
&+B_xB_y(\sigma_2(c-U_2)-\sigma_1(c-U_1))-\Gamma(\frac{2\pi}{\lambda})^2=0
\end{aligned}
\tag{C.21}
$$

,where $U_1=U_1(a),\ U_2=U_2(a)$.

Consider the case that $U_2=0, \frac{dU_2}{dy}=0, \rho_2=0, \sigma_2=0$. This would correspond to the stationary fluid on the upper and the density and conductivity of the upper fluid are very small compared with these of the lower fluid. The wave velocity is represented as follow.

$$
\begin{aligned}
c=[\ \ &-\rho_1\frac{dU_1}{dy}+B_xB_y\sigma_1-iB_y^2\sigma_1+2(\frac{2\pi}{\lambda})\rho_1U_1\\
&\pm\sqrt{\rho_1^2(\frac{dU_1^2}{dy})+4(\frac{2\pi}{\lambda})\cos\theta g\rho_1^2-2B_xB_y\rho_1\sigma_1\frac{dU_1}{dy}+2iB_y^2\rho_1\sigma_1\frac{dU_1}{dy}}\\
&\overline{+B_x^2B_y^2\sigma_1^2-2iB_xB_y^3\sigma_1^2-B_y^4\sigma_1^2+4(\frac{2\pi}{\lambda})^3\rho_1\Gamma}\ \ ]\times\frac{1}{2(\frac{2\pi}{\lambda})\rho_1}
\end{aligned}
\tag{C.22}
$$